

UNIVERSITÀ DEGLI STUDI DI NAPOLI FEDERICO II



SCUOLA POLITECNICA E DELLE SCIENZE DI BASE

CLASSE DELLE LAUREE MAGISTRALI IN INGEGNERIA AEROSPAZIALE E
ASTRONAUTICA

DIPARTIMENTO DI INGEGNERIA INDUSTRIALE
SEZIONE AEROSPAZIALE

MASTER THESIS

DORSAL FIN PRELIMINARY DESIGN PROCEDURE THROUGH CFD ANALYSIS

SUPERVISOR:

Prof. Eng.
FABRIZIO NICOLOSI

CANDIDATE:

EMANUELE DELLA VOLPE
Matr.: M53/000372

CO-SUPERVISOR:

Eng.
CILIBERTI DANILLO

ANNO ACCADEMICO 2014/2015

Dedicated to all those who supported me in this project.

Dedicated to all those who believed in my motivation.

Dedicated to all the professors who have helped to make me passionate about
aerospace engineering.

Dedicated to the colleagues with which I shared the studies and with whom I have built
my training.

Dedicated to my family that more than any other was near in difficult times.

ABSTRACT

This thesis is part of a wider issue, which is the development of methods for the prediction of the aerodynamic characteristics of the aircraft.

The present work seeks to provide guidelines on preliminary sizing of a dorsal fin of an aircraft of turboprop class, through computational fluid dynamics, and aims to extend the initial planning method of the vertical tail developed at the Department of Industrial Engineering, sect. Aerospace, by Professor Nicolosi and his collaborators.

After characterizing the phenomena of directional stability, the work is divided into two phases. The first is the search for what literature offers on the stability characteristics in the presence of dorsal fin. After identifying the report more responsive about the needs of our work, we start from that point of reference, so test cases are performed in order to verify the compliance between CFD results and experimental data.

The second phase involves the construction of a preliminary design procedure through a series of parametric analyzes performed with the software Star-CCM+. Are so carried out a series of test cases, based on the report of the above. Then collecting a large amount of numerical data, it is possible to extract the qualitative trend of the parametric analysis.

A large number of simulations were run in the SCoPE grid infrastructure of the University of Naples 'Federico II', that gave the possibility to simulate complex 3D geometries in a small amount of time.

SOMMARIO

Questo lavoro di tesi si inserisce in una tematica più ampia, che è quella dello sviluppo di metodologie per la predizione delle caratteristiche aerodinamiche dei velivoli.

Il presente lavoro vuole fornire delle linee guida sul dimensionamento preliminare di una dorsal fin di un velivolo di classe turboprop, attraverso la fluidodinamica computazionale, e mira ad estendere il metodo di avanprogetto del piano verticale di coda sviluppato presso il Dipartimento di Ingegneria Industriale, sez. Aerospaziale, dal Prof. Nicolosi e dai suoi collaboratori.

Dopo aver caratterizzato i fenomeni della stabilità direzionale il lavoro si articola in due fasi.

La prima prevede la ricerca di quanto la letteratura offre sulle caratteristiche di stabilità in presenza di dorsal fin. E stato quindi identificato il report maggiormente rispondente alle necessità del nostro lavoro, ed a partire da tale punto di riferimento sono stati effettuati dei test case in modo da verificare la rispondenza dei risultati CFD con i dati sperimentali.

La seconda prevede la realizzazione di una procedura di design preliminare attraverso una serie di analisi parametriche eseguite con il software STAR-CCM+. Sono quindi effettuati una serie di test case, basati sul report di cui sopra, il cui scopo è quello di collezionare una grande quantità di dati dai quali è possibile estrarre i trend qualitativi dell'analisi parametrica.

Questo gran numero di simulazioni è stato elaborato nella griglia di calcolo SCoPE dell'Università di Napoli 'Federico II', con lo scopo di analizzare complesse geometrie 3D in un tempo relativamente breve.

<u>FIGURE INDEX</u>	6
<u>TABLE INDEX</u>	12
<u>SHORT LIST OF SYMBOLS</u>	13
1. <u>INTRODUCTION</u>	16
1.1 PHENOMENOLOGY	16
1.1.1 THE CONCEPT OF STABILITY.....	16
1.1.2 DIRECTIONAL STABILITY PROBLEM.....	17
1.1.3 FUNDAMENTALS OF STATIC DIRECTIONAL AND LATERAL STABILITY.....	18
1.1.4 REQUIREMENTS FOR STATIC DIRECTIONAL STABILITY.....	19
1.2 NECESSITY OF DORSAL FIN	21
1.2.1 GENERAL DEFINITION OF DORSAL FIN.....	21
1.2.2 RUDDER DEFLECTION & PEDALBOARD EFFORT.....	21
1.2.3 THE RUDDER LOCKING PHENOMENON.....	22
1.2.4 DORSAL FIN AS SOLUTION FOR RUDDER LOCKING	23
1.2.5 OTHER REASON FOR DORSAL FIN.....	26
1.3 METHODOLOGY EVOLUTION FOR THE STUDY OF LATERAL-DIRECTIONAL STABILITY	27
2. <u>DORSAL FIN INVESTIGATION</u>	29
2.1 SEARCH FOR REFERENCES IN LITERATURE.....	29
2.2 SYNTHESIS OF DORSAL FIN SIZING METHOD NO.1	33
3. <u>NUMERICAL STUDY THROUGH CFD</u>	37
3.1 THE CFD APPROACH	37
3.2 THE SOFTWARE STAR-CCM+.....	37
3.3 SIMULATION WORKFLOW.....	37
3.3.1 MESH GENERATION.....	39
3.3.2 DEFINING THE PHYSICS.....	39
3.3.3 CONVERGENCE.....	40
3.4 THE SCOPE GRID INFRASTRUCTURE [6],[1].....	40
3.5 MY SIMULATION.....	42
4. <u>SETUP SIMULATION</u>	54
4.1 MESH ANALYSIS.....	54
4.2 MESH CHOICE.....	58
4.2.1 CLARIFICATION ON THE COEFFICIENT OSCILLATIONS.....	61

4.3 AERODYNAMICS RESULTS.....	63
4.3.1 VORTEX LIFT	63
4.3.2 CONTRIBUTION TO DIRECTIONAL STABILITY.....	65
4.3.3 SUMMARY OF RESULTS FOR BVD CONFIGURATION	66
4.4 MACRO JAVA FOR THE AUTOMATED PROCEDURE.....	66
4.5 PARTIAL CONFIGURATIONS	67
4.6 AERODYNAMIC INTERFERENCE SIGNIFICANCE	70
4.6.1 MUTUAL EFFECT BETWEEN BODY, VERTICAL & DORSAL.....	72
5. <u>BASELINE</u>.....	78
5.1 DORSAL FIN PRIMARY EFFECT ON THE VERTICAL TAIL STABILITY.....	78
5.1.1. RELEASED VORTICITY.....	82
5.1.2 QUALITATIVE COMPARISON ABOUT VORTICITY.....	84
5.2 DORSAL FIN EFFECT ON THE FUSELAGE STABILITY.	93
5.3 DORSAL FIN PRIMARY EFFECT ON THE OVERALL STABILITY.....	94
5.3.1 PRESSURE REDISTRIBUTION.	95
5.4 PARTICULAR DORSAL FIN EFFECT ABOUT DIRECTIONAL STABILITY.....	100
5.5 CONCLUSIONS FOR BASELINE.....	103
6. <u>PARAMETRIC ANALYSIS</u>.....	104
6.1 MOTIVATION.....	104
6.2 WORKFLOW.....	104
6.2.1 BASIC STEPS.....	105
6.3 PARAMETRIC ANALYSIS EXTRACTION FROM THE REPORT	
INFORMATION.....	106
6.4 GEOMETRIC CONTROL OF PARAMETERIZATION.....	107
6.5 AERODYNAMIC RESULT OF PARAMETERIZATIONS.....	108
6.5.1 CHANGE OF h, df.....	108
6.5.2 CHANGE OF L, df.....	120
6.5.3 COMPARISON OF EQUAL VARIATION OF SURFACE.....	131
6.5.4 CHANGE OF L,df & h,df, TO KEEP CONSTANT ARROW AND VARY THE	
SURFACE.....	136
6.5.5 CHANGE OF L,df & h,df, TO KEEP SURFACE CONSTANT AND VARY THE	
SWEEP.....	147
6.5.6 EQUAL SURFACE VARIATION AT TWO DIFFERENT ANGLES OF	
SWEEP.....	155
7 <u>CORRELATED STUDIES</u>.....	167
7.1 CHARACTERISTIC TIMES OF ANALYSIS	167
7.2 DRAG PENALTY.....	167
7.3 REYNOLDS EFFECT INVESTIGATION.....	169

8 CONCLUSION.....	172
<u>APPENDIX A.....</u>	173
<u>BIBLIOGRAPHY.....</u>	175

Figure Index

<i>Figure 1 – Directional Dynamics.....</i>	16
<i>Figure 2 – Roll or Bank.....</i>	18
<i>Figure 3 – Yaw.....</i>	18
<i>Figure 4 – Definition of slipping (sideslip) and skidding.....</i>	19
<i>Figure 5 – Reference system of the analysis.....</i>	20
<i>Figure 6 – Requirements for static directional stability of an aircraft [2].....</i>	20
<i>Figure 7 –Dorsal Fin example.....</i>	21
<i>Figure 8 – Rudder deflection $\delta r,eq$ & $\delta r,float$ [10].....</i>	21
<i>Figure 9 – Pedalboard Effort as function of Sideslip Angle.....</i>	22
<i>Figure 10 – Lift curve as function of AR.....</i>	22
<i>Figure 11 – How a dorsal fin prevents rudder lock [2].....</i>	24
<i>Figure 12 – Rudder Lock in presence of Anti-Tab Conceptual effect.....</i>	24
<i>Figure 13 – Rudder Lock in presence of Dorsal fin conceptual effect.....</i>	25
<i>Figure 14 – Effect of a dorsal fin on the yawing moment coefficient [4].....</i>	25
<i>Figure 15 – Rudder lock in presence of Dorsal Fin (Actual).....</i>	26
<i>Figure 16 – Different dorsal fin investigated for a Fokker F-27 [4].....</i>	30
<i>Figure 17 – Effect of a dorsal fin on the yawing moment coefficient [4].....</i>	30
<i>Figure 18 – Effect of a dorsal fin on the yawing moment coefficient [4].....</i>	31
<i>Figure 19 – Vortex formations by a dorsal fin [3].....</i>	31
<i>Figure 20 – Side view of three vertical tail surfaces and a dorsal fin investigated during the development of the Fokker F-28 [4].....</i>	32
<i>Figure 21 – Effect of sweep angle on vertical tailplane lift curve. Angle of attack 0° [4].....</i>	32
<i>Figure 22 – Effect of sweep angle on vertical tailplane lift curve. Angle of attack 8° [4].....</i>	33
<i>Figure 23 – Vertical & Dorsal fin Geometric Parameters [3].....</i>	33
<i>Figure 24 – Dorsal fin resulting from the Geometric-statistical Method no.1 [3].....</i>	34
<i>Figure 25 – The Final Reference Geometry of Dorsal fin.....</i>	36
<i>Figure 26 – General sequence of operation for a STAR-CCM+ analysis.....</i>	38
<i>Figure 27 –Optical fibers network link for the Grid SooPE [1].....</i>	40
<i>Figure 28 –SCoPE data Center, Device & Connections [6].....</i>	41
<i>Figure 29 – Root Section of Dorsal fin in CAD design environment in STAR-CCM+.....</i>	42
<i>Figure 30 – Tip Section of Dorsal fin in CAD design environment in STAR-CCM+.....</i>	42
<i>Figure 31 – Leading Edge of Root Section of Dorsal fin.....</i>	43
<i>Figure 32 – 3D View and Perspective View of Final Geometry of Dorsal fin.....</i>	43
<i>Figure 33 – List of investigated section of Dorsal fin.....</i>	44
<i>Figure 34 – $Z = 85\%$ of h,df.....</i>	44
<i>Figure 35 – $Z = 50\%$ of h,df.....</i>	44
<i>Figure 36 – $Z = 15\%$ of h,df.....</i>	45
<i>Figure 37 – Top view to evaluate the tangency condition between Dorsal and Vertical for the root station.....</i>	45
<i>Figure 38 – 3D View for ATR as Example of Dorsal Fin Geometry.....</i>	45
<i>Figure 39 – Different Example of Dorsal Fin Geometry, C-40_B-737, II-18D, ERj-190,</i>	46

<i>Figure 40 – View and side view of conventional tail without dorsal fin (with sharp leading edge) of a Cessna Citation CJ3 (automobile 2013 and Blueprints 2013).</i>	47
<i>Figure 41 – View and side view of a dorsal fin of a Fokker 70 (Aero 2013 and Fly Fokker 2013).</i>	47
<i>Figure 42 – View and side view of a round edge dorsal fin of an A 320 (Prendrel 2013 and Aerospaceweb 2013).</i>	47
<i>Figure 43 – View and side view of a dorsal fin of a Fokker 70 (Aero 2013 and Fly Fokker 2013).</i>	47
<i>Figure 44 – View and side view of combined dorsal fin with dorsal extension of a Q-400 dash 8 (Aerospace 2013 and Aviastar 2013c).</i>	47
<i>Figure 45 – View and side view of combined dorsal fin with dorsal extension blending into one another on a Bae 146 (Tutavia 2013 and Aviastar 2013).</i>	48
<i>Figure 46 – Physics Model Selection windows control of STAR-CCM+.</i>	48
<i>Figure 47 – Computational Domain of Simulation of STAR-CCM+.</i>	49
<i>Figure 48 – Geometry list of Simulation of STAR-CCM+.</i>	49
<i>Figure 49 – Relative Dimension between Aircraft and overall Domain of STAR-CCM+.</i>	50
<i>Figure 50 – Final Computational Domain of simulation of STAR-CCM+.</i>	50
<i>Figure 51 – Tetrahedral Mesh Surface of STAR-CCM+.</i>	51
<i>Figure 52 – No Structural Mesh Volume of STAR-CCM+.</i>	51
<i>Figure 53 – Properties Windows for Coefficient Setting of STAR-CCM+.</i>	52
<i>Figure 54 – Residual Example of a simulation of STAR-CCM+.</i>	52
<i>Figure 55 – Report Plot Example of a simulation of STAR-CCM+.</i>	53
<i>Figure 56 – Output Report Example of a simulation of STAR-CCM+.</i>	53
<i>Figure 57 – Trade off on Base size.</i>	54
<i>Figure 58 – Macroscopic Visual Analysis of the sample mesh.</i>	55
<i>Figure 59 – Curved Surfaces of the sample mesh.</i>	55
<i>Figure 60 – Geometric Discontinuities of the sample mesh.</i>	56
<i>Figure 61 – Fusion between the Dorsal fin and the Vertical of the sample mesh.</i>	56
<i>Figure 62 – $Z = 85\%$ of h,df.</i>	56
<i>Figure 63 – Intersection between the vertical plane and fuselage.</i>	57
<i>Figure 64 – Sharp edges of the vertical edges of the tip section and the trailing edge.</i>	57
<i>Figure 65 – CPU Time Trend for the analyzed mesh.</i>	57
<i>Figure 66 – Result as function of Mesh Refinement's Level for $\beta=5^\circ$.</i>	58
<i>Figure 67 – Result as function of Mesh Refinement's Level for $\beta=19^\circ$.</i>	58
<i>Figure 68 – Result as function of Mesh Refinement's Level for $\beta=38^\circ$.</i>	59
<i>Figure 69 – Tread of Analysis of Mesh Refinement's Level for Total yawing moment result.</i>	60
<i>Figure 70 – Tread of Analysis of Mesh Refinement's Level for Dorsal yawing moment result.</i>	60
<i>Figure 71 – Coefficient Oscillation Example for Mesh 3.</i>	61
<i>Figure 72 – Coefficient Oscillation Example for Mesh 2.</i>	61
<i>Figure 73 – Coefficient Oscillation Influence Example</i>	62
<i>Figure 74 – Comparison with Military Wings Type.</i>	63
<i>Figure 75 – Vortex Lift Generation for Delta Wings</i>	63
<i>Figure 76 – Vortex Lift Generation for my Geometry resulting from CFD Analysis.</i>	64
<i>Figure 77 – Contribute summation to directional stability of Vertical + Dorsal for BVD configuration.</i>	64
<i>Figure 78 – Contribution to directional stability comparison between Literature [3] and CFD results.</i>	65
<i>Figure 79 – Individual contributions to directional stability for BVD configuration, CFD Results.</i>	66

<i>Figure 80 – Summary of the contributions to directional stability for partial configuration, CFD Result.</i>	68
<i>Figure 81 –Dorsal fin effect on Vertical tailplane in term of stability increment, CFD Result.</i>	69
<i>Figure 82 – Summary of total contribution of yawing moment for V, BV, BVD configuration, CFD results.</i>	70
<i>Figure 83 – Summary of total contribution of sideforce for V, BV, BVD configuration, CFD results.</i>	71
<i>Figure 84 – Mutual effect between Body & Vertical, CFD results.</i>	72
<i>Figure 85 – Mutual effect between Body & Vertical, CFD results.</i>	73
<i>Figure 86 – Dorsal fin effect on yawing moment for Body, Vertical, Body + Vertical, CFD.</i>	74
<i>Figure 87 – Dorsal fin effect on sideforce Body, Vertical and Body + Vertical, CFD results.</i>	75
<i>Figure 88 – Effects on body yawing moment contribution of consecutive adding of parts, CFD results.</i>	76
<i>Figure 89 – Effects on body sideforce contribution of consecutive adding of parts, CFD results.</i>	76
<i>Figure 90 – Effects on Vertical yawing moment contribution of consecutive adding of parts, CFD results.</i>	77
<i>Figure 91 – Effects on Vertical sideforce contribution of consecutive adding of parts, CFD results.</i>	77
<i>Figure 92 – Dorsal fin Effects on vertical empennage stability, CFD results.</i>	78
<i>Figure 93 – Dorsal fin Effects on vertical empennage stability, Literature results [4].</i>	79
<i>Figure 94 – Side View of Skin Friction Coefficient in without Dorsal fin.</i>	79
<i>Figure 95 – Side View of Streamline Evolution without Dorsal fin.</i>	80
<i>Figure 96 – Side View of Skin Friction Coefficient with Dorsal fin.</i>	80
<i>Figure 97 – Side View and Frontal View of the Streamline Evolution with Dorsal fin</i>	81
<i>Figure 98 – Side View and Top View of the Streamline evolution with Dorsal fin</i>	81
<i>Figure 99 – How the Vortex splits the fin into Upper and Lower halves.</i>	82
<i>Figure 100 – Side View of Skin Friction, Streamline and Vorticity with Dorsal fin.</i>	82
<i>Figure 101 – Frontal View of Skin Friction, Streamline and Vorticity with Dorsal fin.</i>	83
<i>Figure 102 – Top view of Skin Friction, Streamline and Vorticity with Dorsal fin.</i>	83
<i>Figure 103 – Visualization of nonlinear range to study the dorsal effect about the aerodynamics phenomena.</i>	84
<i>Figure 104 –Side View of the Streamline with Dorsal fin at $\beta = 19^\circ$.</i>	85
<i>Figure 105 –Side View of the Streamline with Dorsal fin at $\beta = 29^\circ$.</i>	85
<i>Figure 106 –Side View of the Streamline with Dorsal fin at $\beta = 40^\circ$.</i>	85
<i>Figure 107 – Top View of the Streamline with Dorsal fin at $\beta = 19^\circ$.</i>	86
<i>Figure 108 – Top View of the Streamline with Dorsal fin at $\beta = 40^\circ$.</i>	86
<i>Figure 109 – Frontal View of the Streamline with Dorsal fin at $\beta = 19^\circ$.</i>	87
<i>Figure 110 – Frontal View of the Streamline with Dorsal fin at $\beta = 29^\circ$.</i>	87
<i>Figure 111 – Top View of the Streamline with Dorsal fin at $\beta = 39^\circ$.</i>	87
<i>Figure 112 – Overall Frontal View with Dorsal fin at $\beta = 19^\circ$.</i>	88
<i>Figure 113 – Overall Frontal View with Dorsal fin at $\beta = 43^\circ$.</i>	88
<i>Figure 114 – View of the Streamline with Dorsal fin at $\beta = 10^\circ$.</i>	88
<i>Figure 115 – View of the Streamline with Dorsal fin at $\beta = 15^\circ$.</i>	89
<i>Figure 116 – View of the Streamline with Dorsal fin at $\beta = 19^\circ$.</i>	89
<i>Figure 117 – View of the Streamline with Dorsal fin at $\beta = 21^\circ$.</i>	89
<i>Figure 118 – View of the Streamline with Dorsal fin at $\beta = 23^\circ$.</i>	89
<i>Figure 119 – View of the Streamline with Dorsal fin at $\beta = 26^\circ$.</i>	90
<i>Figure 120 – View of the Streamline with Dorsal fin at $\beta = 29^\circ$.</i>	90

<i>Figure 121 – View of the Sreamline with Dorsal fin at $\beta = 40^\circ$.</i>	90
<i>Figure 122 – List of analyzed section for Pressure Coefficient distribution analysis by varing the sideslip angle, CFD results.</i>	91
<i>Figure 123 – Pressure Coefficient Comparison for BVD Configuration at 15% of vertical aperture.</i>	91
<i>Figure 124 – Pressure Coefficient Comparison for BVD Configuration at 40% of vertical aperture.</i>	92
<i>Figure 125 – Pressure Coefficient Comparison for BVD Configuration at 40% of vertical aperture.</i>	92
<i>Figure 126 – Dorsal effect on Body contribution of yawing moment, CFD results.</i>	93
<i>Figure 127 – Side View for Pressure Coefficient Comparison at Windward Side with and without Dorsal fin at $\beta = 40^\circ$.</i>	93
<i>Figure 128 – Side View for Pressure Coefficient Comparison at leeward Side with and without Dorsal fin at $\beta = 40^\circ$.</i>	94
<i>Figure 129 – Reduction of stability due to Body contribution, CFD results.</i>	94
<i>Figure 130 – Angle selection for the same Value in Different Configuration.</i>	95
<i>Figure 131 – Pressure Coefficient Comparison between BV at 15° and BVD at 19° both stations at 50% of vertical aperture.</i>	95
<i>Figure 132 – Pressure Coefficient Comparison between BV at 15° and BVD at 15° both stations at 50% of vertical aperture.</i>	96
<i>Figure 133 – Pressure Coefficient Comparison between BV at 15° & 19°, stations at 50% of vertical aperture.</i>	97
<i>Figure 134 – Pressure Coefficient Contour Plot for BVD Configuration at 50% of vertical aperture for $\beta = 19^\circ$.</i>	97
<i>Figure 135 – Pressure Coefficient Contour Plot for BV Configuration at 50% of vertical aperture for $\beta = 15^\circ$.</i>	97
<i>Figure 136 – Pressure Coefficient Contour Plot for BV Configuration at 50% of vertical aperture for $\beta = 19^\circ$.</i>	98
<i>Figure 137 – Pressure Coefficient Contour Plot for BV Configuration at 50% of vertical aperture for $\beta = 15^\circ$.</i>	98
<i>Figure 138 – Pressure Coefficient comparison at windward side for BV & BVD Configuration at $\beta = 15^\circ$.</i>	98
<i>Figure 139 – Pressure Coefficient comparison at leeward side for BV & BVD Configuration at $\beta = 15^\circ$.</i>	99
<i>Figure 140 – Summary of the roles of the individual contribution of BVD configuration respect the total contribution of BV configuration.</i>	100
<i>Figure 141 – View of the Sreamline whit & without Dorsal fin at $\beta = 10^\circ$.</i>	101
<i>Figure 142 – View of the Sreamline with & without Dorsal fin at $\beta = 15^\circ$.</i>	101
<i>Figure 143 – Reduction of Vertical contribution of yawing moment in presence of dorsal fin.</i>	102
<i>Figure 144 – Perfect correspondence of yawing moment in linear range with and without dorsal fin.</i>	102
<i>Figure 145 – CLa as function of AR.</i>	103
<i>Figure 146 – Vertical & Dorsal fin Geometric Parameters.</i>	104
<i>Figure 147 – Different Dorsal fin Investigated for a Fokker F-27 [4].</i>	105
<i>Figure 148 – Effect of a Dorsal fin on the Yawing Moment Coefficient [4].</i>	105
<i>Figure 149 – Reference Geometry, viewing and its characteristics value.</i>	108
<i>Figure 150 – h,df parameterization, geometry viewing characteristic values.</i>	109
<i>Figure 151 – Yawing moment coefficient of total contribution of BVD configuration.</i>	110
<i>Figure 152 – Obert investigation results about Yawing moment coefficient.</i>	110

<i>Figure 153 – Yawing moment coefficient of Body + Vertical contribution of BVD configuration.</i>	111
<i>Figure 154 – Yawing moment coefficient of Dorsal fin contribution of BVD configuration. ...</i>	112
<i>Figure 155 – Yawing moment coefficient of Vertical contribution of BVD configuration.....</i>	113
<i>Figure 156 – Yawing moment coefficient of Vertical + Dorsal fin contribution of BVD configuration.....</i>	114
<i>Figure 157 – Yawing moment coefficient of Body contribution of BVD configuration.</i>	115
<i>Figure 158 – h,df parameterization, geometry viewing characteristic values.....</i>	116
<i>Figure 158 – Yawing moment coefficient reduction due to the Body contribution for Dorsal no.1 & Dorsal no.3 of BVD configuration.</i>	116
<i>Figure 160 – Yawing moment coefficient of Vertical + Dorsal summation for Dorsal no.1 & Dorsal no.3 of BVD configuration.</i>	117
<i>Figure 161 – Yawing moment coefficient coincidence between Vertical + Dorsal summation of BVD configuration and Vertical contribution of BV configuration for Dorsal no.1 & Dorsal no.3.....</i>	118
<i>Figure 162 – How the vertical work less in BVD configuration with respect the Vertical contribution of BV configuration for Dorsal no.1 & Dorsal no.3.</i>	119
<i>Figure 163 – L,df parameterization, geometry viewing characteristic values.....</i>	120
<i>Figure 164 – Yawing moment coefficient of total contribution of BVD configuration.</i>	121
<i>Figure 165 – Obert investigation results about Yawing moment coefficient.</i>	121
<i>Figure 166 – Yawing moment coefficient of Body + Vertical contribution of BVD configuration.</i>	122
<i>Figure 167 – Yawing moment coefficient of Dorsal fin contribution of BVD configuration. ...</i>	123
<i>Figure 168 – Yawing moment coefficient of Body + Vertical contribution of BVD configuration.</i>	124
<i>Figure 169 – Yawing moment coefficient of Vertical + Dorsal fin contribution of BVD configuration.....</i>	125
<i>Figure 170 – Yawing moment coefficient of Body contribution of BVD configuration.</i>	126
<i>Figure 171 – Yawing moment coefficient reduction due to the Body contribution for Dorsal no.1 & Dorsal no.5 of BVD configuration.</i>	127
<i>Figure 172 – Yawing moment coefficient of Vertical + Dorsal summation for Dorsal no.1 & Dorsal no.3 of BVD configuration.</i>	128
<i>Figure 173 – Yawing moment coefficient coincidence between Vertical + Dorsal summation of BVD configuration and Vertical contribution of BV configuration for Dorsal no.1 & Dorsal no.3.....</i>	129
<i>Figure 174 – How the vertical work less in BVD configuration with respect the Vertical contribution of BV configuration for Dorsal no.1 & Dorsal no.5.</i>	130
<i>Figure 175 – L,df & h,df parameterization to change S,df, geometry viewing and characteristic values.....</i>	131
<i>Figure 176 – How the vertical work less in BVD configuration respect an variation of $\pm 30\%$ obtained by changing h,df or L,df.</i>	132
<i>Figure 177 – How the fuselage modifies the stability in BVD configuration respect an variation of $\pm 30\%$ obtained by changing h,df or L,df.....</i>	133
<i>Figure 178 – How the Vertical +Dorsal modifies the stability in BVD configuration respect an variation of $\pm 30\%$ obtained by changing h,df or L,df.</i>	134
<i>Figure 179 – How the Dorsal modifies the stability in BVD configuration respect an variation of $\pm 30\%$ obtained by changing h,df or L,df.....</i>	135
<i>Figure 180 – How the total contribution modifies the stability in BVD configuration respect an variation of $\pm 30\%$ obtained by changing h,df or L,df.</i>	136

<i>Figure 181 – S,df parameterization, geometry viewing characteristic values.</i>	138
<i>Figure 182 – Yawing moment coefficient of total contribution of BVD configuration.</i>	138
<i>Figure 183 – Obert investigation results about Yawing moment coefficient.</i>	139
<i>Figure 184 – Yawing moment coefficient of Body + Vertical contribution of BVD configuration.</i>	139
<i>Figure 185 – Yawing moment coefficient of Dorsal fin contribution of BVD configuration.</i>	140
<i>Figure 186 – Yawing moment coefficient of Body + Vertical total contribution of BVD configuration.</i>	141
<i>Figure 187 – Yawing moment coefficient of Vertical + Dorsal fin contribution of BVD configuration.</i>	142
<i>Figure 188 – Yawing moment coefficient of the Body contribution of BVD configuration.</i>	143
<i>Figure 189 – Yawing moment coefficient reduction due to the Body contribution for Dorsal no.3 & Dorsal no.5 of BVD configuration.</i>	144
<i>Figure 190 – Yawing moment coefficient of Vertical + Dorsal summation for Dorsal no.3 & Dorsal no.5 of BVD configuration.</i>	145
<i>Figure 191 – Yawing moment coefficient coincidence between Vertical + Dorsal summation of BVD configuration and Vertical contribution of BV configuration for Dorsal no.3 & Dorsal no.5.</i>	146
<i>Figure 192 – How the vertical work less in BVD configuration with respect the Vertical contribution of BV configuration for Dorsal no.1 & Dorsal no.3.</i>	147
<i>Figure 193 – $\phi_{o,df}$ parameterization, geometry viewing characteristic values.</i>	148
<i>Figure 194 – Yawing moment coefficient of total contribution of BVD configuration.</i>	149
<i>Figure 183 – Obert investigation results about Yawing moment coefficient.</i>	149
<i>Figure 196 – Yawing moment coefficient of Body + Vertical contribution of BVD configuration.</i>	150
<i>Figure 197 – Yawing moment coefficient of Dorsal fin contribution of BVD configuration.</i>	151
<i>Figure 198 – Yawing moment coefficient of Body + Vertical total contribution of BVD configuration.</i>	152
<i>Figure 199 – Yawing moment coefficient of Vertical + Dorsal fin contribution of BVD configuration.</i>	153
<i>Figure 200 – Yawing moment coefficient of Body contribution of BVD configuration.</i>	154
<i>Figure 201 – S,df parameterization for $\phi_{o,df} = 77^\circ$, geometry viewing characteristic values.</i>	155
<i>Figure 202 – Yawing moment coefficient of Body + Vertical contribution of BVD configuration for Surface variation, fixed sweep angle 77°.</i>	156
<i>Figure 203 – Yawing moment coefficient of Vertical contribution of BVD configuration, for Surface variation fixed sweep angle 77°.</i>	157
<i>Figure 204 – Yawing moment coefficient of Dorsal fin contribution of BVD configuration, for Surface variation fixed sweep angle 77°.</i>	158
<i>Figure 205 – Yawing moment coefficient of Vertical + Dorsal fin contribution of BVD configuration, for Surface variation fixed sweep angle 77°.</i>	158
<i>Figure 206 – Yawing moment coefficient of Body contribution of BVD configuration, for Surface variation fixed sweep angle 77°.</i>	159
<i>Figure 207 – Yawing moment coefficient of total contribution of BVD configuration, for Surface variation fixed sweep angle 77°.</i>	160
<i>Figure 208 – S,df parameterization for $\phi_{o,df} = 66^\circ$, geometry viewing characteristic values.</i>	161
<i>Figure 209 – Yawing moment coefficient of Body + Vertical contribution of BVD configuration fixed sweep angle 65°.</i>	162

<i>Figure 210 – Yawing moment coefficient of Body + Vertical total contribution of BVD configuration, fixed sweep angle 65°.</i>	163
<i>Figure 211 – Yawing moment coefficient of Dorsal fin contribution of BVD configuration fixed sweep angle 65°.</i>	164
<i>Figure 212 – Yawing moment coefficient of Vertical + Dorsal fin contribution of BVD configuration fixed sweep angle 65°.</i>	164
<i>Figure 213 – Yawing moment coefficient of Body contribution of BVD configuration fixed sweep angle 65°.</i>	165
<i>Figure 214 – Yawing moment coefficient of total contribution of BVD configuration fixed sweep angle 65°.</i>	166
<i>Figure 215 – Summary of drag penalty results compared with semi-empirical method.</i>	168
<i>Figure 216 – Reynolds analysis for the contributions of BV configuration.</i>	169
<i>Figure 217 – Difference between the results with different Reynolds numbers for the contributions of BV configuration.</i>	170
<i>Figure 218 – Reynolds analysis for the contributions of BVD configuration.</i>	170
<i>Figure 219 – Difference between the result with different Reynolds numbers for the contributions of BVD configuration.</i>	171

Table index

<i>Table 1 – Application of Method no.1 for Propeller Aircraft List [3].</i>	
<i>Table 2 – Reference Geometry Parameters and characteristics ratio.</i>	
<i>Table 3 – Summary of Mesh parameters for BVD configurations.</i>	
<i>Table 4 – Reference Geometry Parameters and characteristics ratio.</i>	
<i>Table 5 – Summary of drag penalty results and geometry indication.</i>	
<i>Table 6 – Parameter definition for Reynolds investigation.</i>	

SHORT LIST OF SYMBOLS

AR _w	wing aspect ratio
AR	dorsal aspect ratio
Ar _v	vertical tailplane aspect ratio
CL	lift force coefficient
CL _α	lift curve slope
CL _{α,v}	vertical tailplane lift curve slope
CN	yawing moment coefficient
CN _β	yawing moment due to sideslip derivative
CN _{β,v}	vertical yawing moment due to sideslip derivative
CY	sideforce coefficient
Cy _β	sideforce due to sideslip derivative
Cy _{β,v}	vertical sideforce due to sideslip derivative
C _{Nδ_r}	yawing moment due to rudder deflection
C _h	hinge moment
C _{h,α}	hinge moment due to angle variation
C _{h,δ}	hinge moment due to rudder deflection
AOY	angle of yaw
AOA	angle of attack
F	aerodynamic force
M	Mach number
Re	Reynolds number
S	wing planform area
S _v	vertical tailplane area
S _{df}	dorsal fin area
h _{df}	dorsal fin height
L _{df}	dorsal fin length
Cr _{fd}	dorsal root chord
Cr _v	vertical root chord
φ _{o,df}	dorsal fin sweep angle at leading edge
φ _{o,v}	vertical sweep angle at leading edge
Δ AR	aspect ratio variation due to dorsal surface increasing
δ _r	rudder deflection
δ _{r,eq}	balance rudder deflection
δ _{r,float}	floating rudder deflection
V	velocity
h _v	vertical tailplane span
Verticalmac	vertical mean aerodynamic chord
α	angle of attack
β	angle of sideslip
ψ	angle of yaw
λ	taper ratio
ρ	air density
μ	viscosity
C _p	pressure coefficient
X _{LE,v}	vertical leading edge
X _{LE,d}	dorsal leading edge
X _{TE,d}	dorsal trailing edge

LIST OF SYMBOLS OF THE CONFIGURATIONS

CN [BVD] : Yawing Moment for geometry composed by Body, Vertical and Dorsal.

CN_B [BVD] : Body contribution of Yawing Moment for geometry composed by Body, Vertical and Dorsal.

CN_B+V [BVD] : Body + Vertical contribution of Yawing Moment for geometry composed by Body, Vertical and Dorsal.

CN_V [BVD] : Vertical contribution of Yawing Moment for geometry composed by Body, Vertical and Dorsal.

CN_V+D [BVD] : Vertical + Dorsal contribution of Yawing Moment for geometry composed by Body, Vertical and Dorsal.

CN_D [BVD] : Dorsal contribution of Yawing Moment for geometry composed by Body, Vertical and Dorsal.

CN [BV] : Yawing Moment for geometry composed by Body and Vertical.

CN_B [BV] : Body contribution of Yawing Moment for geometry composed by Body and Vertical.

CN_V [BV] : Vertical contribution of Yawing Moment for geometry composed by Body and Vertical.

CN [VD] : Yawing Moment for geometry composed by Vertical and Dorsal.

CN_V [VD] : Vertical contribution of Yawing Moment for geometry composed by Vertical and Dorsal.

CN_V [VD] : Dorsal contribution of Yawing Moment for geometry composed by Vertical and Dorsal.

CN [V] : Yawing Moment for geometry of Vertical.

BVD : geometry composed by Body, Vertical and Dorsal

BV : geometry composed by Body and Vertical.

V : Isolated Vertical

B : Isolated Body

1. INTRODUCTION

1.1 PHENOMENOLOGY

We begin by exposing the phenomenology that concerns directional stability in order to have a general framework for the aspects more or less important to take into account in the analysis.

1.1.1 THE CONCEPT OF STABILITY

If, for example, the airplane is statically stable and the perturbation resulted in an increased angle of attack, there can be three cases. In the first case the aircraft responds by decreasing the angle of attack to a value less than the initial equilibrium configuration, leading to a subsequent reaction that further increases the angle of attack but with subsequent oscillations amplitude gradually smaller tends to bring it back to the initial balance. In this case it is said that the airplane is dynamically stable and, once trimmed in its equilibrium position, requires no additional corrective action by the pilot to maintain the flight configuration set. If the aircraft responds by continuing to oscillate around the position of equilibrium with constant amplitude has a neutral dynamic stability. On the contrary, if the oscillations around the static equilibrium position will be increasing in amplitude over time, it will has a dynamically unstable aircraft. Considering that the motion of an aircraft can be divided into three basic dynamics, longitudinal, lateral and directional one, it is easy to understand that the above mentioned phenomena that determine whether or not the system is stable, concern precisely these three dynamics.

The directional stability involves the degrees of freedom related to the forward direction, so the yaw (see Figure 1). Actually considering that arise coupling phenomena which also involve the lateral degrees of liberty as roll, these two aspects of stability merge into a single issue that is called lateral-directional stability. Our interest is to focus on a specific aspect for the design with respect to performance of directional stability, so now we deepen the discussion on this kind of stability.

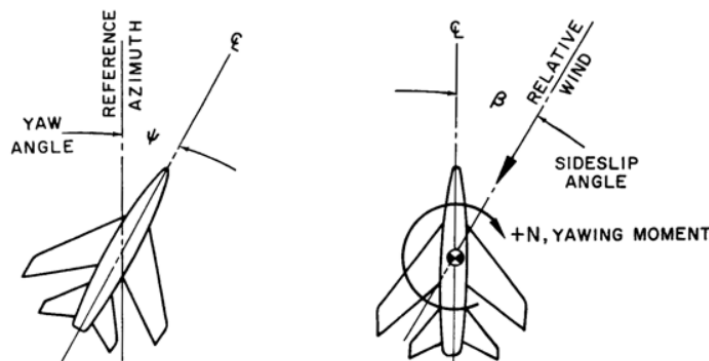


Figure 1 – Directional Dynamics.

From analytical point of view the sideslip angle β is like the yaw angle ϕ but in the opposite way. It means that there are not difference with respect our future consideration, we need just to remember this when we read some chart because in this paper there are different reference.

1.1.2 DIRECTIONAL STABILITY PROBLEM

The problem of directional stability and control is first to ensure that the airplane will tend to remain in equilibrium at zero sideslip and second to provide a control to maintain zero sideslip during maneuvers that introduce moments tending to produce sideslip. The vertical plane is the very main component of directional stability.

Extreme flight conditions often set design requirements for tail surfaces, like minimum control speed with One Engine Inoperative (OEI) or maximum cross-wind capability, so stability and control must be ensured even in very large angles of sideslip, up to 25°.

Design of vertical planes depends on the type of airplane (and so the flow regime), engine numbers and position, wing-fuselage and horizontal tail position.

The following design requirements can be formulated for vertical tail planes [1]:

1. They shall provide a sufficiently large contribution to static and dynamic stability that is the side-force derivative of the isolated vertical tail has to be determined.

$$C_{Y_{\beta,V}} = C_{L_{\alpha,V}} \frac{S_V}{S} \quad (1)$$

The vertical tail directional stability derivative is $C_{N_{\beta,V}}$, that is the yawing moment coefficient due to sideslip, however it can be shown that it depends from the coefficient just defined. If a high lift gradient is desirable the aspect ratio should be the largest possible with the minimum sweep.

2. The same can be stated for sufficient control capability. Moreover control should be possible with acceptable control force

$$F = C_h \frac{\rho V^2}{2} S_c \bar{c}_c \quad (2)$$

3. High angles of sideslip (up to 25°) can be reached and this condition is more serious when flying in possible icing conditions. In this case a low aspect ratio is required and sweep is beneficial (they delay the stall at higher angle of sideslip, but reduce the lift gradient).
4. Equilibrium has to be achieved in all flight conditions. This gives specific requirements on tail surface areas and on the maximum lift coefficient with various amount of control surface deflection and should include the effect of ice roughness.
5. A high aspect ratio has an adverse effect on weight. Also, for T-tails the flutter analysis requires extra care.
6. Excessive taper ratio may lead to premature tip stall. On the other hand, tapering leads to lower height.

So a compromise in high lift gradient and low aspect ratio and taper ratio must be considered.

1.1.3 FUNDAMENTALS OF STATIC DIRECTIONAL AND LATERAL STABILITY

Before embarking on the analysis of lateral and directional stability, a few terms must be defined [2].

Roll or Bank:

An airplane is said to be rolling or banking if a line drawn from wingtip to wingtip (assuming a symmetrical airplane) or some other normally horizontal reference line is sloped with respect to the y-z-axis as defined in Figure 2. This implies a rotation about its longitudinal axis (the x-axis or the roll-axis). Roll is the primary method used to change heading (direction of flight) and is controlled using the ailerons. The rudder is merely used to “fine tune” the heading change through coordination (in other words prevent skidding or slipping (discussed below)). The reason why the rudder is far less effective in changing heading than the bank maneuver can be explained using mechanics. A heading change results from acceleration in the horizontal plane that changes the original flight direction. To accomplish this rapidly, substantial force is required. The force generated by the VT through the deflection of a rudder is not a force large enough to change the heading fast enough for safe flight e for this a side force obtained using wing lift is required.

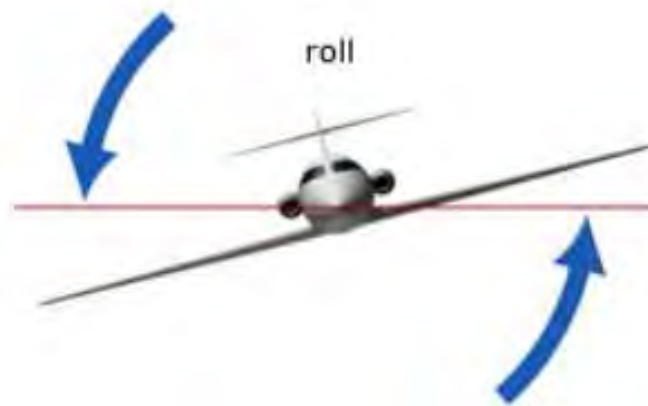


Figure 2 – Roll or Bank.

Yaw:

An airplane is said to be yawed if its centerline is not parallel to the x-z-plane (see Figure 3). This implies a rotation about its vertical axis (the z-axis or the yaw-axis). Based on the assumption that most airplanes are designed to be symmetrical about the x-z-plane, this rotation makes it unsymmetrical with respect to the airflow, which inevitably generates a side force and moment about the yaw axis.

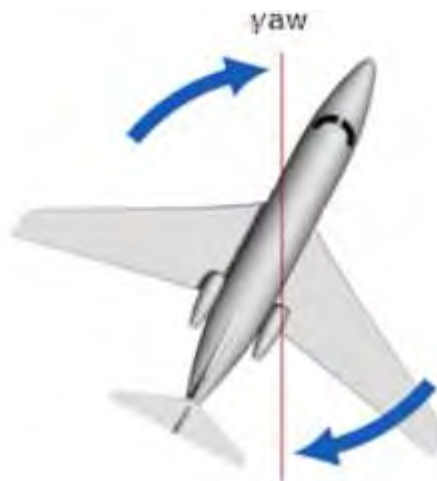


Figure 3 – Yaw.

Slipping or Sideslip:

If the airplane is “yawed out of a turn”, i.e. if the nose points outside of the trajectory of the turn, it is said to be slipping (see Figure 4). If banking left, this means the nose points to the right. Effectively, the bank angle of the airplane is steeper than the rate of turn would indicate. Slips primarily happen in two ways: (1) as a consequence of uncoordinated deflection of ailerons and rudder or (2) the consequence of the intentional application of opposite rudder during a bank to increase drag or align the ground track while landing in a crosswind. Slip is a trick sometimes used by pilots for altitude or airspeed control because the yaw that results increases the drag of the airplane.

If the airplane is “yawed into a turn”, i.e. if the nose points to the inside of the trajectory of the turn, it is said to be skidding (see Figure 4). If banking left, this means the nose points further left than the rate of turn indicates; the bank angle of the airplane is shallower than indicated by the rate of turn. Skids primarily happen in two ways: (1) as a consequence of uncoordinated deflection of ailerons and rudder or (2) the consequence of the intentional and excessive application of pro-bank rudder

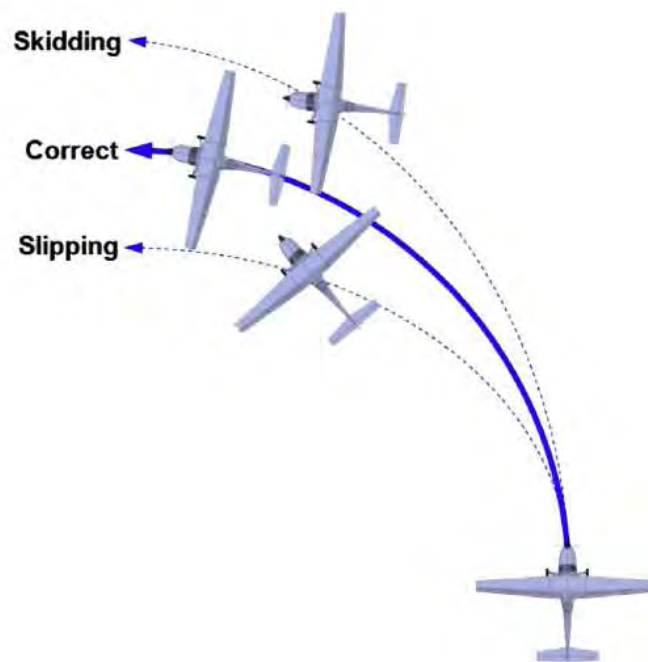


Figure 4 – Definition of slipping (sideslip) and skidding.

1.1.4 REQUIREMENTS FOR STATIC DIRECTIONAL STABILITY

The Figure 5 show our reference system, how we consider the axis direction and the verse of the yawing moment coefficient and sideforce coefficient when the wind has a negative β respect the previous definition of directional stability angle (see Figure 1).

Directional stability is the capability of the vehicle to weather vane. Imagine standing behind an actual weather vane with the wind directly in your face. If the vane is rotated so its nose points, say, right (and the tail points left) intuition tells us its tail will generate lift that points to the right, in the positive y -direction (see depiction in Figure 6). This, in turn, generates a moment whose tendency is to rotate the nose left and align it (and the tail) with the wind.

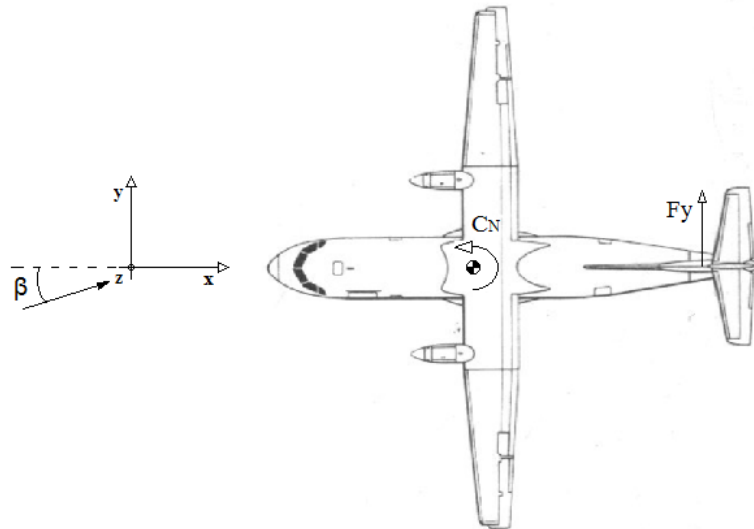


Figure 5 – Reference system of the analysis.

Since the moment corrects the alignment, it is said to be restoring. If the above weather vane is yawed nose right, then, using the stability coordinate system (SCS), the angle $\beta < 0$. This means that if looking along the centerline of the vane, the wind would strike the left cheek. The restoring moment is negative because per the right-hand rule, the resulting rotation is analogous to grabbing around the z-axis with the right hand to rotate it with the right thumb pointing upward e in the negative z-direction. The opposite holds true if the weather vane is rotated nose left e a positive moment (thumb pointing down) is then required to bring the nose right to the initial position.

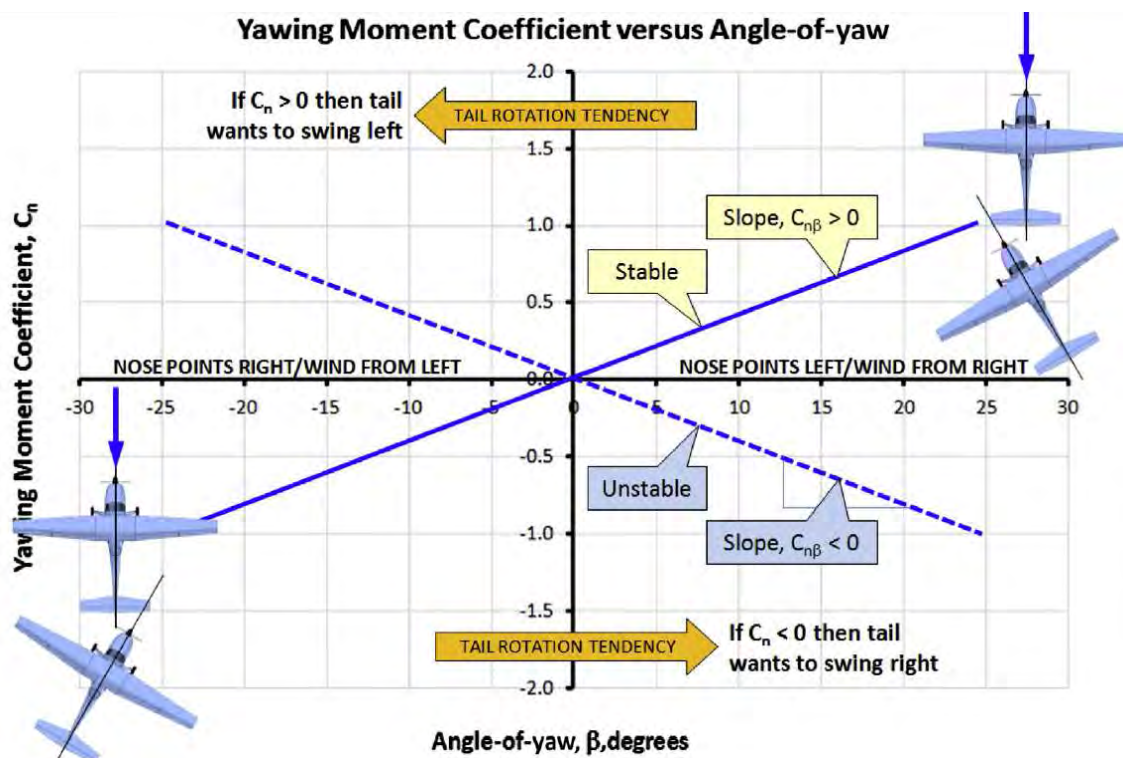


Figure 6 – Requirements for static directional stability of an aircraft [2].

1.2 NECESSITY OF DORSAL FIN

1.2.1 GENERAL DEFINITION OF DORSAL FIN

A dorsal fin is a small surface extension installed at the leading edge of the root of the vertical tail (see Figure 7).

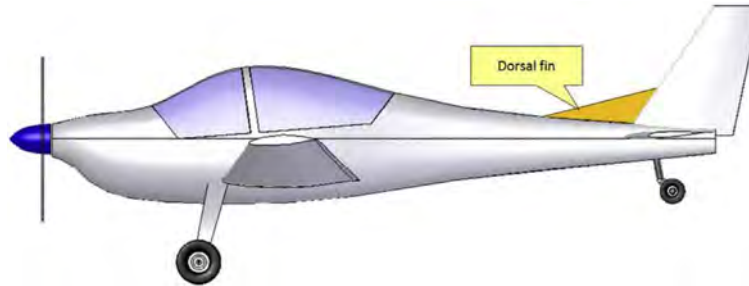


Figure 7 –Dorsal Fin example.

Its purpose is to add directional stability to the aircraft and that way prevent a serious condition known as rudder-lock. The dorsal fin, or dorsal as it is often referred to, can be as simple as a thin flat plate or as complicated as a curved compound surface stamped aluminum fairing riveted to an existing fin. In any case, its presence causes the leading edge to feature a discontinuity and this is imperative to its functionality

1.2.2 RUDDER DEFLECTION & PEDALBOARD EFFORT

We start from the premise that it is necessary to define the concepts of balance rudder deflection ($\delta_{r,eq}$) and floating rudder deflection ($\delta_{r,float}$):

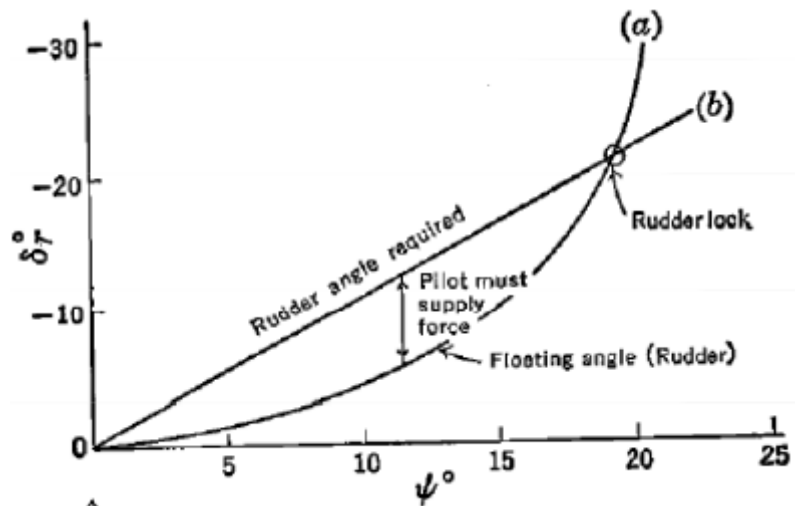


Figure 8 – Rudder deflection $\delta_{r,eq}$ & $\delta_{r,float}$ [10].

- **$\delta_{r,eq}$:** Is the deflection which must have the rudder to ensure the balance, so to ensure that the value of the sideslip angle is maintained constant instant by instant. If this deflection is not realized, the inherent stability related to the vertical, lead the nose in the direction flow canceling the sideslip. Increasing the requested sideslip angle such request deflection increases almost linearly.

- **$\delta r, \text{float}$:** Represents the deflection that occurs automatically in free controls for a given value of the sideslip angle, related to aerodynamic phenomena that characterizes the directional control. Increasing the sideslip angle such deflection increases in a nonlinear way.

We understand that for every value of the yaw, the pilot must carry an effort that allows to compensate for the gap in δr from $\delta r, \text{float}$ to $\delta r, \text{eq}$. For each value of β this gap is different, so will be different also the effort employed by the pilot that can be identified in the Figure 8.

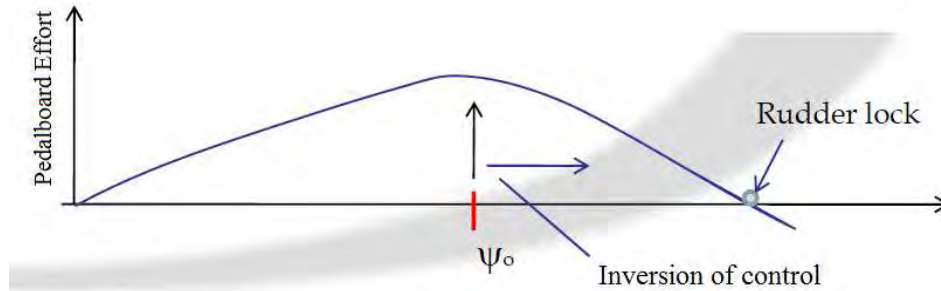


Figure 9 – Pedalboard Effort as function of Sideslip Angle.

1.2.3 THE RUDDER LOCKING PHENOMENON

The phenomenon of rudder locking is largely caused by insufficient directional stability of the airplane at high angles of yaw (AOYs). As the airplane is yawed to a high AOY (for instance in a side-slip maneuver) two things may happen:

- 1) Case of tail designed with very high aspect ratio (AR)

In this case are achieved very low values of the stall angle, as you can see from the chart of lift curves as a function of AR.

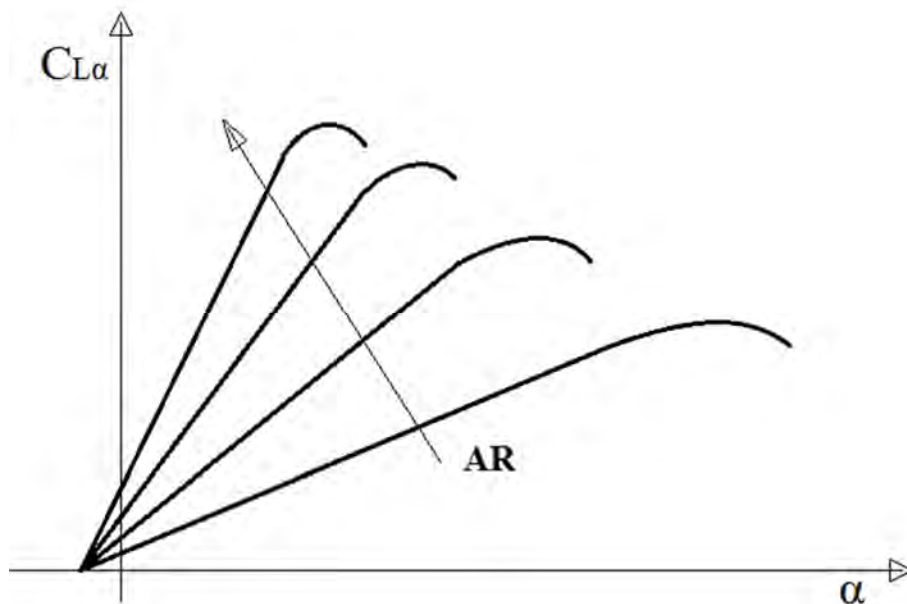


Figure 10 – Lift curve as function of AR.

When the angle increases, and reaches the stall, you get a strong reduction of the C_Y and C_N , then the vertical reduces its contribution to stability. This reduction of stability, implies in general greater ease for the aircraft to change its direction. In particular, the stabilizing moment generated

by the tail that has been reduced because of the stalling vertical can become smaller than the destabilizing moment generated by the fuselage.

2) Case of tail designed with very low aspect ratio (AR)

The side loading resulting from the yaw will tend to force the rudder to the leeward side. This is due to depression that is realized on the leeward side, which is in steady state conditions as stronger as greater is the rudder deflection. As before increasing the angle of yaw, the vertical plane stall and reduces its contribution to directional stability. In this case, however, to understand the phenomenon of Rudder Locking we focus on the graph which shows the gradients of the efforts of the bar also (see Figures 9).

In fact it is possible to identify a β value for which the δr_{eq} is equals to δr_{float} , condition for which the efforts of bar are null. Intuitively, if we imagine that the pilot commitments always the same force on the joystick, when the necessary efforts become void, it appears that the pilot pushes the pedal way down, since does not meet any resistance.

If the pilot wants to leave this condition and bring the angle of yaw to zero, it has to achieve a deflection of the rudder in the opposite direction, so acting on the control pedal. Since the pedal is at the bottom of the movement, the excursion of the rudder is maximum, so due to the aerodynamics problem very high hinge moments are generated. These hinge moments must be overcome if the pilot wants to move the rudder in the opposite direction and leave the actual sideslip.

If the pilot fails to win these moments, the rudder will remain locked:

- In one direction can't rotate over δr_{max} because the pedal is at the bottom of the displacement.
- In the other direction can't rotate because the pilot failed to win the moments hinge.

1.2.4 DORSAL FIN AS SOLUTION FOR RUDDER LOCKING

One solution for a rudder lock condition is to mount a fin on the dorsal [2]. This will partition the vertical into two low-aspect-ratio segments. The smaller one will remain unstalled to an even higher yaw angle (because small AR surfaces stall at a higher angles than high AR surfaces as we can see from Figure 10) and this helps maintain sufficient directional stability up to the higher AOY than without dorsal.

Another solution, often featured on aircraft designed in the 1930s and 1940s, is an H-tail configuration, with small low-aspect-ratio ($AR_w = 1$) tail surfaces. Such surfaces stall at very high AOAs, as high as 30° and 40° .

In the absence of the dorsal, the entire tail would be stalled. Its presence introduces a discontinuity in the leading edge of the vertical tail, which at non-zero AOY generates a vortex as shown in Figure 11. The vortex effectively splits the fin into upper and lower halves. The upper half has a higher AR than the lower one and, thus, stalls at a lower AOY. And that is the important thing. The fact that the lower half is only partially stalled renders the $C_{N,\beta}$ greater than if the dorsal was absent. This allows at $C_{N,\beta}$ to be maintained to a higher AOY. Not only the $C_{N,\beta}$ is increased due to the added area of the dorsal fin, it also guarantees it stays higher to greater AOY.

The recovery from a rudder lock requires the airspeed to be reduced by a roll or a pull-up maneuver to be performed or so the hinge moment drops to a magnitude that allows the pilot to bring the rudder to neutral with force.

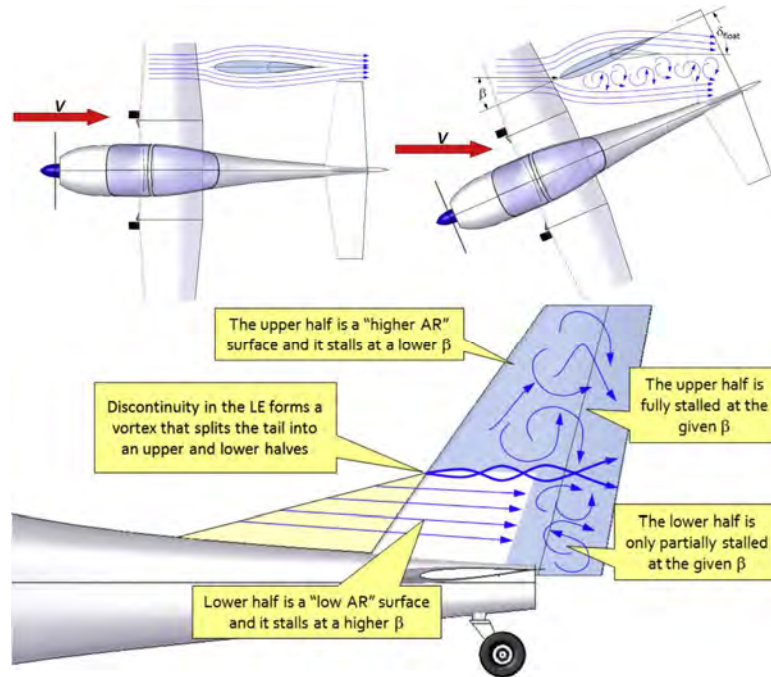


Figure 11 – How a dorsal fin prevents rudder lock [2]

To delay the rudder lock phenomenon at high angles one can use:

- Dorsal fin
- Reduce elongation of the vertical plane (increases the angle of stall but decreases the lift slope, so the vertical tail is less cooperative)
- Introduce an anti-tab which increases the effort needed to avoid lunging pedals (see Figure 12)
- Try changing the ratio $C_{h,\alpha}/C_{h,\delta}$ acting on the hinge axis of the rudder

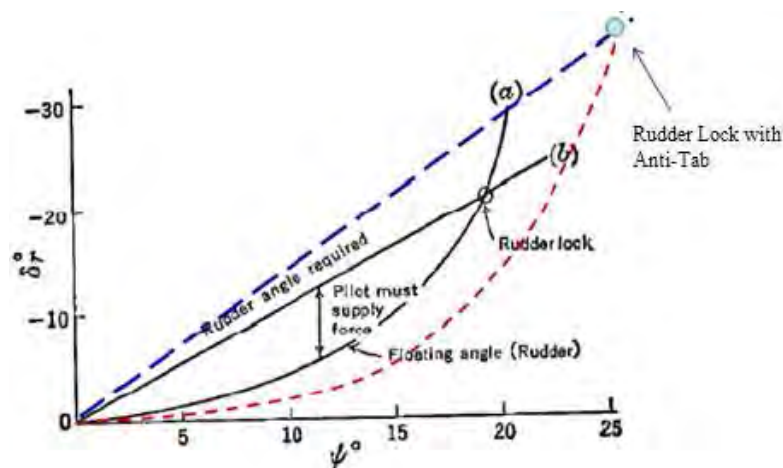


Figure 12 – Rudder Lock in presence of Anti-Tab Conceptual effect.

Using dorsal fin the following results can be met (see Figure 13):

- Increased stability of the fuselage at high angles β (requesting a greater δ_r, eq)
- Reduces elongation of the vertical tail (greater angle of stall)
- Further effect of the vortex that is detached reducing the problems of stall and the strong float rudder

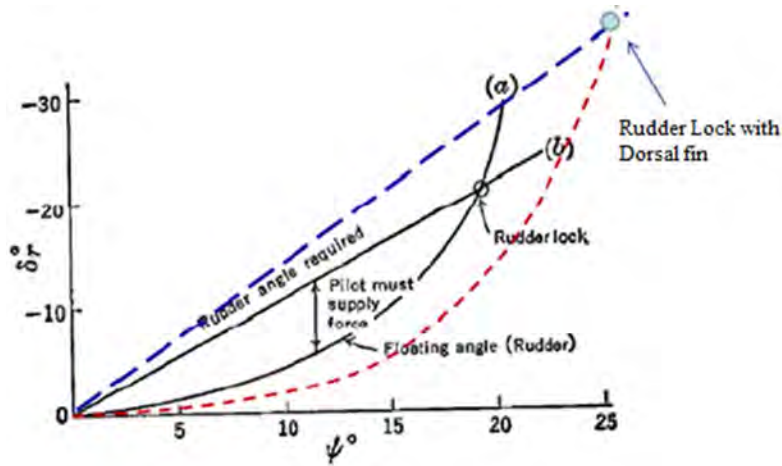


Figure 13 – Rudder Lock in presence of Dorsal fin conceptual effect.

This graph does not represent the actual phenomenon, since in the linear part, the δr_{eq} in the case of dorsal and not dorsal are coincident, so the slope should be the same.

If using a dorsal fin we get an increase in stability, then we can say that:

The δr_{eq} needed for a particular β is greater, as greater is the stability (the slope of the δr_{eq} curve becomes steeper in the non-linear range). This is explainable by the simple consideration that the stability determines the difficulty with which changes the equilibrium condition, being with dorsal fin the lift curve is different in slope respect the configuration without dorsal fin, will be needed different rudder deflections to achieve the lateral force to maintain the same β so the balance. The Figure 14 taken from the literature [4] helps us to better understand.

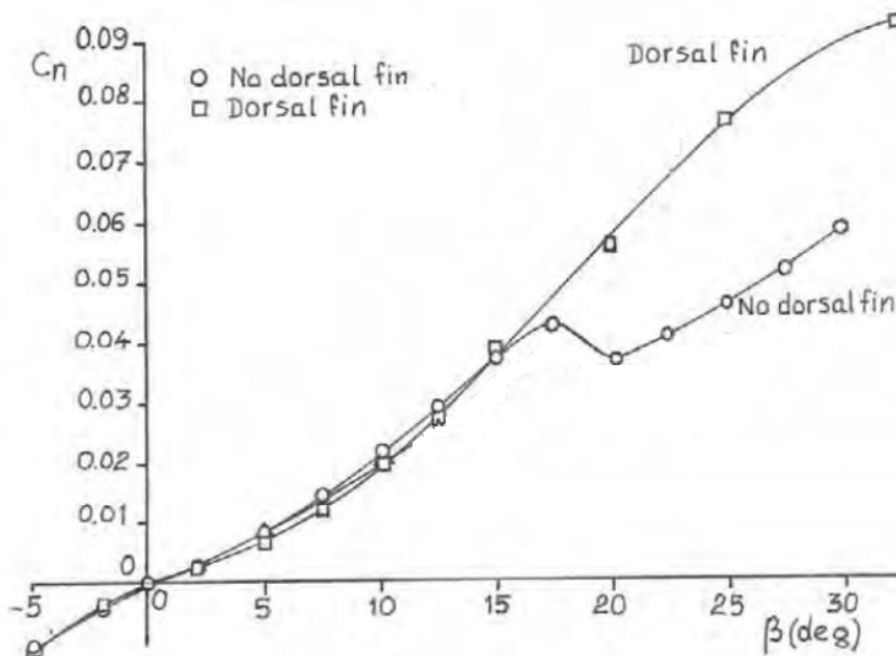


Figure 14 – Effect of a dorsal fin on the yawing moment coefficient [4].

It is clear that considering as vertical empennage, the only vertical plane or vertical + dorsal fin has no effect in the linear range, indicating that one can get the same forces at the same angle.

So for a given β , the rudder deflection which ensures the equilibrium is the same for both configurations. In the nonlinear range the achieved force for a given beta is greater in the presence

of the dorsal, related with major stability, so the rudder deflection that ensures the balance must necessarily be greater. The $\delta r, \text{float}$ obtained for a given beta is lower if the stability is greater, so the curve of $\delta r, \text{float}$ become ever more open (the flow is deviated with more difficulty in presence of the dorsal fin).

Downstream of these considerations, we get a graph of Figure 15 related to the actual effect of dorsal fin on Rudder Lock phenomena.

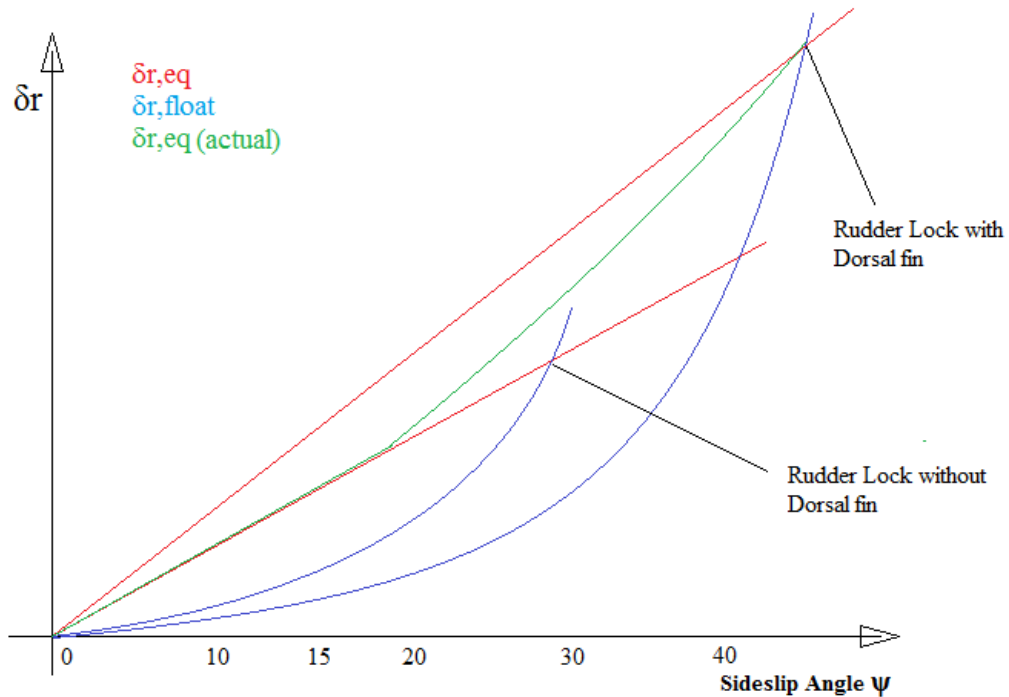


Figure 15 – Rudder lock in presence of Dorsal Fin (Actual).

However, you can identify a delay of the rudder lock phenomenon in the presence of the dorsal fin.

Increasing β we showed how $C_{N\beta}$ increases and we are considering that this leads to an growing of $\delta r, \text{eq}$. Actually the value of $\delta r, \text{eq}$ is given by the ratio between $C_{N\beta}$ and $C_{N\delta r}$. Therefore, we must still consider that the chart above is neglecting the variation of power control $C_{N\delta r}$. In fact, if we consider that increasing β also increases $C_{N\delta r}$, then the curve will not have this strong gain in slope but a small increase.

1.2.5 OTHER REASON FOR DORSAL FIN.

Often the Dorsal Fin is however present even for:

- aesthetic reasons
- Serves as aerodynamic fairing at the root of the vertical plane reducing the parasitic resistance
- It is useful in some cases to pass to the control cables

1.3 METHODOLOGY EVOLUTION FOR THE STUDY OF LATERAL-DIRECTIONAL STABILITY

From the '30s to the '50s, in the USA, the National Advisory Committee for Aeronautics (NACA) provided some results on the directional stability on isolated vertical tailplanes, partial and complete aircraft configurations through many hours of wind tunnel tests, results that were summed up in a method of analysis completely reported and described in the USAF DATCOM [5].

From the '50s to the '90s in the USA researches were concentrated mainly on high subsonic and supersonic flow field and until the '70s only wind tunnel tests could fit for the objective. Usually the directional stability of the models tested deteriorated with increasing angle of attack and increasing Mach number. Interference effects had a strong influence upon the vertical-tail effectiveness and, consequently, upon the directional stability. These effects are, for the most part, associated with complex flow involving vorticity or shock waves and therefore were difficult to analyze at that time.

In the '70s first computer programs began to appear on the scene, with the application of linear, potential, subsonic flow theory. Initially the quasi vortex-lattice method was applied and modified to account for wing-body effect in sideslip, then more and more sophisticated panel methods, developed for rapid accurate estimates of the aerodynamic characteristics of aircraft and missile configurations at supersonic speeds, provided solution (in potential flow) for almost any geometry.

Panel methods are numerical schemes for solving the Prandtl-Glauert equation for linear, inviscid, irrotational flow about aircraft flying at subsonic or supersonic speeds. There are fundamental analytic solutions to the Prandtl-Glauert equation known as source, doublet and vorticity singularities. Panel methods are based on the principle of superimposing surface distributions of these singularities over small quadrilateral portions, called panels, of the (approximate) aircraft surface. The resulting distribution of superimposed singularities automatically satisfies the Prandtl-Glauert equation. To make the solution correspond to the desired geometry, boundary conditions are imposed at discrete points (named control points) of the panels.

Since panel methods are restricted to inviscid, irrotational and linear flow it is common practice to include the presence of the boundary layer with a viscous code coupled with the panel method, so that the pressure distribution from the latter is the input for the former to compute the displacement thickness. This incremental thickness is the new input geometry for the panel code and so on, until convergence is reached.

Most recent panel codes are used to determine the stability and control derivatives of new aircraft configurations early in the design process, since these parameters are important also to most control law design methods and their early estimate may permit significant improvement in configuration weight, cost, performance and even stealth, through multidisciplinary design

These panel methods are part of the Computational Fluid Dynamics (CFD), though the approach with the Prandtl-Glauert equation has little physics inside. The Prandtl-Glauert equation model involves only a scalar potential and the free stream Mach number. It's just the wave equation in a steady compressible flow regime.

Among the different fluid dynamic models which may be employed for the solution of the motion fields that are carried out around geometries of aeronautical interest are the Navier-Stokes equations. Because of the equations complexity that are of mixed hyperbolic-parabolic kind, mediated forms are often used. In this paper, I make use of CFD in the sense of the Navier-Stokes averaged (RANS, Reynolds Averaged Navier-Stokes equations) with the software STAR-CCM+ [7].

Using the CFD will have the opportunity to size the aerodynamic characteristics related to the interference between the individual components. It has been stated that the panels method are an important part of the CFD, so at this point it is necessary to make a clarification. Panels method are not ideal for determining the effects of aerodynamic interference, they 'solve' the flow field by summing the results of distributed aerodynamic singularities. It has been shown by [7] that the aerodynamic interference effects can be caught with RANS calculations. In fact, recent (last 15 years) CFD methods makes use of finite differences, Finite Element Method (FEM) and finite volume methods.

Any further step in stability and control analysis techniques saw a return to the study of the low subsonic flow field.

Viscosity is responsible of momentum loss in boundary layer because of skin-friction and pressure drag, increasing boundary layer thickness, decreasing lift gradient and flow separation. Neglecting viscosity gives a good approximation only in attached flow regime. This limit can be overcome by modern CFD [1].

Nowadays powerful computational fluid dynamics obtained thanks to Navier-Stokes equations tools offer significant benefits as a support to the experimental methods to predict aerodynamic parameters [1]. In fact, the wind tunnel is traditionally the primary tool to provide aerodynamic inputs for simulation data bases and to predict stability and control characteristics, but shortcomings exist in wind tunnel testing methods (for example operation at a lower than free flight Reynolds number causes large discrepancies on boundary layer separation in certain configurations) that can result in serious errors in the predicted stability and control characteristics. Moreover wind tunnel tests require both the construction of a model and an adequate test facility. Additionally, the lag time between the paper design and the wind tunnel results can be considerable. Furthermore, any configuration change requires a change of the test model. This greatly increases the cost of the product and the time to market.

On the other hand, the simple theory at the base of the USAF DATCOM or other semi-empirical method is only accurate for preliminary relationships between the overall aircraft geometry and stability.

CFD offers a more direct approach in finding stability coefficients, computing aerodynamic forces and moments by integration of surface pressures along the aircraft boundaries. In general, the most complicated geometry can be solved with the proper selection of a CFD method and right boundary conditions, so it is believed that CFD tools can completely cope with stability and control issues and complement the traditional wind tunnel data sources [1]. The decreasing costs and the increasing power of the computers makes the CFD more and more attractive.

2 DORSAL FIN INVESTIGATION

2.1 SEARCH FOR REFERENCES IN LITERATURE

Following a phase of understanding of the issues related to the stability of lateral-directional I could start an investigation process of the dorsal fin, which aims to identify relationships between the analyzed geometries, and the stability characteristics. Again, this thesis is part of a wider issue, which is the development of methods for the prediction of the aerodynamic characteristics of the aircraft.

The first step was to look in literature references about the design of the dorsal fin. I selected about 20 different reports on the Lateral-Directional stability characteristics and for each one of them I search the experimental data on the use of the dorsal fin. After excluding those who did not deal with the problem or not treated in depth, I searched among the remaining information that link the phenomenon of Lateral-Directional stability with the dorsal fin geometry ([2], [8], [9], [10], [11], [12], [13], [14]). They only provide general information on the functionality of the dorsal fin. At this point it is appropriate to focus on the fact that although there are reports in literature that describe and analyze the problem of stability related to the dorsal fin they are mostly related to studies done on models tested in a wind tunnel or on geometries particularly obsolete. This implies that on the one hand, often lack quantitative geometric references of the models, on the other hand, since most of these reports are relate to a historical moment different from the current one, the analyzed geometries concern to mainly post-war phase aircraft or immediately next.

Is easy to understand the need for a procedure involving the quantitative analysis of the performance variability compared to the change of dorsal geometry. In this sense, I am going to do the analysis related to a geometry attributable to those of today for turboprop both for fuselage, empennage and wings characteristics.

As evidence of the foregoing the most complete among those analyzed which are publicly available is Empennage Statistics and Sizing Methods for Dorsal Fins [3].

We used this report regard to two aspects:

The first is to use the Geometric-Statistics procedure for the reference dorsal fin sizing that led us to identify the starting geometry for our studies, described in chapter 2.2. This geometry will be modified to permit a parametrical study where the excursion, of the geometric involved parameters, have a symmetrical variation respect the reference value of the starting dorsal. In fact the resulting dorsal of method 1 will be really small to permit a large symmetrical variation of his geometric parameters. The second, which involves the numerical analysis portion of my thesis, is to extract the experimental data carried on the Fokker F-27 in terms of obtained trend. From these results have been identified four main parameterizations, that we have replicated on reference geometry using a CFD software to evaluate the qualitative correspondence between the experimentally obtained trends collected from **Obert** [4] and those numerically obtained.

Since it is a guide for the study that I am going to do I proceed with a summary of the report by Prof. **Scholz** [3]. The report aims at giving users more refined starting values for different parameters of the tailplane and dorsal fin. After analyzing result from literature prior to [3] it was decided to improve these result and to produce values closer to real aircraft. These values may

then be used for the different design parameters. This is to be achieved through statistical method. The tail sizing of [3] is archived through several statistics conducted on various parameters of the tail.

The understanding of dorsal fin mainly started from **Patent US 2356139** [9]. Dorsal fin was patented in the year 1944 and the report explains the aerodynamic behavior of the vertical tail with various type of dorsal fin. Advantages are significant according to the experimental data presented in **Patent US 2356139** [9].

Obert [4] investigated various dorsal fins in the development of Fokker F-27. Figure 16 show different dorsal fins which were investigated.

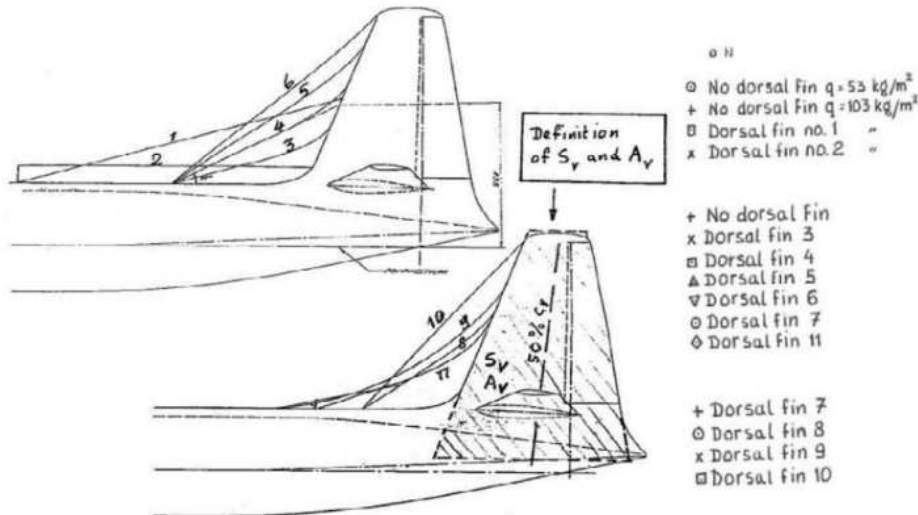


Figure 16 – Different dorsal fin investigated for a Fokker F-27 [4].

The effect of different dorsal fins on the aircraft yawing moment are presented in Figure 17.

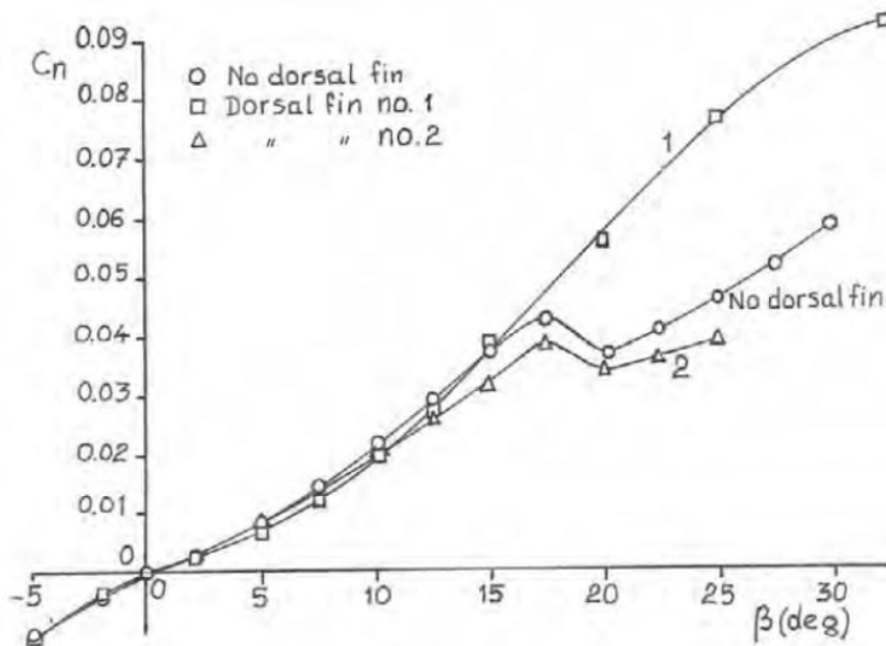


Figure 17 – Effect of a dorsal fin on the yawing moment coefficient [4].

Up to 15° of sideslip angle, the dorsal fin does not affect the lift curve. From 15° on, whereas without dorsal fin the maximum lift is almost reached, the dorsal fin modifies the flow over the vertical tail due to the vortex springing from its leading edge. This is controlled local flow

separation which stabilizes the flow further outboard postponing complete flow separation to a higher angle of sideslip. Thus a higher maximum lift and a higher stall angle are achieved.

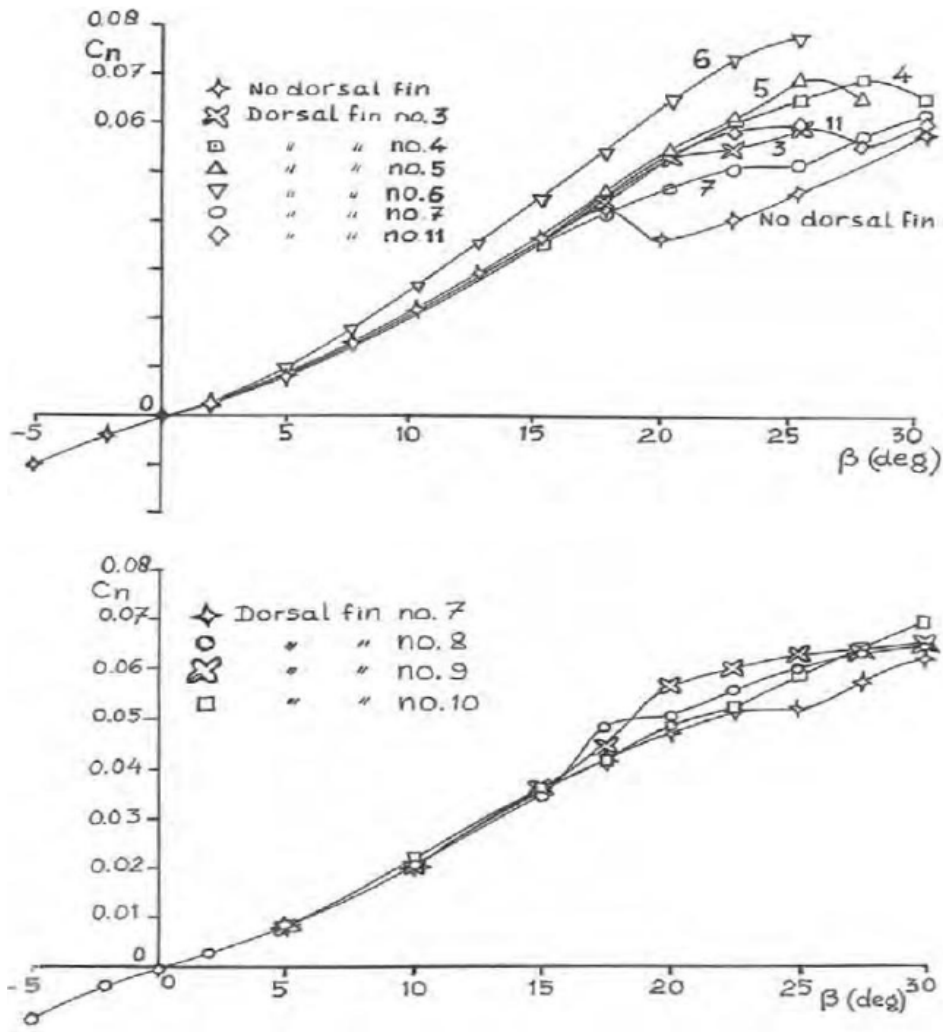


Figure 18 – Effect of a dorsal fin on the yawing moment coefficient [4].

On the full-scale F-27 dorsal fin no. 1 was selected. The reason is evident although fin no. 6 could also have been a candidate (see Figure 18). Instead of a lightly-swept leading edge in combination with dorsal fin also a fully-swept-back leading edge on a vertical tail surface may produce favorable sideslip characteristics. This was already demonstrated by fin no.6. [4].

Figure 19 shows the vortex generation by a dorsal fin at high sideslip angle.



Figure 19 – Vortex formations by a dorsal fin [3].

Figure 20 shows side views of vertical tail surfaces and dorsal fin chosen to further investigate if all of them exhibit same characteristics concerning the angle-of-attack variations.

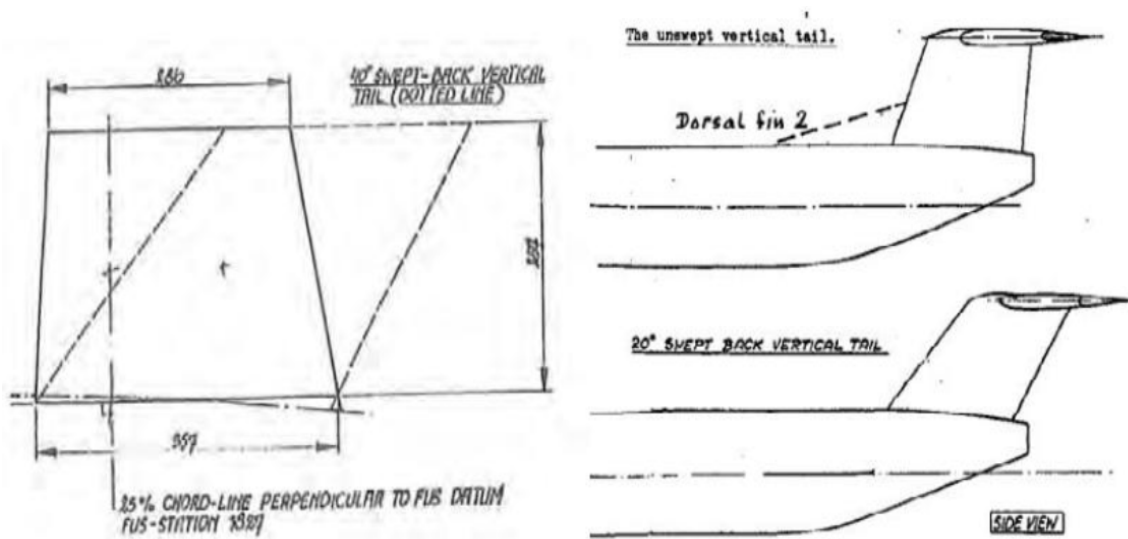


Figure 20 – Side view of three vertical tail surfaces and a dorsal fin investigated during the development of the Fokker F-28 [4].

For the linear regime, the three curves practically coincide. At higher side-slip angles above $\beta = 15^\circ$. It appears that for zero angle-of attack applying fin sweep or adding a dorsal fin has nearly the same favorable effect on the yawing moment curve. But, when aircraft angle-of-attack is increased to 8° , the lightly-swept tailplane with a dorsal fin performs better than the fully-swept-back vertical tail surface, although also the latter performs better than the basic tail surface without dorsal fin.

Again from Figure 21 & 22 it is clear that a dorsal fin or a high leading-edge sweep angle improves the sideslip characteristics of tail surface also in angle-of attack variation.

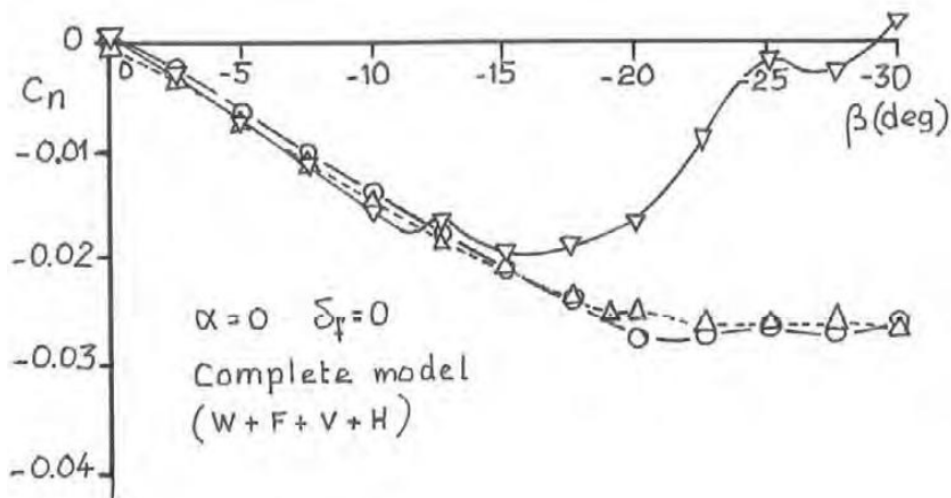


Figure 21 – Effect of sweep angle on vertical tailplane lift curve. Angle of attack 0° [4].

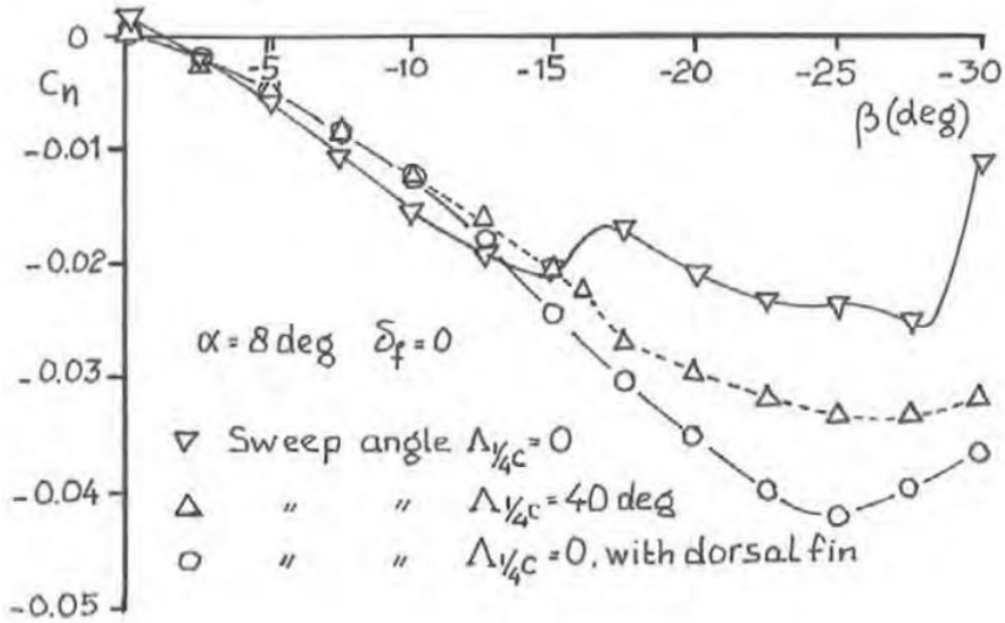


Figure 22 – Effect of sweep angle on vertical tailplane lift curve. Angle of attack 8° [4].

2.2 SYNTHESIS OF DORSAL FIN SIZING METHOD NO.1

It is necessary to consider the statistical relations on two parameters, the other will be determined geometrically. The result will be a geometry conforming to statistical surveys. Depending on which statistical laws are considered, have been made seven sizing methods. We can see from Figure 23 how **Scholz** [3] consider the involved parameters concerning the statistical study.

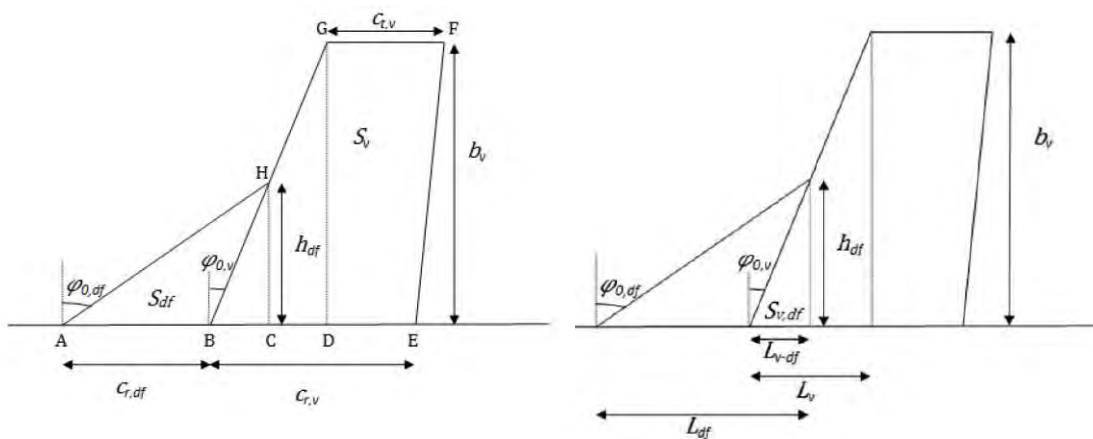


Figure 23 – Vertical & Dorsal fin Geometric Parameters [3].

What the report proposes how best is the number 1 method that uses as input the statistical laws on the following two parameters. :

- $\varphi_{0,df}$: Sweep angle of Leading edge of Dorsal fin
- $S_{,df}$: Dorsal fin Surface

Application Method no.1

I made a routine that allowed me to use the method no.1, controlling the two input parameters which are the surface of the vertical and the sweep angle at the leading edge of the vertical. The result of the method for the input parameters considered plausible is the following:

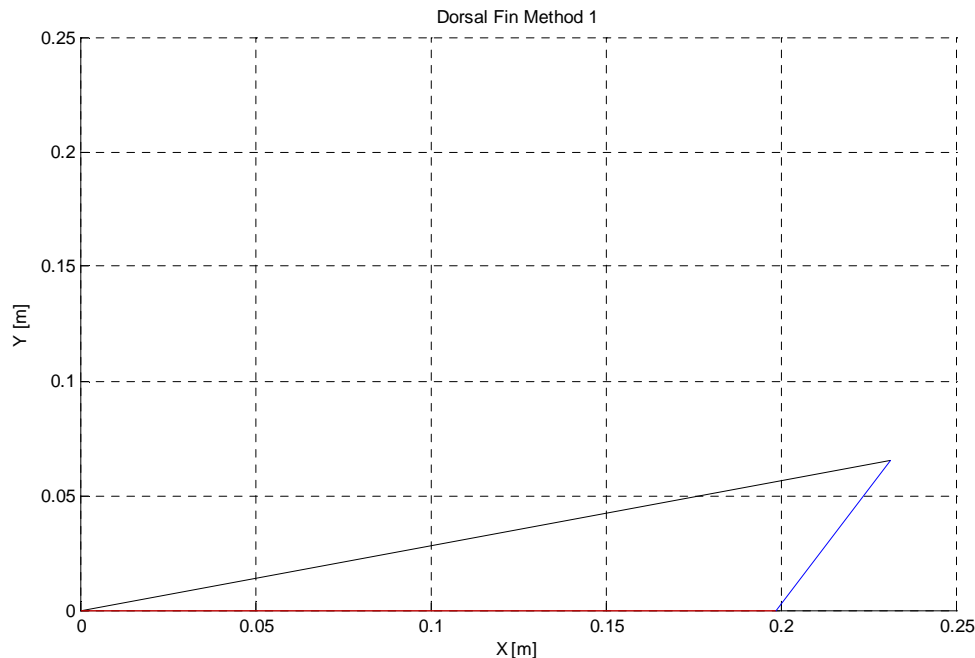


Figure 24 – Dorsal fin resulting from the Geometric-statistical Method no.1 [3].

Considering that the next phase of the thesis concerns simulations carried out on a reference geometry, it seems reasonable to start with the resulting geometry from the statistical-geometric method described above. In parallel with the aim of realizing an experimental study in the wind tunnel therefore we propose the reference values of the vertical consistent with a possible scale model that could be achieved precisely for these experimental studies.

We have to specify from now, that our goal is not to testify the validity of the method, i.e. to determine a consistent geometry which results from statistical surveys, but simply to choose a starting surface for parametric study. The resulting geometry can be modified in accordance with the possibility realization rules (actual building of the fin) and those of common sense design.

Since this hypothetical scale model has not been realized still, so there are no design constraints, it is thought to act on some parameters of the determined dorsal fin using the method 1. In this way we move away from the regression line of the input chosen parameters but is approached to the other.

In Table 1 presents the results of applying the method no.1 for aircraft seen from the report [3] for the statistical surveys. This allows us to make a comparison between the result of the method for our geometry and the medium resulting from the list of aircraft.

	S_v	S_{df}	S_v/S_{df}	$\Phi_{i_o,v}$	$\Phi_{i_o,df}$	$\Phi_{i_o,v}/\Phi_{i_o,df}$	$h_{fd} \text{ calculated}$	L_{df}	L_v-df	L_v-df / L_{df}	Cr_{fd}	Cr_v	L_{df}/Cr_v	L_{df}/h_{df}
Saab 340	7,500	1,230	6,098	38,900	76,275	0,510	0,865	3,541	0,698	0,197	2,843	1,053	3,362	4,093
Saab 2000	10,480	1,719	6,098	36,790	75,977	0,484	1,028	4,113	0,768	0,187	3,345	1,239	3,319	4,002
Q-400	16,480	2,703	6,098	31,090	75,174	0,414	1,305	4,929	0,787	0,160	4,142	1,535	3,212	3,776
Q-300	16,420	2,693	6,098	32,740	75,406	0,434	1,298	4,984	0,835	0,167	4,149	1,537	3,242	3,839
EMB 120	6,500	1,066	6,098	38,850	76,268	0,509	0,806	3,295	0,649	0,197	2,646	0,981	3,361	4,090
EMB 110/111	5,620	0,922	6,098	32,010	75,303	0,425	0,761	2,899	0,475	0,164	2,423	0,898	3,228	3,811
il 114	15,710	2,576	6,098	34,840	75,702	0,460	1,264	4,957	0,880	0,177	4,077	1,511	3,281	3,922
il 18	18,270	2,996	6,098	17,850	73,307	0,243	1,411	4,702	0,454	0,097	4,248	1,574	2,988	3,333
F-27	16,480	2,703	6,098	23,510	74,105	0,317	1,326	4,654	0,577	0,124	4,077	1,511	3,081	3,510
An-140	12,360	2,027	6,098	31,610	75,247	0,420	1,129	4,286	0,695	0,162	3,591	1,330	3,221	3,796
Bae 748	11,610	1,904	6,098	12,090	72,495	0,167	1,135	3,598	0,243	0,068	3,355	1,243	2,895	3,170
Beriev 32k	5,250	0,861	6,098	42,040	76,718	0,548	0,719	3,044	0,648	0,213	2,396	0,888	3,429	4,234
de havilland dash 7	15,900	2,608	6,098	34,110	75,600	0,451	1,273	4,958	0,862	0,174	4,095	1,517	3,267	3,893
Aerospatiale N262	8,350	1,369	6,098	10,560	72,279	0,146	0,965	3,018	0,180	0,060	2,839	1,052	2,870	3,128
Fokker F-27-500	15,050	2,468	6,098	25,160	74,338	0,338	1,263	4,502	0,593	0,132	3,909	1,448	3,108	3,565
Bae jetstream 41	6,640	1,089	6,098	33,910	75,571	0,449	0,823	3,199	0,553	0,173	2,645	0,980	3,264	3,885
Fairchild metro iii	5,340	0,876	6,098	27,900	74,724	0,373	0,748	2,738	0,396	0,145	2,342	0,868	3,155	3,660
Grumman G-159	8,860	1,453	6,098	34,550	75,662	0,457	0,950	3,714	0,654	0,176	3,060	1,134	3,276	3,911
ATR 42	14,240	2,335	6,098	45,610	77,221	0,591	1,175	5,176	1,200	0,232	3,977	1,473	3,513	4,407
ATR 72	15,180	2,490	6,098	44,790	77,105	0,581	1,215	5,304	1,206	0,227	4,098	1,518	3,493	4,366
Vickers Vanguard	24,620	4,038	6,098	22,620	73,979	0,306	1,623	5,651	0,676	0,120	4,975	1,843	3,066	3,481
NAMC Ys-11	14,870	2,439	6,098	23,690	74,130	0,320	1,259	4,427	0,552	0,125	3,874	1,435	3,084	3,516
Average	12,351	2,026	6,098	30,692	75,118	0,407	1,106	4,168	0,663	0,158	3,505	1,299	3,214	3,791

Table 5 – Application of Method no.1 for Propeller Aircraft List [3].

The vertical has the following geometric parameters.

$b_v [m]$	$Cr_v [m]$	$V_{m.a.c.} [m]$	$S_v [m^2]$	AR_v	$\phi_{o,v} [^\circ]$	$\phi_{t.e,v} [^\circ]$
0.2434	0.2	0.1652	0.0395	1.5	26.6	10.8

The resulting Dorsal fin by Method 1 has the following geometric parameters.

$L_{df} [m]$	$Cr_{df} [m]$	$h_{df} [m]$	$S_{df} [m^2]$	AR_v	$\phi_{o,df} [^\circ]$	$\phi_{t.e,v} [^\circ]$
0.2312	0.1985	0.0653	0.0065	1.5	74	10.8

It appears that

L_{df}/Cr_v	L_{df}/Cr_{df}	L_{df}/h_{df}	h_{df}/h_v	S_v/S_{df}	$\phi_{o,v}/\phi_{o,df}$
1.156	1.165	3.5	0.268	6.07	0.3594

We focus our attention specifically on two parameters:

- L_{df}/Cr_v is very low compared to most aircraft.
- L_{df}/h_{df} is slightly low compared to most of the aircraft.
- S_v/S_{df} coincident with the statistical values.
- $\phi_{o,v}/\phi_{o,df}$ coincident with the statistical values.

We note that specifically for L_{df} / Cr_v there is a strong discrepancy between what appears from the method for our case and as shown in the table that lists the aircraft. This means that the regression statistics line for this parameter was not used as input in the procedure for the geometry determination.

Since the relations of entry of method 1 are related to other parameters such as the surface of the vertical and the sweep angle to the leading edge of the vertical, obviously there will be strong correspondence between the latter and the majority of those of the propeller considered.

Equations by statistics analysis on similar aircraft:

- $S_{,df} = 0.164 * S_{,v}$
- $S_{,df} + = 0.190 * S_{,v}$
- $\varphi_{o,df} = 2.244 * \varphi_{o,v};$ or $\varphi_{o,df} = 70.49 + 0.141 * \varphi_{o,v}$
- $\Delta\varphi = 70.49 - 0.859 * \varphi_{o,v}$
- $Cr_{,df} = 2.699 * Cr_{,v}$
- $L_{,df} = 1.156 * Cr_{,df}$
- $h_{,df} = 3.664 * b_{,v}$

In general, we don't care about these discrepancies, because the starting geometry that we want to use is just like a reference for subsequent parametric analyzes. In fact, in the next phase we approach to a problem of preliminary analysis, which focuses exclusively on resulting trends from various parameterizations and not on the values in absolute terms. We can therefore in an independent way from the results of Method 1 to act on some parameters without any particular criteria, just those of common sense design. The final result is show in Figure 25 & Table 2.



Figure 25 – The Final Reference Geometry of Dorsal fin.

h,v [m]	S,v [m]	S,df [m]	$\varphi_{o,v}$ [°]	$\varphi_{o,df}$ [°]	h,df [m]	L,df [m]
0,2434	0,0395	0,012437	26,6	77,06555	0,0756	0,329028
Lv-df	Lv-df/Ldf	Cr_df	Cr,v	h,df/h,v	Ldf/hdf	Sdf/Sv
0,038	0,115	0,291	0,200	0,311	4,352	0,315
Ldf/Cr_v		Ldf/hdf		Sv/S,df		$\varphi_{o,v}/\varphi_{o,df}$
1.645		4.35		3,18		0.34

Table 6 – Reference Geometry Parameters and characteristics ratio.

Since our aim is to perform a parametric study, we will analyze several geometries changing different parameters in different combination. So our final dorsal even if is very different from method 1 have a good reference geometric value considering the excursion about them in parametric phase. For example, even if the final surface is almost double with respect the method results, when we will perform the parameterization about the dorsal surface we analyze also dorsal with a lower surface respect the method 1 result.

3 NUMERICAL STUDY THROUGH CFD

3.1 THE CFD APPROACH

Technological progress in the aerodynamics design phase is the possibility of Computational Fluid-Dynamics (CFD). This chapter is a description of the main tool that was used to fulfill the objective of this work, the commercial CFD software STAR-CCM+ [15]. This tool requires the definition of a physical model responsive to the actual phenomena to be analyzed. The more accurate the physics models involved, the more realistic will be the results. Section 3.4 will describe the SCoPE computational grid, necessary to deal with lots of simulations of millions of cells [6].

3.2 THE SOFTWARE STAR-CCM+

STAR-CCM+ is more than a CFD solver [1]. It is an entire engineering process for solving problems involving flow (of fluids or solids), heat transfer and stress, based on object-oriented programming technology.

The resolution of the problems of our interest is supported by the use of integral-differential equation models as complex as we want more detail analysis. One of the most used models in aerodynamics, for its completeness is the Navier-Stokes model. Solving the Navier-Stokes equations, even in their simplest form, for a three-dimensional complex geometry, it's not a trivial task. It is necessary a (bundle) software that provides Computer Aided Design (CAD) geometry import, mesh generation, solver and post-process analysis. In general is a program characterized by ease of use and high reliability [1].

It can handle large models with parallel solver both in local (desktop computer) and on hundreds of CPUs on a cluster grid by Command Line Interface (CLI). In the local client everything run in a single environment, from the geometry creation to the results visualization.

Another interesting feature is the possibility to automate tasks with Java macros. They can be recorded and played inside the software environment, though they can be edited manually and called from CLI. This resulted convenient in the present work, since lot's of runs were similar, changing only a parameter per run, e. g. the flow angle of attack or a component position on the airplane. Java macros are mandatory when executing STAR-CCM+ on a cluster grid like SCoPE.

Star-CCM + solver is based on the finite volume method [1]. The solution domain is subdivided into a finite number of small volumes of control, said cells, formed by a set of faces, which in turn area set of vertices namely points in the space defined by a position vector .The faces of a cell must not intersect each other, except along the common edges, i.e. the control volumes must not overlap. The volume mesh obtained is the mathematical representation of the space where the problem is being solved, i.e. the computational domain. To preserve sharp edges, feature curves can be defined. Last, but not least, the software generates a single simulation (.sim) file, containing everything necessary to run locally.

3.3 SIMULATION WORKFLOW

We show in Figure 26 the general sequence of operation which have be done for the realization of a generic simulation [15], [1].

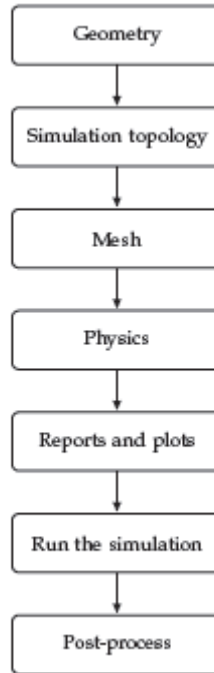


Figure 26 – General sequence of operation for a STAR-CCM+ analysis.

- **Geometry:** Can be imported from other CAD software or created directly in STAR-CCM+, though in version 6 (used in this work) the CAD environment can handle only very simple shapes. Whatever the method, geometry is a collection of surfaces and curves.
- **Simulation Topology:** Is the computational model defined as regions and boundaries to which physics can be applied. For external aerodynamics, a volume (e. g. a block shape) representing the fluid domain to be simulated must contain the entire geometry inside.
- **Mesh:** Is the numerical domain. STAR-CCM+ can easily and automatically generate surface and volume mesh, once defined several parameters, including size and refinement quality.
- **Physics Models:** Can be easily enabled. STAR-CCM+ can handle single and multi-phase fluid flow, heat transfer, turbulence, solid stress, dynamic fluid-body interaction, aeroacoustics and related phenomena.
- **Reports, Monitors and Plots:** Should be defined and activated to check for convergence, since STAR-CCM+ uses an iterative procedure to reach the solution to the transport equations that satisfies the boundary conditions for a chosen scenario.
- **Run the simulation:** Will automatically initialize the solution and launch the solver. For an interactive session, residuals will be plotted in the client workspace and reported in the output window. For batch sessions, residuals will be echoed to the command console. The simulation can be stopped and resumed anytime.
- **Results:** Can be visualized with scenes as contours, vectors and streamlines. It is possible to create animated scenes. Scatter plots are also possible. In an interactive session, graphical results can be visualized as the simulation run, step by step.

3.3.1 MESH GENERATION

The starting point for generating a mesh is a surface description. These surfaces usually come from CAD or similar packages. Mesh in STAR-CCM+ can be imported from an external source or generated within the software CAD environment.

The core volume mesh can contain either trimmed, polyhedral or tetrahedral type cells. Prismatic cell layers can be included next to wall boundaries to account for boundary layers. Volumetric controls using shapes as rectangles (bricks) and spheres can also be included to increase or decrease the mesh density of both the core mesh and/or prism layer mesh. Alternatively, the thin mesher can be used to produce either a tetrahedral or polyhedral volume mesh for thin geometries. The mesh is automatically built on the regions and boundaries defined earlier by the user (see figure workflow), once defined (at least) a mesh continuum and its parameters. A mesh continuum is the collection of meshing models that are used to generate the surface and volume mesh for the input geometry representing the individual regions to be used for the simulation.

Basically the mesh size can be defined in two ways: relative and absolute. The relative size consists in choosing the base size of the mesh, that is the reference length of the problem to study, and all other sizes will be a percentage of this base size. On the contrary, an absolute size will be fixed and unrelated to the reference value. Of course it is possible to have a part defined with relative sizes and another part defined in an absolute way. Volume mesh is always created on a surface mesh. That is volume mesh size propagates from the surface mesh size. Three different parameters are used to control the surface size, namely:

- target size;
- minimum size;
- maximum size.

The target size is the desired edge cell length on the surface while the minimum and maximum sizes control the lower and upper bounds of the cell edge lengths (when refinements from curvature and/or proximity effects are included). Three combinations of the target, minimum and maximum surface sizes are allowed:

- minimum and target size;
- minimum and maximum sizes;
- only minimum size.

3.3.2 DEFINING THE PHYSICS

The mechanism is the same of the mesh generation: one or more physics continua models must be enabled.

In general, STAR-CCM+ models and solvers rely on the following areas:

- space, time and motion;
- materials;
- flow and energy;
- species;
- turbulence and transition;
- radiation;
- aeroacoustics;
- combustion;
- multiphase flow;
- solid stress;
- electromagnetism.

The analysis carried on for this work required only a steady state solver and an incompressible viscous flow model. It is known [4] that a viscous flow can be laminar or turbulent and that viscosity can be accounted only in a small region of the fluid adjacent to the body surface – the boundary layer. The flow regime imposed in the simulation files of this work is turbulent, since a laminar flow around an airplane is unrealistic.

The turbulence model chosen is Spalart-Allmaras. The original Spalart-Allmaras model was developed primarily for the aerospace industry and has the advantage of being readily implemented in an unstructured CFD solver, unlike more traditional aerospace models. It solves a single transport equation that determines the turbulent viscosity. This is in contrast to many of the early one-equation models that solve an equation for the transport of turbulent kinetic energy and required an algebraic prescription of a length scale [15]. It gives good results with attached boundary layers and flows with mild separation. In short, it's simple, fast and suitable for the scope of this work [7].

3.3.3 CONVERGENCE

The stopping criterium chosen is a prescribed number of iterative steps order of magnitude as thousand. Convergence is judged by looking at the residual plot and the wall y^+ . The residual r in each cell represents the degree to which the discretized equation is not completely satisfied. In a perfectly converged solution, the residual for each cell would be equal to machine roundoff. So the residual is the error generated by the approximate solution when it is substituted into the linear system. This is the concept of the residual and it is always valid, no matter how complicated its mathematical expression.

3.4 THE SCoPE GRID INFRASTRUCTURE [6],[1]

At time of writing, no desktop computer could handle CFD 3D simulations of millions of cells in a reasonable amount of time. This work saw the light also thanks to the availability of the University's cluster grid, since lots of configurations (lost dorsal fins), at several angles of incidence had to be analyzed. Runs with 16, 32 or 64 CPUs per simulation were commons to get results within a day.



Figure 27 – Optical fibers network link for the Grid SooPE [1].

Sistema Cooperativo per Elaborazioni Scientifiche Multidisciplinari (SCoPE) is a scientific data center, based on a grid computing infrastructure, and it is a collaborative system for scientific applications in many areas of research. Figure 28 is a glance of the data center.

It is a project started in 2006 by the University of Naples 'Federico II'. The data center hosts about 300 eight-core blade servers, 220 terabyte of storage, and is already able to accommodate 500 more servers. Actually it has over 2400 CPUs.

The scientific applications are of the areas of Astrophysics, Chemistry, Mathematics, Medicine, Engineering and Physics. The data center is located in the Monte S. Angelo Campus, which already hosts the Faculty of Sciences and it is close to the Faculty of Engineering, with kilometers of preexisting optical fibers. The network infrastructure is shown in Figure 27.

Here follows some interesting data:

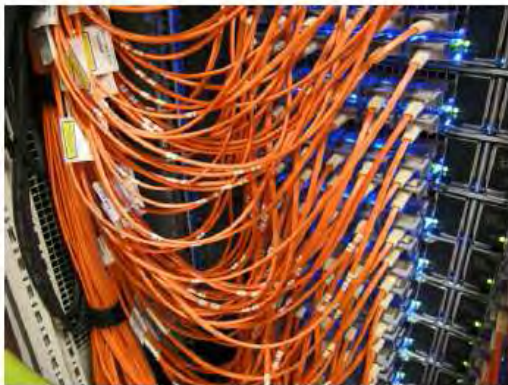
- localization in a building of about 150 m^2 .
- power plant capable of delivering 1MW of electric power in a continuous mode;
- efficient cooling system, capable of dissipating $2000\text{W}/\text{m}^3$ and $30\ 000\text{W}$ per rack;
- standard (Gigabit Ethernet) networking infrastructure, with a high capacity switching fabric;
- low latency (Infiniband) networking infrastructure, with a single switching fabric for each group of 256 servers;
- large storage capacity, both NAS (Network Attached Storage) working with the ISCSI protocol, and SAN (Storage Area Network), working with a Fibre Channel Infrastructure (see Figure 27);
- open source (Scientific Linux) for the operating system;
- integrated monitoring system for all the devices of the data center, able to monitor the most relevant parameters of server, storage, networking, as well as all the environmental parameters (as temperature, humidity and power consumption).



(a) Three rack servers of the data center.



(b) Storage devices.



(c) Fiber optic connections.



(d) Cables above the racks.

Figure 28 –SCoPE data Center, Device & Connections [6].

3.5 MY SIMULATION

We show which kinds of operation were carried out to perform a simulation.

1) *I imported the geometry of the vertical and fuselage*

After being made the geometry of vertical and the fuselage in a CAD environment with CatiaV5, these geometries were imported in the geometric environment of STAR-CCM+ as parts.

2) *I realized the parametric geometry of the Dorsal fin*

The program gives the possibility of Design Parameters Manager. In my case the parameters for the successive parameterization are h_{df} and L_{df} thanks to which I can control the overall geometry variation also in terms of dorsal fin surface (S_{df}) and sweep angle ($\varphi_{o,df}$). I defined two planes spaced by a value equal to the height of fin. In these two planes I made sketches that represent the profile of base and tip of the dorsal (see Figures 29 & 30).

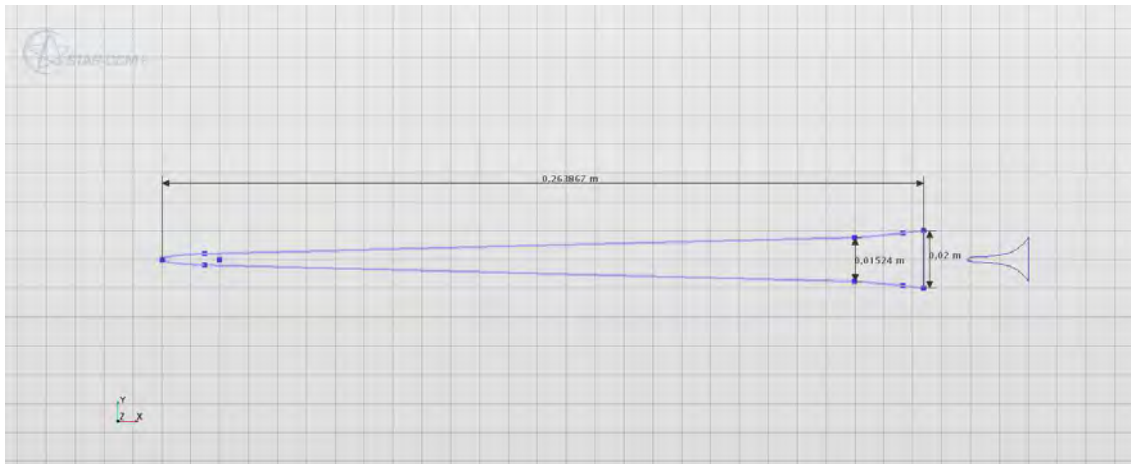


Figure 29 – Root Section of Dorsal fin in CAD design environment in STAR-CCM+.

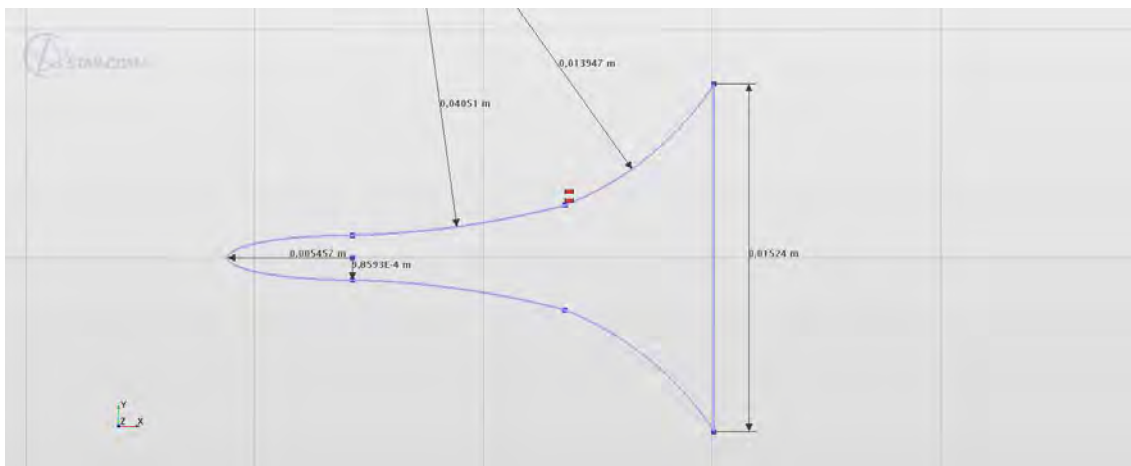


Figure 30 – Tip Section of Dorsal fin in CAD design environment in STAR-CCM+.

I want to highlight the characteristic shape of these profiles which have a very sharp leading edge (see Figure 31).

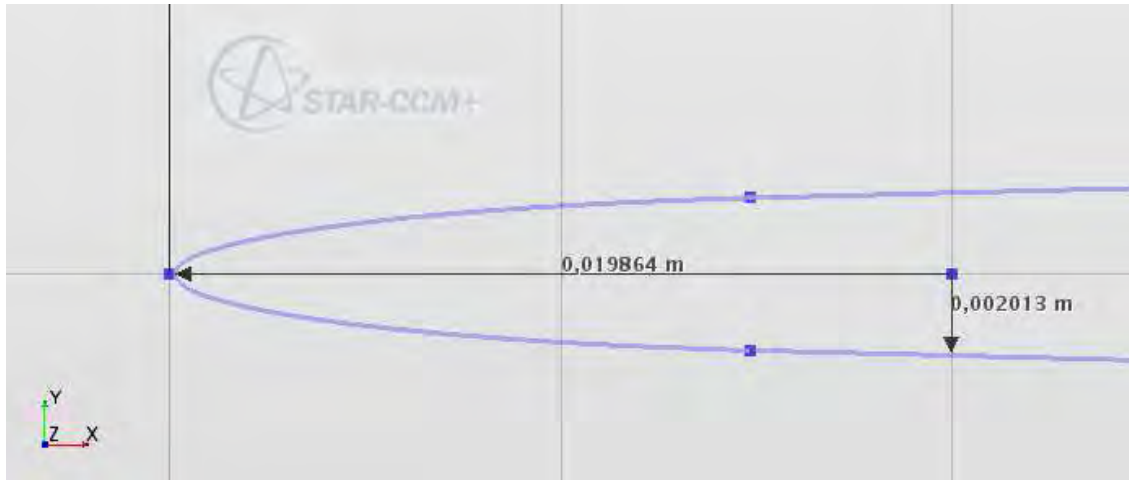


Figure 31 – Leading Edge of Root Section of Dorsal fin.

This characteristic has been sought specifically to ensure the phenomenology of vorticity. A less sharp leading edge, would not allow those high pressure gradients high as to generate vorticity.

With the loft function I made the final surface that has been transformed into a geometric part as Vertical and fuselage. The final result for the reference geometry of the dorsal is shown in Figure 32 in which the images representing the 3D views and a perspective view.

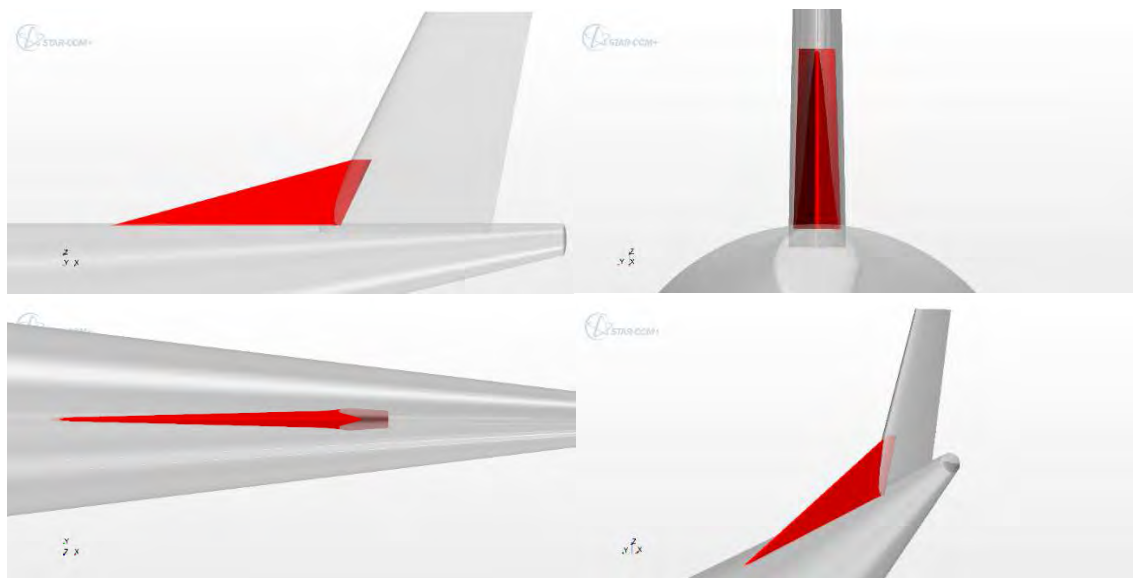


Figure 32 – 3D View and Perspective View of Final Geometry of Dorsal fin.

We present now the cross sections for three equally spaced stations respect to the height of the dorsal fin (see Figure 33) in order to understand some geometric characteristic of the resulting profiles.

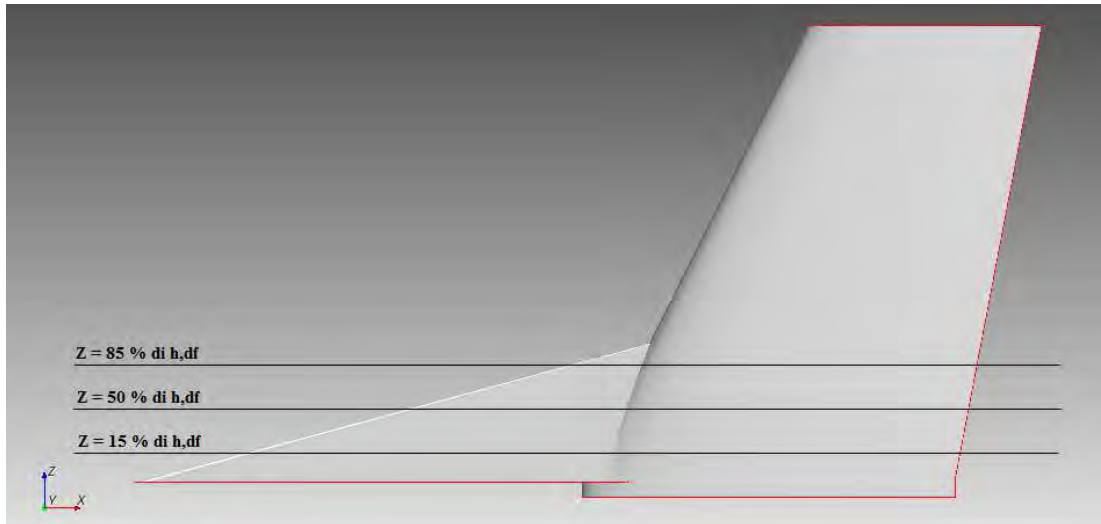


Figure 33 – List of investigated section of Dorsal fin.

We can see from Figures 34 & 35 & 36 that the dorsal, is inserted in the vertical with a strong geometric discontinuity. This discontinuity is getting stronger by the stations that are close to the tip profile of the dorsal, in fact, the dorsal becomes increasingly thin having a taper vertically also. This discontinuity is softened by the stations that are close to the root profile of the dorsal. Such root profile has been achieved considering the tangency condition with the root profile of the vertical as shown in Figure 37.

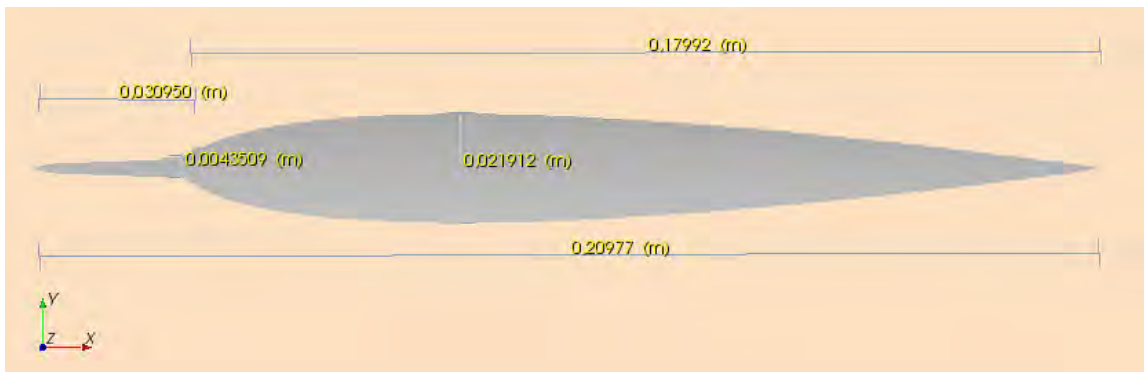


Figure 34 – Z = 85 % of h,df.

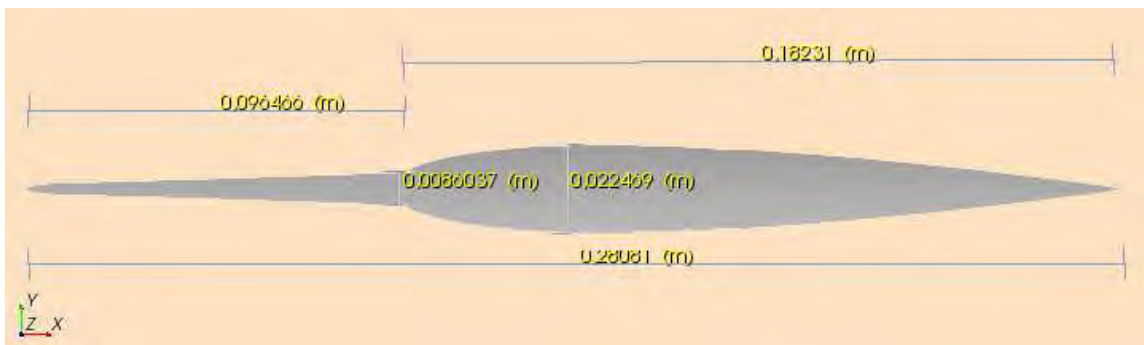


Figure 35 – Z = 50 % of h,df.

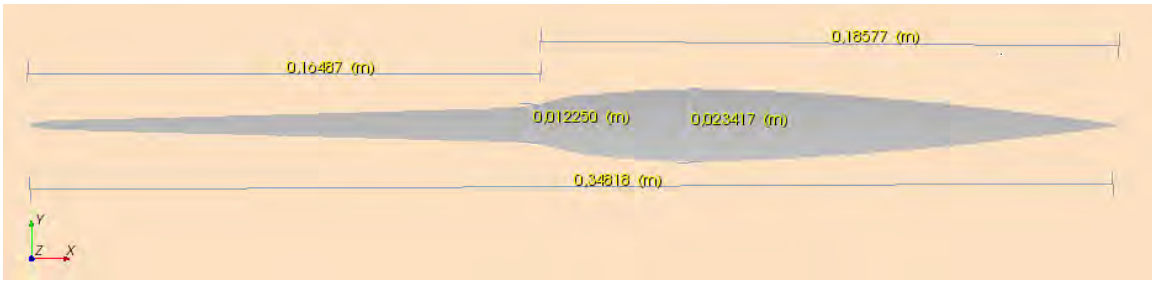


Figure 36 – $Z = 15\%$ of h,df .

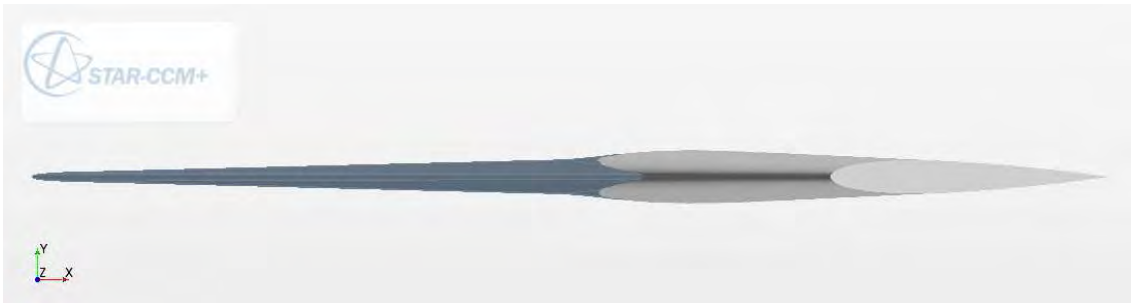


Figure 37 – Top view to evaluate the tangency condition between Dorsal and Vertical for the root station.

The geometry of the reference dorsal fin complies with certain characteristics that are found in the dorsal fin of the ATR 72 in Figure 38 where we see a tangency of the root profile of the dorsal, with the root of the vertical plane and which has a taper, even in vertical direction.

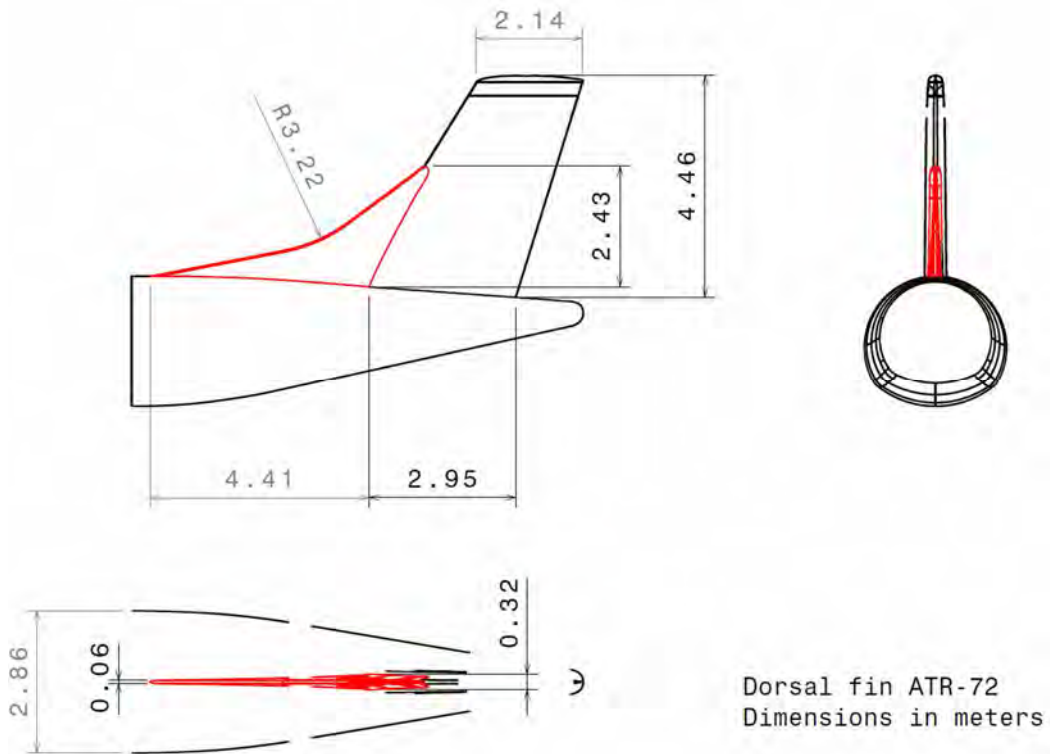


Figure 38 – 3D View for ATR as Example of Dorsal Fin Geometry.

Unlike the ATR 72, our dorsal geometry does not have a radius of curvature (round edge dorsal fin), in fact it keeps constant sweep from the leading edge to the trailing edge.

In Figure 39 there are some real examples of dorsal fin to which our geometry is inspired.

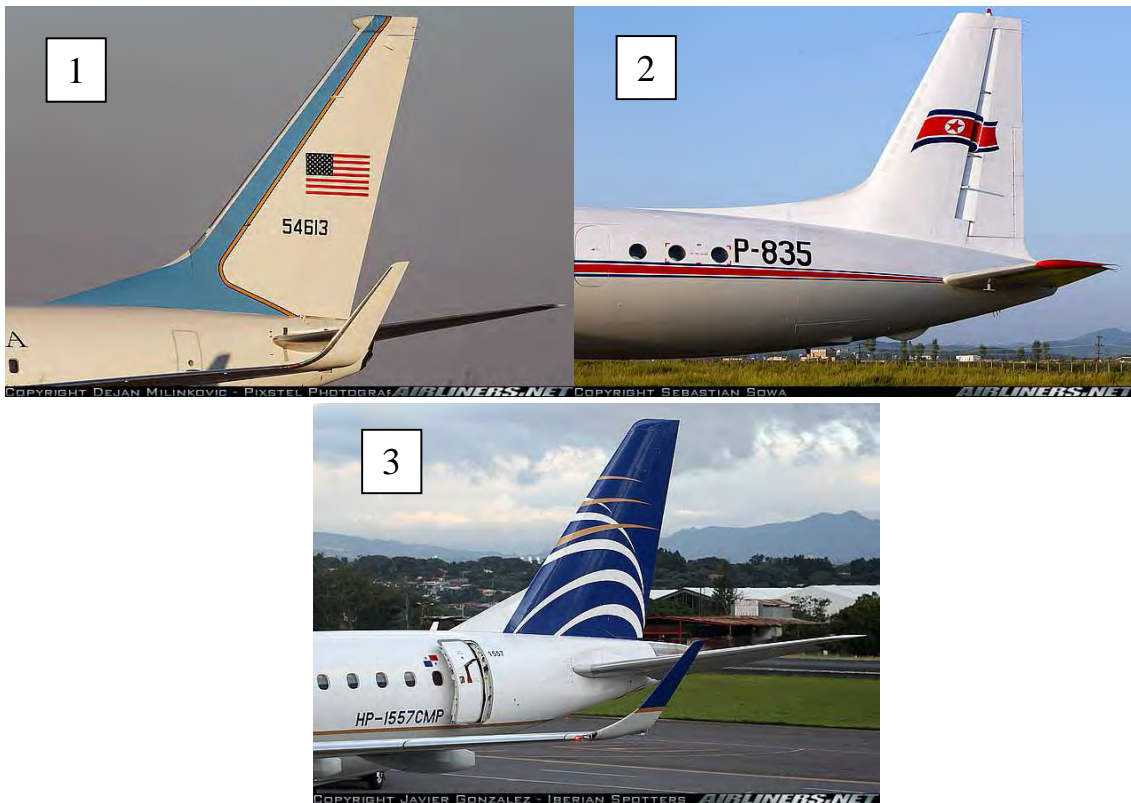


Figure 39 – Different Example of Dorsal Fin Geometry, C-40_B-737, II-18D, ERj-190, .

Types of Dorsal fin

For the purpose of **Scholz** [3] several aircraft have been examined. Aircraft have different types of dorsal fin.

Figure 40 shows an aircraft with a conventional tail with no dorsal fin or any extension of vertical tail. It has a straight leading edge from tip of the vertical tail to the root, where it joins with the fuselage. This sharp blend between leading edge and fuselage may be called here “sharp leading edge”. Generally, it is the design of this is conventional tail which is given in aircraft design book. Figure 41 present an aircraft with a dorsal fin added fin added to the conventional vertical tail. Figure 42 present an aircraft with round edge dorsal fin. Figure 43 shows a dorsal fin with an integrated air intake ram. This is done probably to save space and provide better support to the component. Figures 44 and 45 show aircraft with dorsal fin extension. In Figure 44 the vertical tail, dorsal fin and dorsal fin extension can be distinguished as separate entities joined together. However, in Figure 45 can be observed that the dorsal fin and dorsal fin extension merge gradually with the vertical tail.

Figure are compiled from an internet image search. The rear segment of the aircraft in each picture was cropped to present an orthogonal view of the tail section.

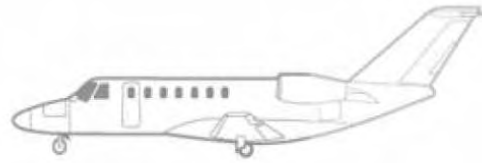


Figure 40 – View and side view of conventional tail without dorsal fin (with sharp leading edge) of a Cessna Citation CJ3 (automobile 2013 and Blueprints 2013).



Figure 41 – View and side view of a dorsal fin of a Fokker 70 (Aero 2013 and Fly Fokker 2013).



Figure 42 – View and side view of a round edge dorsal fin of an A 320 (Prendrel 2013 and Aerospaceweb 2013).

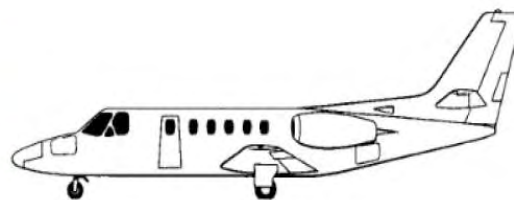


Figure 43 – View and side view of a dorsal fin of a Fokker 70 (Aero 2013 and Fly Fokker 2013).

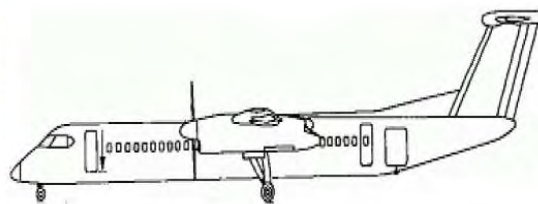


Figure 44 – View and side view of combined dorsal fin with dorsal extension of a Q-400 dash 8 (Aerospace 2013 and Aviastar 2013c).

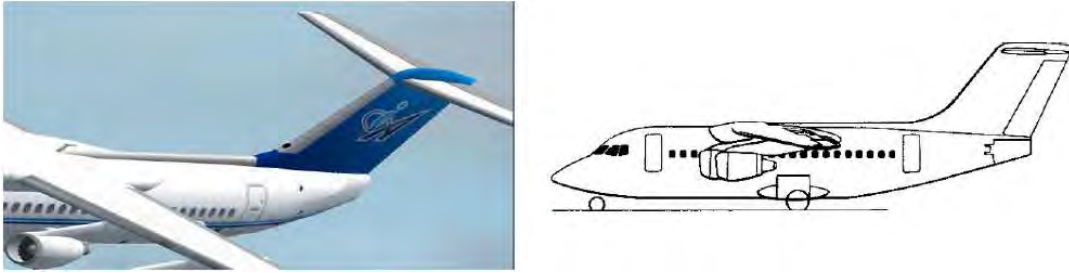


Figure 45 – View and side view of combined dorsal fin with dorsal extension blending into one another on a Bae 146 (Tutavia 2013 and Aviastar 2013).

3) Selection of the physical model:

- The flow is steady and incompressible, with a Reynolds number, about 1 million (assessed on the mean aerodynamic chord of the vertical).
- The turbulence model used is Spalart-Allmaras.
- The flow is fully turbulent (fully turbulent flow) then the transition is set to the leading edge.

This model represents very well the physics of the problem until the stall, provided that the mesh is enough dense to capture the phenomenology. We can refer to [7] which showed that actually, the results are complying with what occurs in the real case.

We show in Figure 46 the QuickMask that the software provides to control the physical choice for analysis.

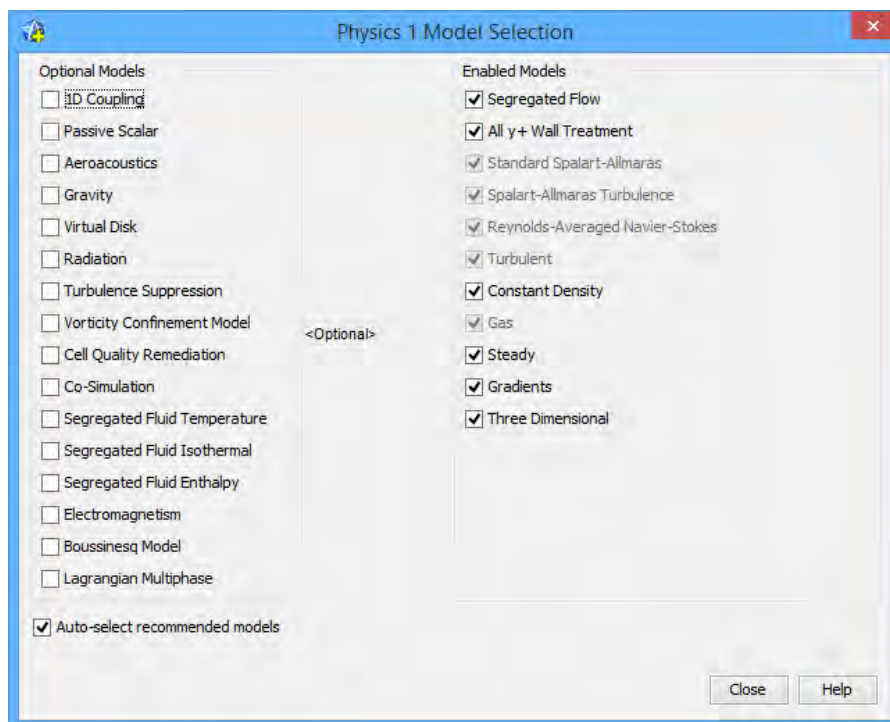


Figure 46 – Physics Model Selection windows control of STAR-CCM+.

4) Creation of the calculation domain requiring the physical characteristics for the various regions

I made first of all the volume of calculation (see Figure 47). I defined surfaces of Inflow and Outflow, which combined create the block when is positioned the geometry to analyze.

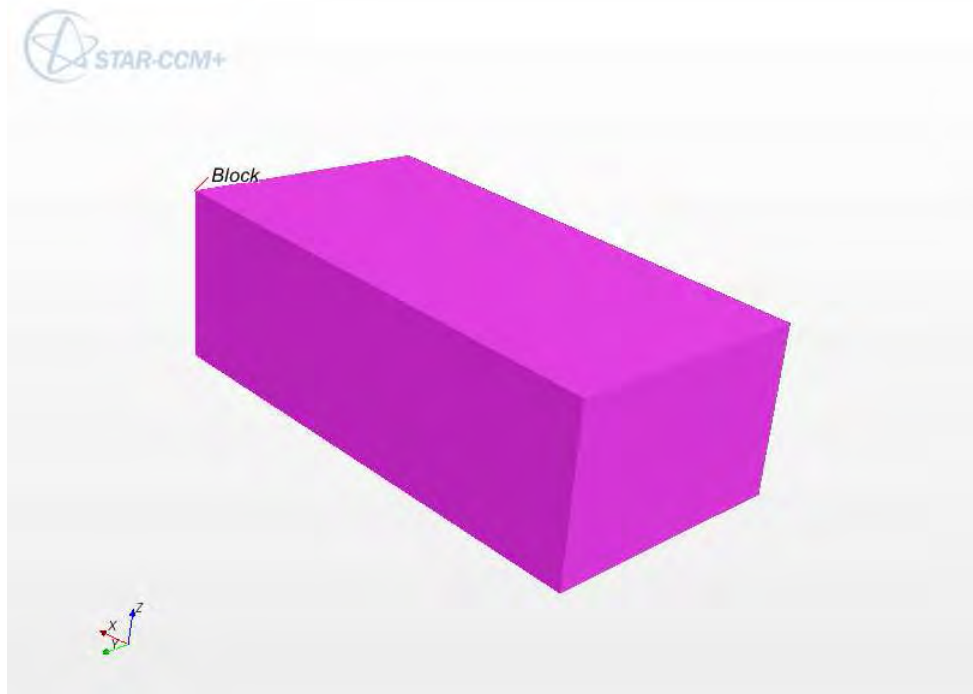


Figure 47 – Computational Domain of Simulation of STAR-CCM+.

I selected the three geometries (Fuselage, Vertical, Dorsal fin) which determine the overall geometry to be analyzed (see Figure 48).

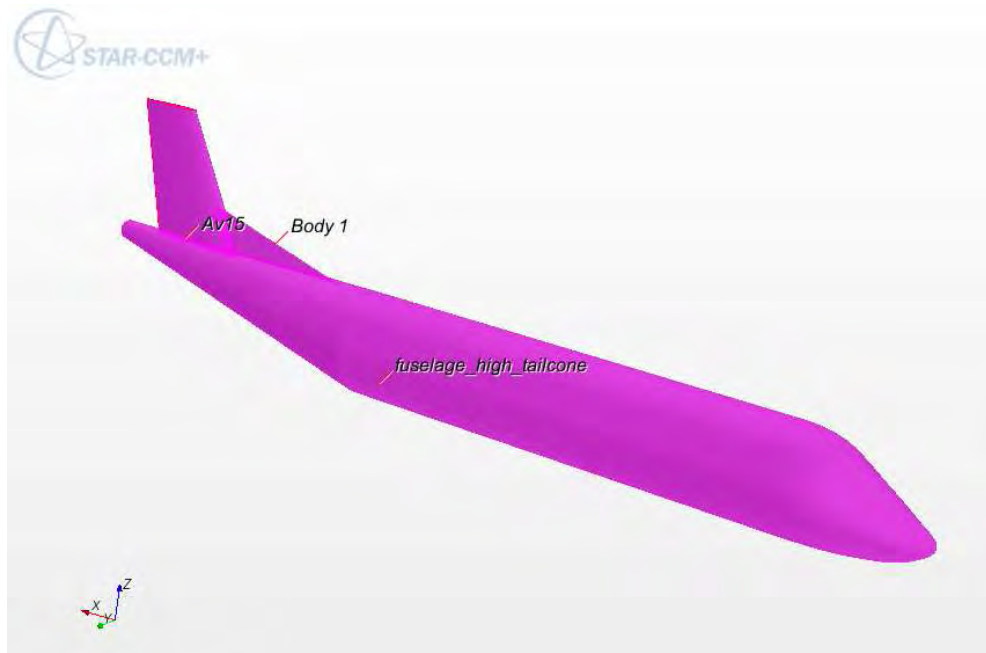


Figure 48 – Geometry list of Simulation of STAR-CCM+.

This geometry is very small compared to the size of the block, in order to be safe, relatively to wall phenomena (see Figure 49).

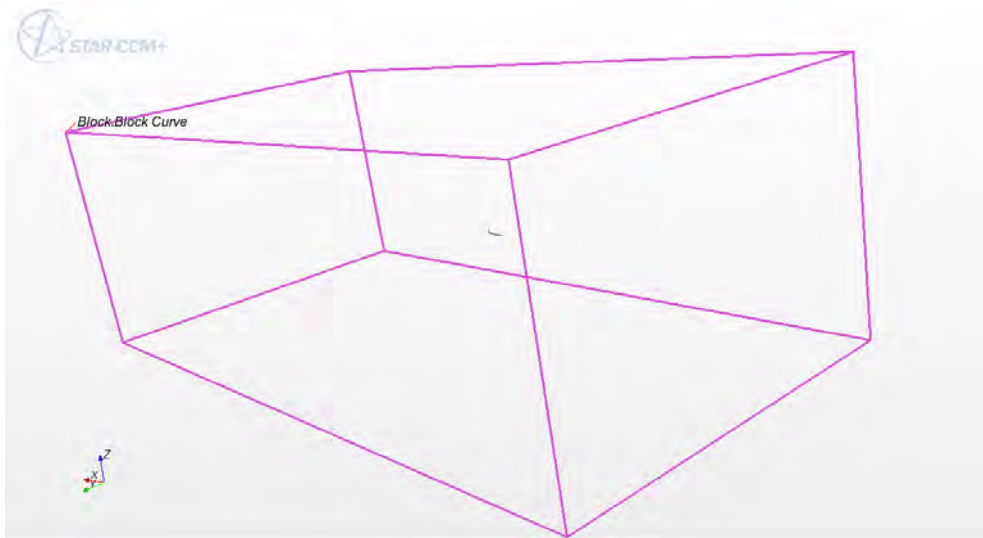


Figure 49 – Relative Dimension between Aircraft and overall Domain of STAR-CCM+.

Using a Boolean operation of subtraction between the block and the overall geometry I realized the computational domain that I called Fluid Dorsal (see figure 50).



Figure 50 – Final Computational Domain of simulation of STAR-CCM+.

This is the domain in which the RANS will be resolved with the finite volume method. I had to then assign the regions to the parts of our domain by selecting a region for each part and a boundary for each part surface.

For each created region, I selected the type of part surface, which for Dorsal, fuselage and vertical, is of Wall, for Inflow is Velocity inlet and for Outflow is Pressure Outlet.

5) Creation of the mesh size and Volume

For each region I chose the degree of refinement according to need. This can be expressed in terms of Minimum size & Target size relative to the Base size. It was then realized a tetrahedral mesh surface (see Figure 51) and an unstructured mesh volume (see Figure 52).



Figure 51 – Tetrahedral Mesh Surface of STAR-CCM+.

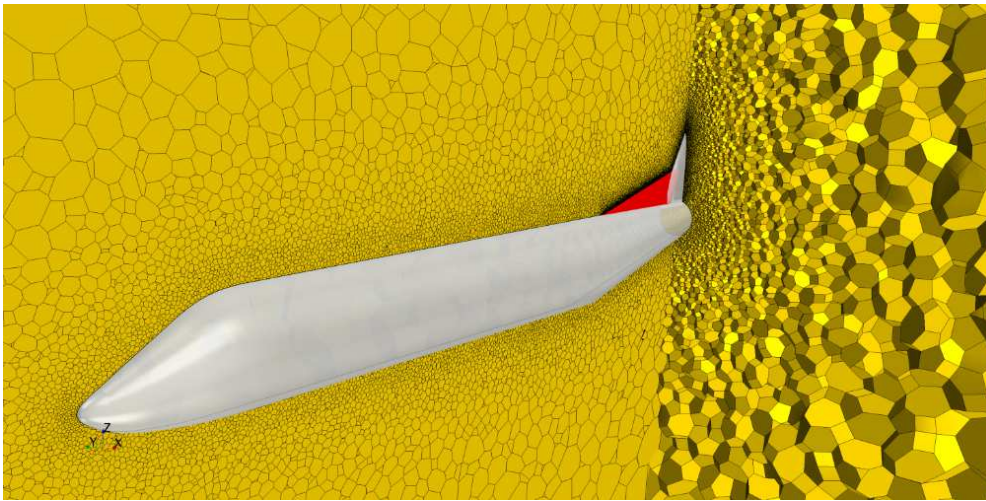


Figure 52 – No Structural Mesh Volume of STAR-CCM+.

6) Report realization

Were defined reports as force coefficient and momentum coefficient and were set the following items for the correct determination of these coefficients (see Figure 53).

We remember that all the coefficients are obtained by considering the reference surface of the wing that can be attributed at a possible model for wind tunnel test amounted to $0.225 [m^2]$. To evaluate the moment coefficient we use a possible position of CG like reference point as show in Figure 5. After defining the report I had to select the regions for which they had to be determined.

Properties	
Reference Area	0.225 m ²
Reference Radius	1.5 m
Reference Velocity	83.0 m/s
Reference Density	1.22 kg/m ³
Axis Origin	[0.78, 0.0, 0.0347] m
Axis	[1.0, 0.0, 0.0]
Force Option	Pressure + Shear
Reference Pressure	0.0 Pa
Coordinate System	Laboratory
Parts	[Fluid Dorsal 5: Dorsal 5, ...]
Units	
Expert	
Number of Bands	0
Representation	Volume Mesh
Smooth Values	<input type="checkbox"/>

Figure 53 – Properties Windows for Coefficient Setting of STAR-CCM+.

7) Run the simulation

I made starting the iterative process of calculation by selecting as stopping criteria the maximum number of iterations around 3000.

8) Monitoring results

I proceeded with the visualization of the residues to control their convergence in the case in which the calculation is successful or possible divergence in the case in which the coefficients can't be determined.

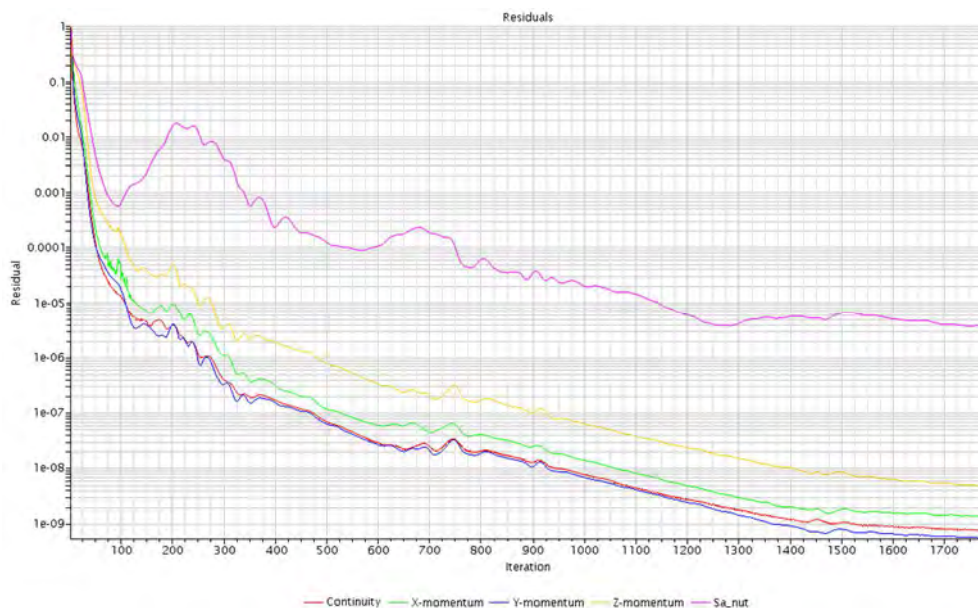


Figure 54 – Residual Example of a simulation of STAR-CCM+.

Where residues reach almost zero the iteration process could be considered as gone to convergence (see Figure54).

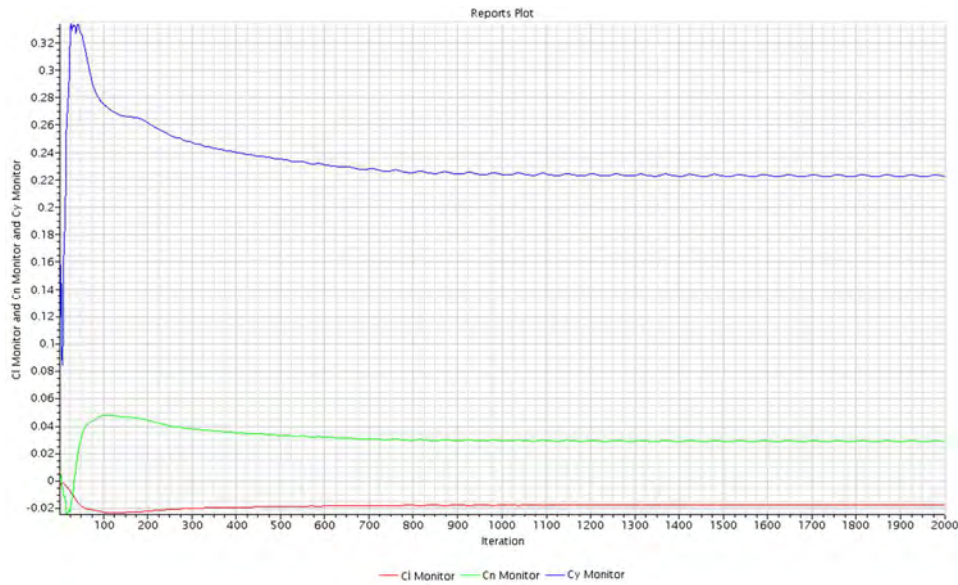


Figure 55 – Report Plot Example of a simulation of STAR-CCM+.

Analyzing the coefficients then we see that they have stabilized at constant values (see Figure55), so we are quite sure that the calculation is gone to convergence.

4) Collection of the results

The results are presented in tabular form by the program (see Figure 56) which automatically divide all contributions returning this:

```

Output - Cn Report
Origin: [0.78, 0.0, 0.0347] m
Axis: [0.0, 0.0, 1.0]
Coordinate System: Laboratory
Reference Radius: 1.5 m

Vectors

Part      Pressure()      Shear()      Net()
-----
Fuselage [ 6.590407e-04, 1.359583e-02, -4.106559e-02] [ 1.472187e-05, 1.000953e-04, -3.637903e-04] [ 6.737626e-04, 1.369592e-02, -4.142938e-02]
Vertical [-2.007920e-02, -3.172306e-03, 7.356837e-02] [-1.368570e-05, -1.095016e-04, 5.295034e-05] [-2.009289e-02, -3.281808e-03, 7.362132e-02]
-----
Totals: [-1.942016e-02, 1.042352e-02, 3.250278e-02] [ 1.036167e-06, -9.406272e-06, -3.108400e-04] [-1.941913e-02, 1.041412e-02, 3.219194e-02]

Component in direction: [ 0.000000e+00, 0.000000e+00, 1.000000e+00] in Laboratory coordinate system
Part      Pressure()      Shear()      Net()
-----
Fuselage -4.106559e-02 -3.637903e-04 -4.142938e-02
Vertical 7.356837e-02 5.295034e-05 7.362132e-02
-----
Totals: 3.250278e-02 -3.108400e-04 3.219194e-02

Monitor value: 0.032191942510018584
    
```

Figure 56 – Output Report Example of a simulation of STAR-CCM+.

I exported the data into a spreadsheet by which I could make the graphical visualization of the curve so the various considerations.

4 SETUP SIMULATION

4.1 MESH ANALYSIS

Defined the starting geometry on the basis of statistical data, the first step is to choose the degree of refinement of the mesh that should guarantee an adequate level of safety in the validity of the results sense.

For the configuration BVD I set the parameters of the mesh as a percentage of the base size, which is a reference dimension that regroups the dimensional characteristics min size and target size, so refinement's level (see Table 4). In particular, we have made 4 settings with different values of the base dimension of that defines in turn the number of Surface Cells and Volume Cells (see Table 3).

<i>Mesh</i>	<i>Base size (m)</i>	<i>Surface Cells</i>	<i>Volume Cells</i>
4	1,00	501122	6966634
1	1,65	207934	3001701
2	2,00	141234	2082253
3	3,00	74366	1130199

Table 7 – Summary of Mesh parameters for BVD configurations.

As a percentage of base size have been defined the settings of regions Fuselage Vertical & Dorsal fin:

	Fuselage	Vertical	Dorsal fin
Min	0,1	0,05	0,015
Target	0,3	0,1	0,1
Thickness Prism Layer [m]	3,30E-04	1,65E-04	1,65E-04

Table 8 – Reference Geometry Parameters and characteristics ratio.

From the Figure 57 is clearly seen as the base size determines the number of cells. So the first step is to choose the value of Base size that would guarantee on the one hand a number of cells adapted to the study carried out, and on the other hand, a number cells not too high to avoid a sharp increase in computation time.

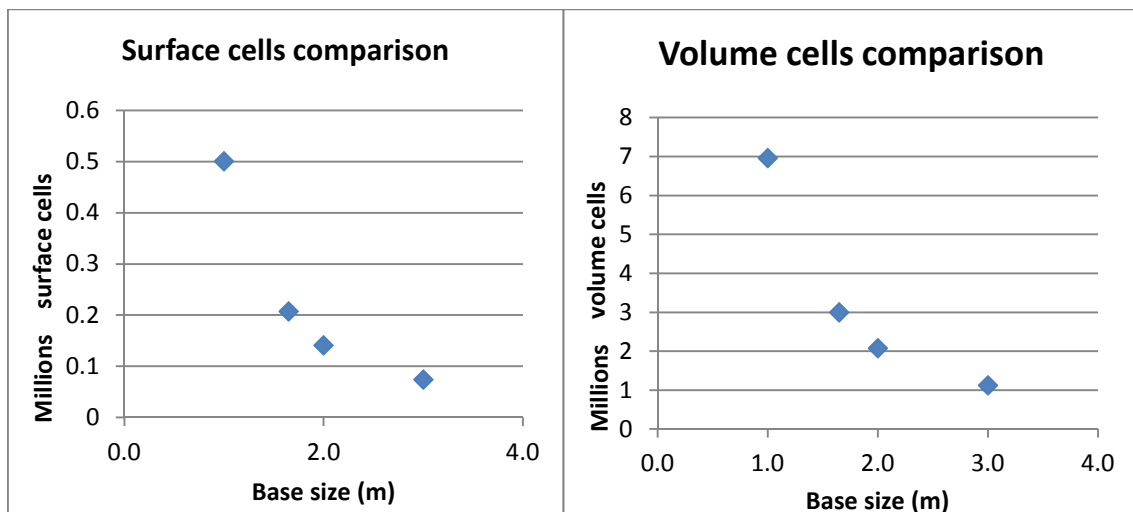


Figure 57 – Trade off on Base size.

For each one of these mesh, before starting the aerodynamic calculations, is necessary to assess whether the number of cells is adequate to the desired refinement's level overall. I have proceeded with a visual analysis for each one of those mesh looking for any problem concerning their correctness.

We make an example for a specific mash, however for all mesh I confirmed the good characteristics as well as for the sample mesh. I have focused the attention on certain areas of the surface mesh that is also the refinement index mesh volume used by the software as the computational domain. So, first of all, I have rated the overall goodness of the mesh and then I excluded the possibility that had not been respected the settings that were set during pre-processing.(see Figure 58)



Figure 58 – Macroscopic Visual Analysis of the sample mesh.

Confirmed the goodness of the mesh by a macroscopic visual analysis, I have focused the attention on the critical areas for the surface mesh. Such areas are represented by curved surfaces with a high radius of curvature, discontinuity surfaces at the intersections between the elements, and edges alive.

For surfaces with high curvature radius we mean primarily the dorsal fin and the leading edge of the vertical. The Figure 59 help us to see that the refinement's level is such as to ensure the correct curvature for both the dorsal fin and vertical.

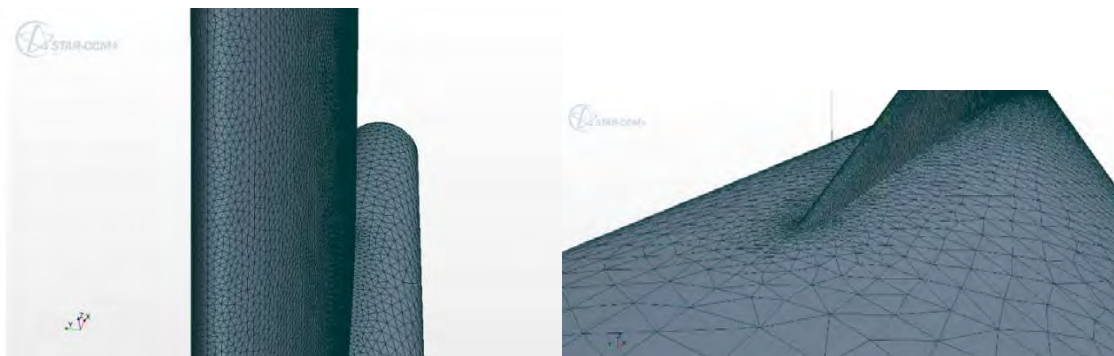


Figure 59 – Curved Surfaces of the sample mesh

For geometric discontinuities of the dorsal fin is obtained a satisfactory mesh both in the area of intersection with the fuselage, that the area of intersection with the vertical (see Figure 60).

The Figure 61 shows in particular the good success of the fusion between the dorsal fin and the vertical. The mesh have a single curvature close to the fuselage, while achieving the sharp edge in a gradual and continues manner, with the move away from the fuselage.

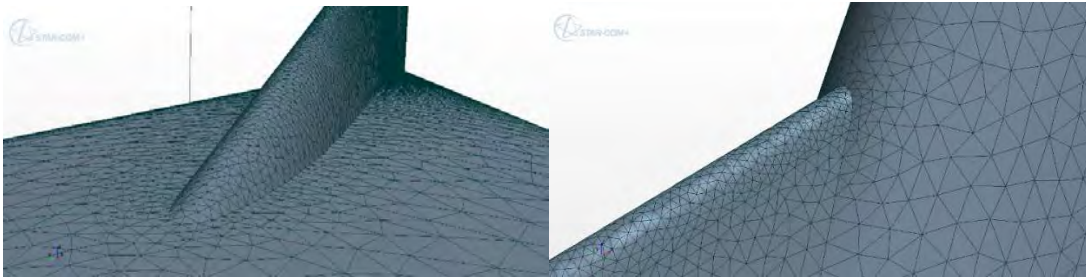


Figure 60 – Geometric Discontinuities of the sample mesh.

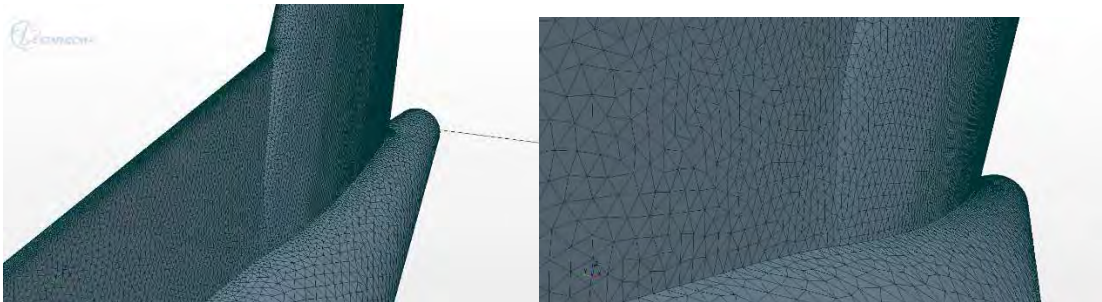


Figure 61 – Fusion between the Dorsal fin and the Vertical of the sample mesh.

We also remember at this stage that the geometry of the dorsal was desired with two kind of characteristics:

- The sharp edge in which there is an overpressure due at high pressure gradients
- The high radius of curvature that occurs at the tip of the dorsal fin, with which it generates the vortex that we talked about above.

In fact we can see from Figure 62 that the dorsal is inserted in the vertical with a strong geometric discontinuity.

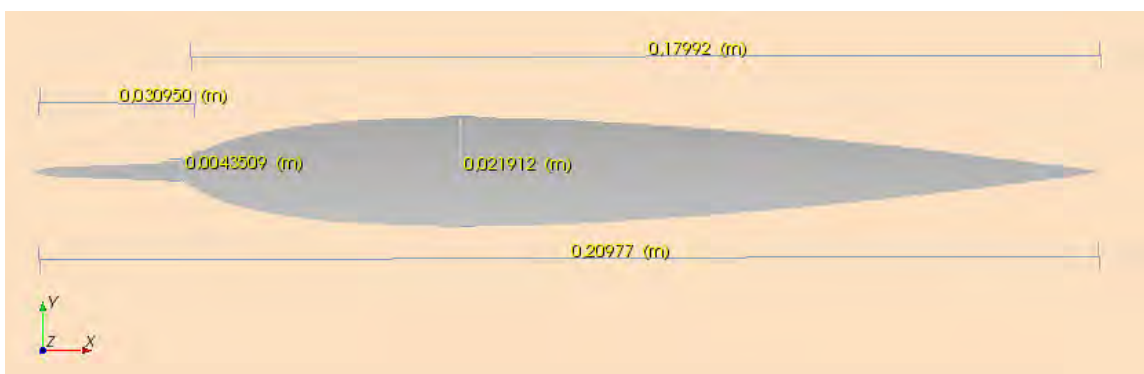


Figure 62 – $Z = 85\%$ of h, df .

Other sharp edges on which to pay attention are those of intersection between the vertical plane and fuselage, finally for the vertical edges of the tip section and the trailing edge (see Figure 63 & 64).

Since there was no problems evidence related to the mesh realization, I moved on to the next step which involves the aerodynamic analysis of this analyzed geometry.

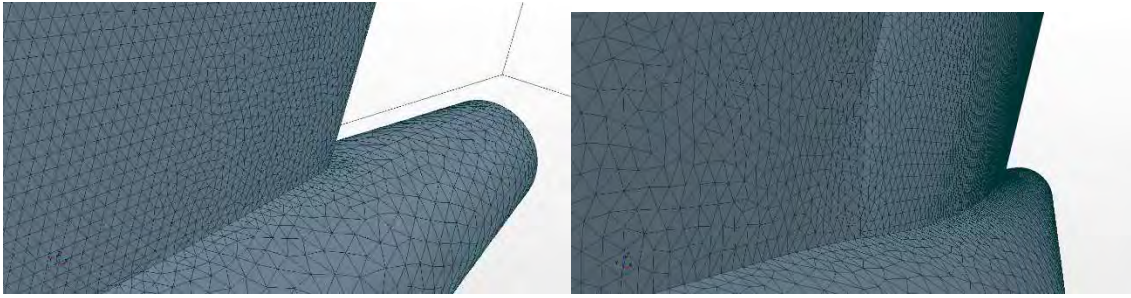


Figure 63 – Intersection between the vertical plane and fuselage



Figure 64 – Sharp edges of the vertical edges of the tip section and the trailing edge.

The next graph which shows the characteristic calculation time of my personal computer with 8 logical processors, is indicative of the calculations amount for each mesh. You might think that is useless to show such calculation time because is related to performance of a specific machine.

Actually we are not interested in the curve for the values in absolute terms point of view, but to understand the trend in calculation time increasing number of cells, which is independent of the type of machine. For example we can see from Figure 65 seen that the mesh 2 has a total calculation time which is about 40% of that of the mesh 4.

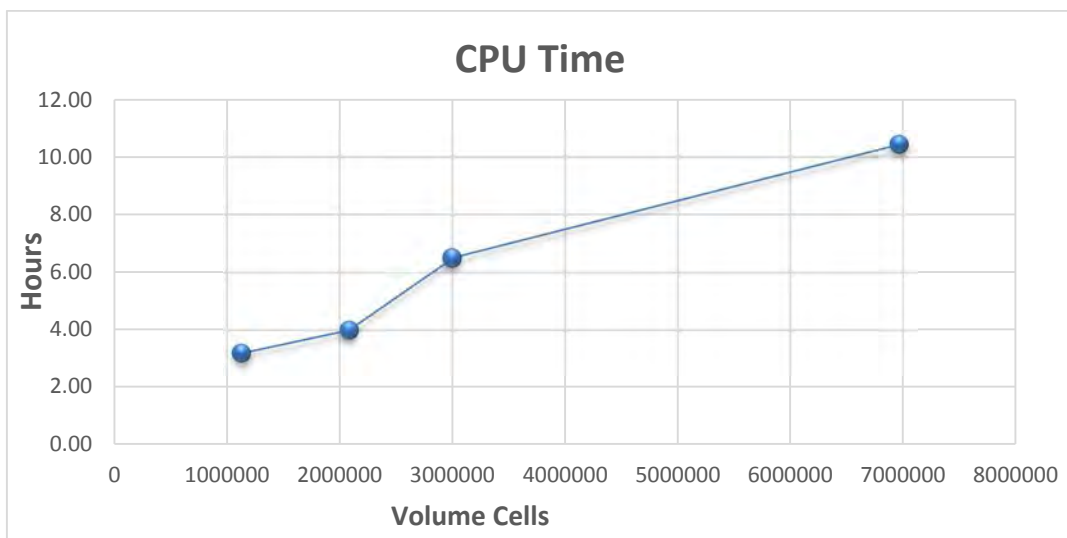


Figure 65 – CPU Time Trend for the analyzed mesh.

4.2 MESH CHOICE

The following graphs show in sequence the results of the BVD configuration for the four mesh. We can understand if the values between two consecutive mesh, for which there is a variation in the refinement's level, deviate a few percentage points or more.

To be sure of choice, these graphs have been reported for three characteristic angles 5° , 19° , 38° in order to have an overview of the influence of the number of cells on the aerodynamic results for the linear and non-linear operating conditions (see Figure 66, 67, 68).

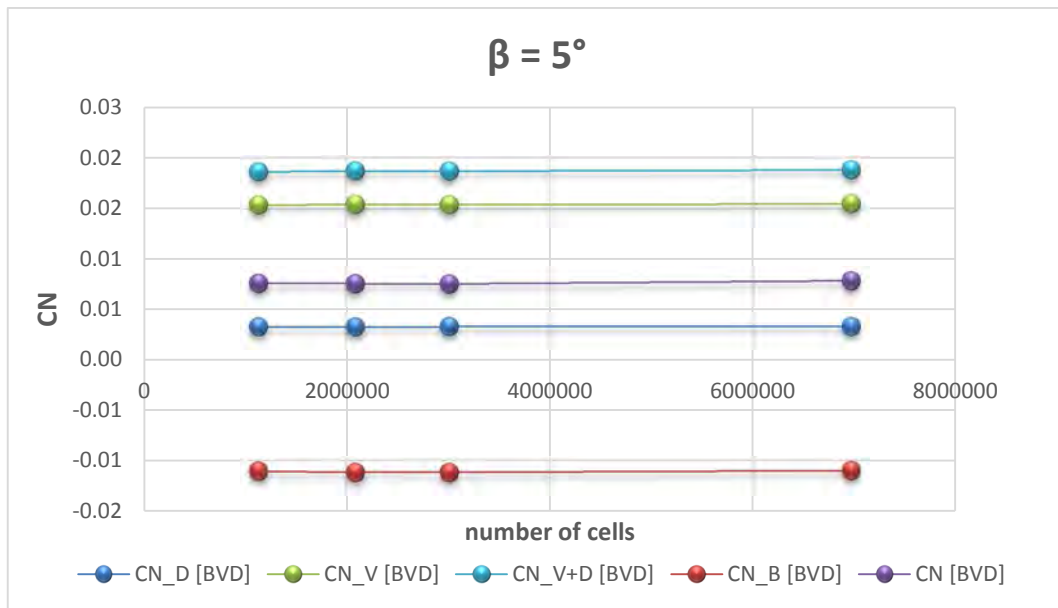


Figure 66 – Result as function of Mesh Refinement's Level for $\beta=5^\circ$.

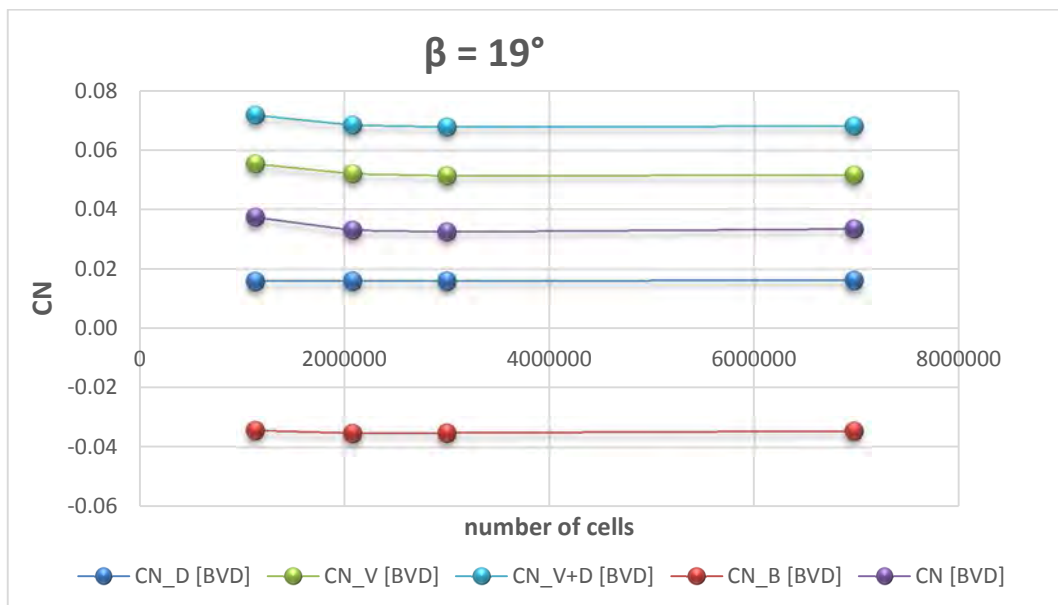


Figure 67 – Result as function of Mesh Refinement's Level for $\beta=19^\circ$.

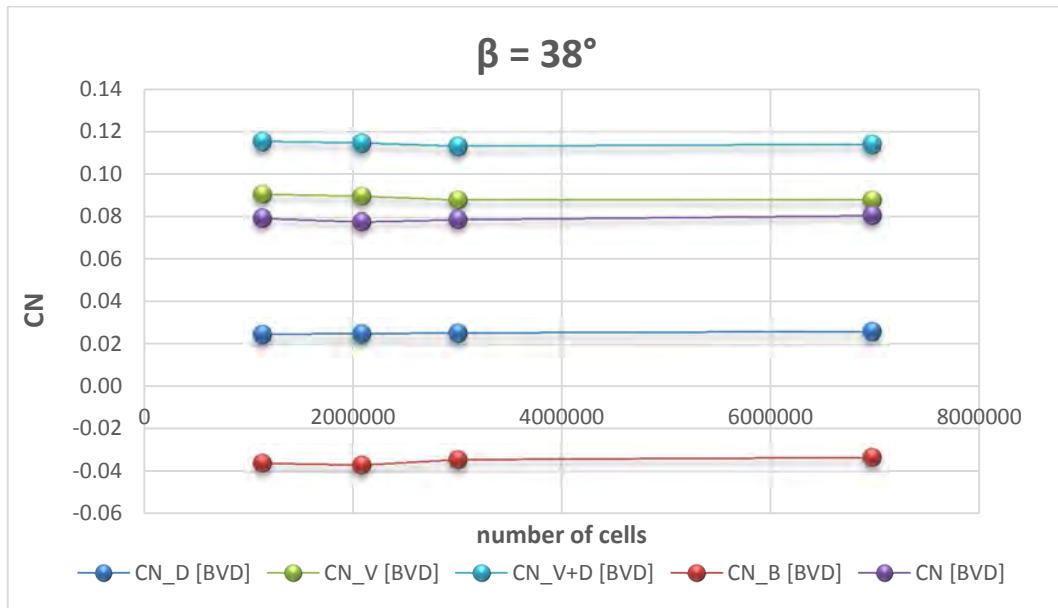


Figure 68 – Result as function of Mesh Refinement's Level for $\beta=38^\circ$.

It is clearly seen that while in the linear regime deviations are practically zero, in the nonlinear regime such deviations between the various mesh become perceptible. Downstream of this consideration we need to make another observation. The representation's scale of the graphs above is in the order of 10^{-1} and 10^{-2} , so that deviations which are noticed visually are about the second & third significant digit. This comforts us that we can't make significant mistakes in the choice of the mesh, even if we pick the one with the lower number of cells.

Analyzing the mesh 1 and 2, actually we see a deviation for the results which leads us to prefer the second mesh since having a higher refinement's level is better able to simulate the physics of the problem. Continuing this analysis, the mesh 2, 3 and 4 instead determines a consistency in the values, which are constant or with different about few percentage points.

Because this is an engineering analysis process, as such is always guided by the concept of optimization, which in this specific analysis about the possible mesh, leads us to choose the one with 2 million cells in order to ensure a greater speed in the determination of aerodynamic results for all configurations that will be analyzed later.

Confirmation that the mesh 2 is a right choice there is by comparing the CN total curve for all mesh in Figure 69. Is visible, that with respect to the mesh of 1 million the other three analyzed mesh tend to overlap for wide part of the curve. As could be expected the mesh denser analyzed is also the one for which corresponds the stall with greater delay. The less dense instead presents the stall at lower angles. The intermediate about 2 and 3 million are virtually coincident, so it's easy to see the motivation in the choice of the mesh 2 concerning the base size for successive configurations.

Concerning just the dorsal contribution it's clear from Figure 70 that there are very limited deviation which affect primarily the non-linear range in highest angle of sideslip.

Please note that even if we consider the deviance very limited, between the mesh 1, 2, 3 and 4 are still present deviations.

This aspect does not interest us because these deviations are due to numerical errors. Moreover remember that the purpose of this thesis is to identify the qualitative trend, so even if you find errors, they are not likely to jeopardize the evaluations on aerodynamic coefficients trends. So as mentioned above these errors are actually not influential to our reasoning.

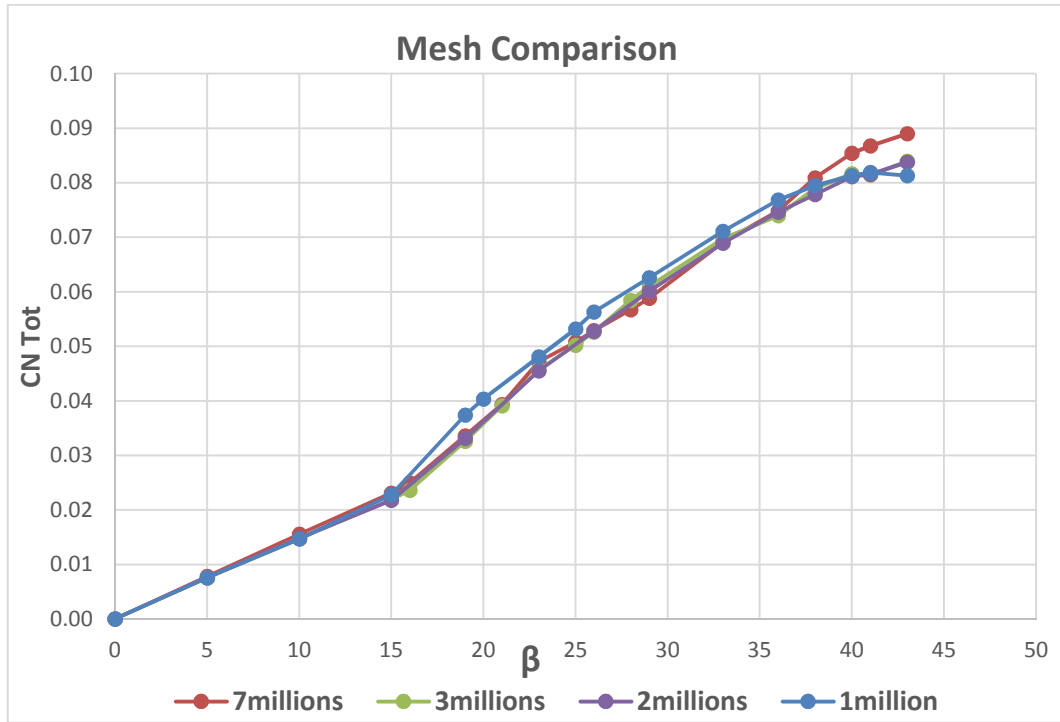


Figure 69 – Tread of Analysis of Mesh Refinement’s Level for Total yawing moment result.

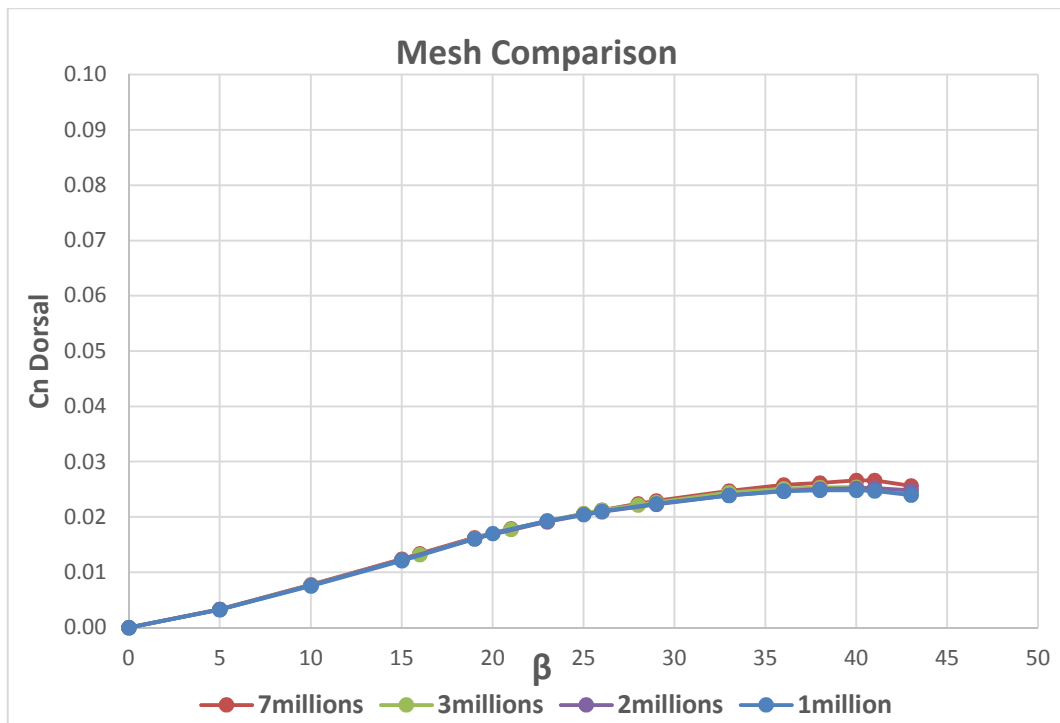


Figure 70 – Tread of Analysis of Mesh Refinement’s Level for Dorsal yawing moment result.

4.2.1 CLARIFICATION ON THE COEFFICIENT OSCILLATIONS.

Since the coefficients determination is the result of an iterative analytical procedure, for some simulations it was found an oscillatory behavior of the coefficients themselves.

In general in this circumstance I determined the coefficient as the average value of the oscillation. However, to give general validity of the results I wanted to focus on the fact that the amplitude of the oscillations is likely to compromise the results obtained in terms of qualitative trend.

Here below in Figure 71 & 72 is an oscillation example of the coefficients for two different mesh.

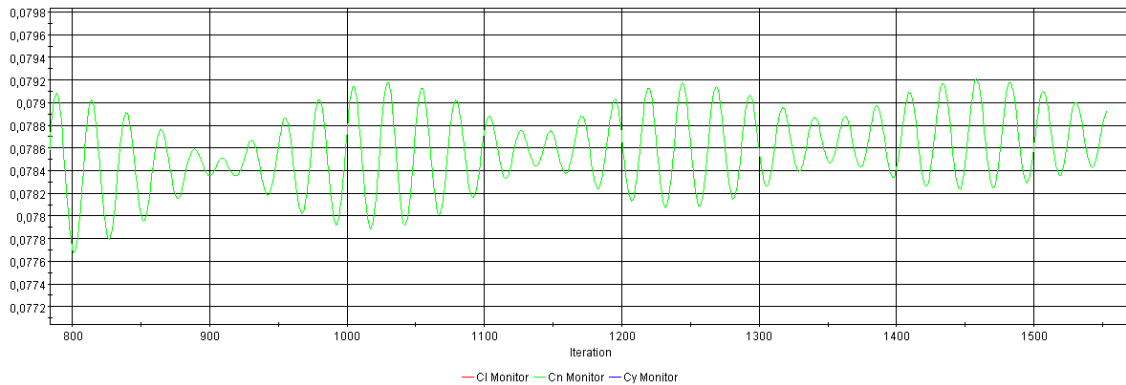


Figure 71 – Coefficient Oscillation Example for Mesh 3.

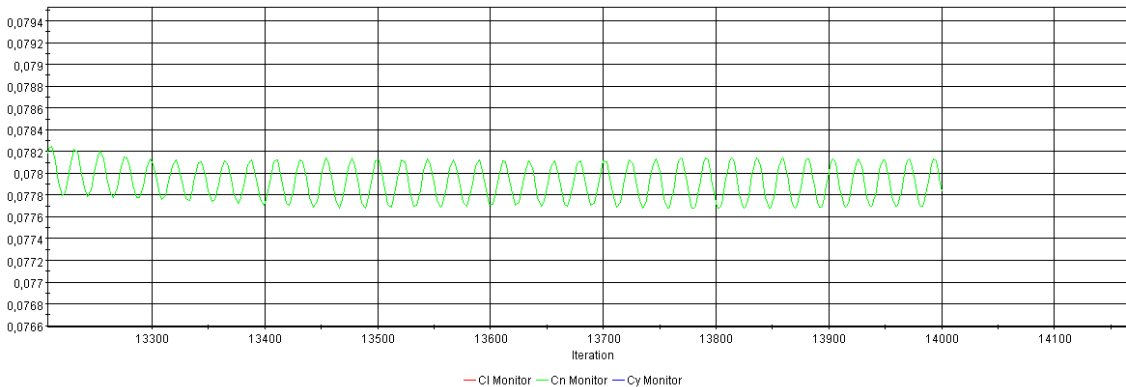


Figure 72 – Coefficient Oscillation Example for Mesh 2.

With Figure 73 we want to show that the oscillations obtained for some coefficients have a reduced amplitude compared to the average for other coefficients this magnitude is greater.

This makes us understand that it is necessary to take the average, what we have done for the simulations in which there are these oscillations, to ensure to not alter the conclusions in terms of trend.

Should be noted that, while in this type of analysis oscillations of a few percent can lead to wrong conclusions about the choice of the mesh, for the rest of our study in which we must evaluate the characteristic trend of the parametrizations, the amplitude of oscillations loses its critical. Indeed evaluate the effect of Cn for two Dorsal fin of different height, involves significantly different values that can't be influenced by any fluctuations in the third or fourth significant digit.

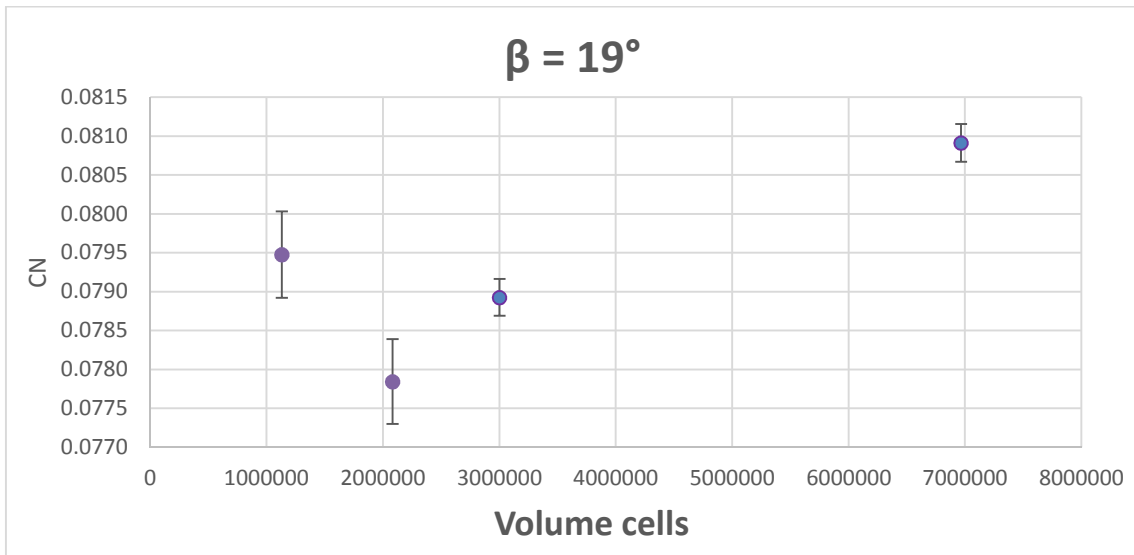


Figure 73 – Coefficient Oscillation Influence Example

4.3 AERODYNAMICS RESULT

For each one of the four sets of obtained simulations we extract the values of the coefficients associated with the individual components contributions. This allowed us to understand what actually post increasing the angle of sideslip and then how the various parts collaborate in the linear and nonlinear regimes.

4.3.1 VORTEX LIFT

A first important aerodynamic result, concerns the C_Y or the C_N , in the BVD configuration, and in particular the contribution of the Vertical + Dorsal fin part. Has found an aerodynamics phenomenon at high angles of attack. We're talking about Super lift or Vortex Lift

Since the geometry of Vertical + Dorsal surface is very comparable to that of delta wings or double delta wings of military aircraft (see Figure 74), they are characterized by the same aerodynamic phenomena as we can see from Figure 75 & 76. The wings of military aircraft shows the Vortex Lift when they have a down to 40° and especially in the landing phase, this has made such Vortex lift a phenomenon of primary importance in the design phase of the military aircraft (see Figure 75).

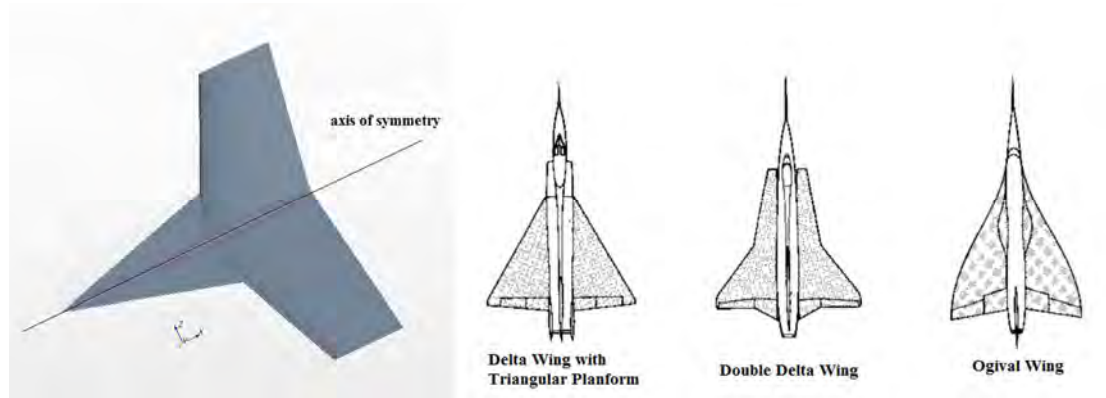


Figure 74 – Comparison with Military Wings Type.

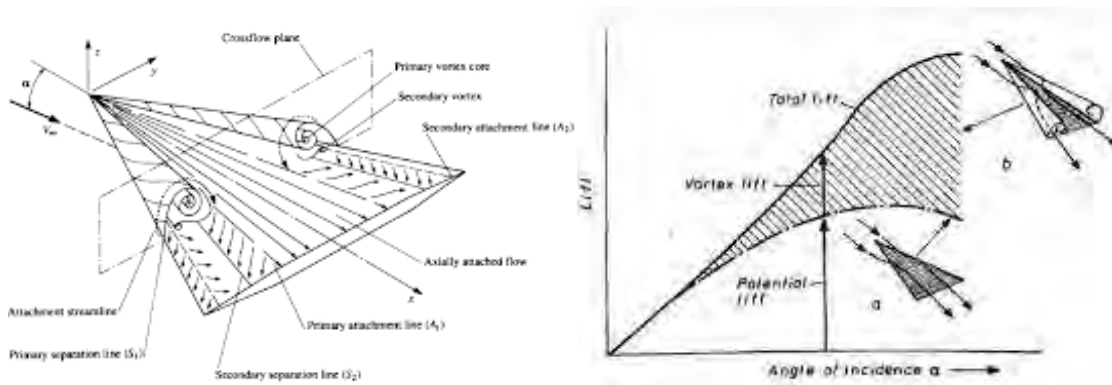


Figure 75 – Vortex Lift Generation for Delta Wings

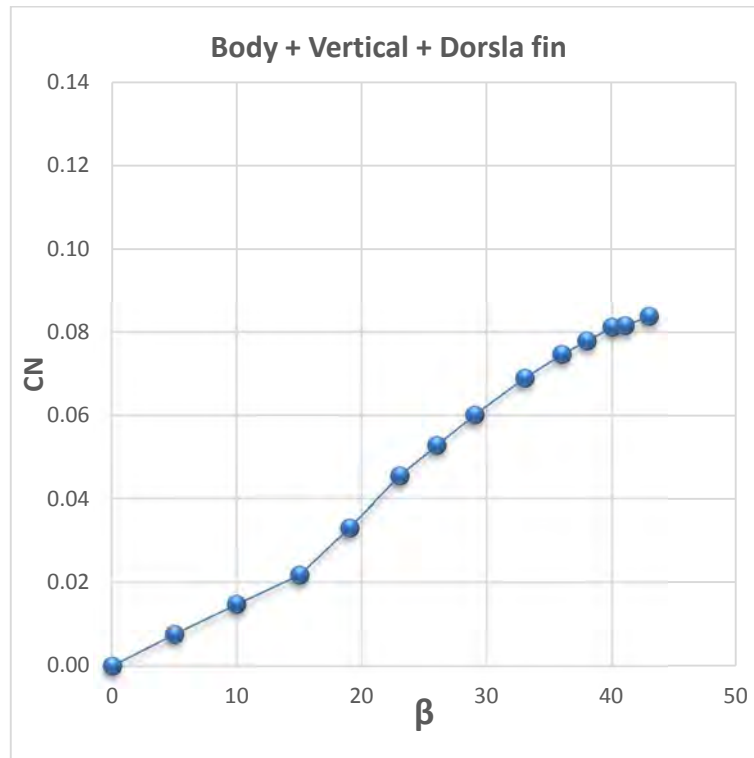


Figure 76 – Vortex Lift Generation for my Geometry resulting from CFD Analysis.

In the Figure 77 we can see the determined trend using the CFD for CN or CY about Vertical + Dorsal which is the sum of two Contributions both collaborating to directional stability.

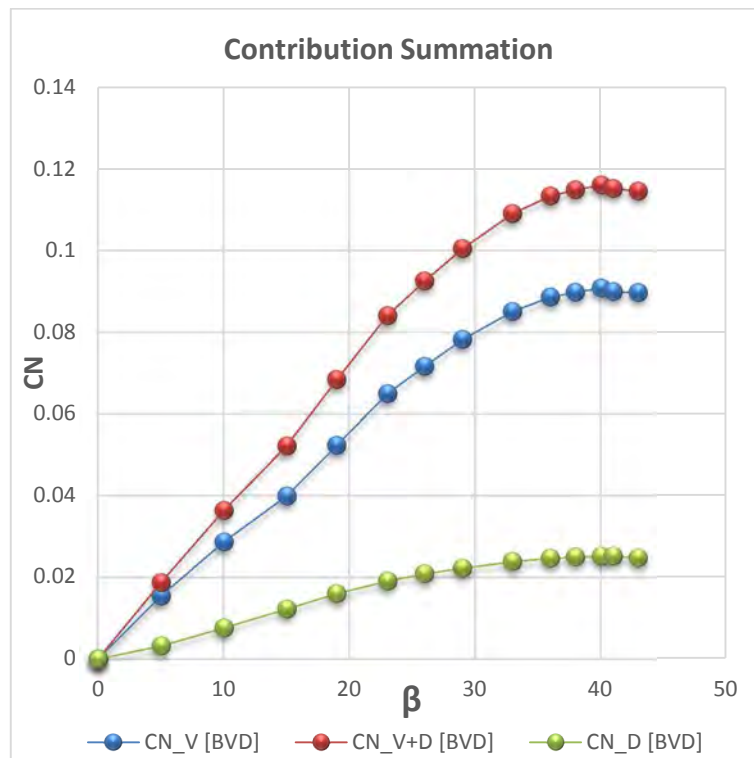


Figure 77 – Contribute summation to directional stability of Vertical + Dorsal for BVD configuration.

4.3.2 CONTRIBUTION TO DIRECTIONAL STABILITY

We find exactly the same trend presented in the report of **Scholz** [3].

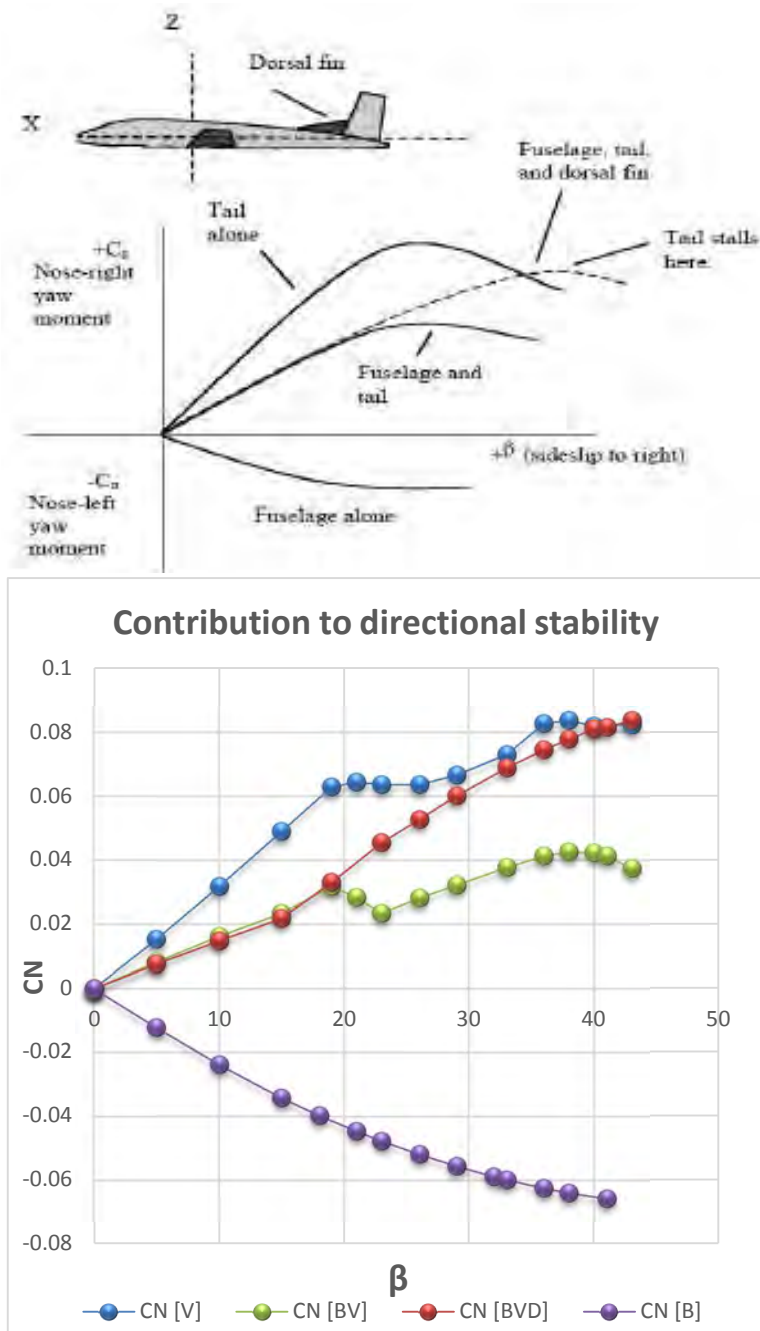


Figure 78 – Contribution to directional stability comparison between Literature [3] and CFD results.

We see from the Figure 78 that for the isolated vertical plane there is a slope greater than the BV & BVD configurations. Actually the sideslip angle for which, we get the stall is almost the same for the V & BV. In the BVD case the curve has the same trend of BV in the linear section, but then reaches higher values of yaw moment and higher angles of stall.

So we can say that altogether numerical results correspond to what should happen according to the literature.

4.3.3 SUMMARY OF RESULTS FOR BVD CONFIGURATION.

In Figure 79 there are the resulting contribution obtained for a precise analyzed mesh, in term of Yawing Moment coefficient. In general for each simulations were carried out for 17 different angles between 0° and 43° .

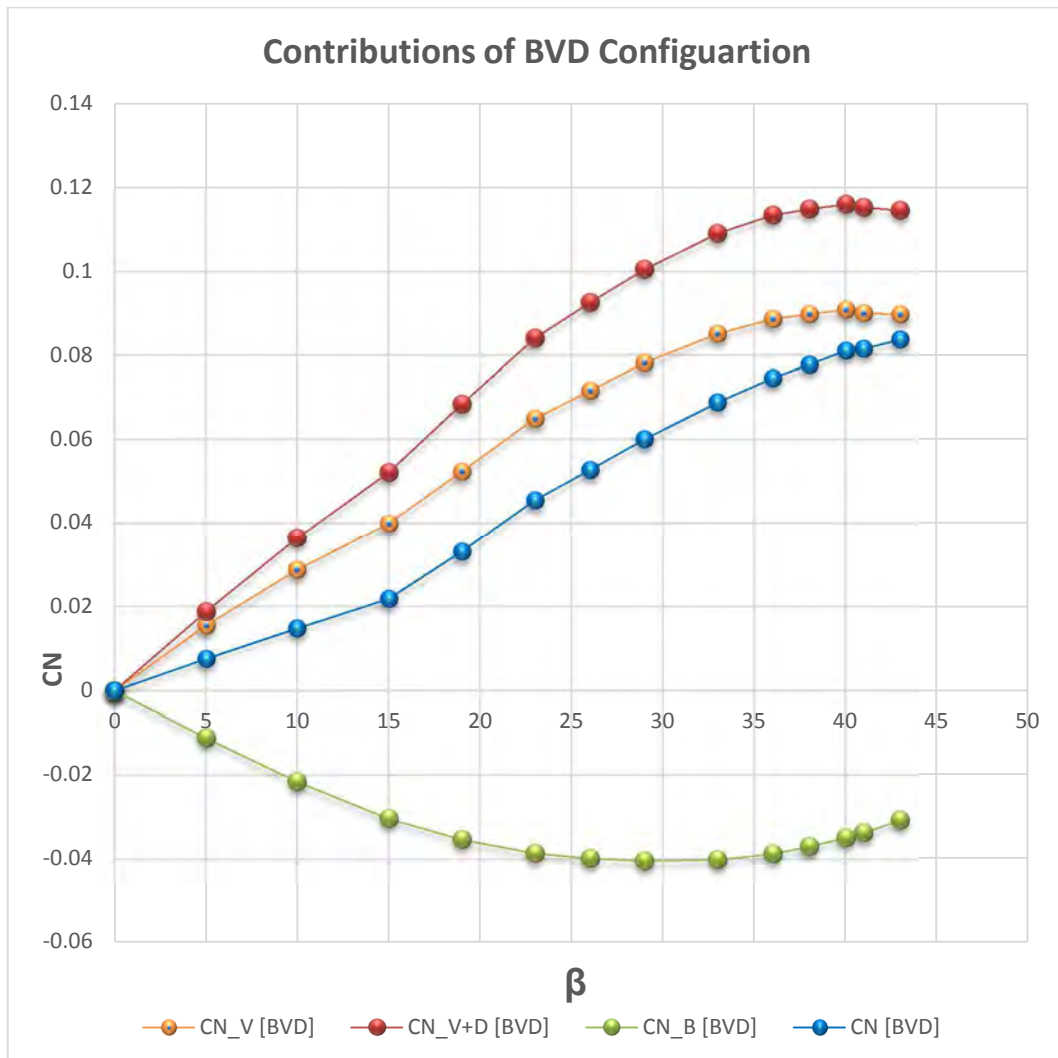


Figure 79 – Individual contributions to directional stability for BVD configuration, CFD Results.

Thanks to this graph we can have an overview about the individual contribution, so we can evaluate how each singular part is working respect the total amount of stability.

4.4 MACRO JAVA FOR THE AUTOMATED PROCEDURE

Considering that these simulations must be repeated for four several configuration is appropriate to introduce the possibility of using the JAVA programming language to support the STAR-CCM+ software to automate all the operations of building the collection of results, and then for faster characteristic times of the data acquisition phase .

The functionality of this macro java is expressed in the following points:

- Automatically defines the components of the flow direction for each angle of yaw content in the programmed array.
- It allows to define the stopping criteria.
- Save the sequence of simulations carried out, thereby generating a list that summarizes in an orderly manner, as well as the array of sideslip angles chosen.

For the proper use of the macro, the starting simulation file, must be in a folder in which is contained also the macro. It must also be guaranteed the correspondence between the name of the fluid region of simulation and the macro object.

After opening the starting simulation, by pressing the PLAY button starts the macro, and then starts recording the macro. This recording can be stopped when the user wants.

Step of Macro:

- Defines an object that represents the currently open simulated.
- Get the name of the opened simulation and assigns it to the string "simName"
- Define an object that represents the region called Fluid Dorsal
- Define an object that considers the border Inflow
- Define an object that considers the values of the flow direction on the boundary defined before
- Define an object that sets the maximum number of iterations
- Define the Array (vector) of the sideslip angles to simulate
- Iterative cycle: changes the direction of the flow, changes the number of iterations, performs - the calculation and saves the simulation
- Change the direction of flow according to the sideslip angle defined by the current iteration
- Defines the maximum number of iterations for each cycle
- Set the maximum number of iterations
- Performs calculations
- Save the file with a name according to the current iteration in the folder where is this macro

By using this macro was easy to collect the simulations for the four different mesh. My work is therefore limited to gather results and view them in a spreadsheet to the valuations that I have alluded above.

4.5 PARTIAL CONFIGURATIONS

Choosing the mesh for BVD configuration we have used the same setting parameters (in term of base size target size and minimum size) to evaluate the partial configurations. So we have collected other packages of simulations, which are realized for the same 17 different angles between 5° and 43°.

In Figure 80 there are the partial analyzed configurations and the total result of BVD configuration.

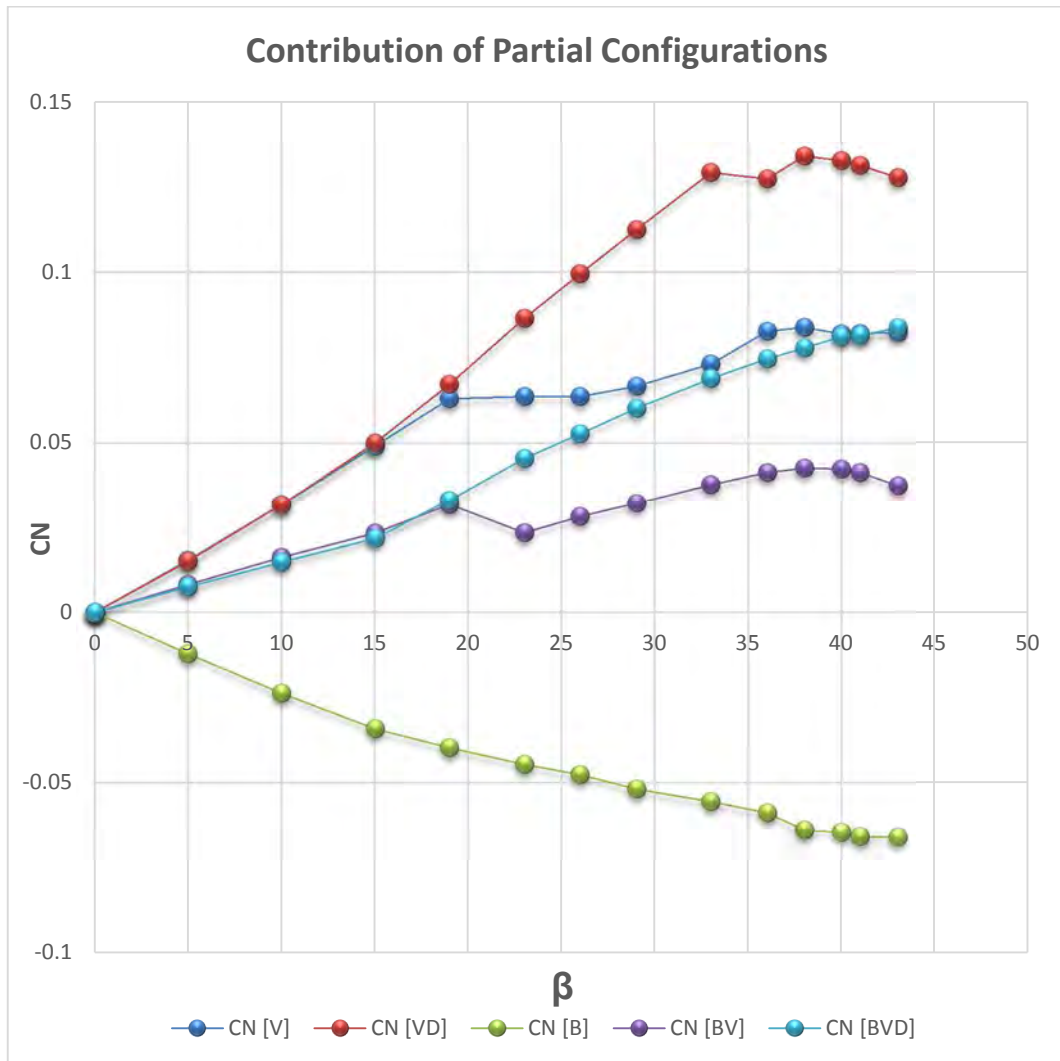


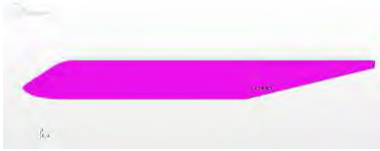
Figure 80 – Summary of the contributions to directional stability for partial configuration, CFD Result.



For the V we obtain an angle-of-stall about $\beta=19^\circ$, then there are a quite constant value until $\beta = 26^\circ$, after we can see an increase of yawing moment due to the low AR which characterize this particular geometry. The actual stall is reached at $\beta = 38^\circ$.



For the VD we obtain the same slope of V in the linear range, but after $\beta=19^\circ$ the slop increase, so we can attribute this effect at the dorsal fin presence. Also in this case the angle-of-stall is reached at $\beta = 38^\circ$.



For B we obtain the negative slope, index of destabilizing yawing moment, characteristics of the fusiform body.



For BV we obtain the same shape of V but with a reduction of stability due to the fuselage negative contribution. Also in this case there is a first negative variation of slope about $\beta=19^\circ$ related to the vertical stall, then after $\beta=26^\circ$ there are an increases of slope until $\beta=40^\circ$.



For BVD we obtain the same shape of VD but with a reduction of stability due to the fuselage negative contribution. Also in this case after $\beta=19^\circ$ the slope increase, so we can attribute this effect at the dorsal fin presence.

Comparing the pairs of curves V & VD and curves of BV & BVD, we note that with the dorsal fin in both cases there is no effect in the linear range, while in the nonlinear regime such effect is remarkable.

4.5.1 DORSAL FIN EFFECT ON VERTICAL

This effect can be readily determined comparing the values of the lateral stability coefficients of the VD and V configuration. The Result is show in Figure 81.

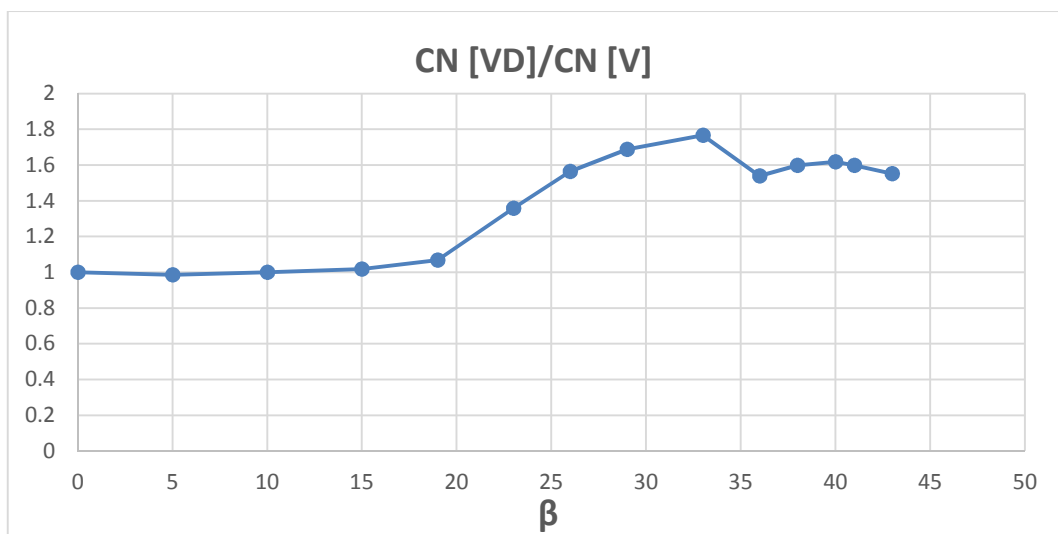


Figure 81 –Dorsal fin effect on Vertical tailplane in term of stability increment, CFD Result.

The curve has a constant unitary feature until $\beta = 19^\circ$, it means that the dorsal never acts in the linear range, then increasing its effect for higher sideslip angles.

4.6 AERODYNAMIC INTERFERENCE SIGNIFICANCE

The final part of this first set of analysis concerns the possibility to identifying the individual contributions of CN for BVD configuration and compare them with the contributions of partial configurations.

In this way we found how interference play a key role in the performance determination. This aspect highlights the importance of CFD calculations which allow to an overall assessment of the aerodynamics phenomena, depending on the chosen model for the physics of the problem.

We specify that actually the wing and horizontal plane are not study because they are indirect effect. So if the BV behavior does not change in the linear range adding dorsal fin, it means that also BVW and BVWH configuration does not change adding dorsal fin, at least in the linear range.

To have a starting overview we show the total contribution of three different configurations:

- Vertical,
- Body + Vertical,
- Vertical + Body + Dorsal.

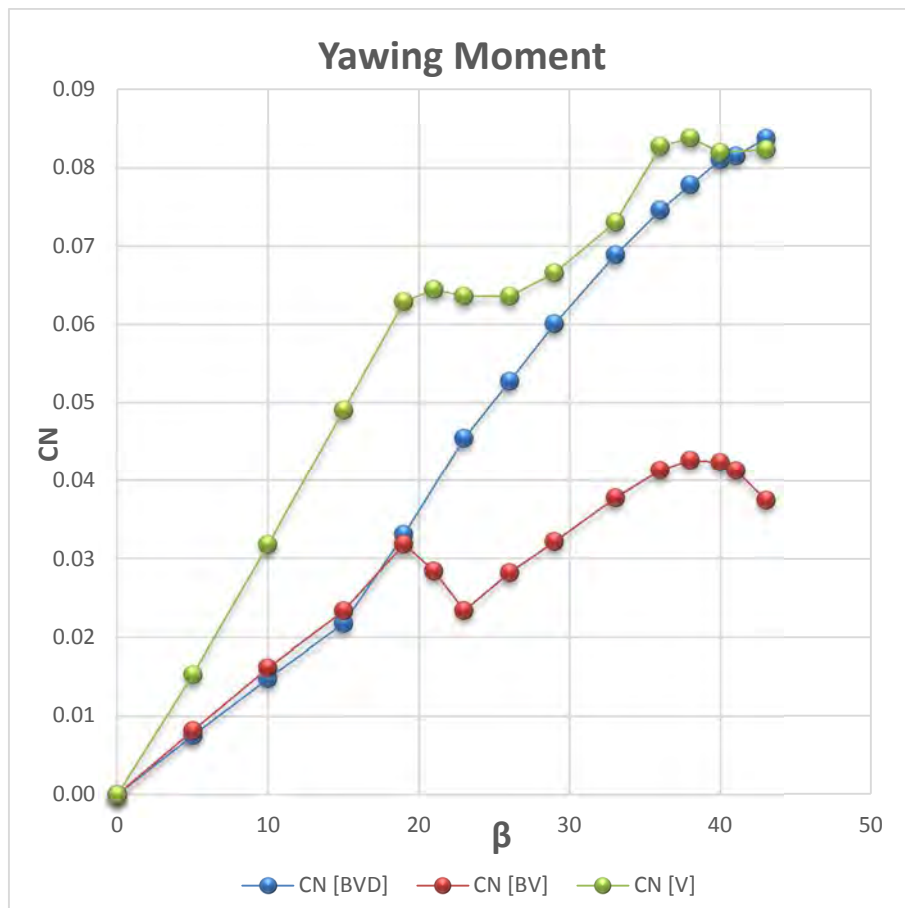


Figure 82 – Summary of total contribution of yawing moment for V, BV, BVD configuration, CFD results.

The isolated vertical have the better stability characteristics. Adding the fuselage there is great reduction of this strong stability and the curve have a slope variation at the same angle of stall of

isolated vertical. Adding even the dorsal there is a strong increases of stability, but exclusively in the nonlinear range.

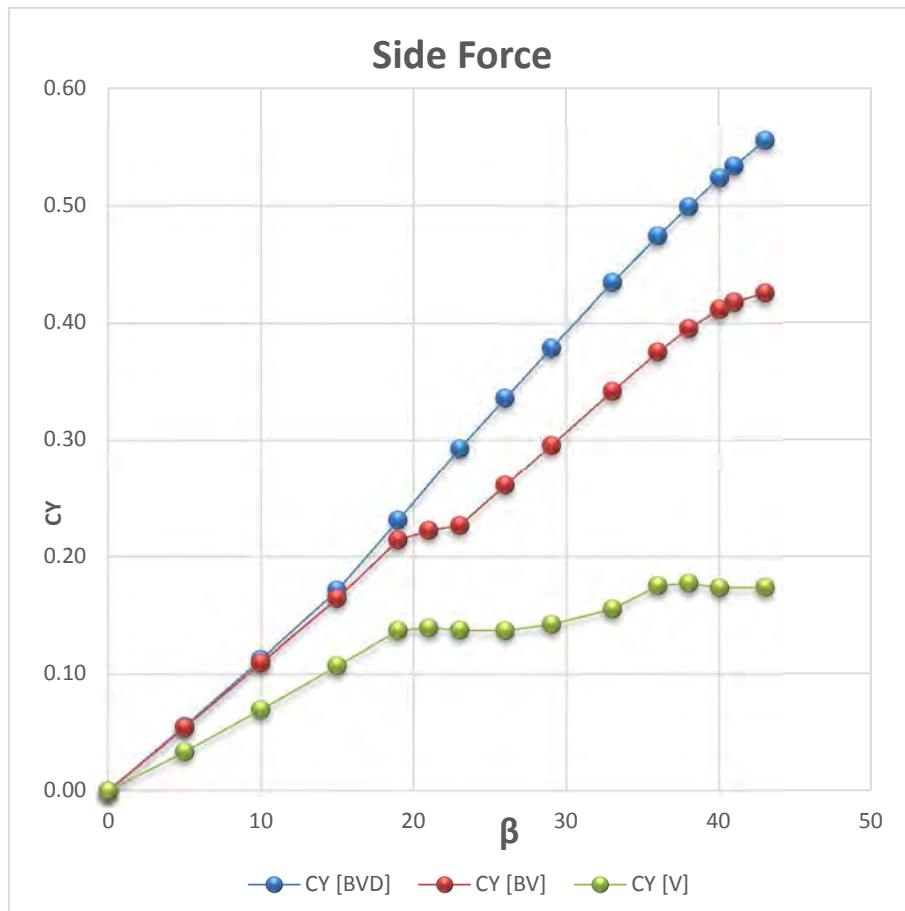


Figure 83 – Summary of total contribution of sideforce for V, BV, BVD configuration, CFD results.

4.6.1 MUTUAL EFFECT BETWEEN BODY, VERTICAL & DORSAL

In this section we can evaluate the effects of aerodynamic interference switching from one partial configuration to another.

We evaluate the effect of the vertical for the Isolated Body, and the Body for the Vertical.

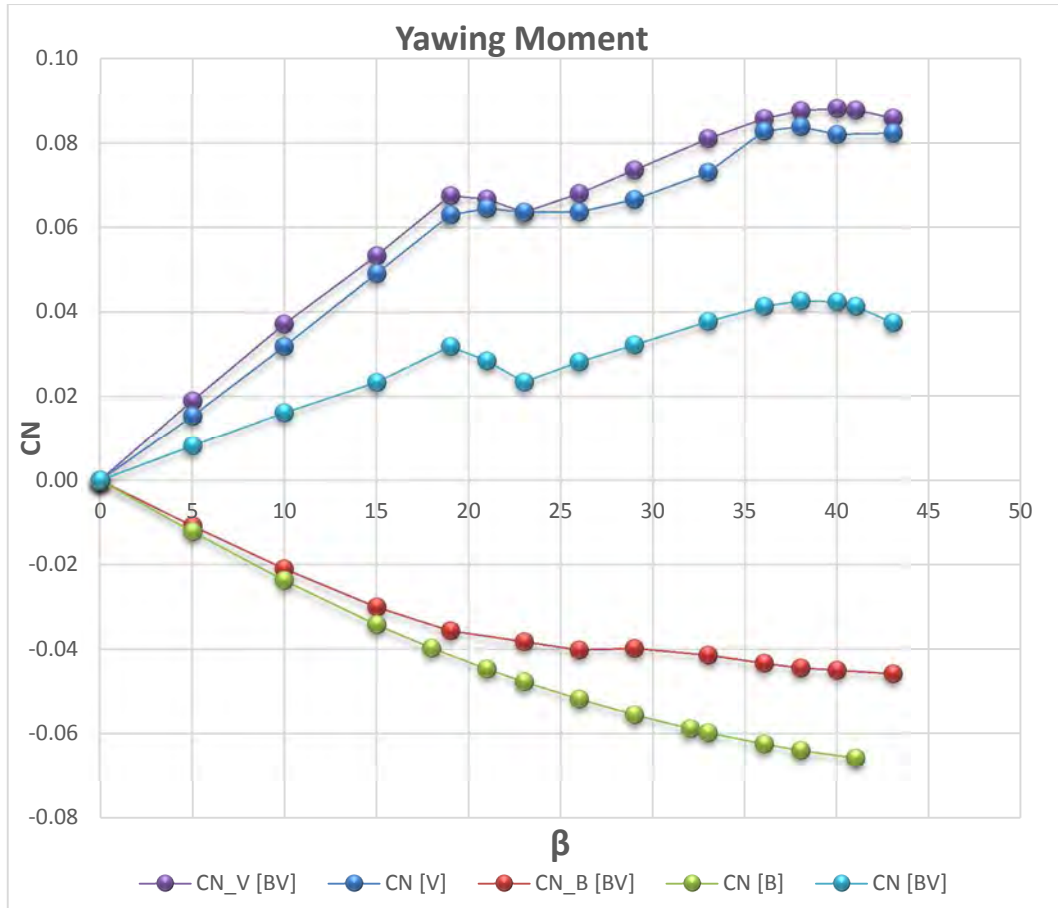
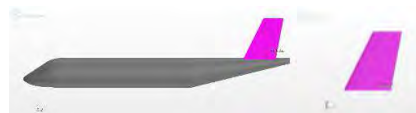


Figure 84 – Mutual effect between Body & Vertical, CFD results.



With the vertical, the fuselage contribution becomes slightly less unstable around $\beta = 26^\circ$, keeping quite the same shape in both cases.



With the fuselage, the vertical contribution becomes slightly more stable, keeping quite the same shape in both cases.



Overall curve whose slope is affected by the negative fuselage contribution and by vertical stalling around $\beta = 19^\circ$.

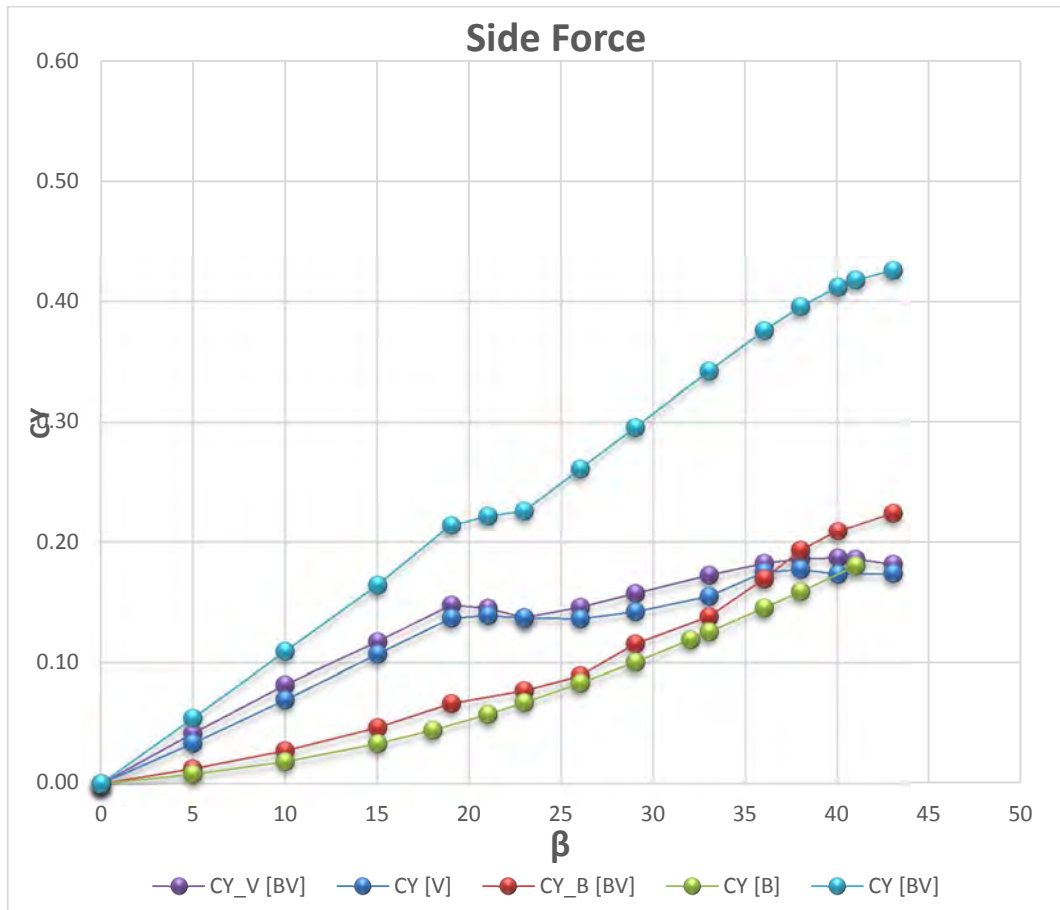
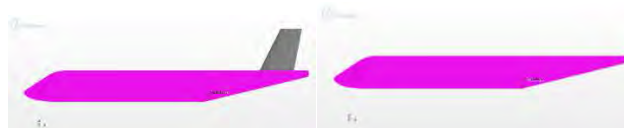


Figure 85 – Mutual effect between Body & Vertical, CFD results.



With the vertical, the fuselage contribution becomes slightly greater for all angles, keeping quite the same shape in both cases.



With the fuselage, the vertical contribution becomes slightly greater, keeping quite the same shape in both cases.



Curve resulting from the sum of partial contribute, whose slope is affected by the vertical stalling around $\beta= 19^\circ$.

We remember that actually have not sense to talk about side force of fuselage but at this level we want show the effect which involves the directional stability just to have an overview of this phenomenon.

Now we evaluate the effect of the introduction of the dorsal fin on the various contributions.

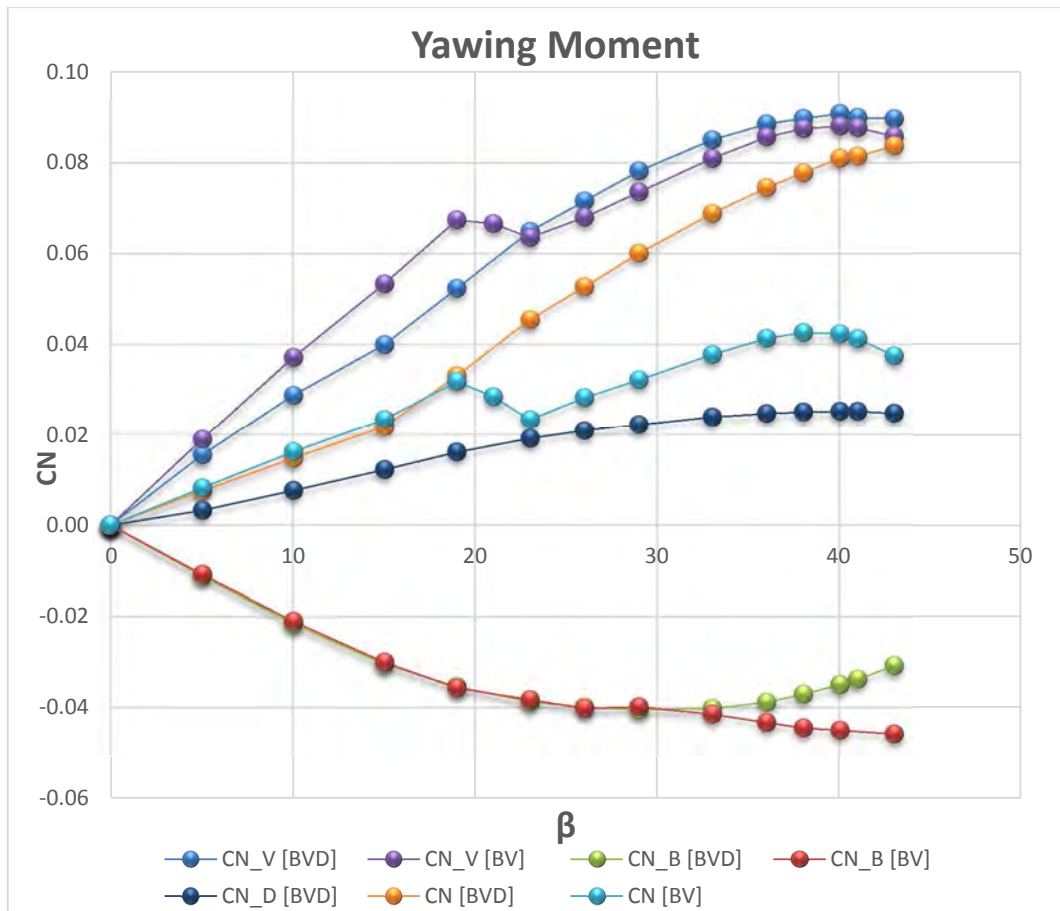


Figure 86 – Dorsal fin effect on yawing moment for Body, Vertical, Body + Vertical, CFD.



For the fuselage after $\beta = 30^\circ$ there is an increase of stability that makes positive the slope of the curve. It means that thanks to the dorsal, the fuselage lost the characteristics destabilizing contribute of fusiform body.



For the vertical is determined a reduction of stability, then the slope of the curve is reduced in linear range. At this point we need to explain that even if the vertical have a reduced contribution, at the same time there are another surface that compensates this variation. So as will be explained in chapter 5 there is a phenomenon of contribute repartition between dorsal and vertical, which added together constitute the contribution of the vertical in the isolated case.



The total contribution has a strong stability increase in the nonlinear range. Additional considerations are made in Chapter 5



Curve to show the magnitude of the dorsal contribution about yawing moment coefficient.

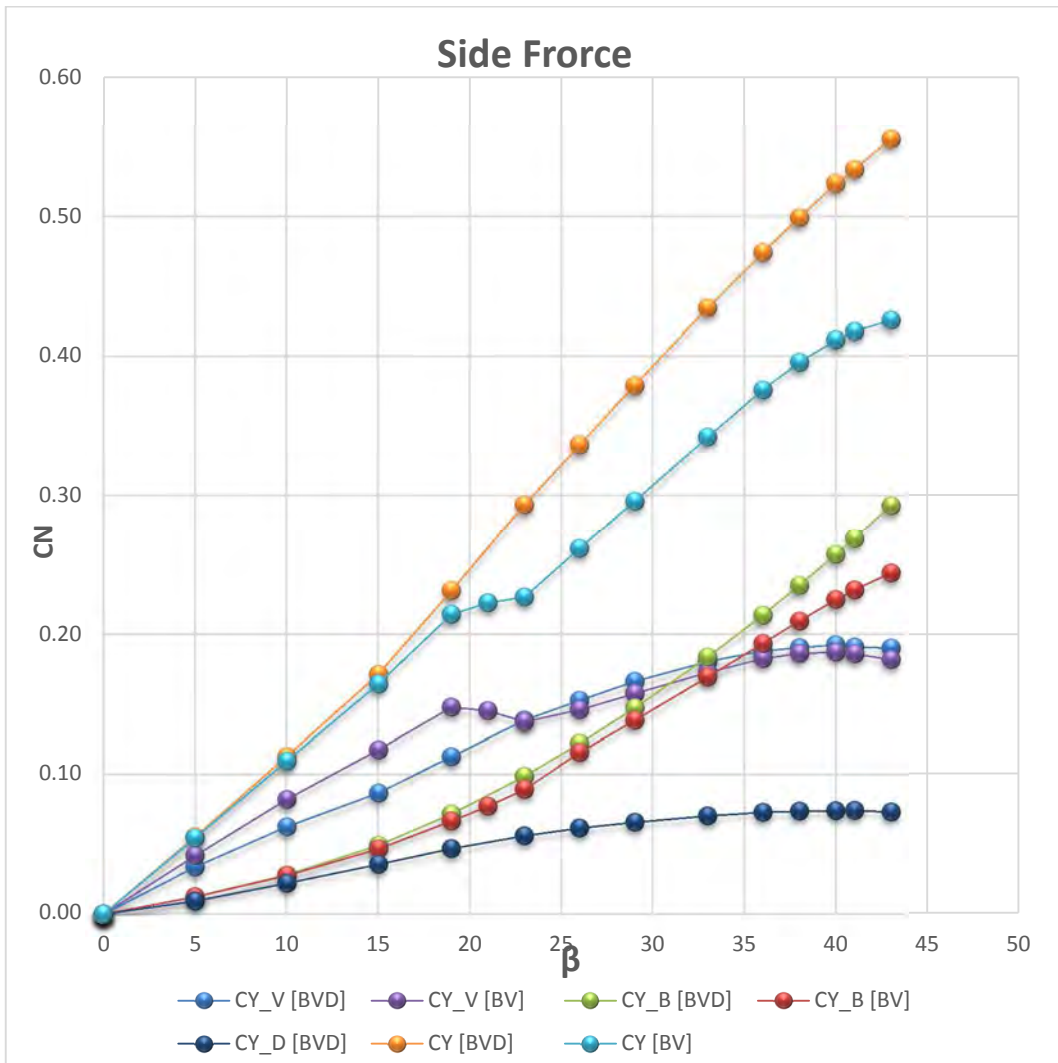


Figure 87 – Dorsal fin effect on sideforce Body, Vertical and Body + Vertical, CFD results.



For the fuselage after $\beta = 30^\circ$ there is an increase of stability that makes more positive the slope of the curve.



For the vertical there is a sharp increase in sideforce, both in the linear range that in nonlinear range.



The total contribution has a strong increase stability in the nonlinear range.



Curve to show the magnitude of the dorsal contribution about sideforce coefficient.

We evaluate for the Isolated Body the effect of the addition of the vertical and then dorsal.

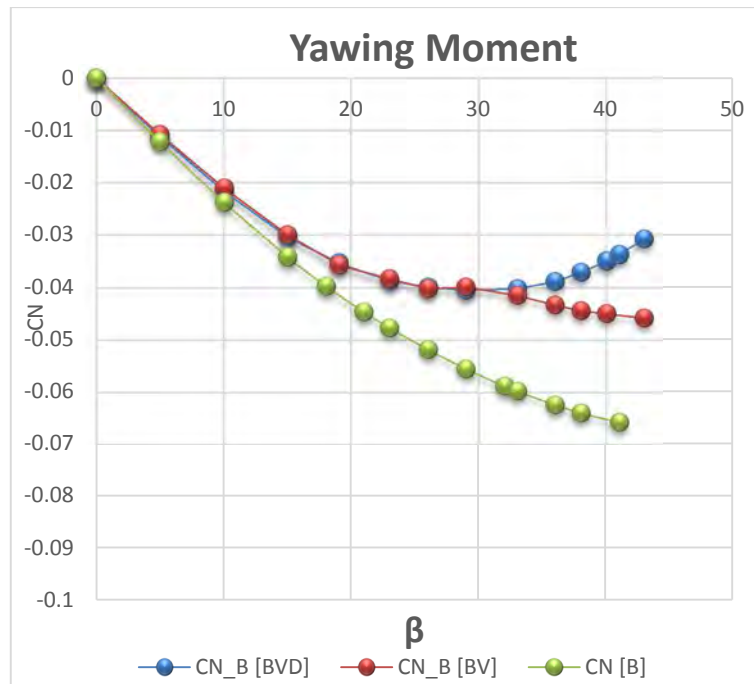


Figure 88 – Effects on body yawing moment contribution of consecutive adding of parts, CFD results.

We can see how respect the isolated body there is a positive variation of stability with vertical addition and very strong positive variation of stability with vertical + dorsal addition.

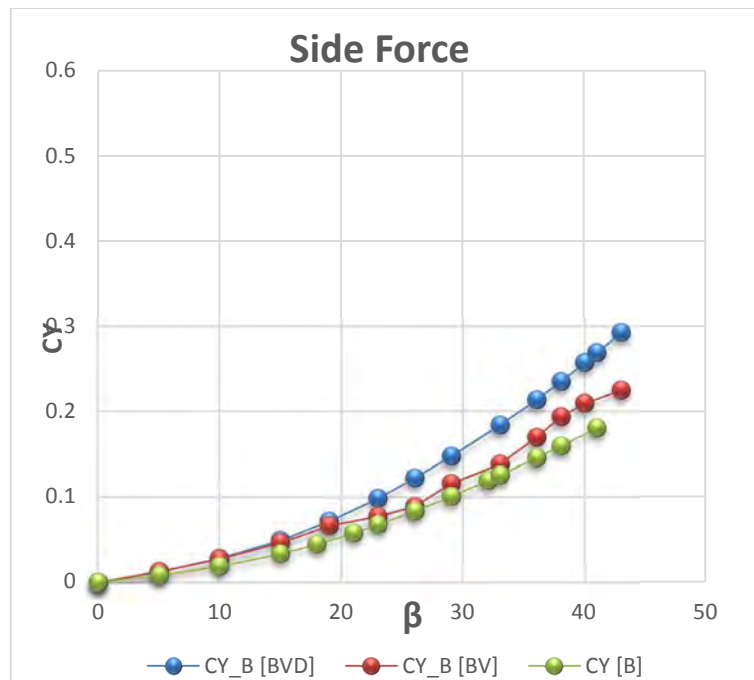


Figure 89 – Effects on body sideforce contribution of consecutive adding of parts, CFD results.

We can see how respect the isolated fuselage there is a positive variation of sideforce with vertical addition and very strong positive variation of sideforce with vertical + dorsal addition.

We evaluate for the isolated Vertical the effect of the addition of the vertical and then dorsal

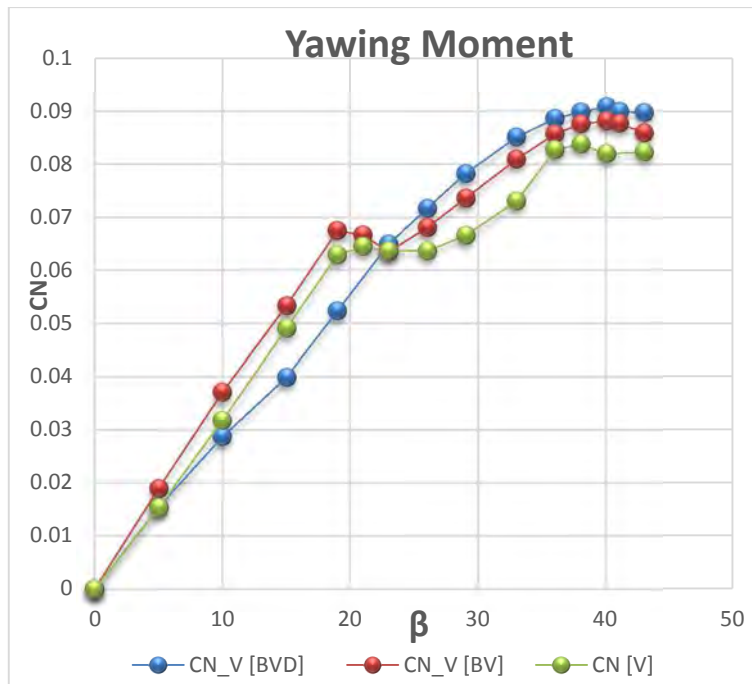


Figure 90 – Effects on Vertical yawing moment contribution of consecutive adding of parts, CFD results.

We can see how respect the isolated vertical there is a positive variation of stability with fuselage addition as explained above, but there is a negative variation of stability with vertical + dorsal addition in linear range due to the redistribution of contribution between vertical and dorsal as explain above. The same concept involves the side force coefficient since his graph is simply scaled with respect the yawing moment coefficient graph.

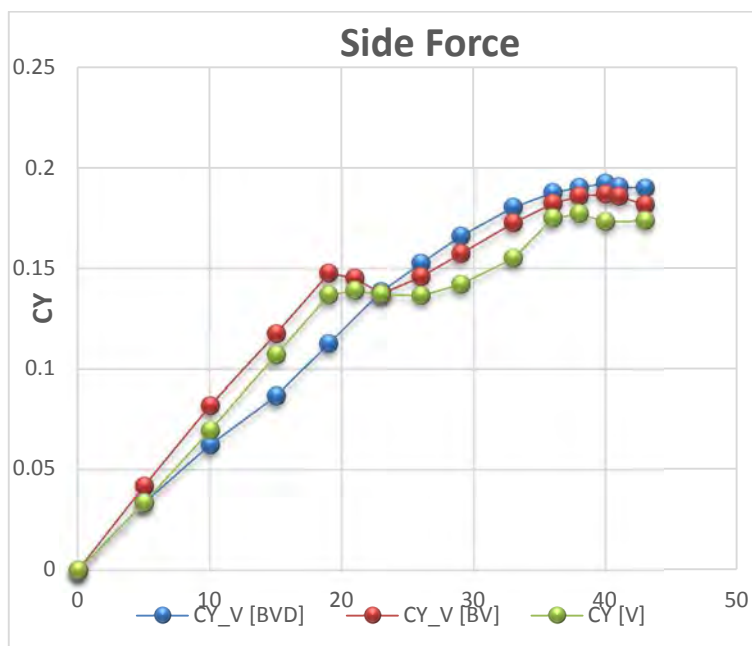


Figure 91 – Effects on Vertical sideforce contribution of consecutive adding of parts, CFD results.

5. BASELINE

The current step is to identify the Base Line of our study, therefore confirm the previously analyzed trends experimentally determined by the Report. The aerodynamic characteristics that we extract, are the starting point for the following considerations regarding trends parameterization.

5.1 DORSAL FIN PRIMARY EFFECT ON THE VERTICAL TAIL STABILITY

We compare the graph that relates the contribution of vertical, in BV configuration, with the curve of the vertical + Dorsal contribution in the BVD configuration.

The chart of Figure 92 expresses the dorsal effect resulting by CFD analysis for our geometry. This result is exactly what say the literature about this issue, as we can see in Figure 93 relate to the experimental data performed by Obert during the development of Fokker F-27.

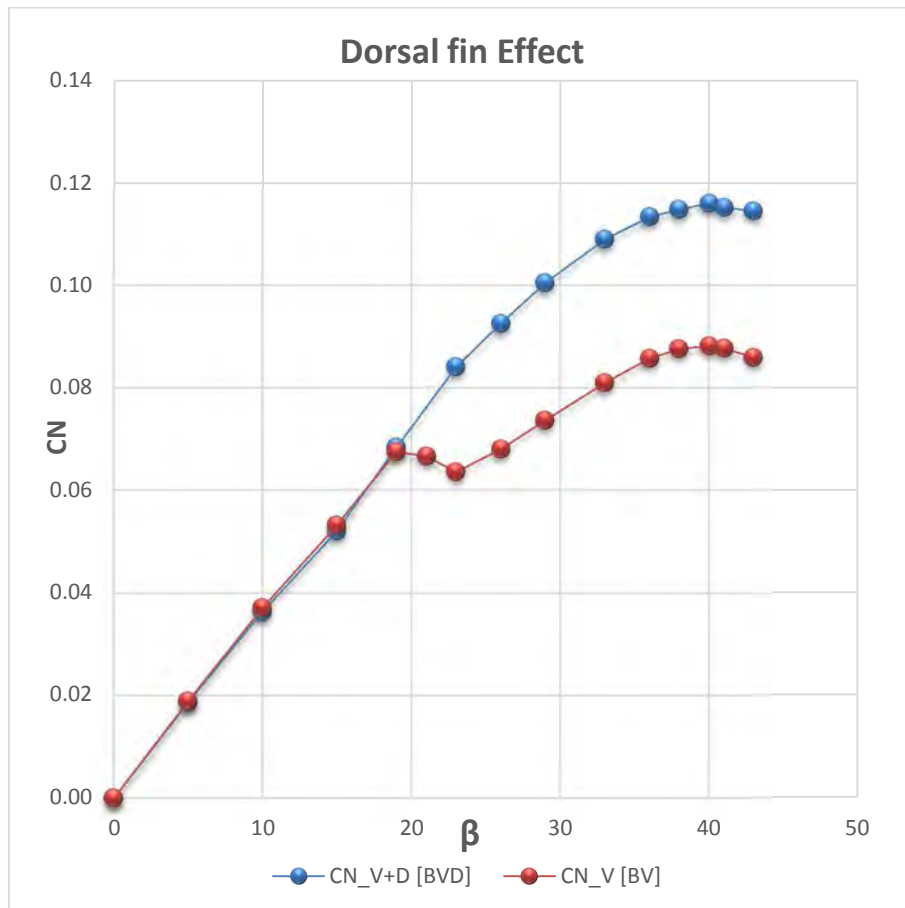
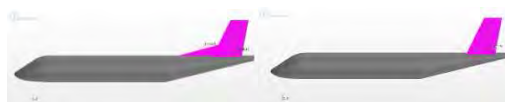


Figure 92 – Dorsal fin Effects on vertical empennage stability, CFD results.



With Dorsal fin there a great increases of stability in the non linear range, delaying the typical angle of stall.

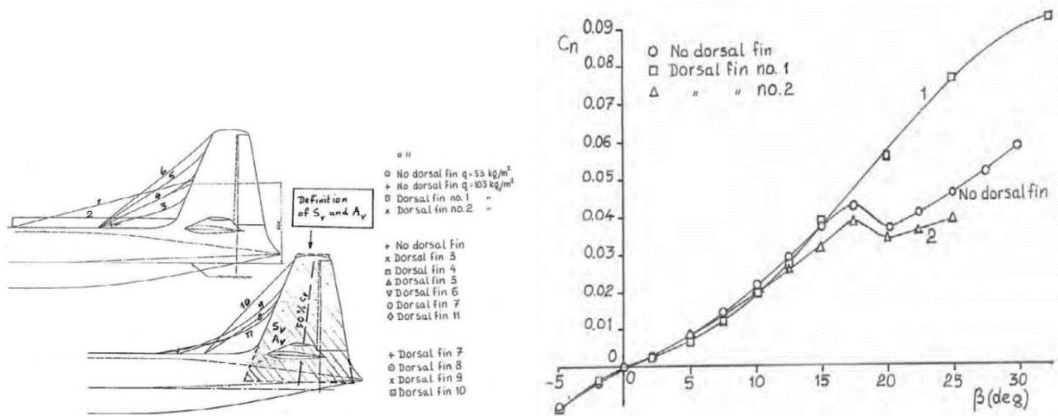


Figure 93 – Dorsal fin Effects on vertical empennage stability, Literature results [4].

The physical explanation is that shown earlier that now we propose in this specific case displaying the behavior with and without dorsal fin in the case of a yaw angle about 26°

In the absence of the dorsal, the entire tail would be stalled. To say that, we need the graph showing the skin friction coefficient, because separation occurs when this coefficient becomes void. To understand the magnitude of the separation, thus the flow dynamics downstream of the separation point, over to this scene there is also the streamline analysis.

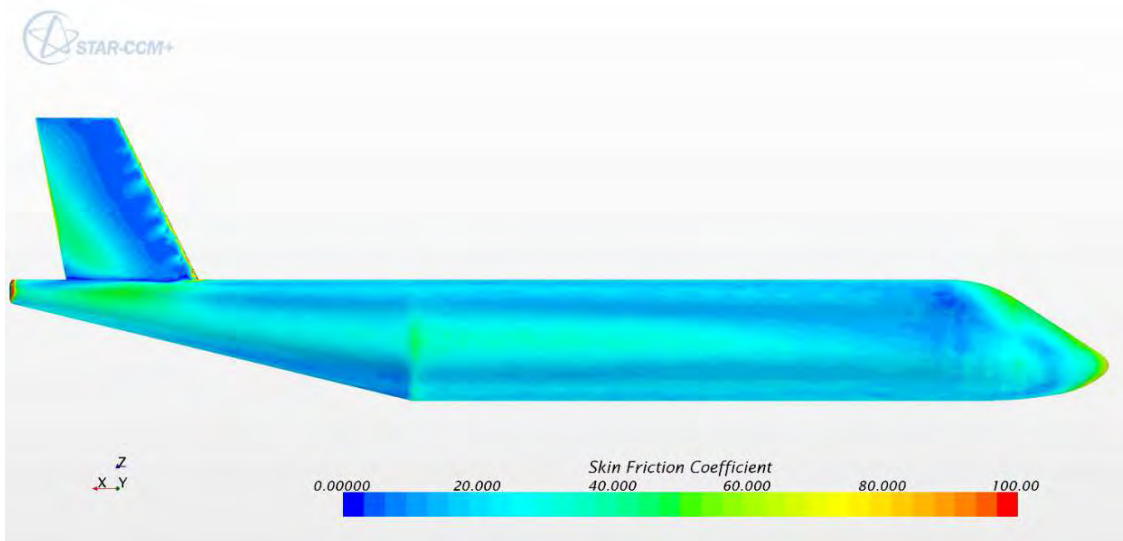


Figure 94 – Side View of Skin Friction Coefficient in without Dorsal fin.

The areas of blue color are those for which the coefficient of friction is close to zero, these areas appear just after the leading edge to the leeward side (see Figure 94).

From Figure 95 we can see how for the vertical leeward side, the streamline become blue, so they have very low speed. This is precisely index of the occurred separation, due to which the flow takes on an irregular trend in terms of direction and speed.

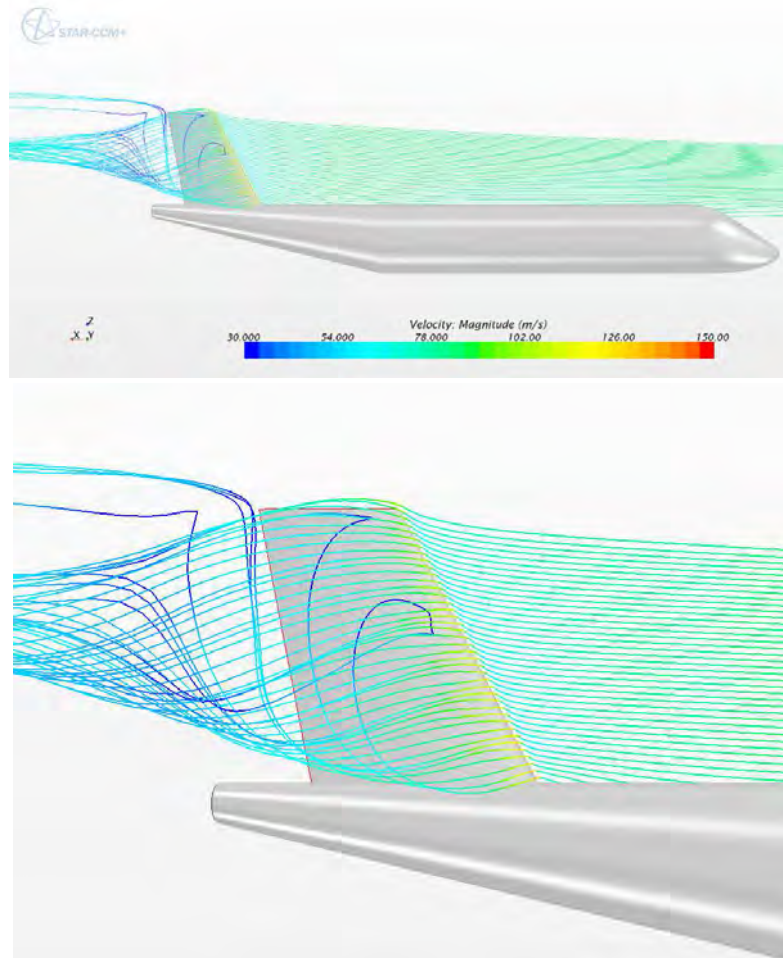


Figure 95 – Side View of Streamline Evolution without Dorsal fin.

We will now assess the dorsal fin effect using the Figure 96. From the comparison for the two configurations, it is seen that while for the BV the vertical plane at 26° is totally separated, and then stalled, with dorsal fin, the energized flow, remains attached and the plane is cooperating to directional stability.

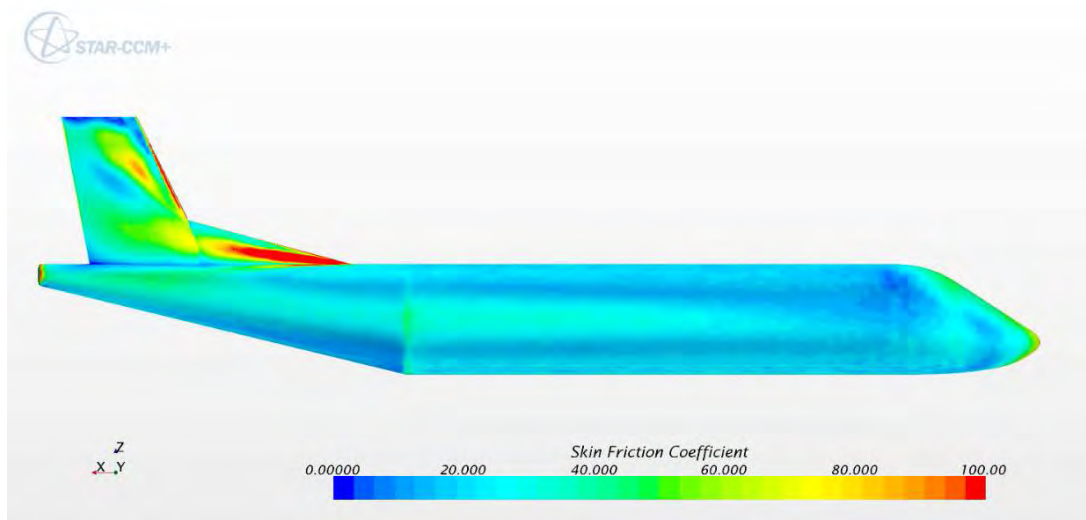


Figure 96 – Side View of Skin Friction Coefficient with Dorsal fin.

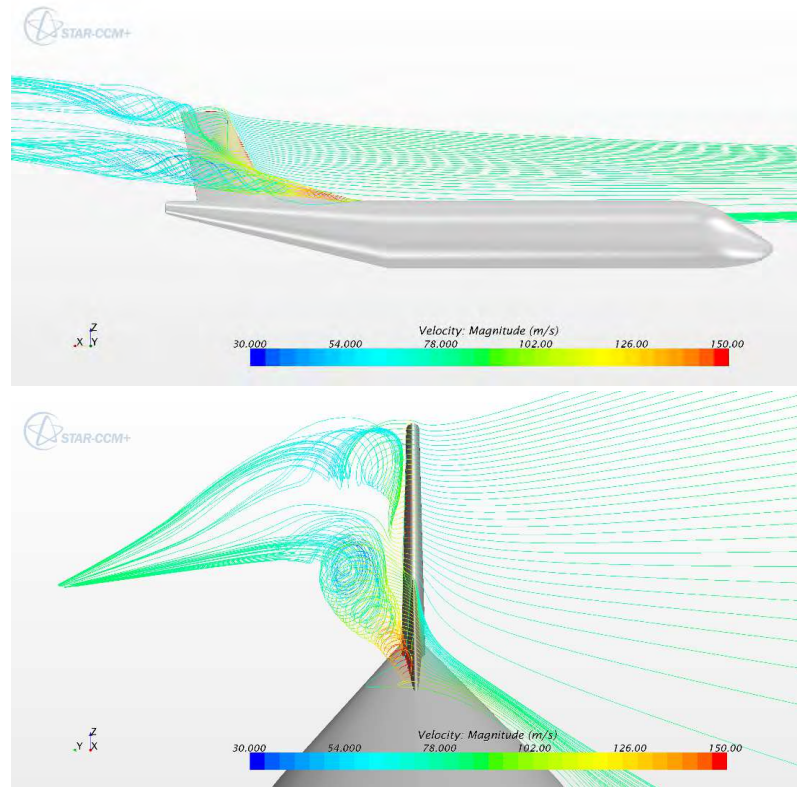


Figure 97 – Side View and Frontal View of the Streamline Evolution with Dorsal fin

Thanks to the streamline representation of the flow we can grasp some aerodynamics fundamental aspects. For example, because of the shape which have such stream line, it is clear that in this condition vorticity is released.

As we can see in Figure 97,& 98 from the dorsal fin two vortices detach which we call primary and secondary vortex.

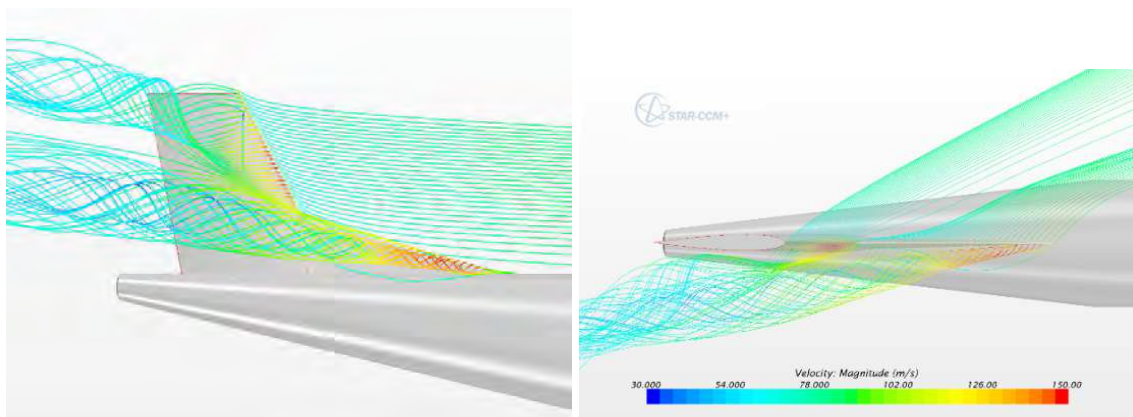


Figure 98 – Side View and Top View of the Streamline evolution with Dorsal fin

The primary one that starts from the geometric discontinuity between the fuselage and dorsal, as mentioned determines the division into two parts of the vertical with different behavior. Thanks to this phenomenon, the flow of the lower part of the vertical is energized, thus with greater ability to remain attached at the surface, this ensures that the lower part of the vertical, does not stall and continues to work even at high angles.

As we can see from Figure 99, vortex effectively splits the fin into upper and lower halves. The upper part has a much higher AR of the lower part.

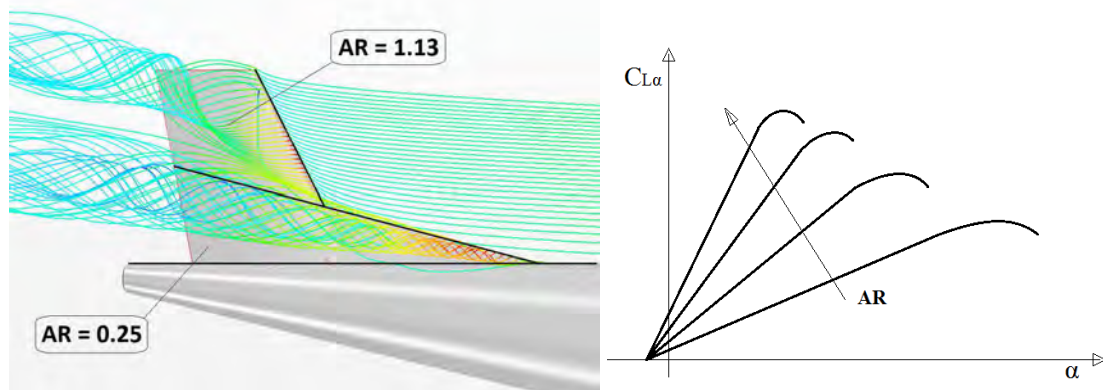


Figure 99 – How the Vortex splits the fin into Upper and Lower halves.

As shown in chapter 1.2.4 the smaller one will remain unstalled to an even higher yaw and this helps maintain sufficient directional stability up to the higher AOY than without dorsal.

The upper half has a higher AR than the lower one and, thus, stalls at a lower AOY. And that is the important thing. The fact that the lower half is only partially stalled renders the $C_{N,\beta}$ greater than if the dorsal was absent. This allows the $C_{N,\beta}$ to be maintained to a higher AOY. Not only the $C_{N,\beta}$ is increased due to the added area of the dorsal fin, it also guarantees it stays higher to greater AOY.

The secondary one, which starts from the geometric discontinuity between dorsal fin and vertical, although with lower speed still manages to energize the flow for the vertical upper part. We can see this very clearly, from the skin friction in Figure 96 for which the bluish color are indicative of a separation, those tending to yellow or red, are an indication of attached flow.

5.1.1. RELEASED VORTICITY

The Figure 100 summarizes in addition to the Skin Friction coefficient and Streamline characteristics also those related to the vorticity.

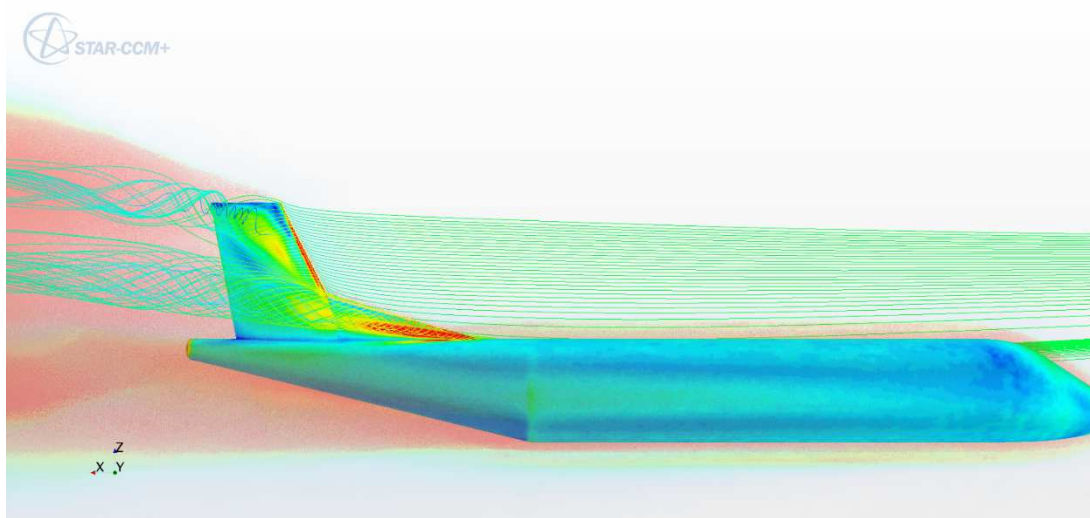


Figure 100 – Side View of Skin Friction, Streamline and Vorticity with Dorsal fin.

The software can create scenes that highlight vector aspects associated with the volume of the analyzed continuum, namely the computational domain. We focus on the volume around the tail plane and I showed the vorticity. We are able to represent in this way the magnitude of the vorticity, in particular, the denser areas of red color are indicative of a vorticity intense.

We can make a first consideration relating to the fact that such colored volume, it is also present around the fuselage for its entire length. However, being at 26° , the fuselage is near the stall, then we can attribute to separation of the flow the phenomenology which liberates a certain vorticity. The very light color shows that the amount is limited.

In vector terms we know that the vorticity magnitude decreases with distance increasing from the vortex core. It can be seen using Figure 101 & 102 where the volume color became pink far away from the vortex core.

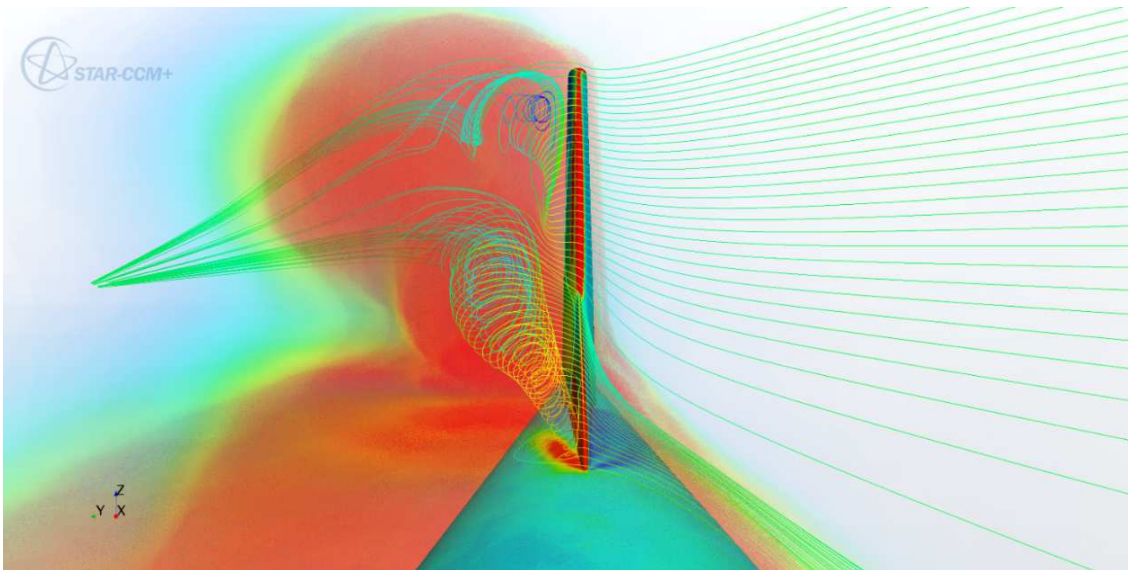


Figure 101 – Frontal View of Skin Friction, Streamline and Vorticity with Dorsal fin.

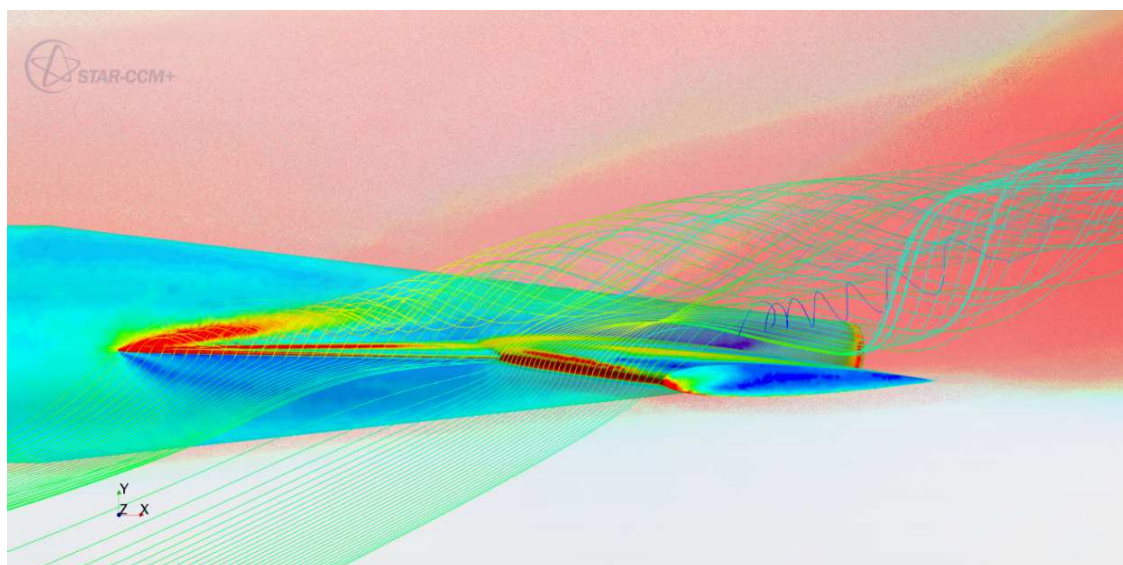


Figure 102 – Top view of Skin Friction, Streamline and Vorticity with Dorsal fin.

From the Figure 102 is possible to identify the two vorticity which are released from the two geometrical discontinuities, and that are joined into a single vortex downstream of the vertical plane which will be more intense as seen from the volume color that is much darker.

5.1.2 QUALITATIVE COMPARISON ABOUT VORTICITY.

a) Changing behaviors in non-linear range

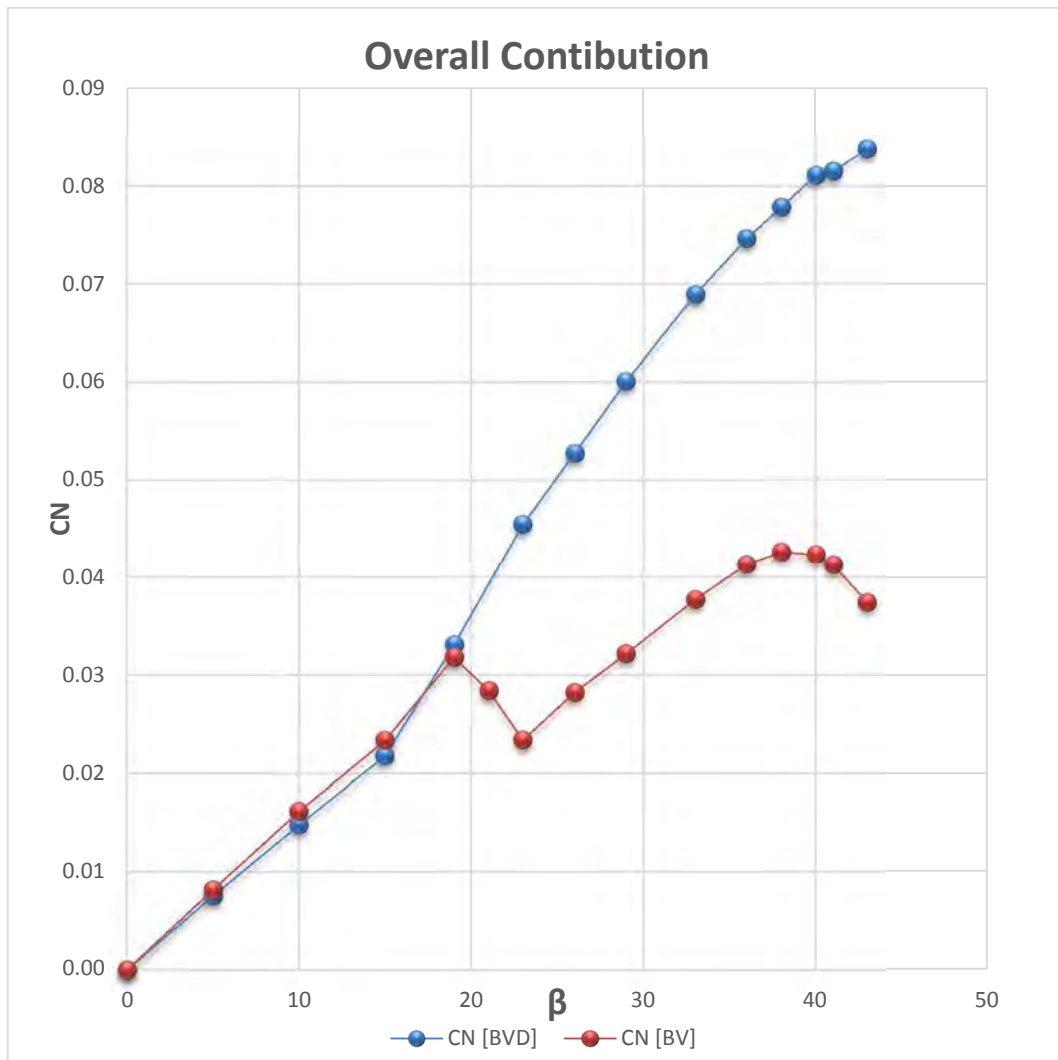


Figure 103 – Visualization of nonlinear range to study the dorsal effect about the aerodynamics phenomena.

It is interesting to show the aerodynamics for some values of β related to the non-linear range (see Figure 103). In particular, we decided to compare the phenomenology for:

- $\beta = 19^\circ$ is the angle at which occurs the phenomenon of the increase in stability compared to the case without dorsal fin, so when the vertical stall (see Figure 104 & 107 & 109 & 112).
- $\beta = 29^\circ$ is an intermediate value of the non-linear range. (see Figure 105 & 110).
- $\beta = 40^\circ$ is about the highest values among those analyzed, then the one for which the derivative of stability is maximal. (see Figure 106 & 108 & 111 & 113).

So, we are considering the evolution of aerodynamics between the minimum and maximum limit angles, for the non-linear range, in which there is the characteristic increase of stability, and in particular assess the evolution of the generated vorticity.

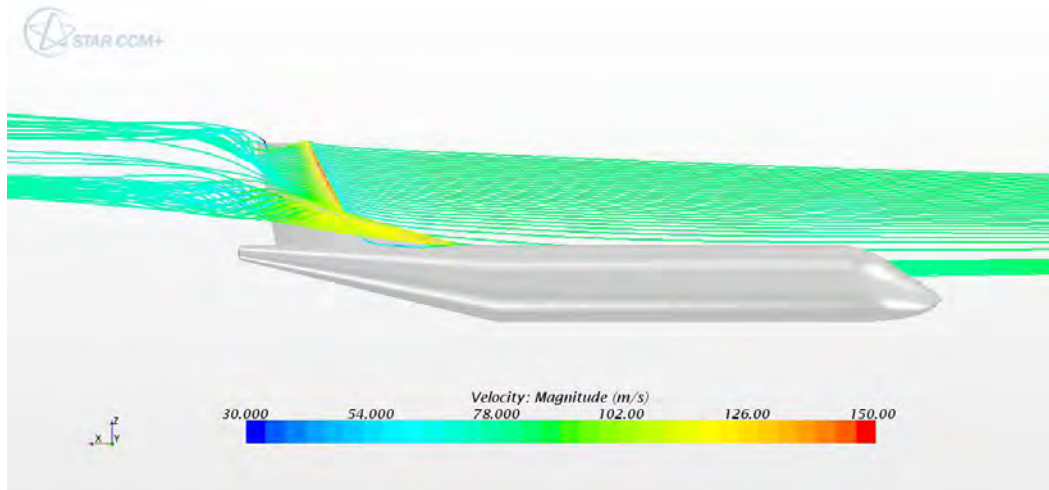


Figure 104 –Side View of the Streamline with Dorsal fin at $\beta = 19^\circ$.

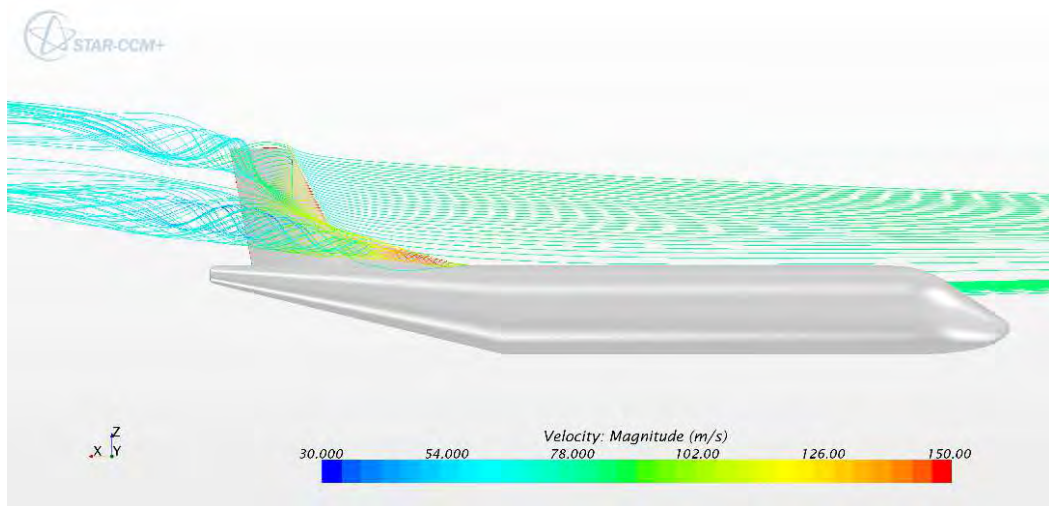


Figure 105 –Side View of the Streamline with Dorsal fin at $\beta = 29^\circ$.

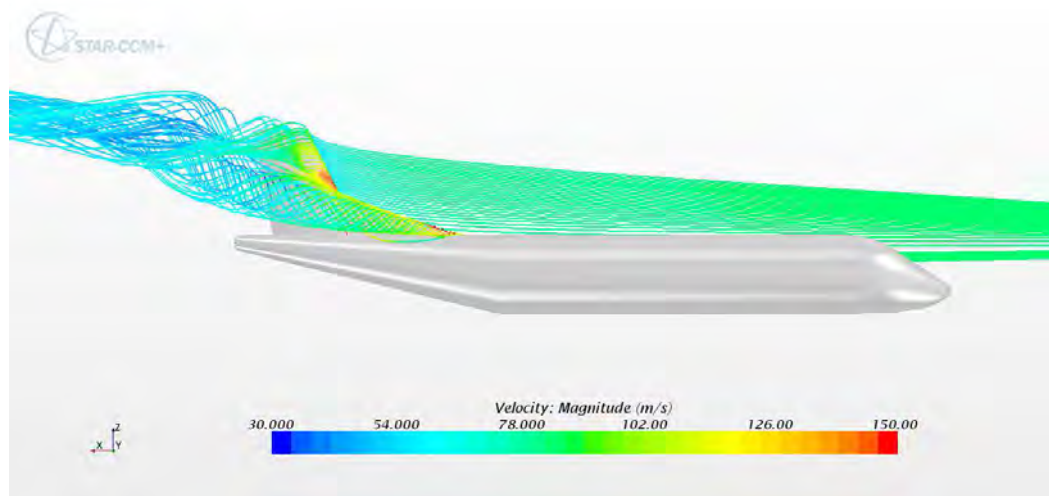


Figure 106 –Side View of the Streamline with Dorsal fin at $\beta = 40^\circ$.

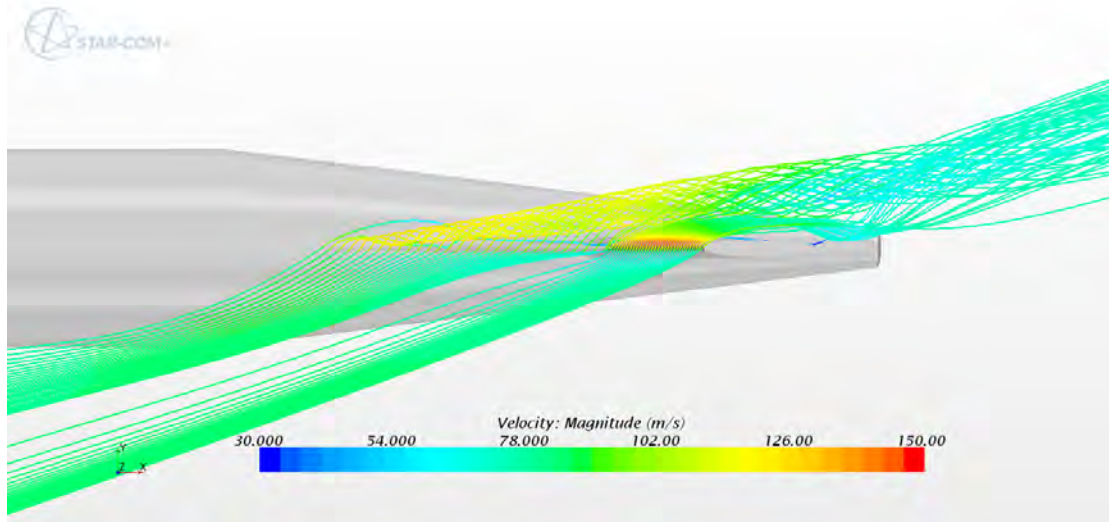


Figure 107 – Top View of the Streamline with Dorsal fin at $\beta = 19^\circ$.

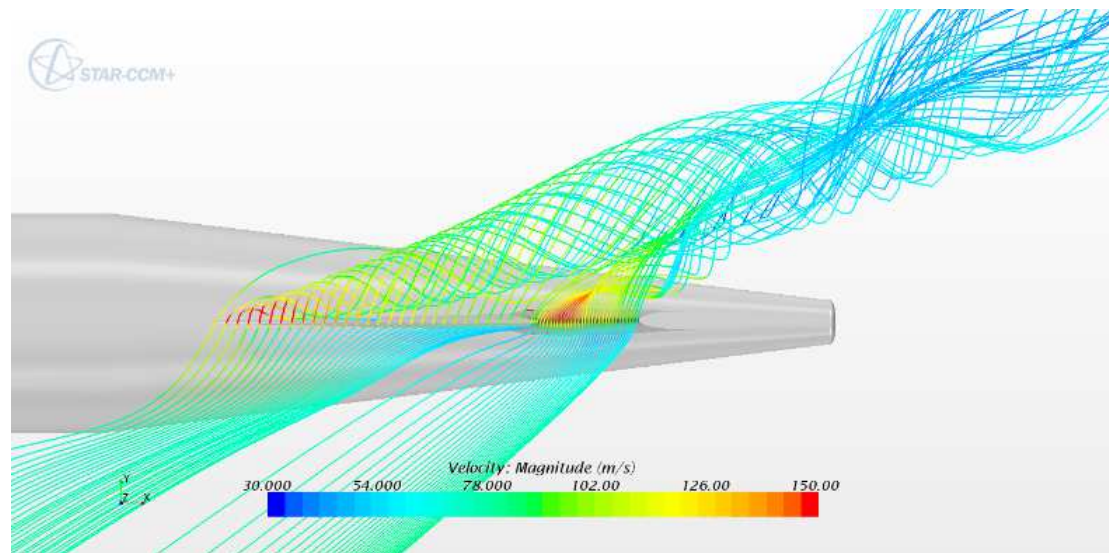


Figure 108 – Top View of the Streamline with Dorsal fin at $\beta = 40^\circ$.

Increasing β the core of the vortex assuming ever greater proportions, creating always strongest depressions in correspondence of the trailing edges (see figure). So the separate area becomes larger and larger, then the depression which is realized on the leeward side is such as to influence the flow behavior on the windward side which has more capacity to remain attached. This is the physics explanation behind the growing stability that occurs increasing sideslip, due to the dorsal fin.

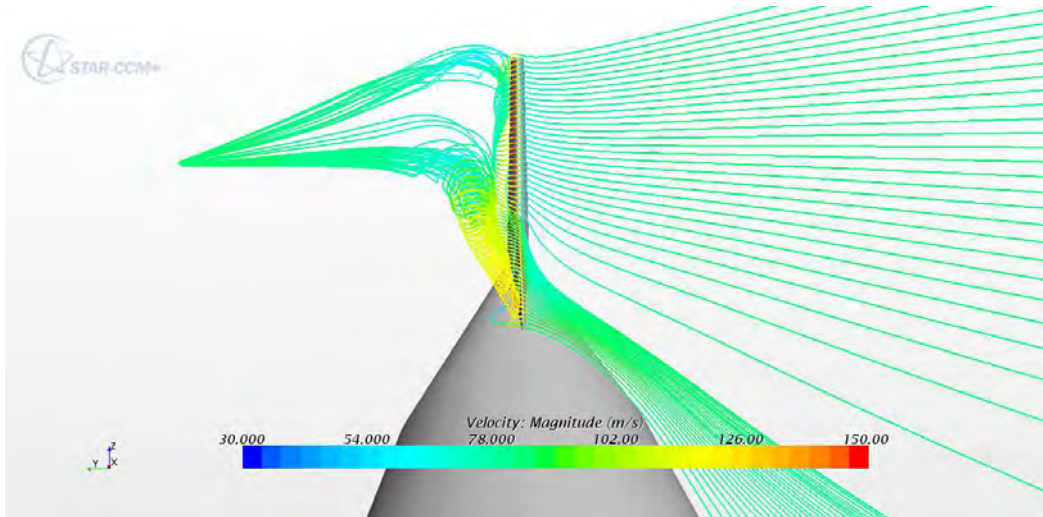


Figure 109 – Frontal View of the Streamline with Dorsal fin at $\beta = 19^\circ$.

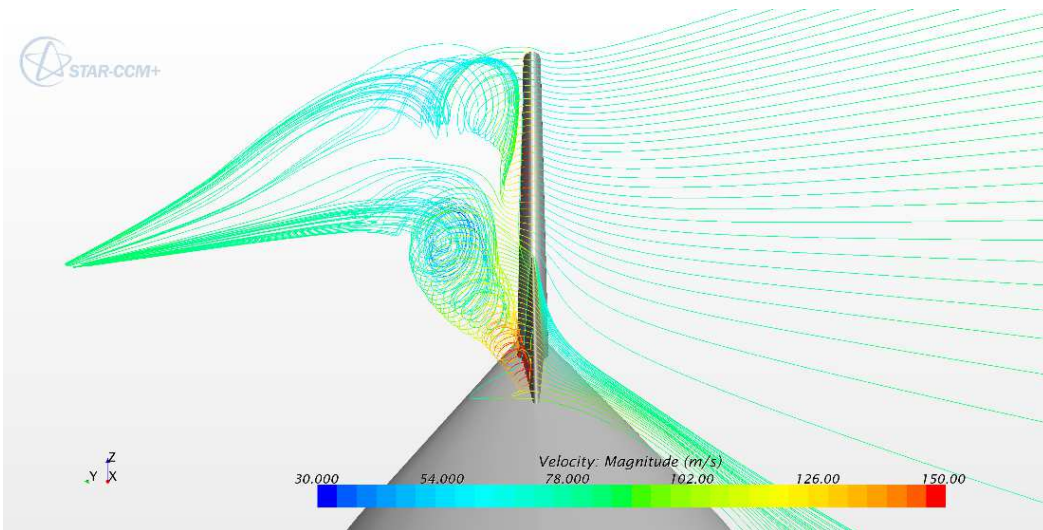


Figure 110 – Frontal View of the Streamline with Dorsal fin at $\beta = 29^\circ$.

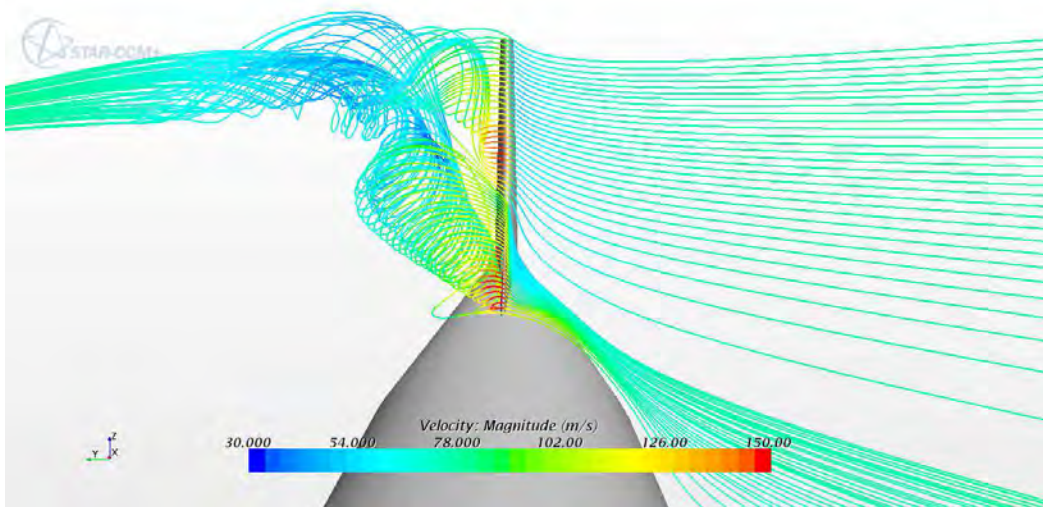


Figure 111 – Top View of the Streamline with Dorsal fin at $\beta = 39^\circ$.

It is interesting to compare the vorticity which is realized at extremely high angles with respect to that which is realized at the beginning of the non-linear range.

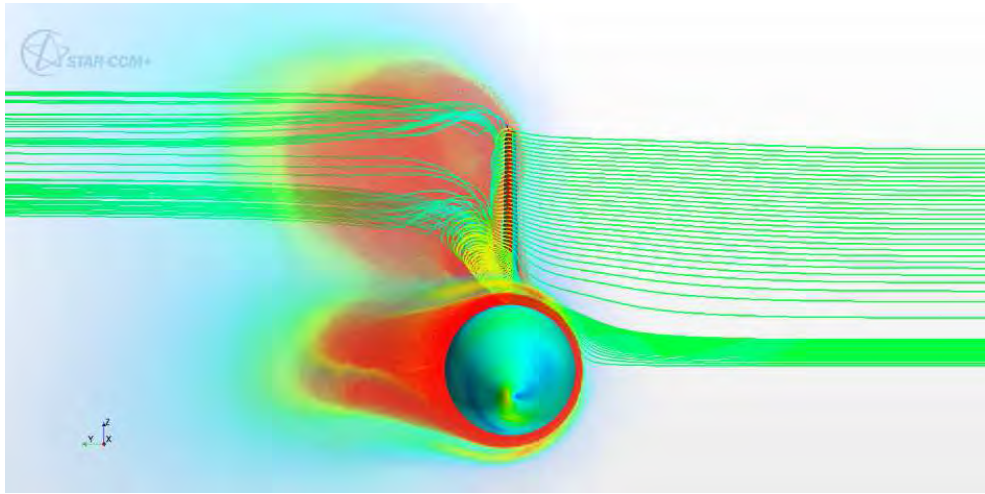


Figure 112 – Overall Frontal View with Dorsal fin at $\beta = 19^\circ$.

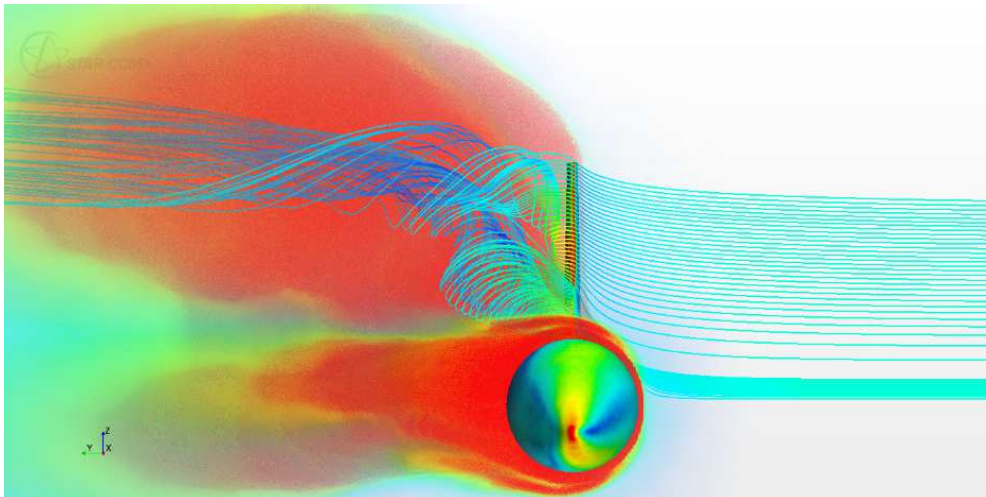


Figure 113 – Overall Frontal View with Dorsal fin at $\beta = 43^\circ$.

b) Evolution of Primary Vortex

We try to understand what happens to the flow that passes close to the dorsal fin increasing β , so we try to qualify the phenomenology studying the vortex evolution.

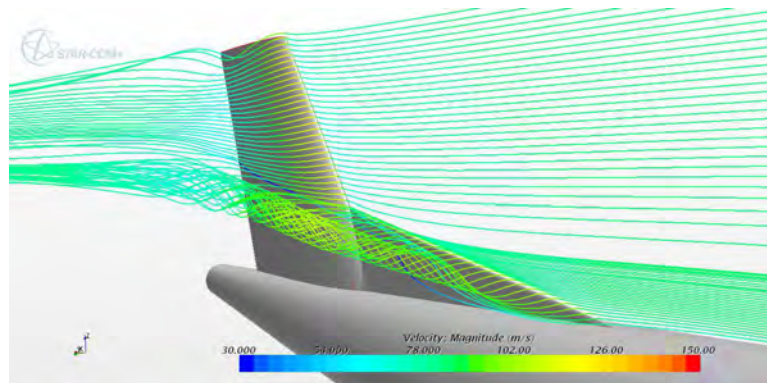


Figure 114 – View of the Streamline with Dorsal fin at $\beta = 10^\circ$.

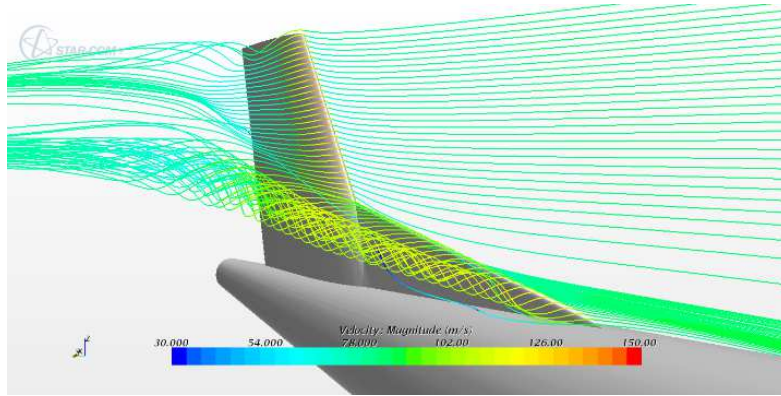


Figure 115 – View of the Sreamline with Dorsal fin at $\beta = 15^\circ$.

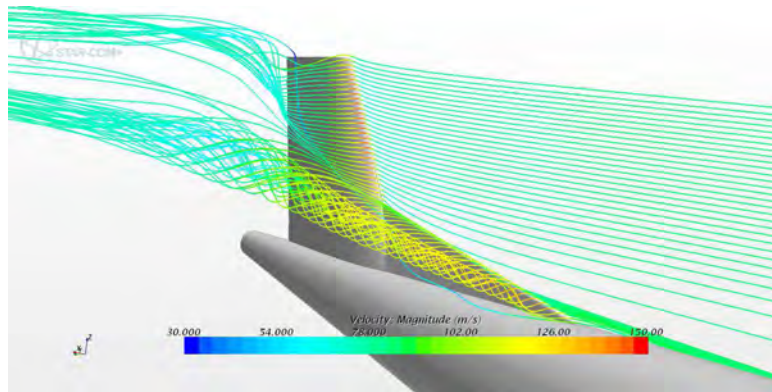


Figure 116 – View of the Sreamline with Dorsal fin at $\beta = 19^\circ$.

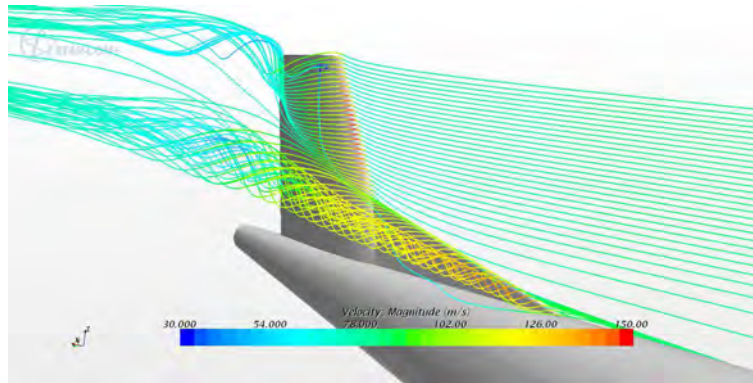


Figure 117 – View of the Sreamline with Dorsal fin at $\beta = 21^\circ$.

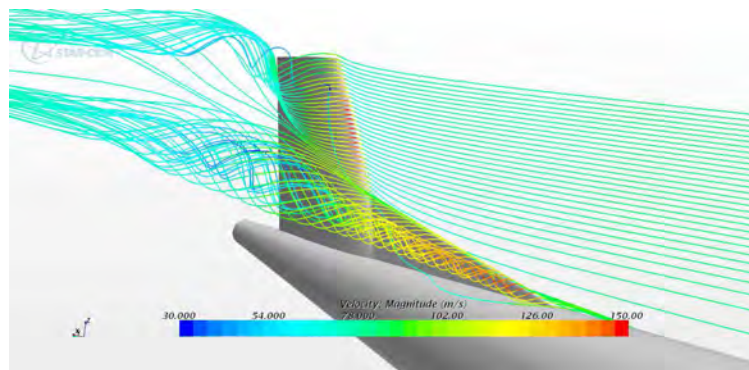


Figure 118 – View of the Sreamline with Dorsal fin at $\beta = 23^\circ$.

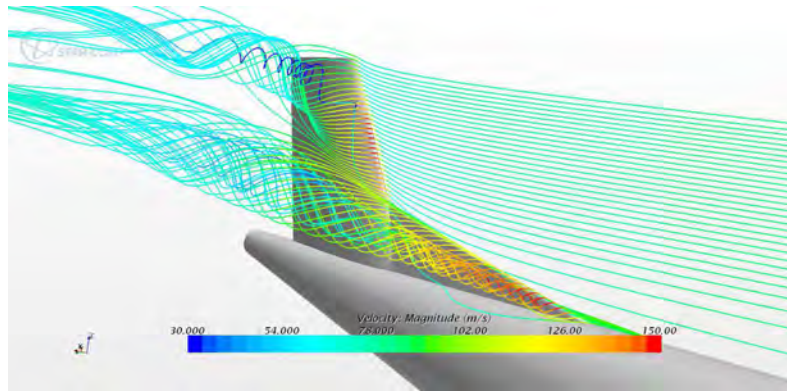


Figure 119 – View of the Streamline with Dorsal fin at $\beta = 26^\circ$.

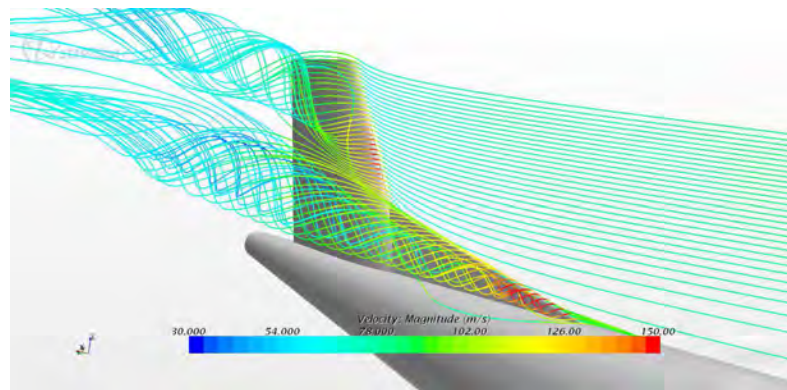


Figure 120 – View of the Streamline with Dorsal fin at $\beta = 29^\circ$.

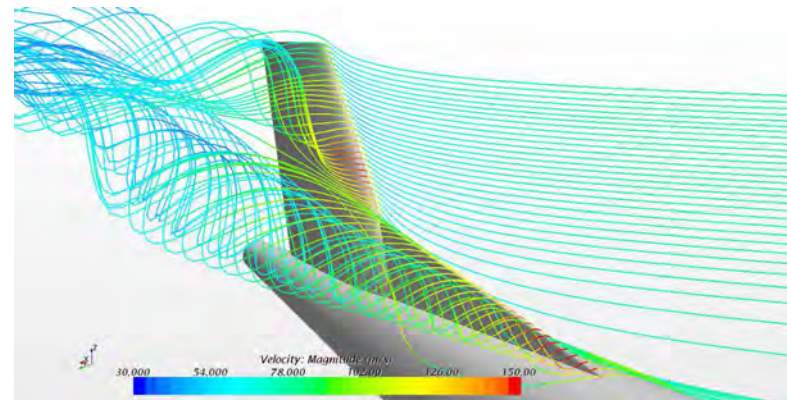


Figure 121 – View of the Streamline with Dorsal fin at $\beta = 40^\circ$.

Increasing β the vortex detaches from the leading edge of the dorsal with increasingly higher speeds as we can see from the color that becomes redder.

Again increasing β the core of the vortex assuming ever greater proportions, creating always strongest and largest depressions in correspondence of the vertical trailing edges.

From the succession of images (see Figure from 114 to 121) we can see how increasing β , the primary vortex, is redder close to the dorsal leading edge at the root station, but at the same time, the blue coloration of streamline is always reached before. It means that the flow arrives tired because of the great energy that provides when the vortex is generated. A stronger vortex, generates an stronger energy level, so the flow is always tired before.

It is interesting to show how does the C_p for various stations of the vertical compared for different angles of sideslip. In particular, we are considering 15° , 26° and 38° .

The analyzed station are (see Figure 122):

- $Z = 15\%$: size and dorsal vertical center line of the dorsal
- $Z = 40\%$: cuts the vertical immediately above the dorsal
- $Z = 76\%$: cuts the vertical far away from the dorsal

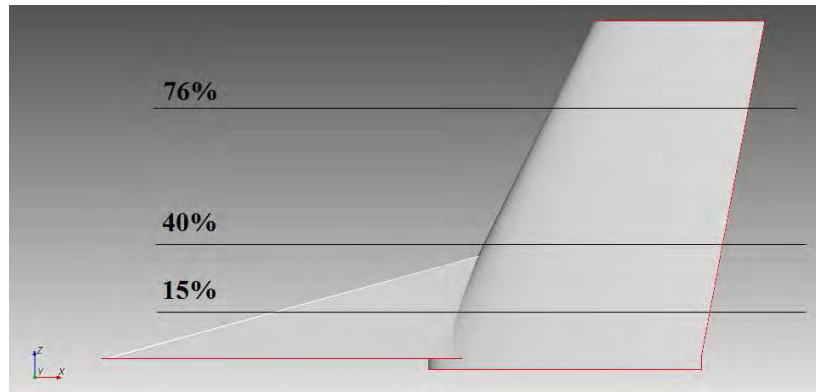


Figure 122 – List of analyzed section for Pressure Coefficient distribution analysis by varying the sideslip angle, CFD results.

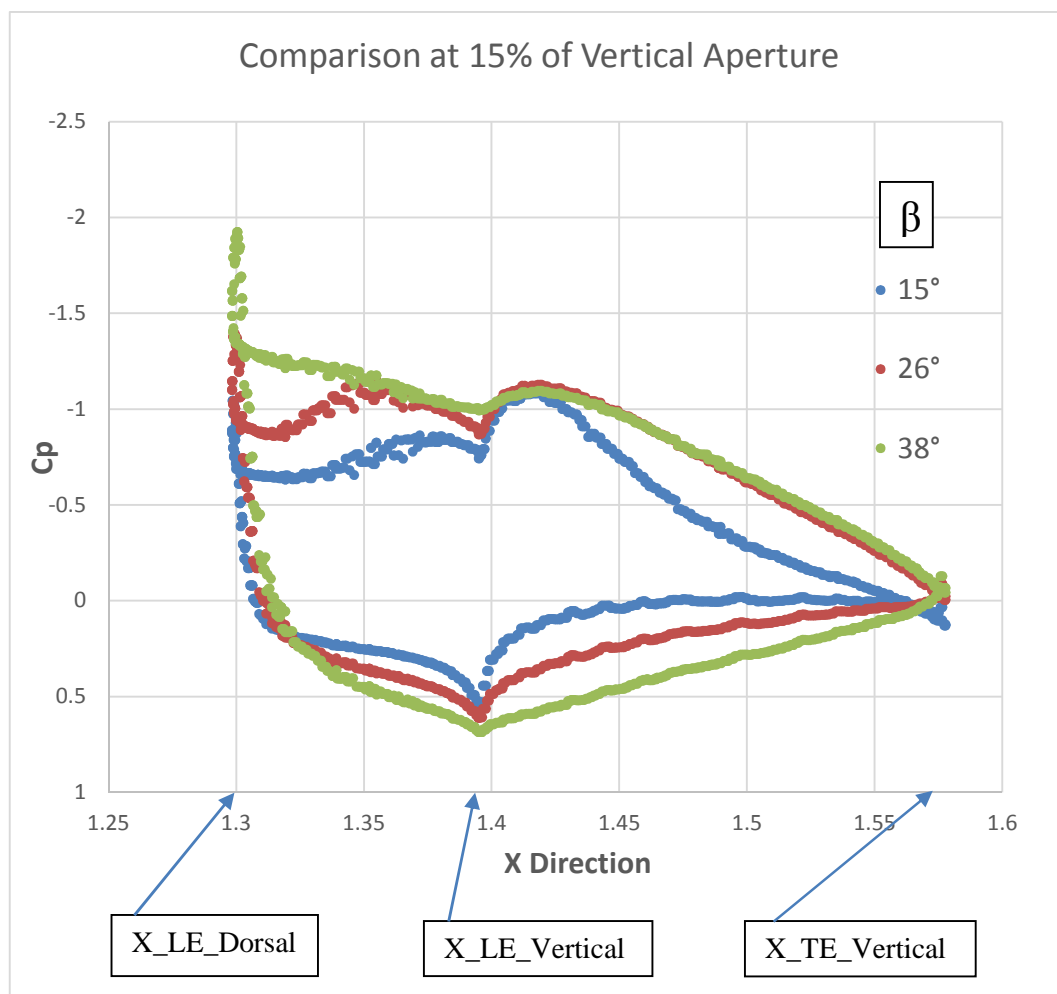


Figure 123 – Pressure Coefficient Comparison for BVD Configuration at 15% of vertical aperture.

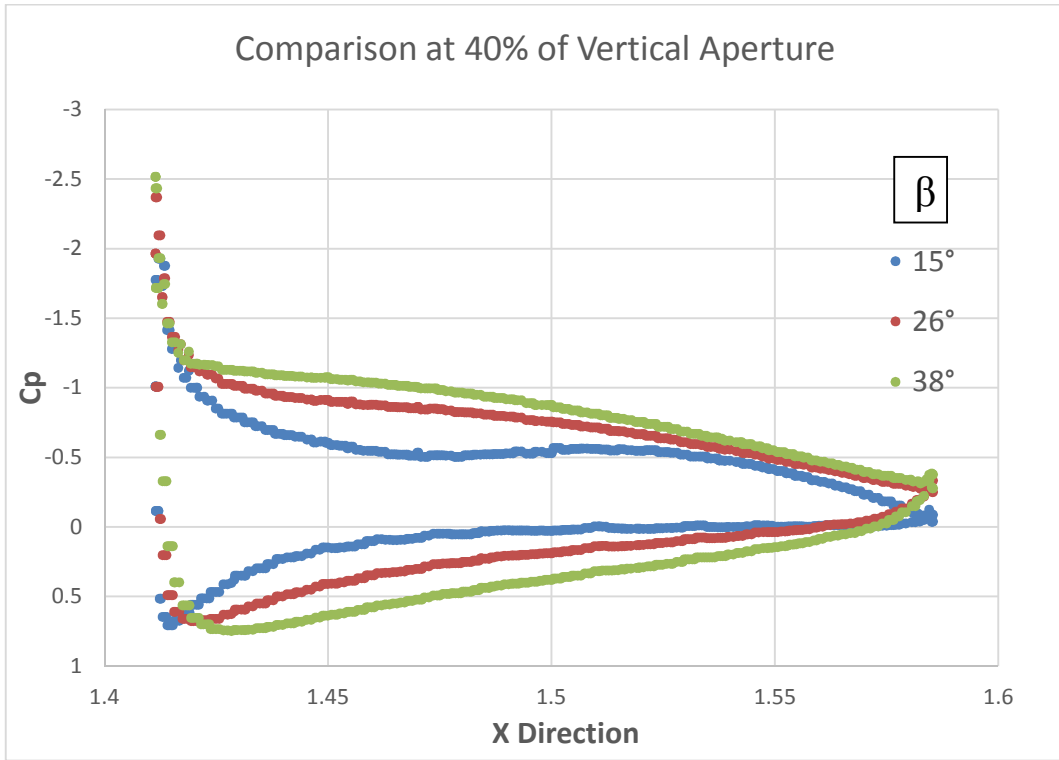


Figure 124 – Pressure Coefficient Comparison for BVD Configuration at 40% of vertical aperture.

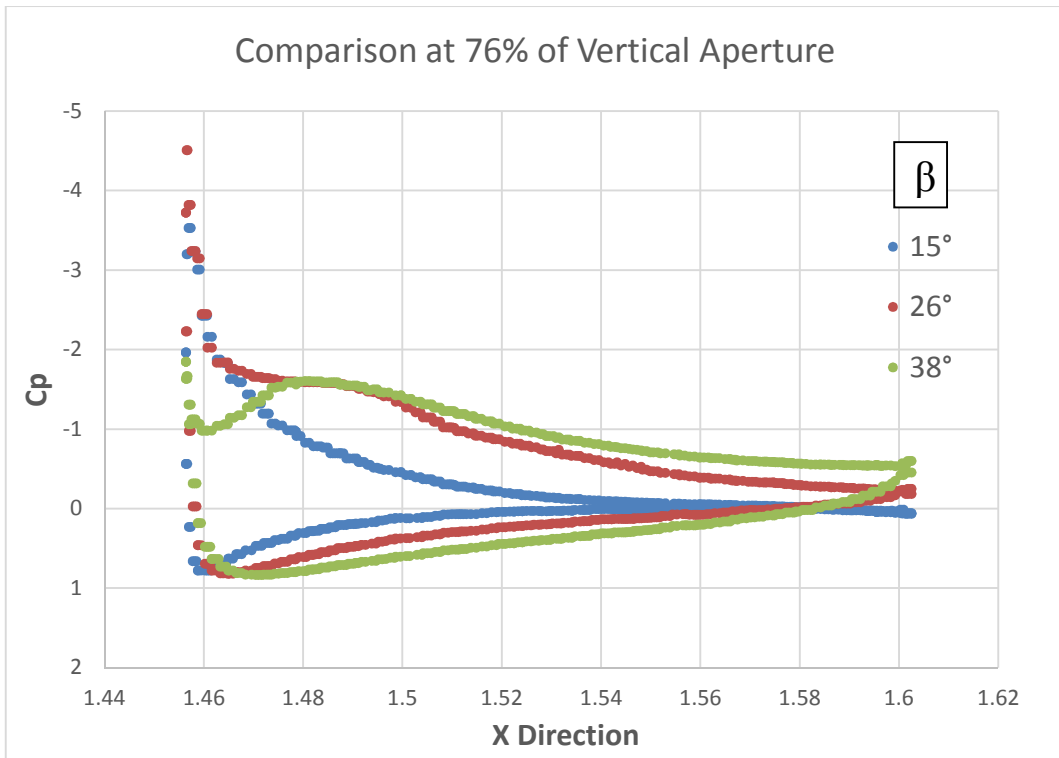


Figure 125 – Pressure Coefficient Comparison for BVD Configuration at 40% of vertical aperture.

5.2 DORSAL FIN EFFECT ON THE FUSELAGE STABILITY.

The Figure 126 shows the dorsal effect on the fuselage aerodynamic.

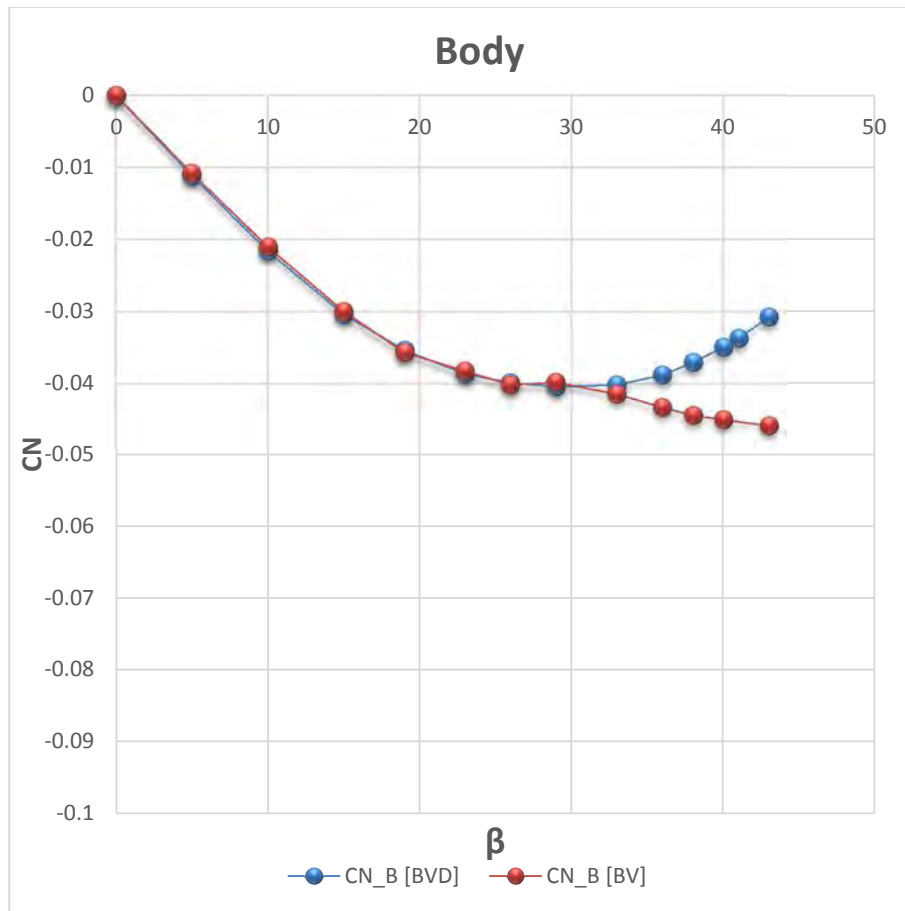


Figure 126 – Dorsal effect on Body contribution of yawing moment, CFD results.

It is clearly seen that the effect of dorsal fin is obtained for angles greater than $20/25^\circ$, providing a stabilizing contribution that makes the curve with positive derivative.

Using Dorsal fin the fuselage loses the destabilizing characteristics of the fusiform bodies, in fact the streamlines that otherwise would turn undisturbed around the caudal part of the fuselage, have a different behavior.

As we can see from Figure 127 an overpressure is realized at the area corresponding to the dorsal on the windward side.

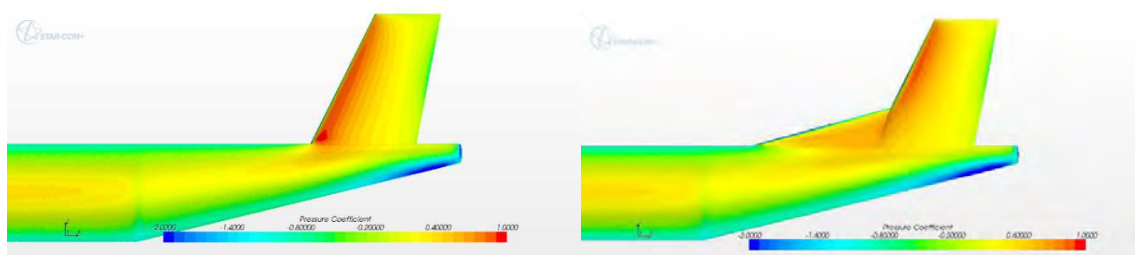


Figure 127 – Side View for Pressure Coefficient Comparison at Windward Side with and without Dorsal fin at $\beta = 40^\circ$.

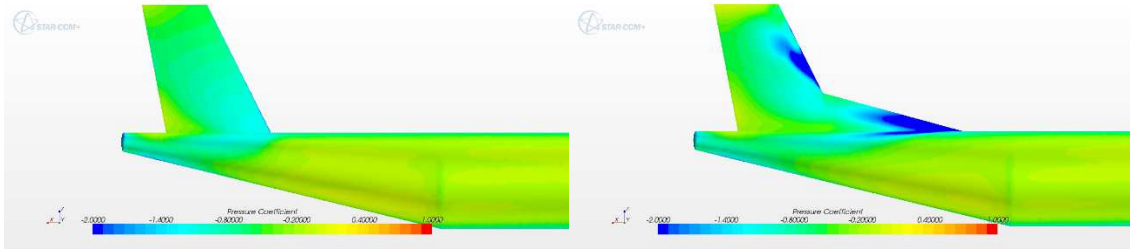


Figure 128 – Side View for Pressure Coefficient Comparison at leeward Side with and without Dorsal fin at $\beta = 40^\circ$.

By analyzing the Figure 106 & 107 we can see that with dorsal fin a very large part of the windward fuselage (the part below the dorsal fin and vertical surfaces) is yellowish. While in the dorsal fin absence such yellowish area, below the vertical, is very low. So the pressures integral acting on the fuselage is greater with the dorsal which acts as a screen to the particles flow. This explains the phenomenon of the stabilizing feature, which has the fuselage in the case of the presence of the dorsal fin.

5.3 DORSAL FIN PRIMARY EFFECT ON THE OVERALL STABILITY

We analyze the curve of the total yawing moment of BV configuration with the curve of total yawing moment of BVD configuration. Compared to the previous case concerning the effect on the vertical tail, now there is a difference equal to the unstable fuselage contribution that reduce these curves. In particular from Figure 129 we can see greater reduction for the curve relative to BV configuration (for which the contribution of the fuselage is greater in absolute value), and a lower reduction for the curve relating to the BVD configuration (for which the fuselage contribution is lower in absolute value due the dorsal fin as mentioned above)

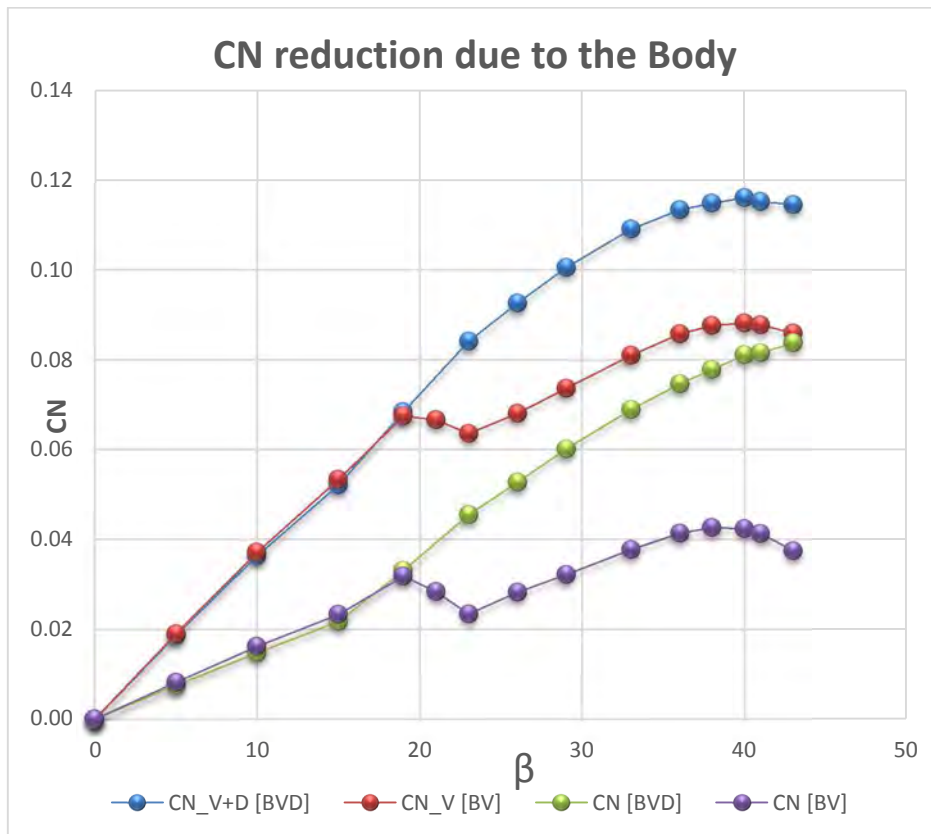


Figure 129 – Reduction of stability due to Body contribution, CFD results.

5.3.1 PRESSURE REDISTRIBUTION.

By the Figure 130 we can show that using the dorsal fin are made the same pressures that are obtained without dorsal fin at lower angles.

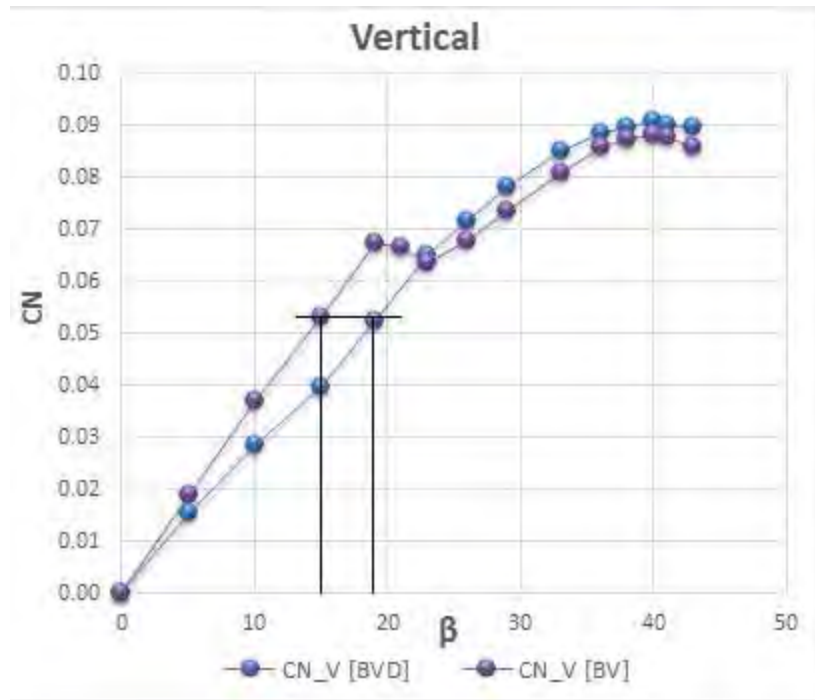


Figure 130 – Angle selection for the same Value in Different Configuration.

Supporting this consideration are inserted graphs of the pressure distribution of profiles in the stations to 50% for the vertical in BV configuration at $\beta = 15^\circ$ and for the vertical in BVD configuration $\beta = 19^\circ$.

From a CP distribution analysis, we can highlight that this two configurations about two different angles generate the same overpressure indicated by the maximums values of CP which are approximately about -4 in both cases (see Figure131).

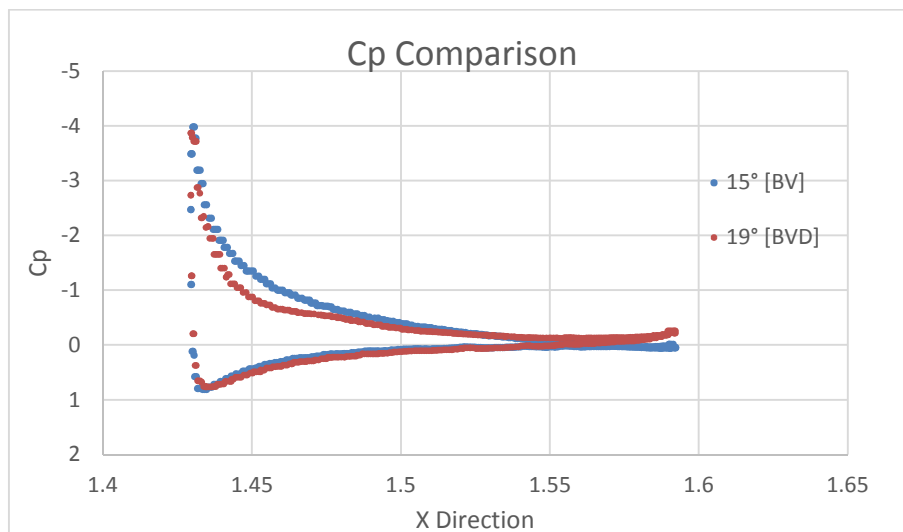


Figure 131 – Pressure Coefficient Comparison between BV at 15° and BVD at 19° both stations at 50% of vertical aperture.

Will have to result that the integral of these two areas is roughly equal in accordance with the fact that it must achieve the same CN as we can see from Figure 130.

Since we show that at different angle vertical section has equal C_p distribution for different configuration, it is appropriate to study what happen for the same angle of this different configuration.

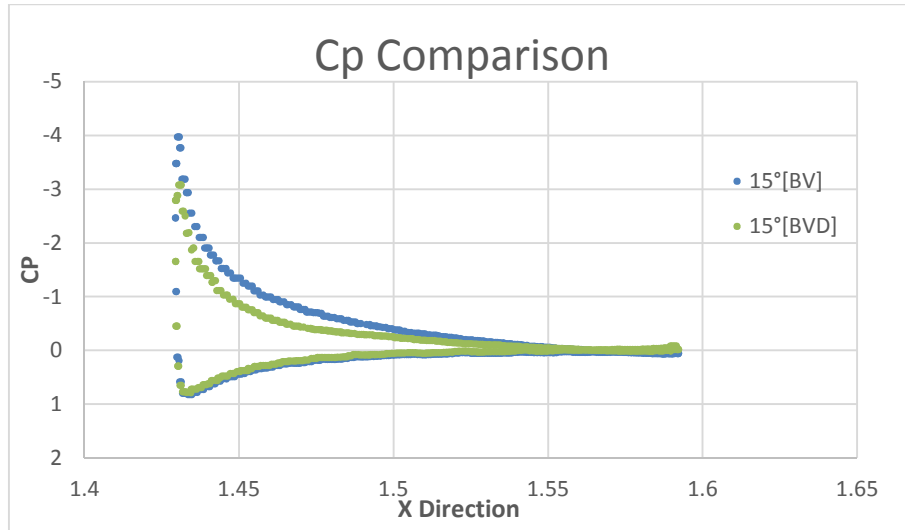


Figure 132 – Pressure Coefficient Comparison between BV at 15° and BVD at 15° both stations at 50% of vertical aperture.

The Figure 132 concern the C_p analysis of BV and BVD for the same angle of $\beta = 15^\circ$, thanks to which we can see how the same angle for the two geometries realize different aerodynamics so different C_p distribution. In fact reducing the sideslip angle from 19° to 15° the C_p distribution of the vertical in BVD configuration is very different from the C_p distribution of the vertical in BV configuration both related at the same section.

It's clear that the dorsal fin presence induce a strong effect about the virtual angle of attack that see the vertical tailplane. To understand the magnitude of this effect we have to compare the C_p distribution of the vertical for BV configuration involving an angle variation like before, so from 15° to 19° . The magnitude of this difference in C_p distribution is index of the significance of dorsal fin presence respect the angle of sideslip reduction point of view.

Considering the same angle variation, for the BV configuration we notice that there is a strong difference between the two depressions, in fact for $\beta = 19^\circ$ should have been achieve a value of C_p about -6. (see Figure 133).

Then we intuit the dorsal effect, which makes the configuration BVD the same as BV, to lower corners. So we can consider this exactly like an angle incidence reduction effect. It means that the vortex act like a reducer of sideslip angle.

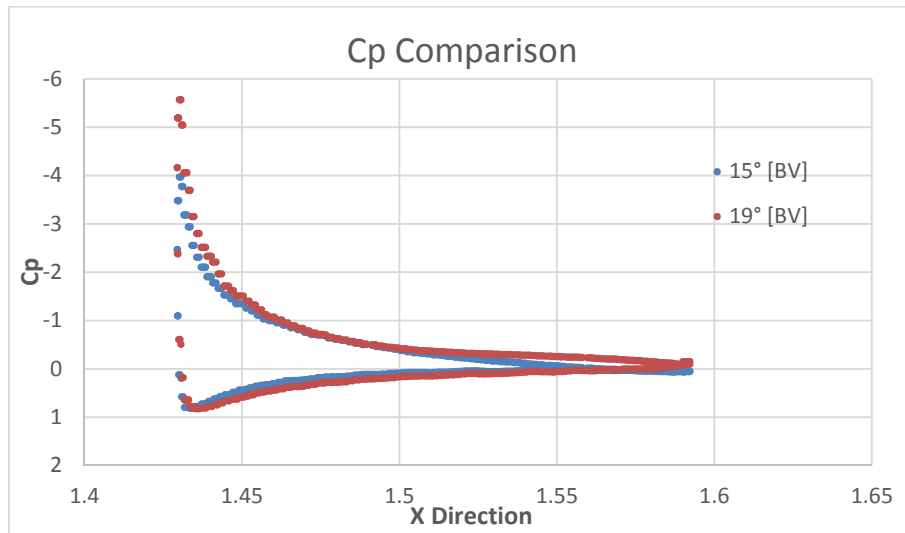


Figure 133 – Pressure Coefficient Comparison between BV at 15° & 19°, stations at 50% of vertical aperture.

Another analysis that allows us to better grasp these concepts is the one with the contour of the Cp. In this way it is possible to visually appreciate the variations of pressure because to them corresponds to a variation in color. Please note at this point that for visually appreciate these aspects from coloration, it is necessary to set the full scale in order that for the two configurations is equal. In this way, the correspondence between the color and the pressure magnitude is the same for both images.

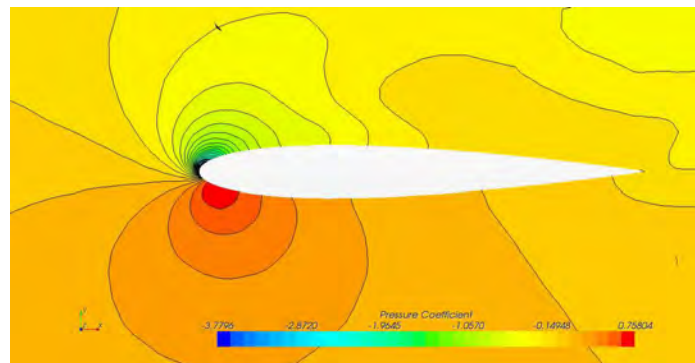


Figure 134 – Pressure Coefficient Contour Plot for BVD Configuration at 50% of vertical aperture for $\beta = 19^\circ$.

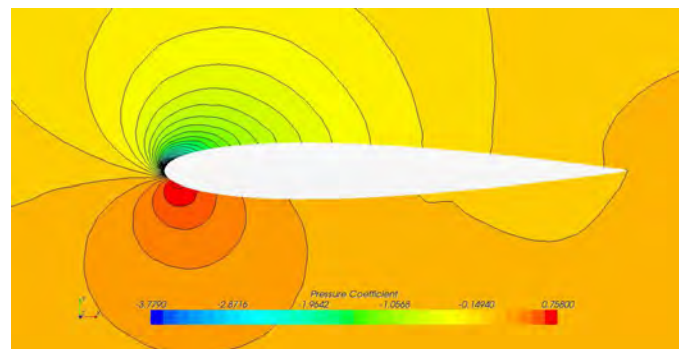


Figure 135 – Pressure Coefficient Contour Plot for BV Configuration at 50% of vertical aperture for $\beta = 15^\circ$.

We can see the strong correlation between the coloration of the two images (see Figure 134 & 135) especially concerning the leading edge zone, that as shown in Figure 130 have to realize the same pressure value of C_p about -4° . Obviously close the trailing edge there is a different behavior due the vortex presence for BVD configuration, but it does not change our consideration.

Being related to two different angles were to be found strong variations in terms of coloration. For a better understanding of how should have been differentiate the pictures, we add to support this analysis also the image on the BV configuration when $\beta = 19^\circ$ (see Figure 136 & 137).

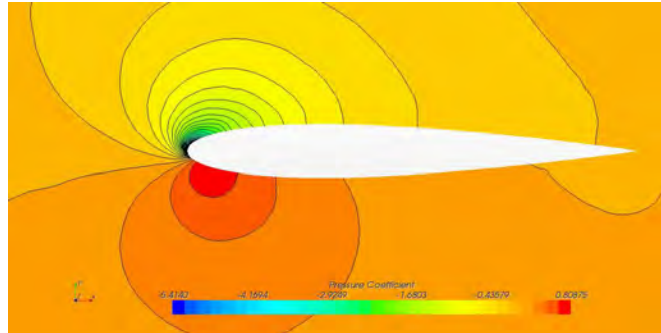


Figure 136 – Pressure Coefficient Contour Plot for BV Configuration at 50% of vertical aperture for $\beta = 19^\circ$.

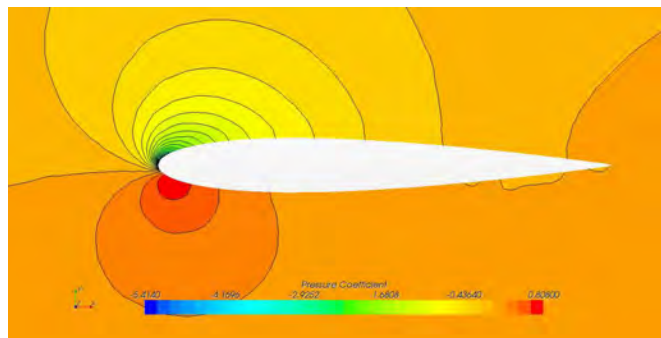


Figure 137 – Pressure Coefficient Contour Plot for BV Configuration at 50% of vertical aperture for $\beta = 15^\circ$.

It is clearly seen from the comparison of these two graphs that the high-pressure zone for $\beta = 19^\circ$ is much more extensive than that for $\beta = 15^\circ$ reflecting that the flow is very different in the two conditions as show in Figure 133 when is compared the C_p value.

We must point out that for these observations was considered a single station of vertical. The comparison between the two curves showed an equal CN for the vertical in BV configuration $\beta = 15^\circ$ and vertical in BVD configuration $\beta = 19^\circ$. Considering that the CN is determined with the integral of the pressures acting on the profile, this analysis can be supported by Figure 138 & 139 that show the magnitude of the pressure on the entirety of the vertical tail, in the two configurations.

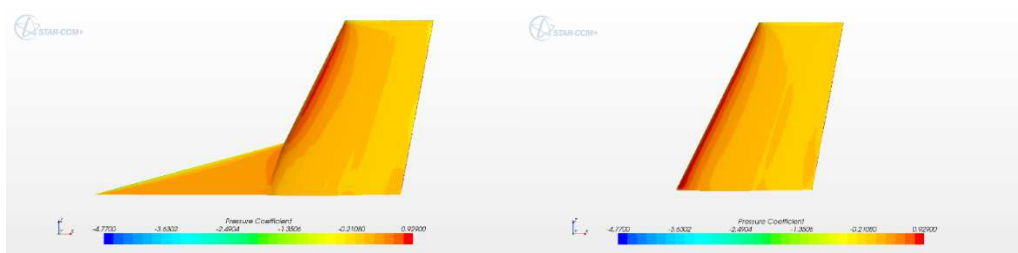


Figure 138 – Pressure Coefficient comparison at windward side for BV & BVD Configuration at $\beta = 15^\circ$.

FOR THE WINDWARD SIDE:

- The RED area corresponds at the maximum pressure at the leading edge
- The ORANGE area corresponds at the high pressure, is characterized by a gradation of color which tends to clear, with the move away from the leading edge.
- The YELLOW area corresponds at the lower pressures next to the trailing edge.

In BV configuration the vertical plane has a RED region of maximum pressure on the leading edge for its entire length; The ORANGE area of high pressure already after 10% of the chord arrives at the gradation clearer relative to a low pressure; Finally, the YELLOW area of lower pressures is very extensive, in particular we can see as closer to the tip of the plan, this area gets bigger and bigger (see Figure 139).

In BVD configuration, the vertical plane has a RED region of maximum pressure on the leading edge but not for its entire length only to the station of the dorsal fin (high pressure area less extended); The ORANGE area of high pressure just after about 18% of the chord reaches the gradation clearer relating to a low pressure; Finally, the YELLOW areas of lower pressures is less extensive of the other configuration, in particular we can see as closer to the tip of the plane that area remains almost constant (see Figure 139).

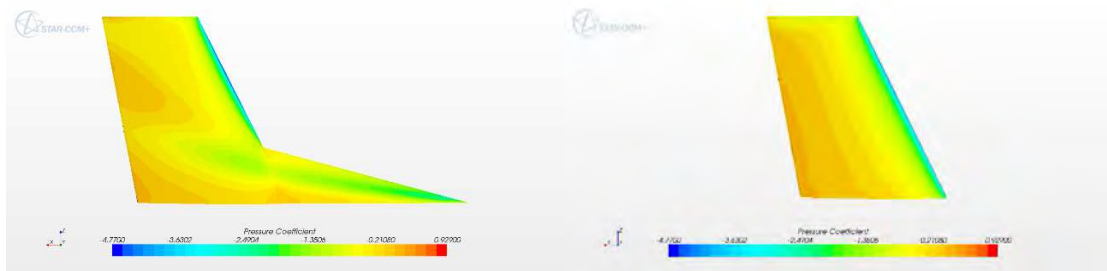


Figure 139 – Pressure Coefficient comparison at leeward side for BV & BVD Configuration at $\beta = 15^\circ$.

FOR SIDE LEEWARD:

- The ORANGE area corresponds at the high pressure is characterized by a gradation of color which tends to darkening, with the move away from the leading edge, this phenomenon is related to the recovery of pressure toward the trailing edge.
- The YELLOW area corresponds at the lower pressures.
- The GREEN area is related to very strong depressions next to the leading edge.
- The LIGHT BLUE area relates to extremely strong depressions at the leading edge.

In BV configuration, the vertical plane has an ORANGE area of high pressure after 40% of the chord which extends for the entire opening of the plan; The YELLOW area of lower pressures is quite confined and extended throughout the opening of the plan; The GREEN area of high depression and LIGHT BLUE of maximum depression, close to the leading edge extends for its entire length (see Figure 140).

In BVD configuration, the vertical plane has an ORANGE area of high pressure very confined and extended in particular areas related to the phenomenology of vorticity explained above; The YELLOW area of lower pressures is quite extensive; The GREEN area of high depression occurs close to the leading edge, not for its entire length, but until the station of the dorsal fin (low pressure area in less extensive). The LIGHT BLUE area of maximum depression on the leading

edge extends not for its entire length but until the station of the dorsal fin (area of maximum depression less extended) (see Figure 140).

For these two configurations is achieved a different pressures distribution which the integral is equal because they determine the same coefficient C_N .

- For example to the windward side, in the BVD case, we can see that the part of high pressure is less extensive than in the BV case, but at the same time, the part of intermediate pressures is more extensive than that of low pressure part unlike the BV case.
- For example to the leeward side, in the BVD case, we can see that the part of strong depressions is less extensive than in the BV case, but at the same time presents itself even away from the leading edge for the phenomenology of vorticity.

From C_p analysis we define quantitatively this difference, here we just showed qualitatively how has been reached the same stability contribution of the vertical tail through a pressures redistribution.

5.4 PARTICULAR DORSAL FIN EFFECT ABOUT DIRECTIONAL STABILITY

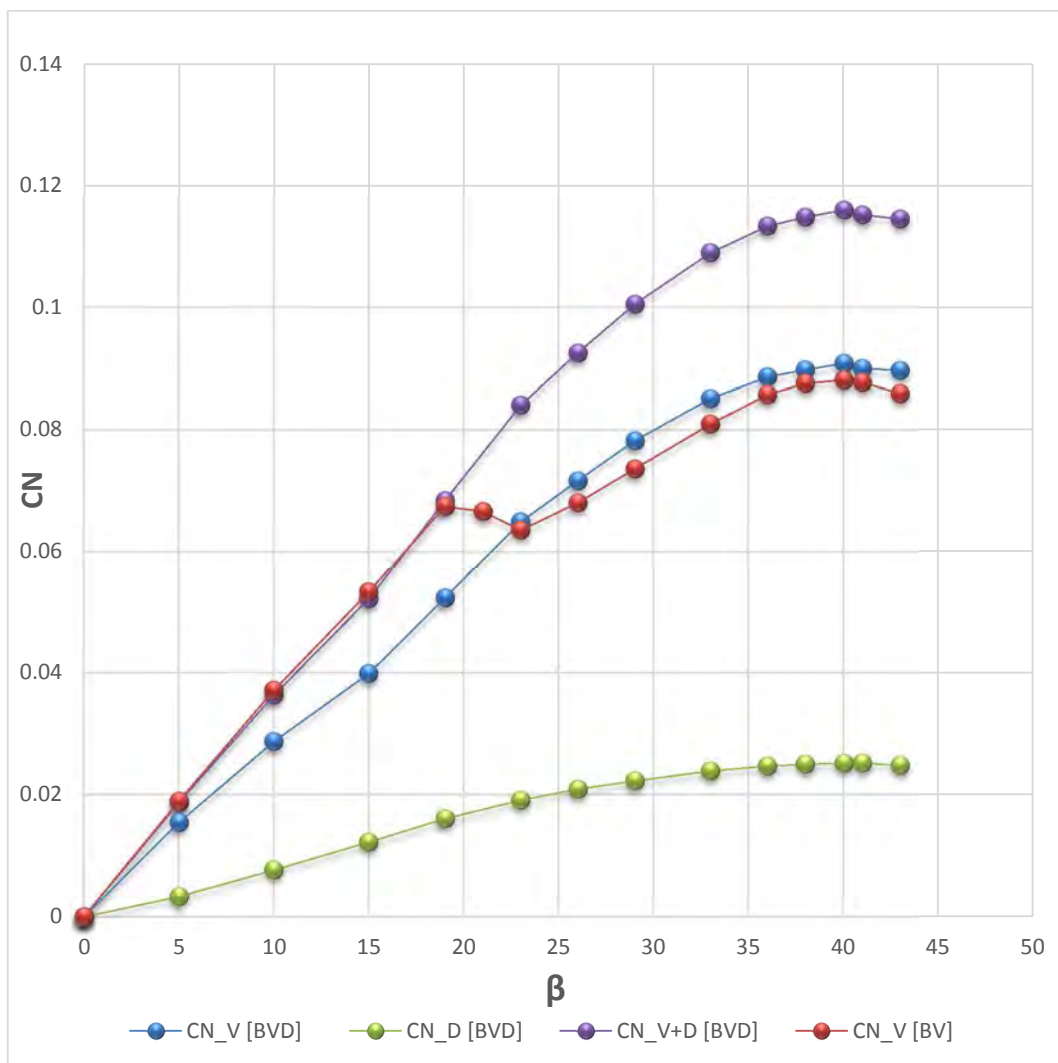


Figure 140 – Summary of the roles of the individual contribution of BVD configuration respect the total contribution of BV configuration.

Thanks to this graph, we can highlight an aspect of the operation in the presence of the dorsal fin for the linear range. Using Figure 140 we focus primarily on how add up the contributions of Dorsal and Vertical get Dorsal + Vertical and their relevance in terms of stability increase.

The aspect that interests us is to understand what phenomenology characterizes the ineffectiveness of the dorsal fin in the linear range, i.e. that there is an almost perfect correspondence between the curves of Vertical in BV configuration and of Vertical + Dorsal in BVD configuration. It may seem strange that, because however there is an area addition which intervenes in the aerodynamics.

To confirm this sentence we focus on linear range where there is perfect correspondence between the curves and show how the different geometry of V+D and V realize a different aerodynamics (see Figure 141 & 142).

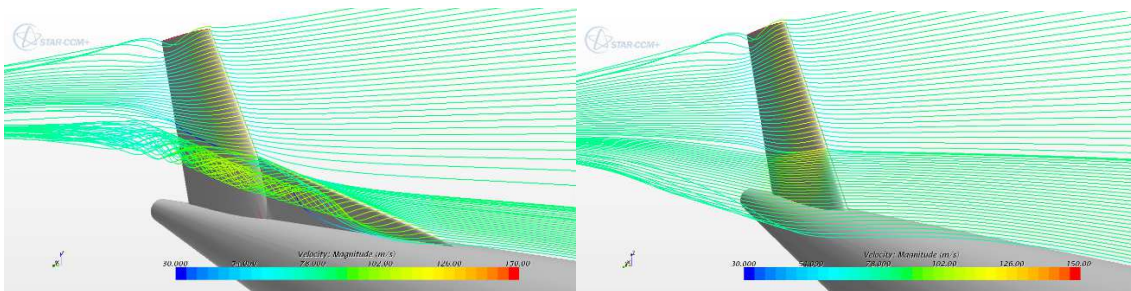


Figure 141 – View of the Streamline with & without Dorsal fin at $\beta = 10^\circ$.

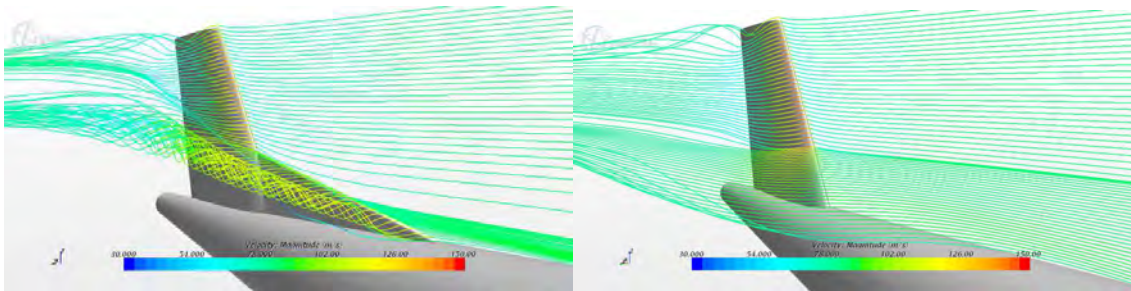


Figure 142 – View of the Streamline with & without Dorsal fin at $\beta = 15^\circ$.

Actually happens that with the addition of the dorsal, the vertical work less how we can see from Figure 130 about the yawing moment coefficients at $\beta = 15^\circ$. In Figure 143 the comparison between the curve of vertical in BV configuration and vertical in BVD configurations. In the presence of dorsal fin there is a lowering of the line slope for the contribution of only vertical.

The difference of this slope shows the aerodynamics difference of the vertical, which works less, but at the same time there is to consider the additional surface of Dorsal fin.

There is this difference of slope because we are neglecting the contribution of the dorsal fin that would bring the two slopes to coincide.

So it is clear as Dorsal and Vertical shall divide their contributions. For example from subsequent analyzes result that an increase of the dorsal height implies a larger decrease of the vertical work which is compensated by a greater increase of the dorsal contribution.

Particularity is that these two variations are practically always equal and opposite.

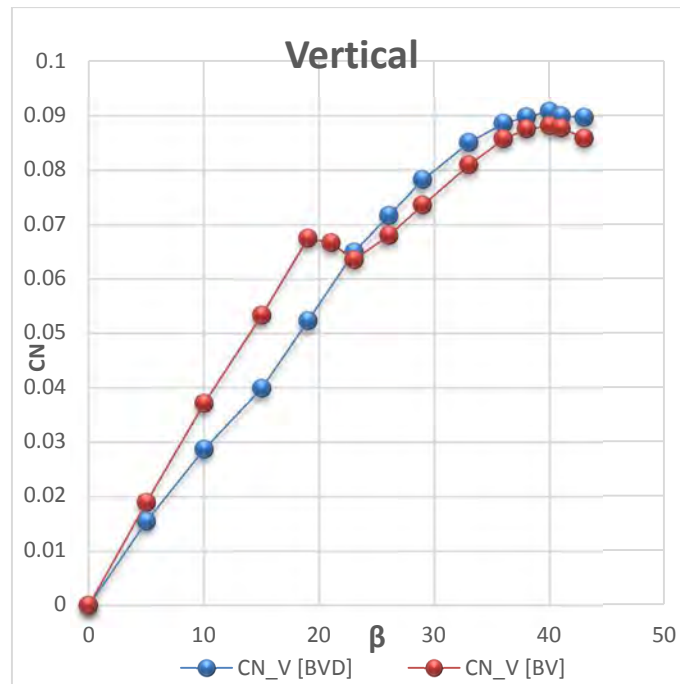


Figure 143 – Reduction of Vertical contribution of yawing moment in presence of dorsal fin.

Consideration about AR variation:

Our consideration are referred to the Figure

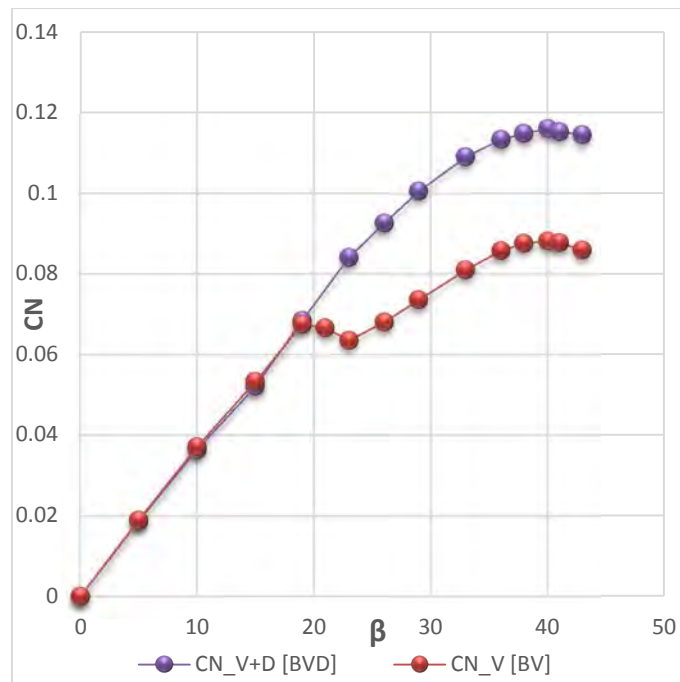


Figure 144 – Perfect correspondence of yawing moment in linear range with and without dorsal fin.

Adding the dorsal fin we obtain a surface increase about 30% at the same wingspan of vertical. Since the relationship between AR and S is inversely proportional, it will result in a decrease about 30% of AR. Considering that the starting value is 1.5, reduced by 30 percent is 1,05.

Should therefore be also for this curve a difference of slope since AR of V is different from the AR of the hypothetical vertical surface that is realized with V+D. So if we consider that V+D have an AR much lower than V the two curves should be necessarily different with reduction of slope adding the dorsal surface (see Figure 145).

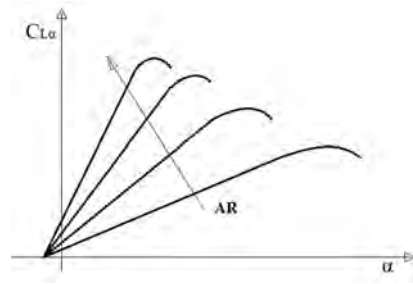


Figure 145 – $CL\alpha$ as function of AR.

Since involving the 3D coefficients, this consideration about the $CL\alpha$ as function of AR can be done only if it's referred to the same wing surface value. Since in our case V + D has a larger surface the slope of the line of lift 3D must necessarily gain slope.

This explains the reason for the coincidence of the curves in the linear regime.

Because of the particular form of D+V with the characteristic kink, aerodynamics that is realized is necessarily different. So what is lost, since there is a rise of the surface (a decrease of AR) is retrieved from the new add surface.

These results allow us to confirm the inaccuracy of considering the dorsal ineffective at low angles of sideslip.

This demonstrates that it is not true the inefficiency of the dorsal fin in linear range, but rather that the equal value of the two configurations (BV & BVD) in the linear range is the result of the coexistence of two phenomena: on the one hand to increase the surface that determines a growing of the slope, on the other hand the AR reduction implies a lowering slope.

This means that increasing the surface area of the dorsal fin results an increasing contribution of the dorsal, which compensates the increasingly intense loss of work that has the vertical.

5.5 CONCLUSIONS FOR BASELINE

We understand, the power of the CFD calculation instrument compared to other types of analysis (tunnel tests, fly test, etc.).

It was possible to make several considerations on the aerodynamic aspects of the current problem and in general on the stability phenomenology due to this tool that allows to divide individual contributions of the various regions of the continuum. While from a tunnel test the results are obtained for the entire analyzed system, by CFD calculations, the results are obtained separate. Therefore we can actually understand the evolution of the individual part contributions and then understand the phenomenology of the problem.

6. PARAMETRIC ANALYSIS

The present work aims to provide guidelines on the dorsal fin preliminary design of an aircraft of turboprop class, and aims to extend the initial planning method of the vertical tail developed at the Department of Industrial Engineering, sect. Aerospace, by Professor Nicolosi and his collaborators.

6.1 MOTIVATION

Among the last words of the report [3], it sets out the possibility improvement:

“Including more practical data like wind-tunnel testing, SIMULATIONS, ADVANCED SOFTWARE, may also improve the approximations given in this report. These can be taken up as Future Work”

In the development phase of the F-27 **Obert** [4] had investigated different types of Dorsal fin. The fact that these geometries are numerous, allowed us to extract from the general study done for the best choice of geometry, parametric evaluations that we can then compare with those made specifically according to the report. In this way we can confirm the trends related to the change a geometric parameter.

So using software STAR-CCM + I made several sets of aerodynamics simulations like in the study of the report, to then proceed in terms of comparison and possible consolidation of some results.

We must start from the premise that the simulations are relative to a hypothetical model, therefore we can confine our interest, rather than obtaining the stability performance in absolute terms, just in the study and understanding of the trend with respect to any geometry changes. It will be possible to evaluate the percentage differences and quantify the characteristic trend. This takes concrete form in a parametric study, with simulations that will be easily sustainable if we proceed to define parametrically the geometry. After the reference geometry realization in the CAD environment of STAR-CCM+, it was easy to make the other, since the parameters of interest were modifiable, therefore instantaneously I created other geometries.

6.2 WORKFLOW

We begins with the geometric parameters definition like in the analyzed Report [4] (Figure 146).

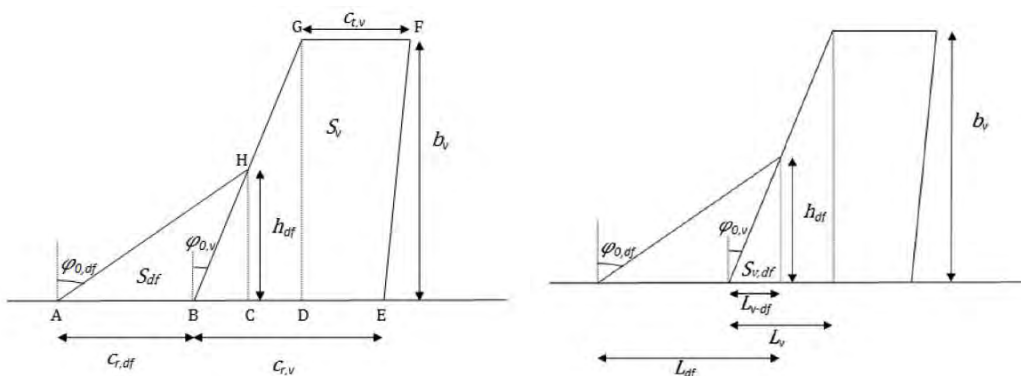


Figure 146 – Vertical & Dorsal fin Geometric Parameters.

We move to the data extraction from experimental curves produced. Obert investigates various dorsal fin in the development of Fokker F-27 (see Figure 147 & 148).

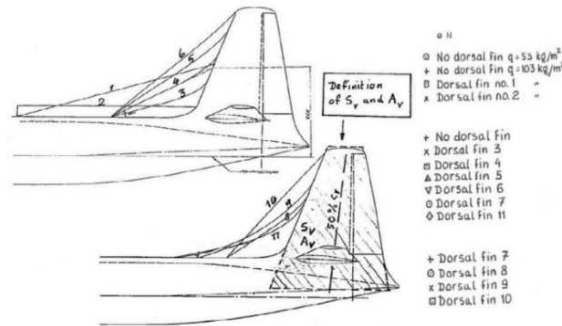


Figure 147 – Different Dorsal fin Investigated for a Fokker F-27 [4].

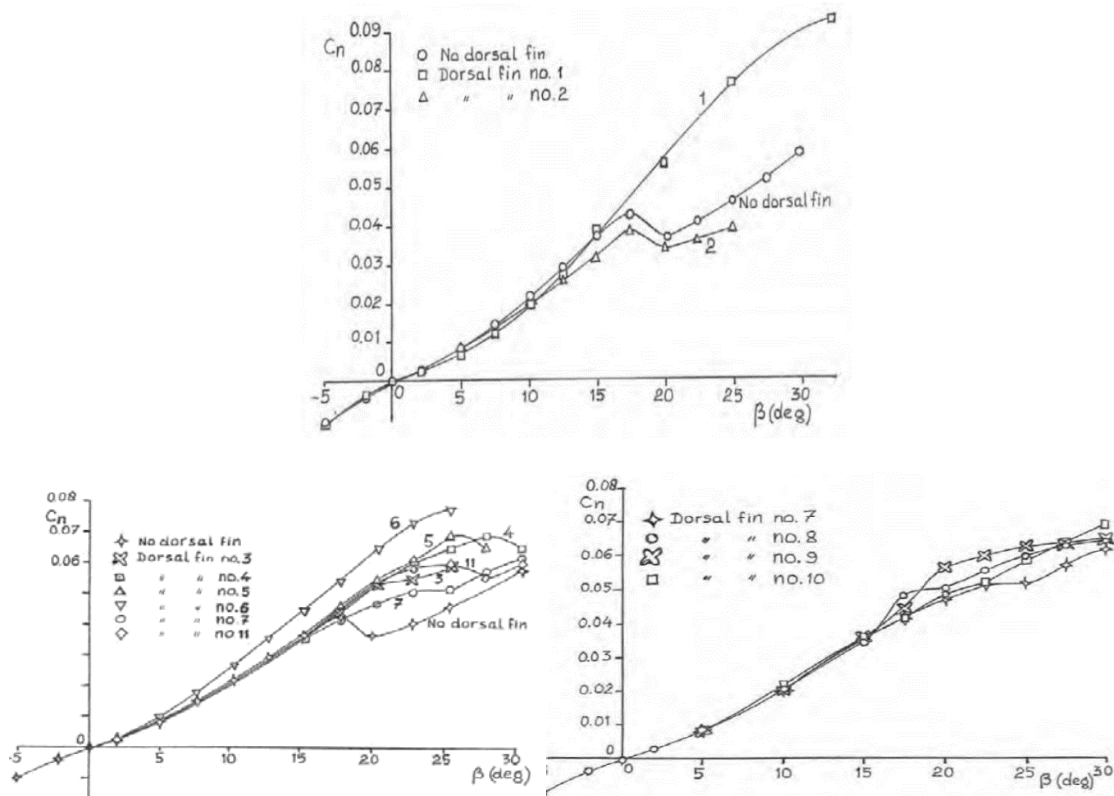


Figure 148 – Effect of a Dorsal fin on the Yawing Moment Coefficient [4].

These curves summarize the stability performance for all analyzed geometries.

6.2.1 BASIC STEP

To give greater immediacy to the assessments on the comparison between the simulated geometries and those experienced thought to proceed in this way:

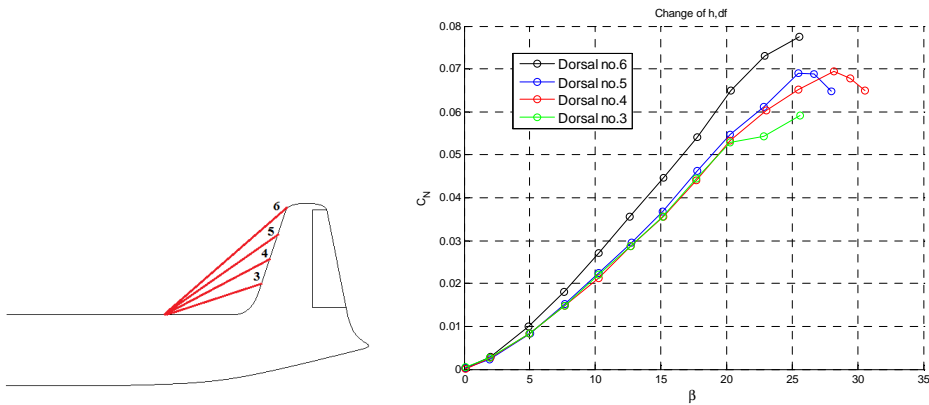
1. I identified the set of dorsal fins for which there is variation in a single geometric parameter
2. I refined this parameter as a variable parameterization
3. I digitized curves of the report and to divide the various sets of dorsal fins
4. I realized different dorsal fins from the reference geometry getting parameterization
5. I summarized the results of the simulations
6. I compared the simulation results with those of the literature [4]

6.3 PARAMETRIC ANALYSIS EXTRACTION FROM THE REPORT INFORMATION

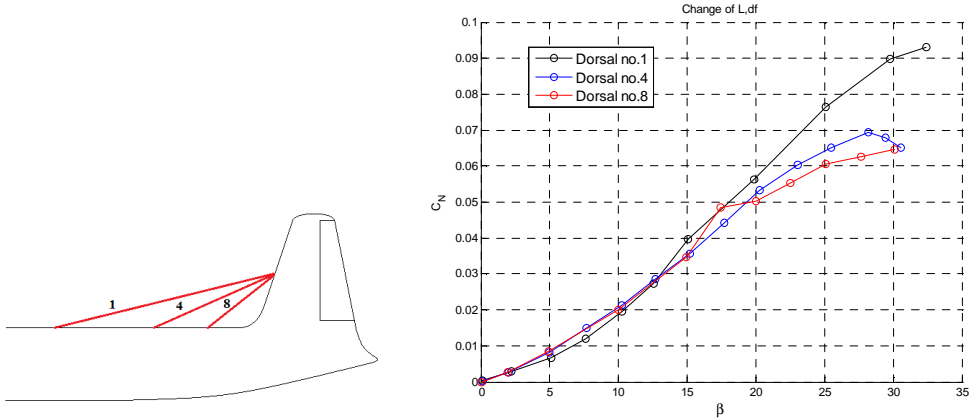
From the study of the "Report" which we discussed earlier, it was possible to identify four types of parameterizations.

- 1) *Change of h,df.*
- 2) *Change of L,df.*
- 3) *Change of L,df & h df, to keep constant arrow and vary the surface.*
- 4) *Change of L,df & h df, to keep surface constant and vary the sweep angle.*

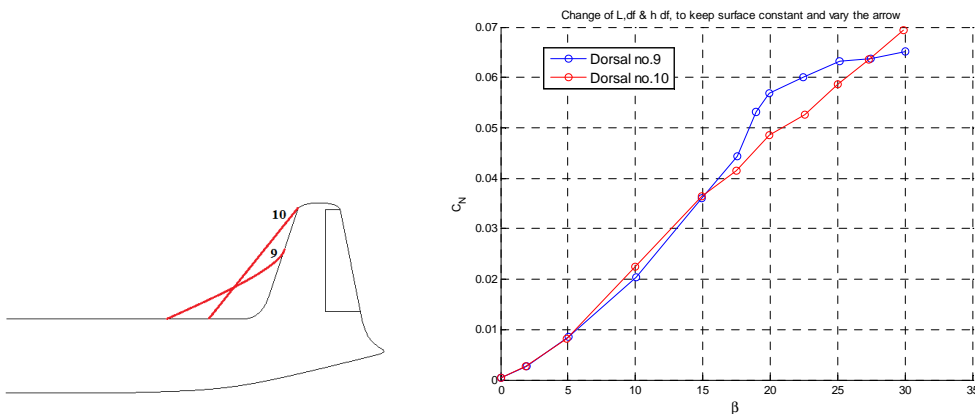
1) Dorsal no. 6, 5, 4, 3 [**h,df** is varying which decreases from no.6 to no.3] :



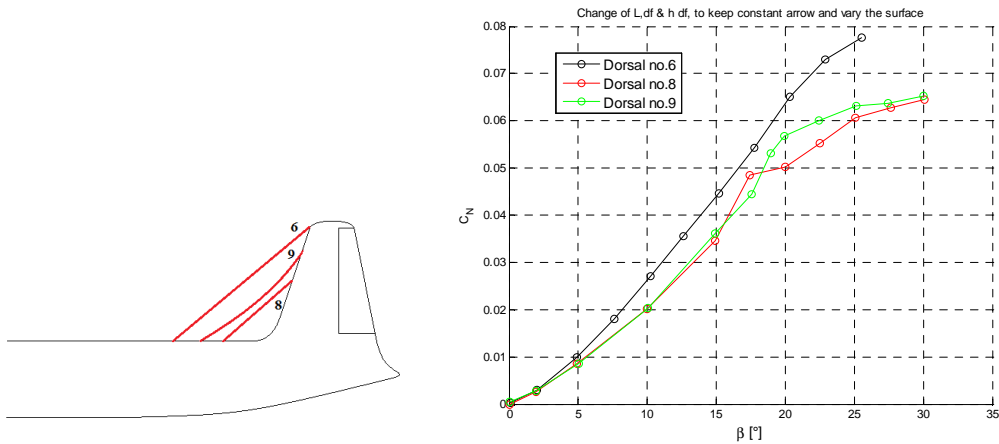
2) Dorsal no. 1, 4, 8 [**L,df** is varying which decreases from no.1 to no.8] :



3) Dorsal no. 9, 10 [**φ_o,df** is varying which increases from no.9 to no.10] :



4) Dorsal no. 8, 9, 6 [S_{df} is varying which increases from the no.8 no.6] :



We specify at this point in the discussion that the report does not quantify the geometry of reference in terms of size, therefore using the figure in which are summarized all the dorsal, we can figure out which parameters are varying but obviously we can't understand precisely how in absolute terms because it does not have geometries listed.

This does not change our approach to the problem that is qualitative, moreover, as detailed above, our objective is to compare the trends, so we still can extract the results and proceed with the comparison.

6.4 GEOMETRIC CONTROL OF PARAMETERIZATION

The first step was to create a routine that would allow me to easily control the geometry of the dorsal fin starting from fixed parameters related to the vertical tail, using input parameters depending on the chosen configuration and determining output parameters as a result of trigonometric relationships of obtained triangles.

Change of h,df						
$S_{v} [m^2]$	$b_{v} [m]$	$S_{df} [m^2]$	$\varphi_{o,v} [^\circ]$	$\varphi_{i_o,df} [^\circ]$	$h_{fd} [m]$	$L_{df} [m]$
0,0395	0.2434	0,01244	26,6	77,07	0,0756	0,329
L_{v-df}/L_{df}	h_{df}/b_{v}	$Cr_{fd} [m]$	$Cr_{v} [m]$	L_{df}/Cr_{v}	L_{df}/h_{df}	S_{df}/S_{v}
0,115	0.310	0,291	0,200	1,645	4,352	0,31487
Input		L1	L2	L Original	L3	L4
L.df (star)		0,15	0,200	0,2490278	0,3	0,35

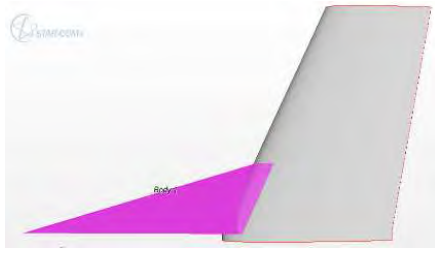
Table 5 –Routine to control the geometric variation of all parameters.

This routine is simply based on the trigonometric relations of construction triangles and lets we know instantly to changing a parameter as change other parameters and some characteristic ratios to control the problem.

For each parameterization, I started setting for the reference geometry:

- what I'm changing,
- how much I'm changing it,
- how many times I'm doing it.

Reference Geometry:



h,v [m]	S,v [m²]	S,df [m²]	φ_o,v [°]
0.2434	0.040	0.012	26.600
φ_o,df [°]	h,fd [m]	L,df [m]	L,df/Cr,v_mean
77.065	0.0756	0.329	1.992
Lv-df	Lv-df/ L,df	Cr,fd [m]	Cr,v [m]
0.0378	0.1150	0.291	0.2
Ldf/Cr,v	L,df/h,df	S,df/S,v	Δ AR
1.645	4.352	0.314	-31%

Figure 149 – Reference Geometry, viewing and its characteristics value.

6.5 AERODYNAMIC RESULT OF PARAMETERIZATIONS

For each one of these parameterizations we show the comparison between the individual CN contributions of each geometry and, depending on our necessity, some curve related to the partial configuration.

That allows to evaluate in a detailed manner what happens from the performance point of view by varying the geometry. Depending on the considered parameterizations, it will be possible to extract different conclusions.

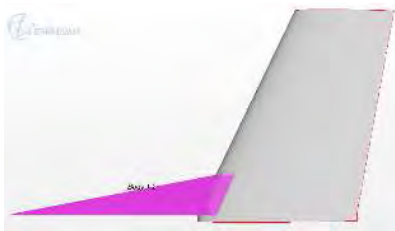
We have to specify at this point that for each parameterization the parameter changing will be done keeping the same percentage difference between two successive geometries.

6.5.1 CHANGE OF h,df

I list below the analyzed dorsal for this parameterization flanking each image whit a summary table of the geometric parameters resulting.

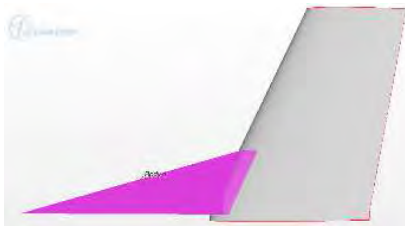
In red there is the parameter that we are changing for this specific parameterization, and in blue there is the considered parameter to distinguish one from the other, i.e. that one specified in the legend of the following graphs.

No.1)



h,v [m]	S,v [m²]	S,df [m²]	φ_o,v [°]
0.243	0.040	0.012	26.600
φ_o,df [°]	h,fd [m]	L,df [m]	L,df/Cr,v_mean
81.706	0.048	0.329	1.992
Lv-df	Lv-df/ L,df	Cr,fd	Cr,v
0.024	0.073	0.305	0.200
h,df/h,v	L,df/h,df	S,df/S,v	Δ AR
0.197	6.855	0.200	-20%

No.2)



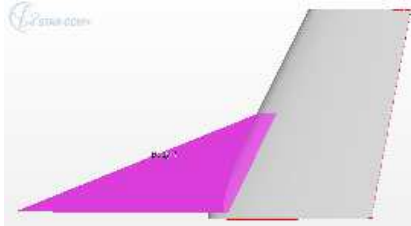
h,v [m]	S,v [m²]	S,df [m²]	φ_o,v [°]
0.243	0.040	0.012	26.600
φ_o,df [°]	h,fd [m]	L,df [m]	L,df/Cr,v_mean
77.065	0.075	0.329	1.992
Lv-df	Lv-df/ L,df	Cr,fd	Cr,v
0.037	0.115	0.291	0.2
h,df/h,v	L,df/h,df	S,df/S,v	Δ AR
0.311	4.352	0.314	-31%

No.3)



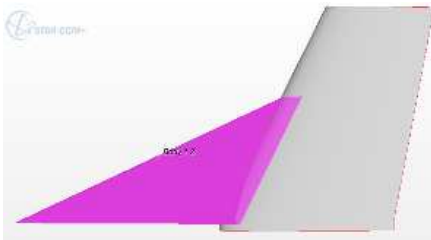
h,v [m]	S,v [m²]	S,df [m²]	φ_o,v [°]
0.243	0.040	0.016	26.600
φ_o,df [°]	h,fd [m]	L,df [m]	L,df/Cr,v_mean
73.740	0.096	0.329	1.992
Lv-df	Lv-df/ L,df	Cr,fd	Cr,v
0.048	0.146	0.281	0.200
h,df/h,v	L,df/h,df	S,df/S,v	Δ AR
0.394	3.427	0.400	-40%

No.4)



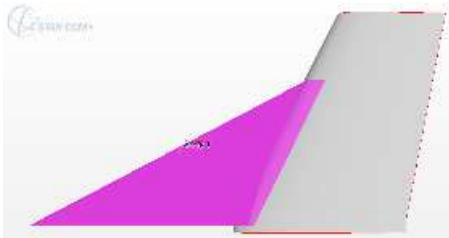
h,v [m]	S,v [m²]	S,df [m²]	φ_o,v [°]
0.243	0.040	0.020	26.600
φ_o,df [°]	h,fd [m]	L,df [m]	L,df/Cr,v_mean
69.968	0.120	0.329	1.992
Lv-df	Lv-df/ L,df	Cr,fd	Cr,v
0.060	0.183	0.269	0.200
h,df/h,v	L,df/h,df	S,df/S,v	Δ AR
0.493	2.742	0.500	-50%

No.5)



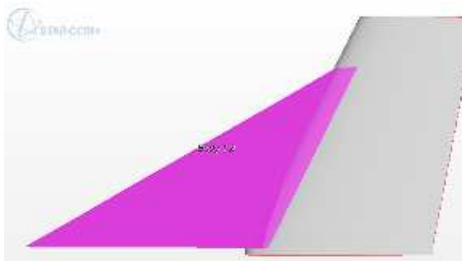
h,v [m]	S,v [m²]	S,df [m²]	φ_o,v [°]
0.243	0.040	0.024	26.600
φ_o,df [°]	h,fd [m]	L,df [m]	L,df/Cr,v_mean
66.368	0.144	0.329	1.922
Lv-df	Lv-df/ L,df	Cr,fd	Cr,v
0.072	0.219	0.257	0.200
h,df/h,v	L,df/h,df	S,df/S,v	Δ AR
0.592	2.285	0.600	-60%

No.6)



h,v [m]	S,v [m²]	S,df [m²]	φ_o,v [°]
0.243	0.040	0.028	26.600
φ_o,df [°]	h,fd [m]	L,df [m]	L,df/Cr,v_mean
62.956	0.168	0.329	1.992
Lv-df	Lv-df/ L,df	Cr,fd	Cr,v
0.084	0.256	0.245	0.200
h,df/h,v	L,df/h,df	S,df/S,v	Δ AR
0.690	1.958	0.700	-70%

No.7)



h,v [m]	S,v [m²]	S,df [m²]	φ_o,v [°]
0.243	0.040	0.032	26.600
φ_o,df [°]	h,fd [m]	L,df [m]	L,df/Cr,v_mean
59.739	0.192	0.329	1.992
Lv-df	Lv-df/ L,df	Cr,fd	Cr,v
0.096	0.292	0.233	0.200
h,df/h,v	L,df/h,df	S,df/S,v	Δ AR
0.789	1.714	0.800	-80%

Figure 150 – h,df parameterization, geometry viewing characteristic values.

In the Following graphs the curves are distinguished according to the value of the ratio between h,df and vertical plane aperture h,v.

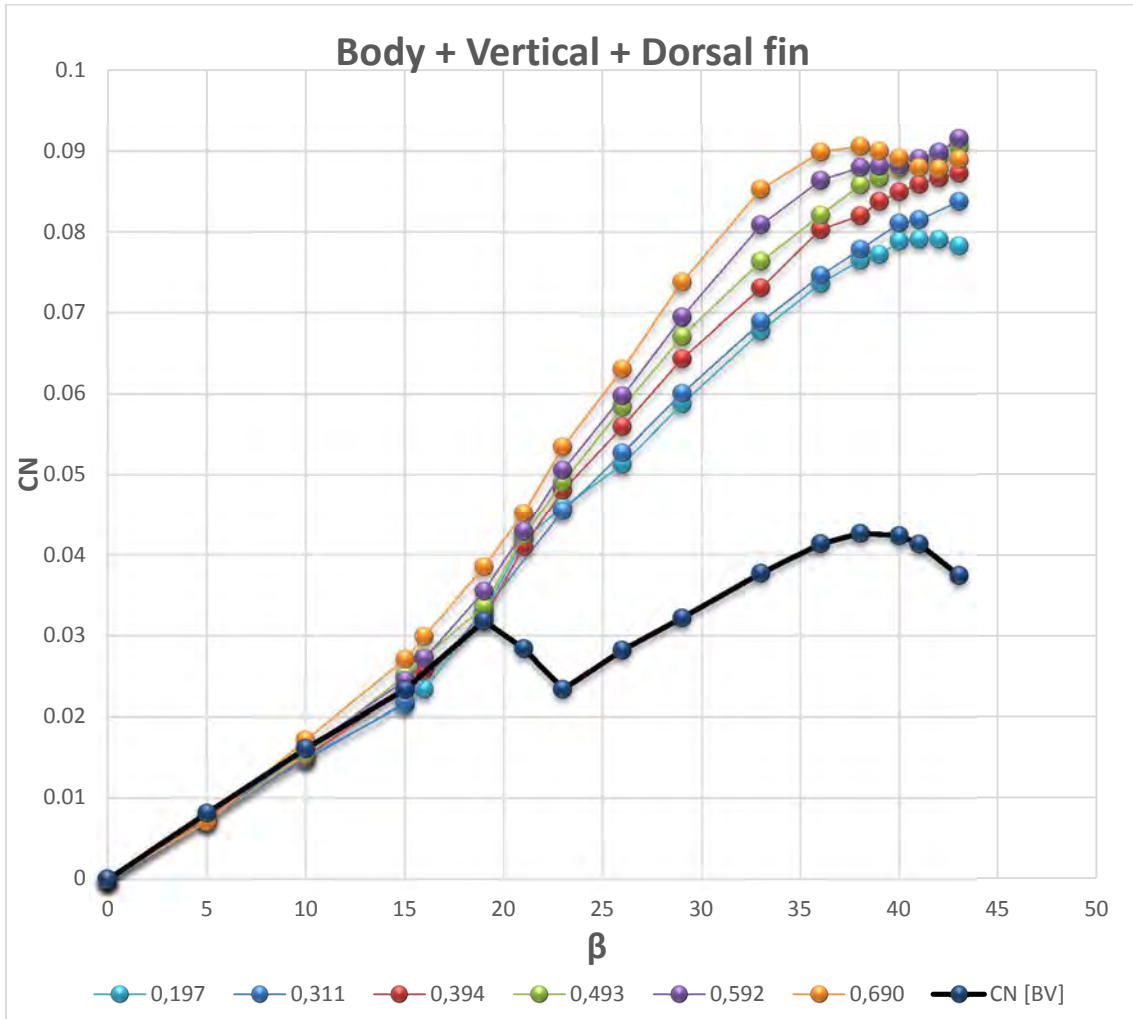


Figure 151 – Yawing moment coefficient of total contribution of BVD configuration.

As shown in Figure 151, the trends in the linear range show a strong correspondence to all the curves until the value 0.493, beyond which the slope increases with increasing height.

The trends in the non-linear range show a CN increase, quite proportional to the increase in height, in fact, the curves seem almost equally spaced. It results in a reduction of the angle of stall increasing height. We also note a difference in behavior between the dorsal with height greater than 0.43, for which exceeded the stall angle is again determined an increase in slope respect to the other for which the trend is monotonous increasing until the last corners

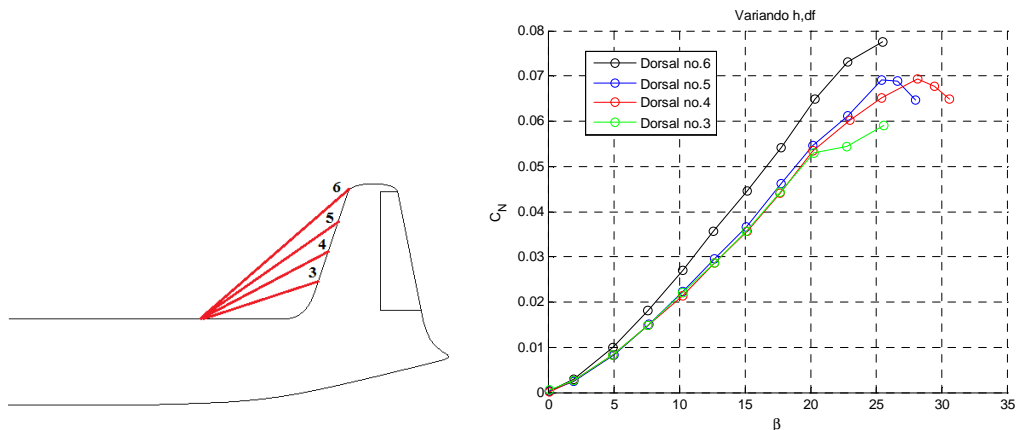


Figure 152 – Obert investigation results about Yawing moment coefficient.

There is a correspondence between the experimental and numerical data. Increasing h,df appears a slight increase of slope in the linear range and a strong increase in the range nonlinear.

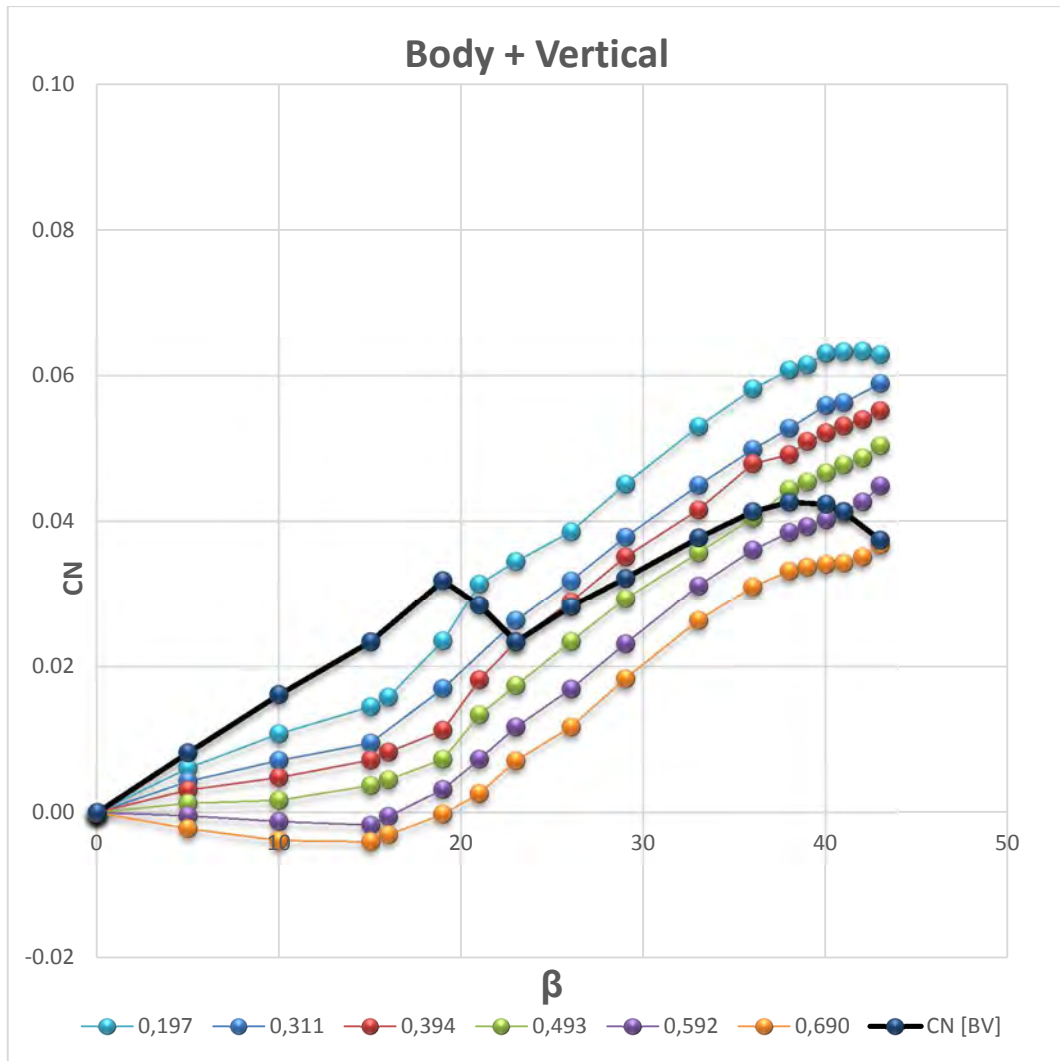


Figure 153 – Yawing moment coefficient of Body + Vertical contribution of BVD configuration.

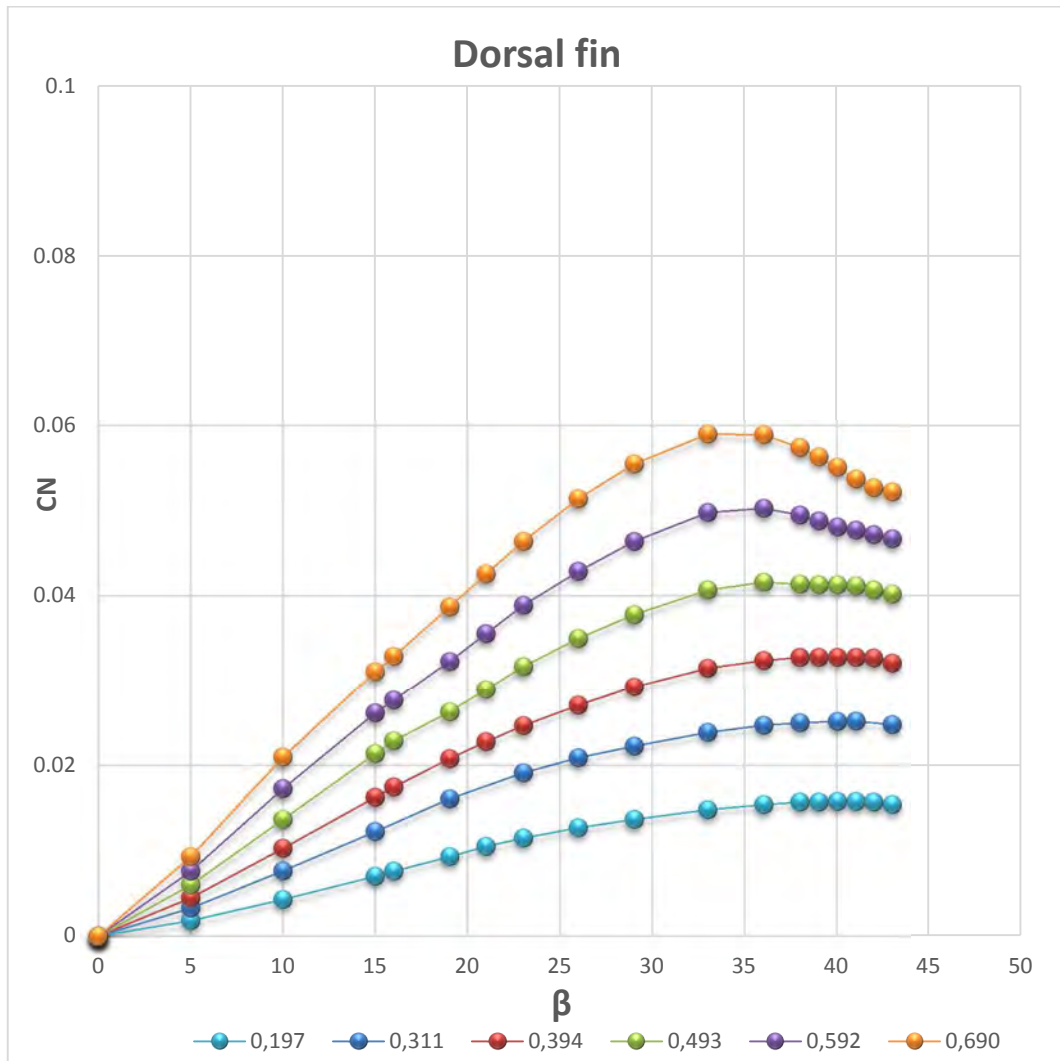


Figure 154 – Yawing moment coefficient of Dorsal fin contribution of BVD configuration.

Increasing the height there is a larger growing of the work of the dorsal. For the Dorsal greater than 0.394 we note a slightly decrease of the stall angle by increasing height.

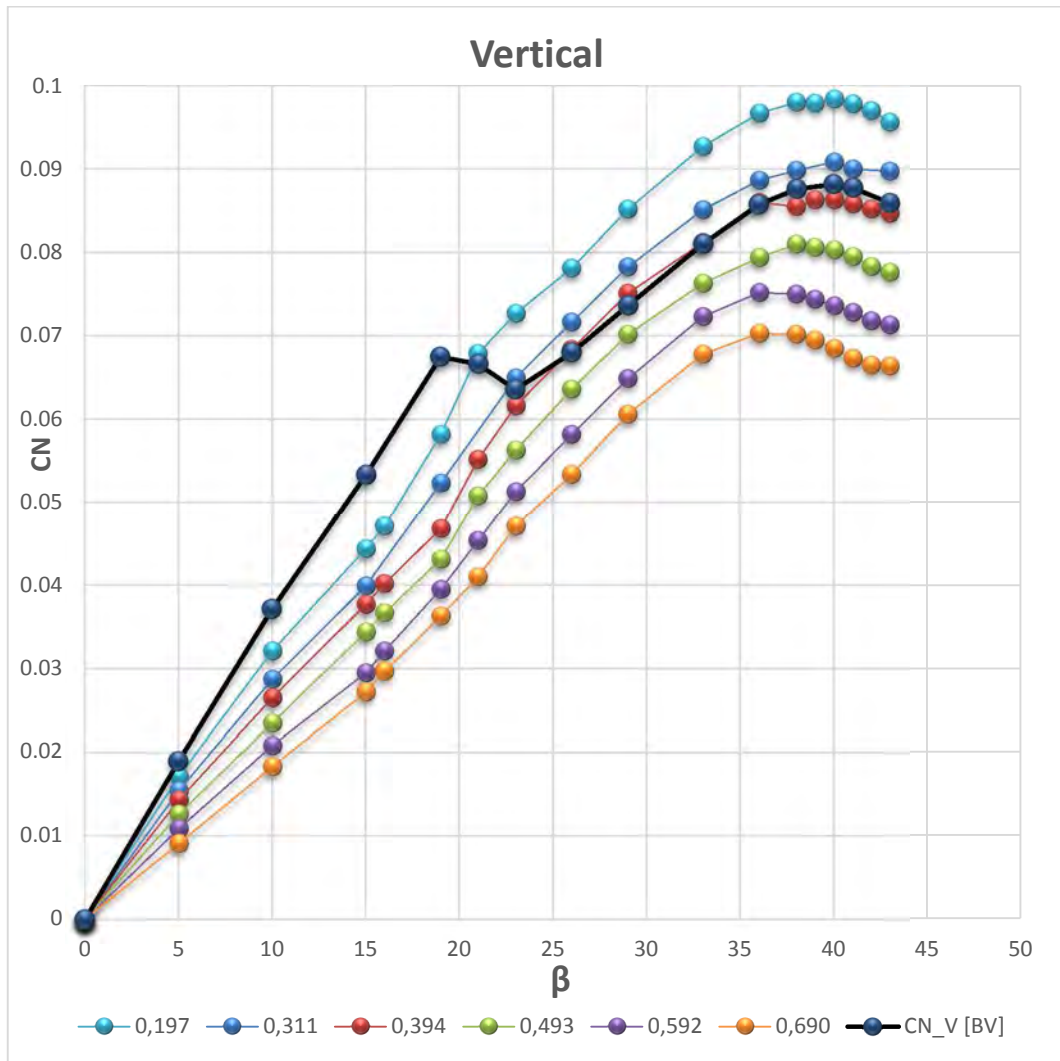


Figure 155 – Yawing moment coefficient of Vertical contribution of BVD configuration.

Increasing the height there is a reduction increasingly strong of the Vertical plane work

We start from the BASELINE phenomena to evaluate the characteristic aspects of this parameterization.

Dorsal Fin primary effect on the vertical tail stability

We compare the graph that relates the contribution of vertical, in BV configuration, with the curve of the Vertical + Dorsal contribution in BVD configuration;

This chart expresses the Dorsal effect on the vertical empennage:

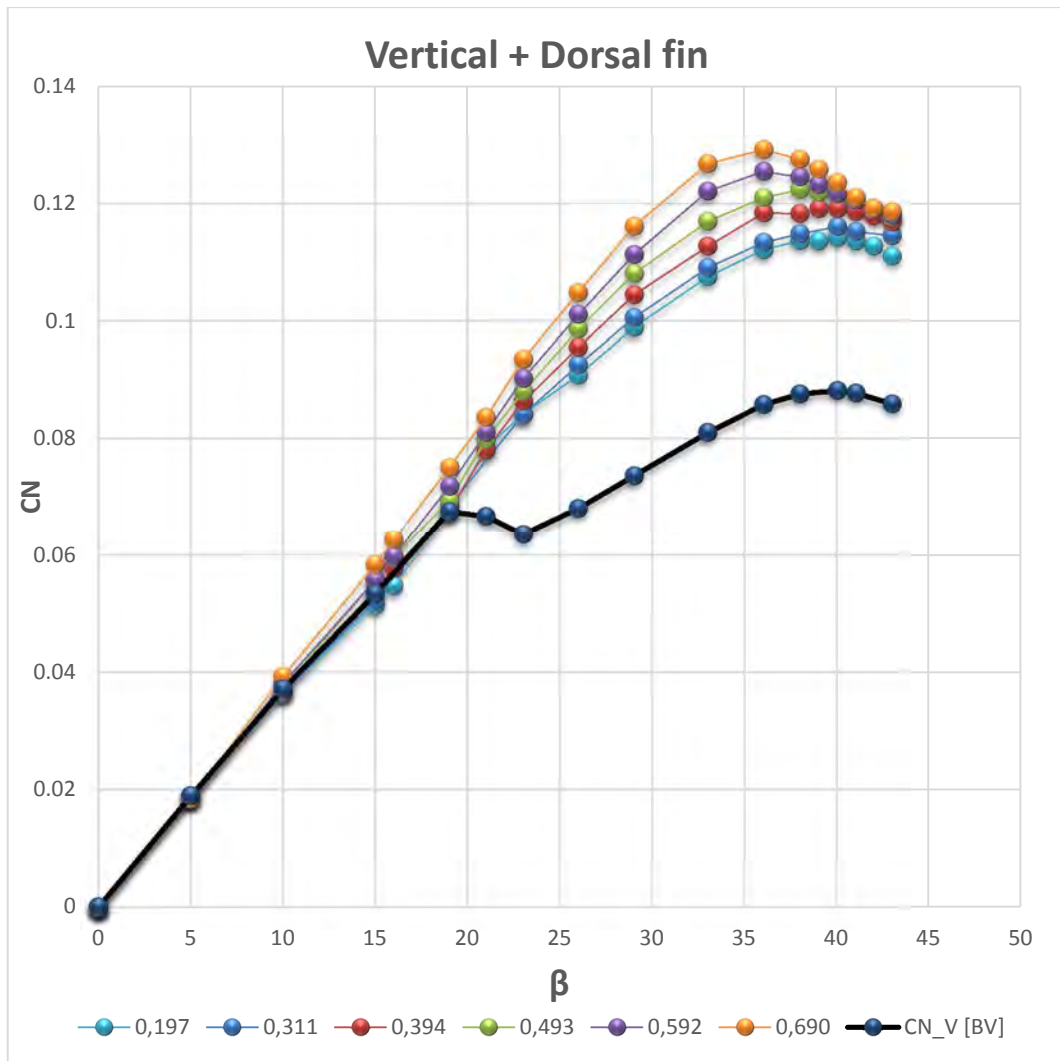


Figure 156 – Yawing moment coefficient of Vertical + Dorsal fin contribution of BVD configuration.

The trends in the linear range, are overlapped for the different dorsal fin, but for those with greater height, exceeded 10° is found a slight increase in slope than the other. It means that what is added by the presence of the dorsal fin is greater than, that which is subtracted from the vertical.

The trends in non-linear range for the different dorsal fin show how increasing the height there is an increase of the maximum achievable CN, and a reduction of the angle of stall.

Dorsal fin effect on the fuselage stability.

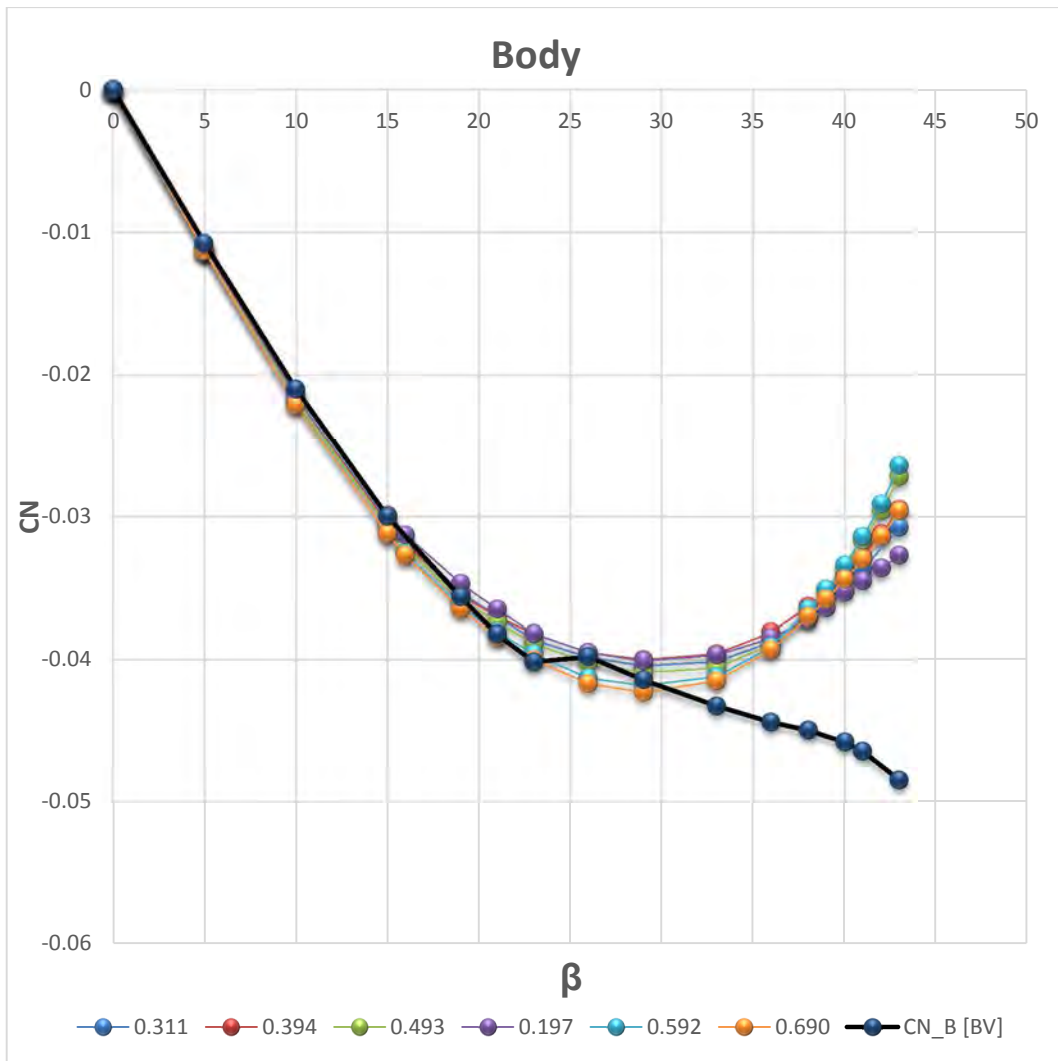


Figure 157 – Yawing moment coefficient of Body contribution of BVD configuration.

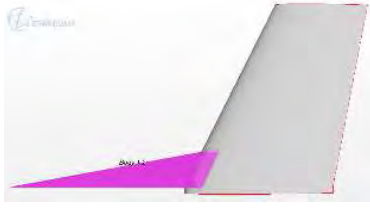
It is clearly seen that the effect of dorsal fin is obtained for angles greater than 15/20°, providing a stabilizing contribution that makes the curve with positive derivative. We should note that varying this parameter the geometry of the dorsal fin is modified increasing the surface area of the upper part of the dorsal fin. In fact we can see that the contribution of the fuselage between the various dorsal is very similar. It is further noted that while in the range between 20° and 35° growing the height there is an increase in the absolute value of the contribution of the fuselage, exceeded 35 ° we can't find this unique correspondence, because increasing the height there is initially a rise of slope but exceeded the value 0.59 there is a reduction of the slope.

Dorsal Fin primary effect on the overall stability

We analyze the curve of the total CN for BV configuration with the curve of total CN of BVD configuration. Compared to the previous case concerning the effect on the vertical tail now there is a difference equal to the unstable fuselage contribution that reduce these curves.

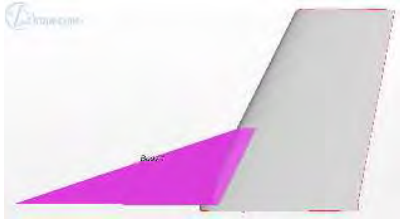
We can show how to subtract the fuselage contributions for two dorsal representing +30% and -30% of dorsal surface respect to the dorsal reference. (Dorsal no.1 & no.3) It means that we are comparing the body effect for 60% of dorsal surface variation.

No.1) $\Delta h,df$ [$\Delta S,df + 30\%$]



h,v [m]	S,v [m^2]	S,df [m^2]	$\phi_{o,v}$ [$^\circ$]
0.243	0.040	0.012	26.600
$\phi_{o,df}$ [$^\circ$]	h,fd [m]	L,df [m]	$L,df/Cr,v_{mean}$
81.706	0.048	0.329	1.992
$Lv-df$	$Lv-df/L,df$	Cr,fd	Cr,v
0.024	0.073	0.305	0.200
$h,df/h,v$	$L,df/h,df$	$S,df/S,v$	ΔAR
0.197	6.855	0.200	-20%

No.2) $\Delta h,df$ [$\Delta S,df - 30\%$]



h,v [m]	S,v [m^2]	S,df [m^2]	$\phi_{o,v}$ [$^\circ$]
0.243	0.040	0.016	26.600
$\phi_{o,df}$ [$^\circ$]	h,fd [m]	L,df [m]	$L,df/Cr,v_{mean}$
73.740	0.096	0.329	1.992
$Lv-df$	$Lv-df/L,df$	Cr,fd	Cr,v
0.048	0.146	0.281	0.200
$h,df/h,v$	$L,df/h,df$	$S,df/S,v$	ΔAR
0.394	3.427	0.400	-40%

Figure 158 – h,df parameterization, geometry viewing characteristic values.

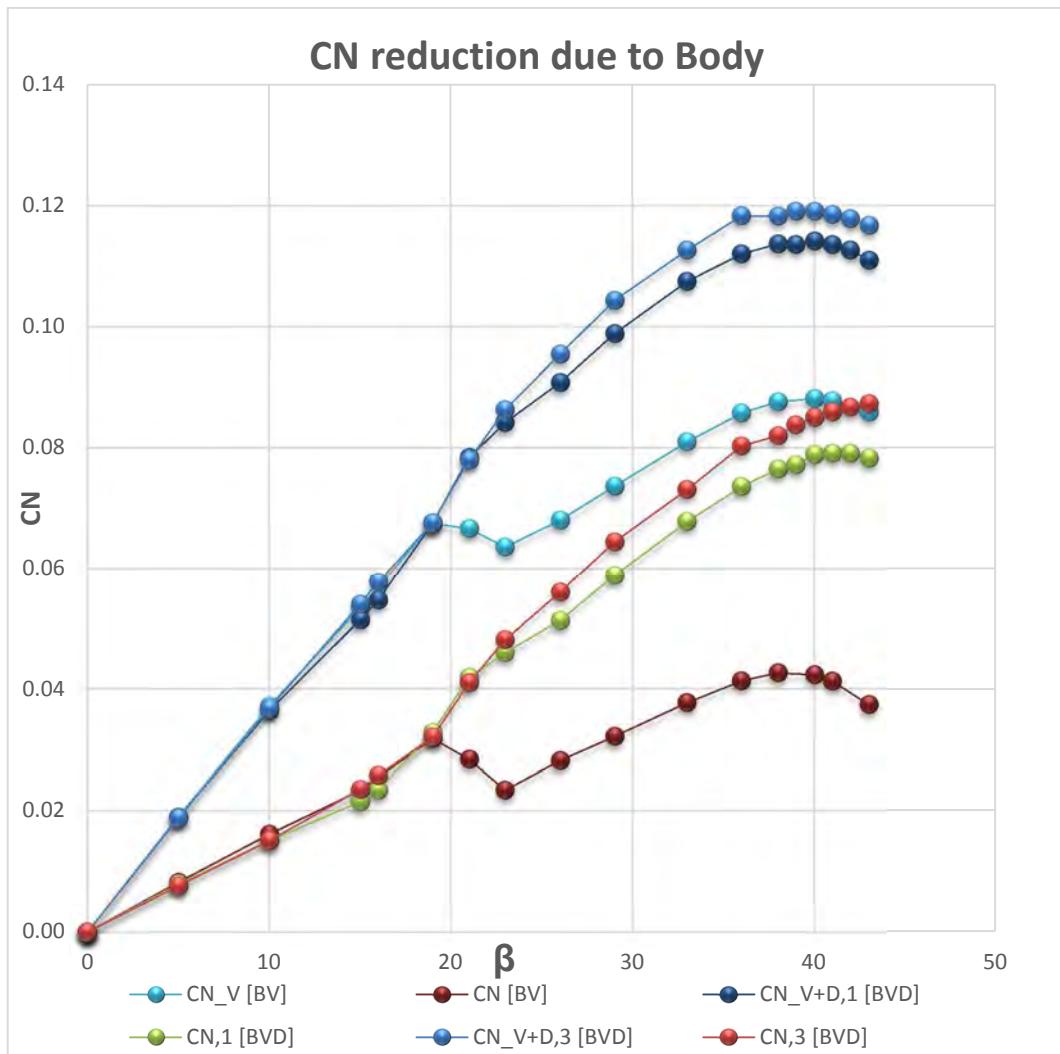


Figure 159 – Yawing moment coefficient reduction due to Body contribution for Dorsal no.1 & Dorsal no.3 of BVD configuration.

In particular greater reduction for the curve relative to BV configuration (for which the contribution of the fuselage is greater in absolute value), and a lower reduction for the curve relating to the BVD configuration (for which the fuselage contribution is lower in absolute value due the dorsal fin as mentioned above)

We propose as done in chapter 5 the concept of contribution redistribution

Again, we show how are the contributions redistribution of two configuration with dorsal representing +30% and - 30% of dorsal surface, compared to the dorsal reference. (Dorsal no.1 & no.3). It means that we are comparing the effects for 60% of dorsal surface variation by changing h,df.

Using the Figure 160 we can see how add up the contributions of Dorsal and Vertical to get Dorsal + Vertical and their relevance in terms of stability increase.

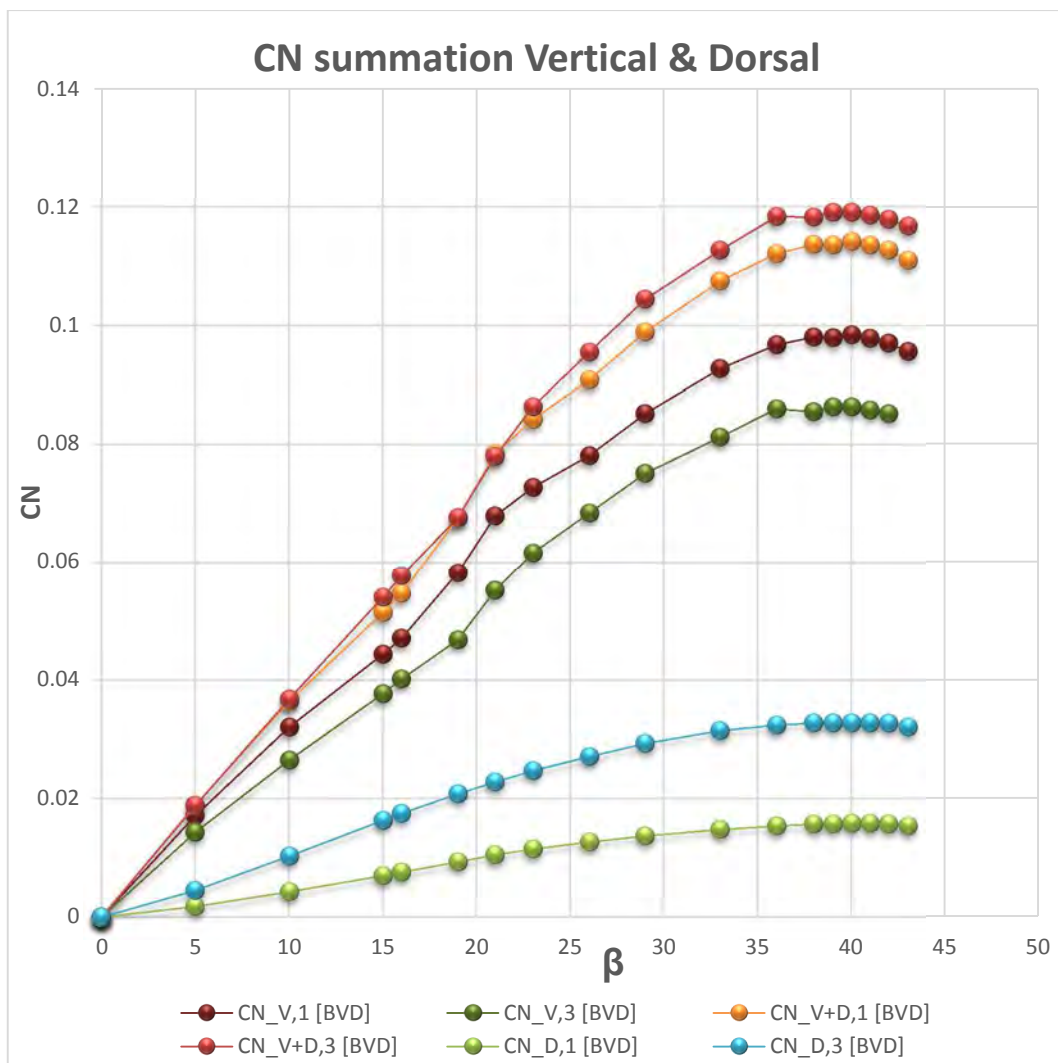


Figure 160 – Yawing moment coefficient of Vertical + Dorsal summation for Dorsal no.1 & Dorsal no.3 of BVD configuration.

The aspect that interests us is to understand what phenomenology is behind the ineffectiveness of the dorsal fin in the linear range, i.e. that there is an almost perfect correspondence between the curves of Vertical in BV configuration and of Vertical + Dorsal in BVD configuration, as show in Figure 161.

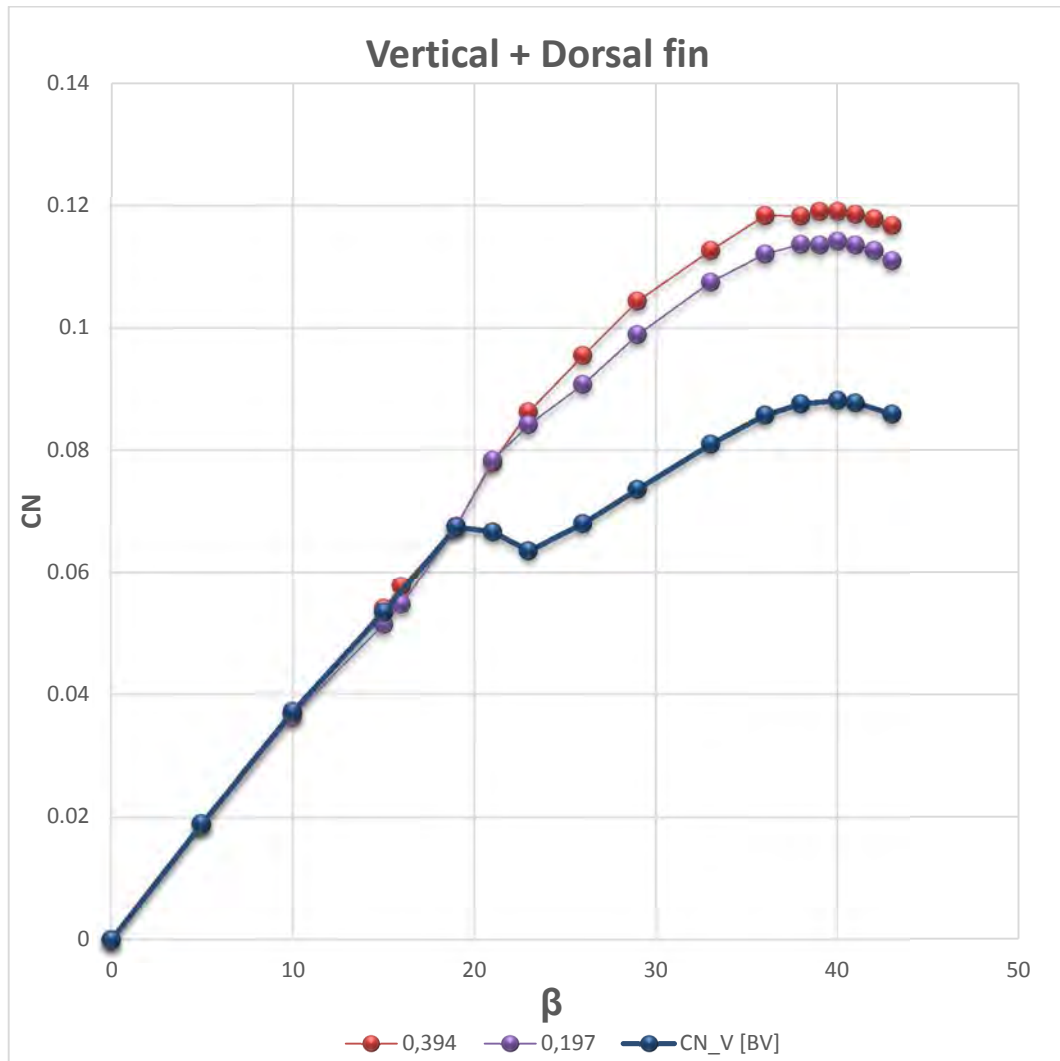


Figure 161 – Yawing moment coefficient coincidence between Vertical + Dorsal summation of BVD configuration and Vertical contribution of BV configuration for Dorsal no.1 & Dorsal no.3.

Again it may seem strange that, however is an area addition which intervenes in the aerodynamics. So with a larger area should be increased at least the slope in linear range.

Actually happens that with the addition of the dorsal, the vertical work less as explained in chapter 5. In Figure 162 there is the comparison between the curve of vertical in BV configuration and of the vertical in BVD configurations. We can evaluate for this parameterization the reduction of work of the vertical concern the + 60 % of dorsal fin surface variation by changing h,df.

We see that the vertical tail, working less and less in proportion to the increase of the dorsal fin height. This proportionality is maintained both in the linear regime that in the nonlinear regime. There is a difference of slope because we are neglecting the contribution of the dorsal fin that would bring the two gradients to coincide (see figure 162 & 160).

These graphs make it possible to identify for example optimum geometry between those analyzed for a particular stability performance.

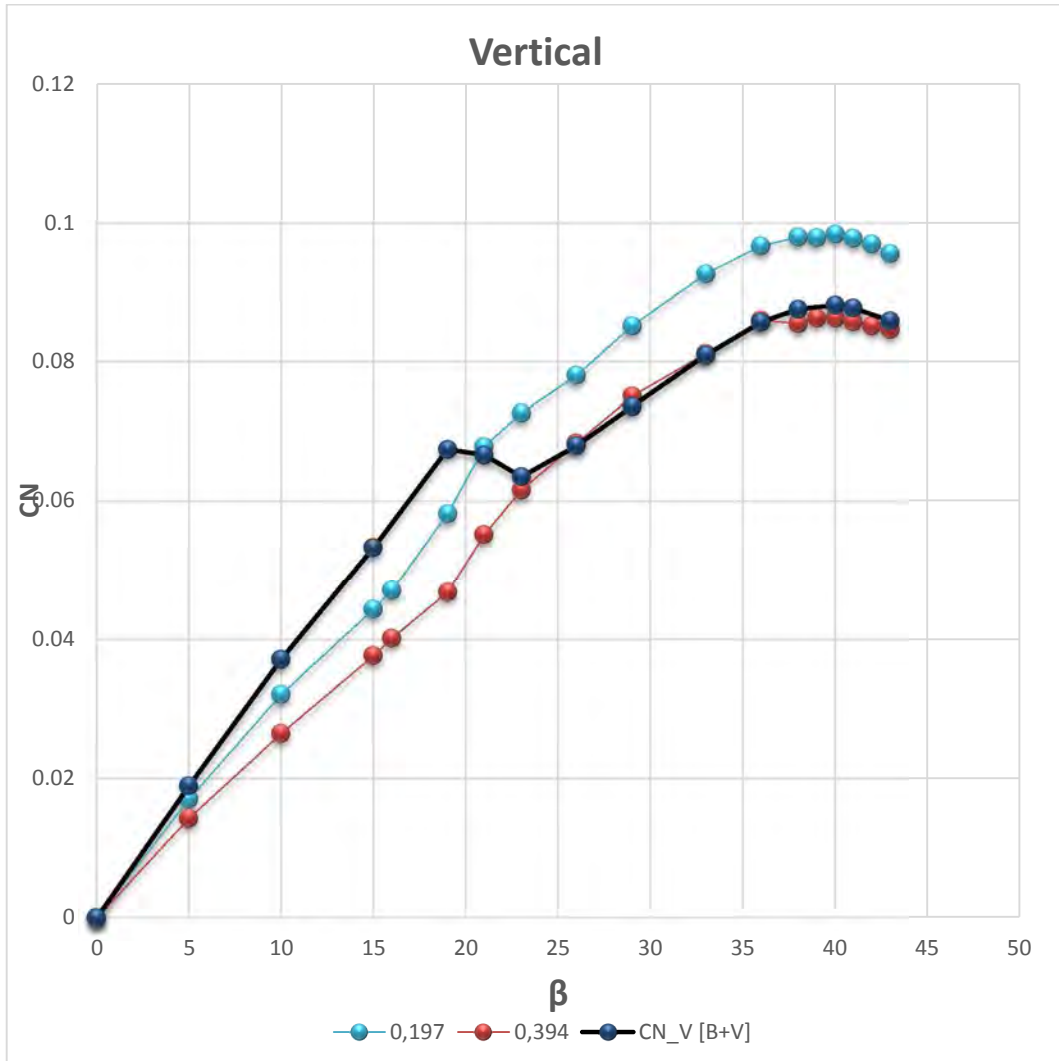
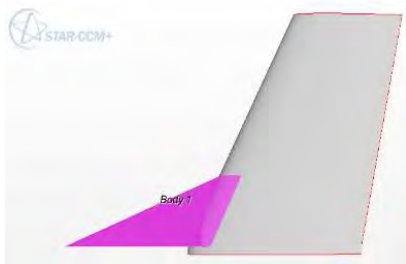


Figure 162 – How the vertical work less in BVD configuration with respect the Vertical contribution of BV configuration for Dorsal no.1 & Dorsal no.3.

6.5.2 CHANGE OF L, df

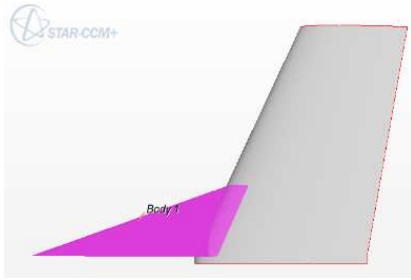
I list below the analyzed dorsal for this parameterization flanking each image whit a summary table of the geometric parameters resulting. In red is the parameter that we are changing for this specific parameterization, and in blue is the considered parameter to distinguish one from the other, i.e., that one specified in the legend of the following graphs.

No.1)



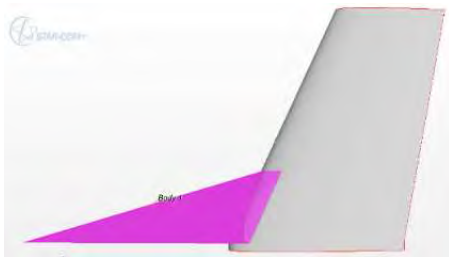
h,v [m]	S,v [m²]	S,df [m²]	$\phi_{o,v}$ [°]
0.2434	0.040	0.009	26.600
$\phi_{o,df}$ [°]	h,fd [m]	L,df [m]	L,df/Cr,v_mean
71.810	0.076	0.230	1.392
Lv-df	Lv-df/L,df	Cr,fd	Cr,v
0.038	0.165	0.192	0.200
Ldf/Cr,v	L,df/h,df	S,df/S,v	Δ AR
1.150	3.042	0.220	-22%

No.2)



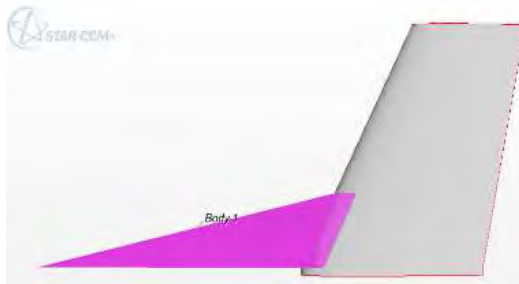
h,v [m]	S,v [m ²]	S,df [m ²]	φ _{o,v} [°]
0.2434	0.040	0.011	26.600
φ _{o,df} [°]	h,fd [m]	L,df [m]	L,df/Cr,v _{mean}
74.896	0.076	0.280	1.695
Lv-df	Lv-df/ L,df	Cr,fd	Cr,v
0.038	0.135	0.242	0.200
Ldf/Cr,v	L,df/h,df	S,df/S,v	Δ AR
1.400	3.704	0.268	-26%

No.3)



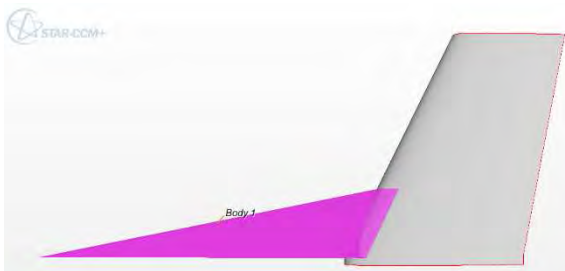
h,v [m]	S,v [m ²]	S,df [m ²]	φ _{o,v} [°]
0.2434	0.040	0.012	26.600
φ _{o,df} [°]	h,fd [m]	L,df [m]	L,df/Cr,v _{mean}
77.065	0.0756	0.329	1.992
Lv-df	Lv-df/ L,df	Cr,fd	Cr,v
0.0378	0.1150	0.291	0.2
Ldf/Cr,v	L,df/h,df	S,df/S,v	Δ AR
1.645	4.352	0.314	-31%

No.4)



h,v [m]	S,v [m ²]	S,df [m ²]	φ _{o,v} [°]
0.2434	0.040	0.014	26.600
φ _{o,df} [°]	h,fd [m]	L,df [m]	L,df/Cr,v _{mean}
78.754	0.076	0.380	2.300
Lv-df	Lv-df/ L,df	Cr,fd	Cr,v
0.038	0.100	0.342	0.200
Ldf/Cr,v	L,df/h,df	S,df/S,v	Δ AR
1.900	5.026	0.364	-36%

No.5)



h,v [m]	S,v [m ²]	S,df [m ²]	φ _{o,v} [°]
0.2434	0.040	0.016	26.600
φ _{o,df} [°]	h,fd [m]	L,df [m]	L,df/Cr,v _{mean}
80.034	0.076	0.430	2.603
Lv-df	Lv-df/ L,df	Cr,fd	Cr,v
0.038	0.088	0.392	0.200
Ldf/Cr,v	L,df/h,df	S,df/S,v	Δ AR
2.150	5.688	0.411	-41%

Figure 163 – L,df parameterization, geometry viewing characteristic values.

In the graphs the curves are distinguished according to the value of the ratio between L,df and the mean aerodynamic chord vertical plane (V_{m.a.c.}).

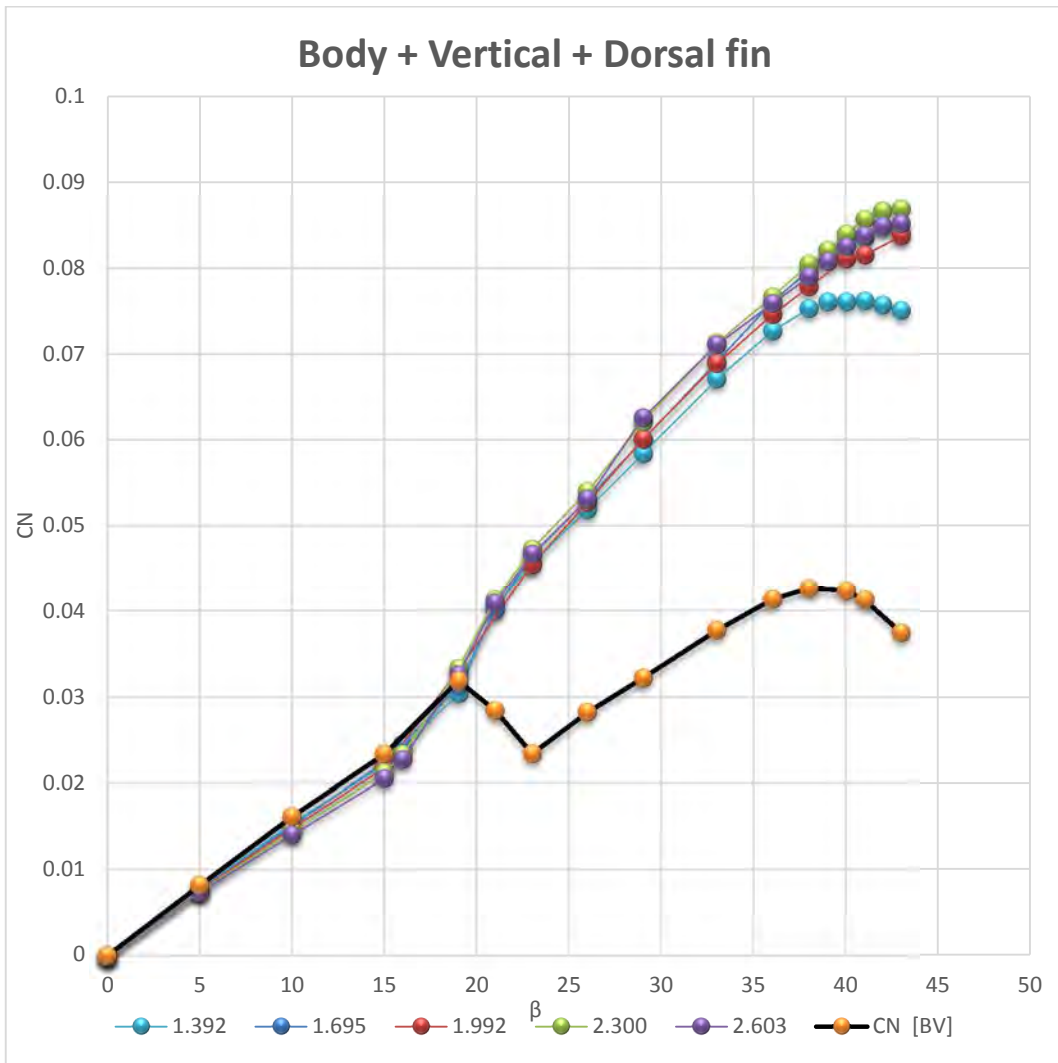


Figure 164 – Yawing moment coefficient of total contribution of BVD configuration.

As shown in Figure 164, trends in the linear range show a strong match for all curves. In general, a slight decrease in slope is observed as the length of the dorsal fin increases. The trends in the nonlinear range show an increase in the CN as the growing length increases until the value 2.3, beyond which we see a reduction. We can also notice that there is no difference in behavior between the various dorsal fins, unlike what happened with the previous parameterization. Just for the smaller dorsal fin, there is an anticipated angle-of-stall.

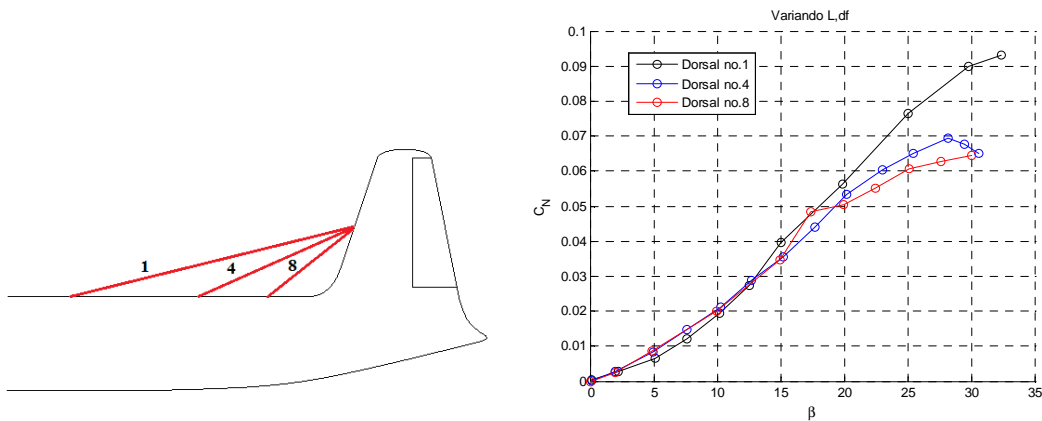


Figure 165 – Obert investigation results about Yawing moment coefficient.

There is a correspondence between the experimental and numerical data. Increasing L_{df} appears a slight reduction of slope in the linear range and a slight increase in the nonlinear range.

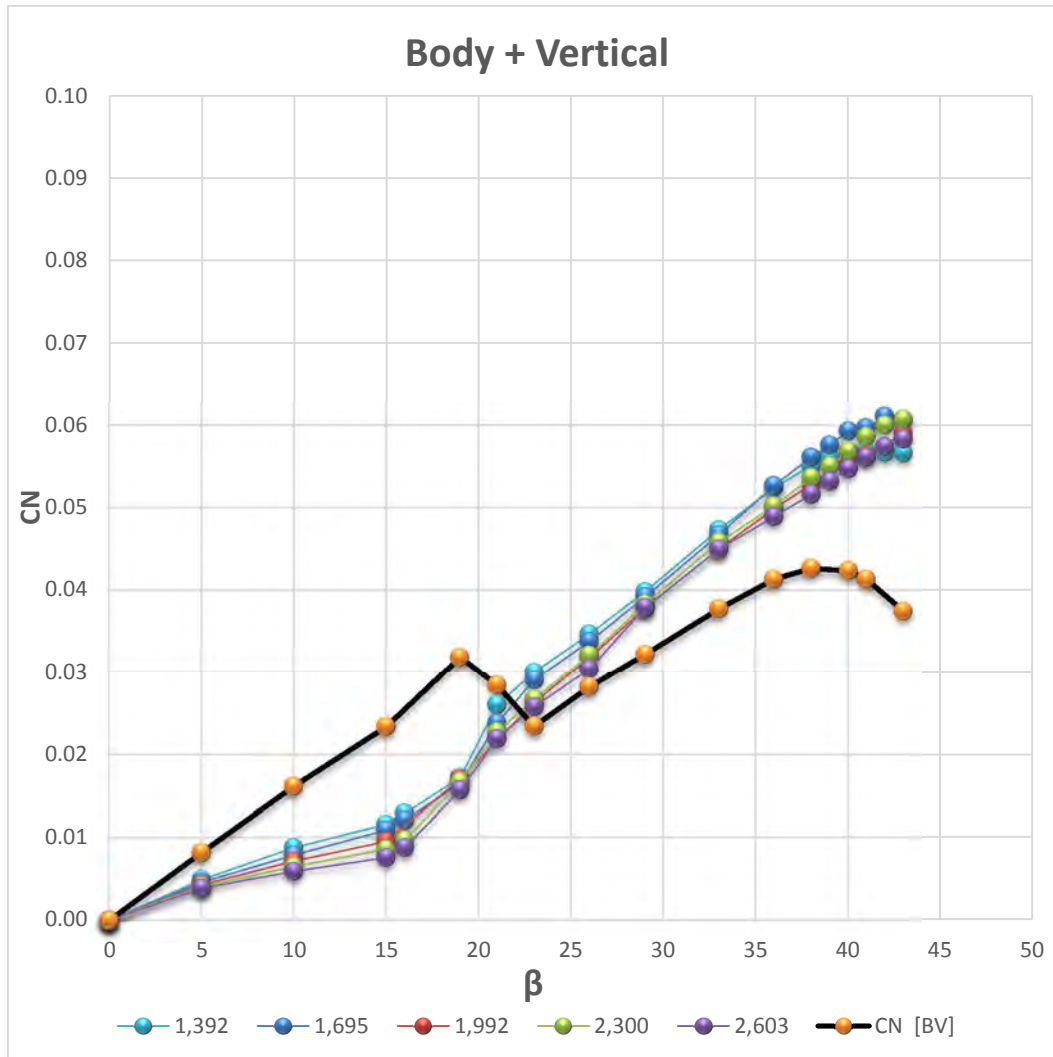


Figure 166 – Yawing moment coefficient of Body + Vertical contribution of BVD configuration.

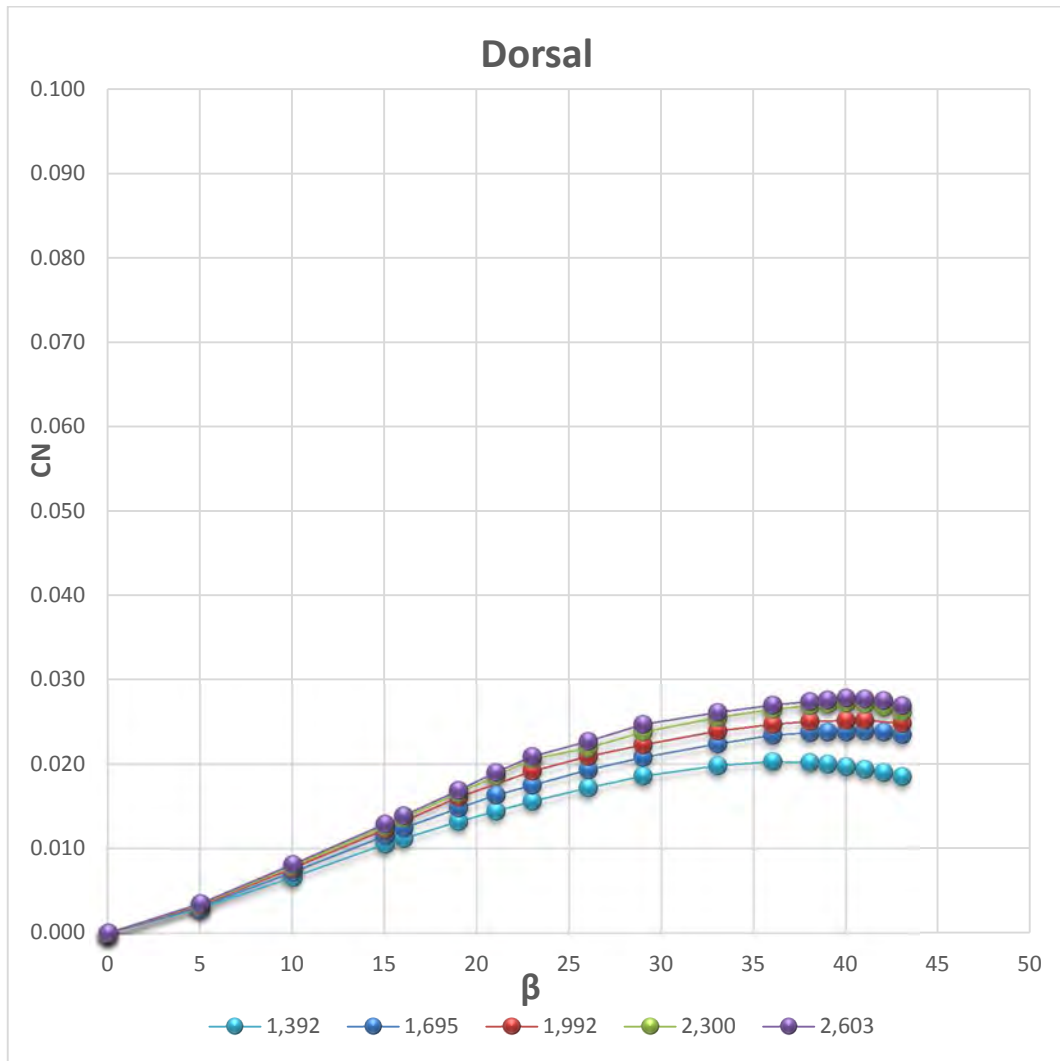


Figure 167 – Yawing moment coefficient of Dorsal fin contribution of BVD configuration.

Increasing the length there is a growing of the work of the dorsal. Compared to the previous parameterization this growing is very limited.

We see that for the smaller dorsal at high β presents a stall anticipated because it is so small that it is no longer able to release an intense vorticity.

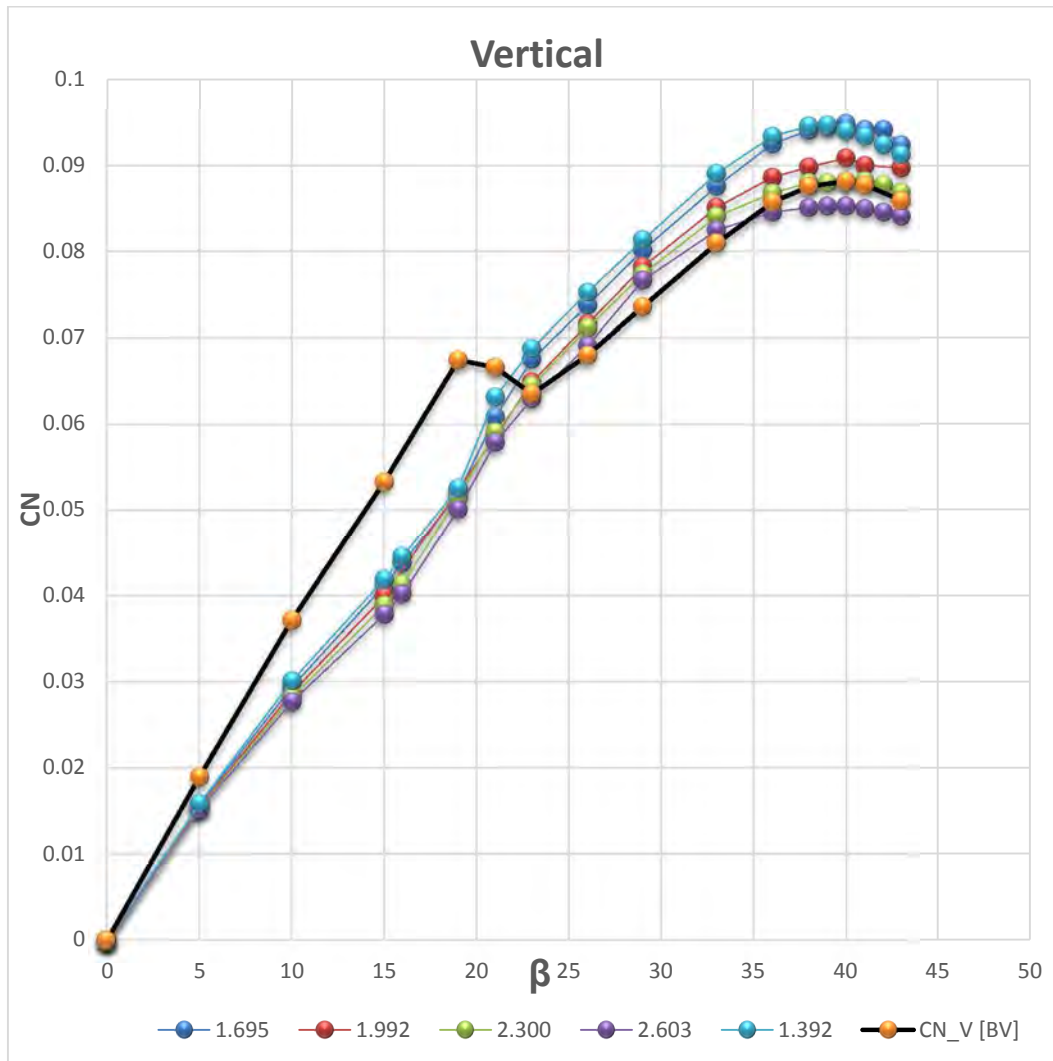


Figure 168 – Yawing moment coefficient of Body + Vertical contribution of BVD configuration.

Increasing the length there is a reduction of the work of the vertical. Compared to the previous parameterization this reduction is very limited.

We start from the phenomena of BASELINE to evaluate the characteristic aspects of this parameterization.

Dorsal Fin primary effect on the vertical tail stability

We compare the graph that relates the contribution of vertical, in BV configuration, with the curve of the vertical + Dorsal contribution in the BVD configuration;

This chart expresses the dorsal effect on the vertical empennage:

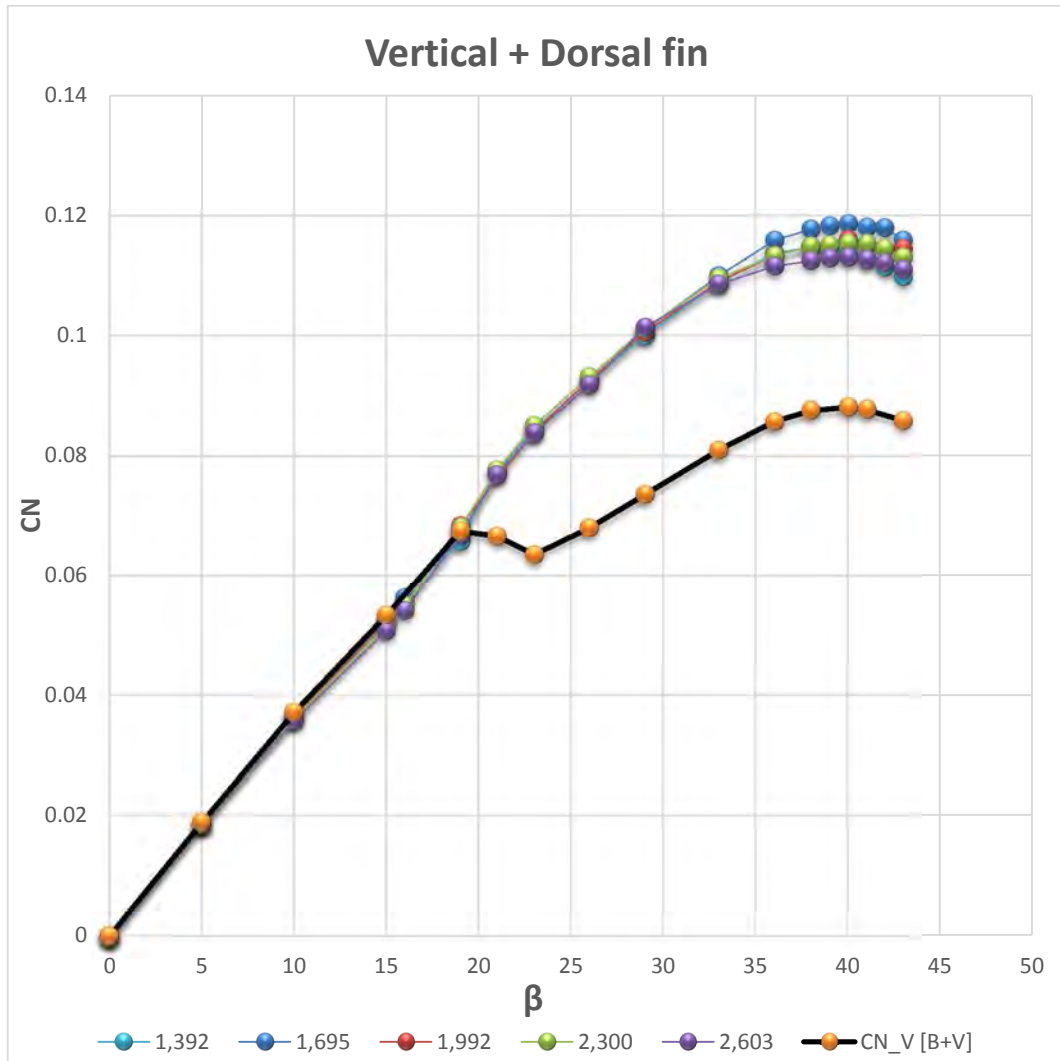


Figure 169 – Yawing moment coefficient of Vertical + Dorsal fin contribution of BVD configuration.

The trends in the linear range are overlapped for various dorsal fin. The trends in non-linear range for various dorsal fin differ only at angles greater than 35°. We see in particular that the longer dorsal has a slightly lower CN than the other. We can't extrapolate a unique reaction between behavior and increase in length.

Dorsal fin effect on the fuselage stability.

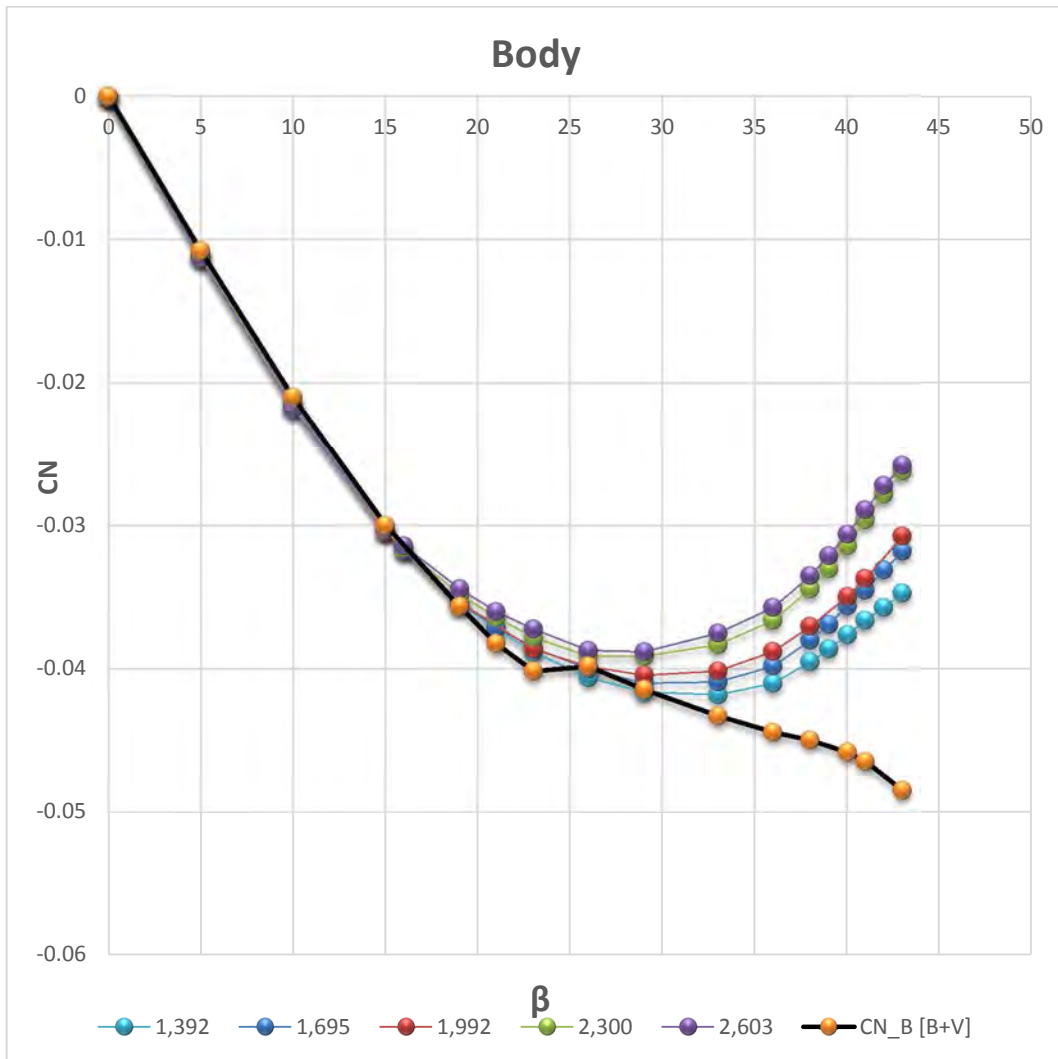


Figure 170 – Yawing moment coefficient of Body contribution of BVD configuration.

It is clearly seen that the effect of dorsal fin is obtained for angles greater than $15/20^\circ$, providing a stabilizing contribution that makes the curve with positive derivative. We should note that, by changing this parameter, the dorsal fin geometry is modified by increasing the surface area of the lower part of the dorsal fin, In fact we can see that the fuselage contribution between the various dorsal is very different.

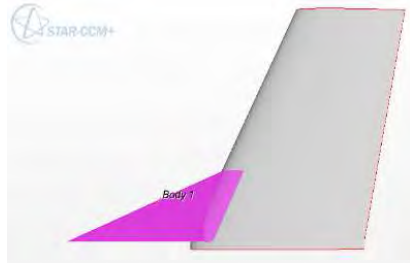
We can therefore conclude that this effect strongly depends by the dorsal fin area close to the fuselage. We can confirm this from the previous graph that highlights a great reduction in the absolute value of the fuselage contribution (fuselage less unstable) increasing dorsal fin length.

Dorsal Fin primary effect on the overall stability

We analyze the curve of the total CN for BV configuration with the curve of total CN of BVD configuration. Compared to the previous case concerning the effect on the vertical tail now there is a difference equal to the unstable fuselage contribution that reduce these curves.

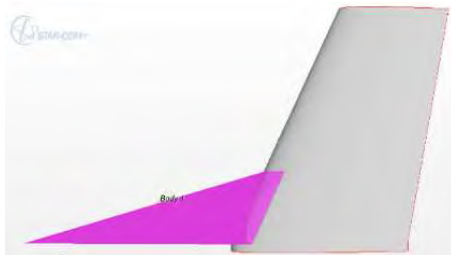
We can show how to subtract the fuselage contributions for two dorsal representing +30% and -30% of dorsal surface respect to the dorsal reference. (Dorsal no.1 & no.5) It means that we are comparing the body effect for 60% of dorsal surface variation by changing L,df

No.1) $\Delta L,df$ [$\Delta S,df$ - 30%]



h,v [m]	S,v [m ²]	S,df [m ²]	$\phi_{o,v}$ [°]
0.2434	0.040	0.009	26.600
$\phi_{o,df}$ [°]	h,fd [m]	L,df [m]	L,df/Cr,v_mean
71.810	0.076	0.230	1.392
Lv-df	Lv-df/ L,df	Cr,fd	Cr,v
0.038	0.165	0.192	0.200
Ldf/Cr,v	L,df/h,df	S,df/S,v	ΔAR
1.150	3.042	0.220	-22%

No.5) $\Delta L,df$ [$\Delta S,df$ + 30%]



h,v [m]	S,v [m ²]	S,df [m ²]	$\phi_{o,v}$ [°]
0.2434	0.040	0.016	26.600
$\phi_{o,df}$ [°]	h,fd [m]	L,df [m]	L,df/Cr,v_mean
80.034	0.076	0.430	2.603
Lv-df	Lv-df/ L,df	Cr,fd	Cr,v
0.038	0.088	0.392	0.200
Ldf/Cr,v	L,df/h,df	S,df/S,v	ΔAR
2.150	5.688	0.411	-41%

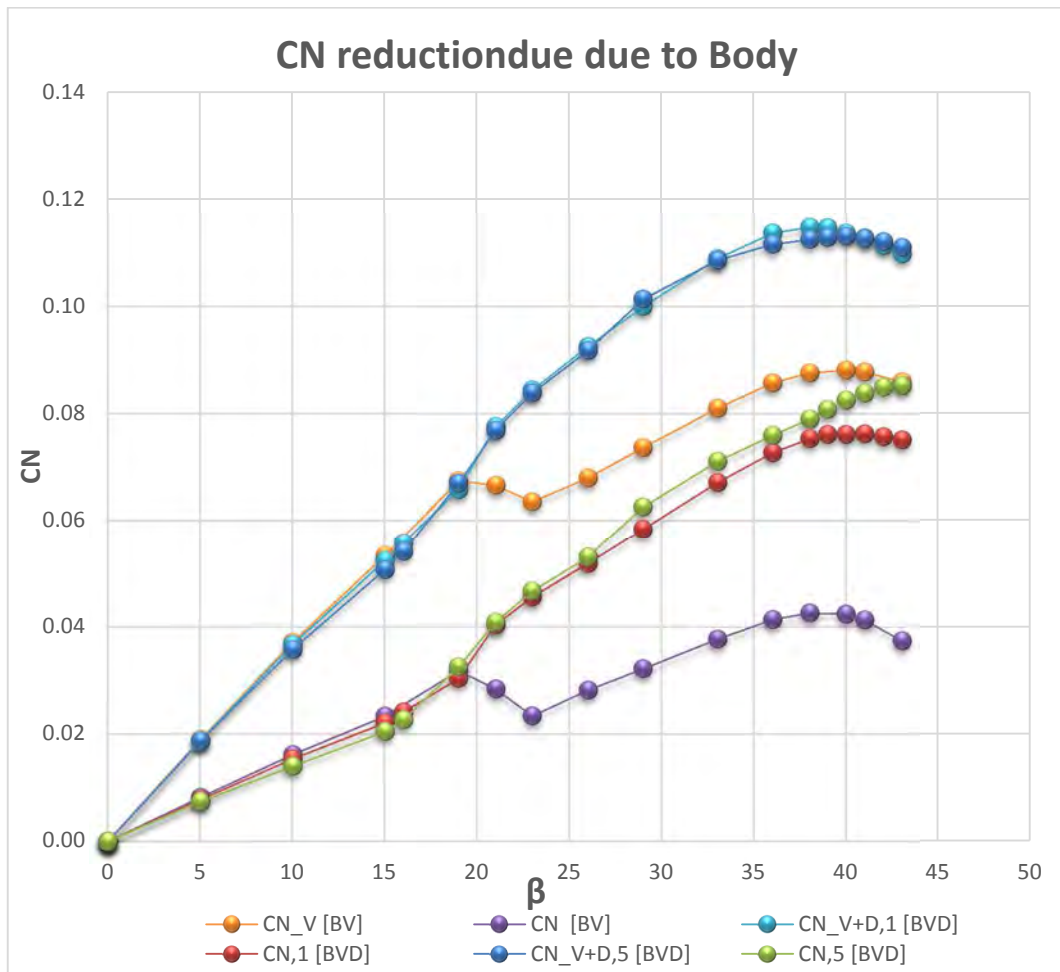


Figure 171 – Yawing moment coefficient reduction due to the Body contribution for Dorsal no.1 & Dorsal no.5 of BVD configuration.

In particular greater reduction for the curve relative to BV configuration (for which the contribution of the fuselage is greater in absolute value), and a lower reduction for the curve relating to the BVD configuration (for which the fuselage contribution is lower in absolute value due the dorsal fin as mentioned above)

We propose as done in chapter 5 the concept of contribution redistribution

Again, we show how are the work redistribution of two configuration with dorsal representing +30% and - 30% of dorsal surface, compared to the dorsal reference. (Dorsal no.1 & no.5). It means that we are comparing the effects for 60% of dorsal surface variation by changing L,df.

Using Figure 172 we can see how add up the contributions of Dorsal and Vertical to get Dorsal + Vertical and their relevance in terms of stability increase.

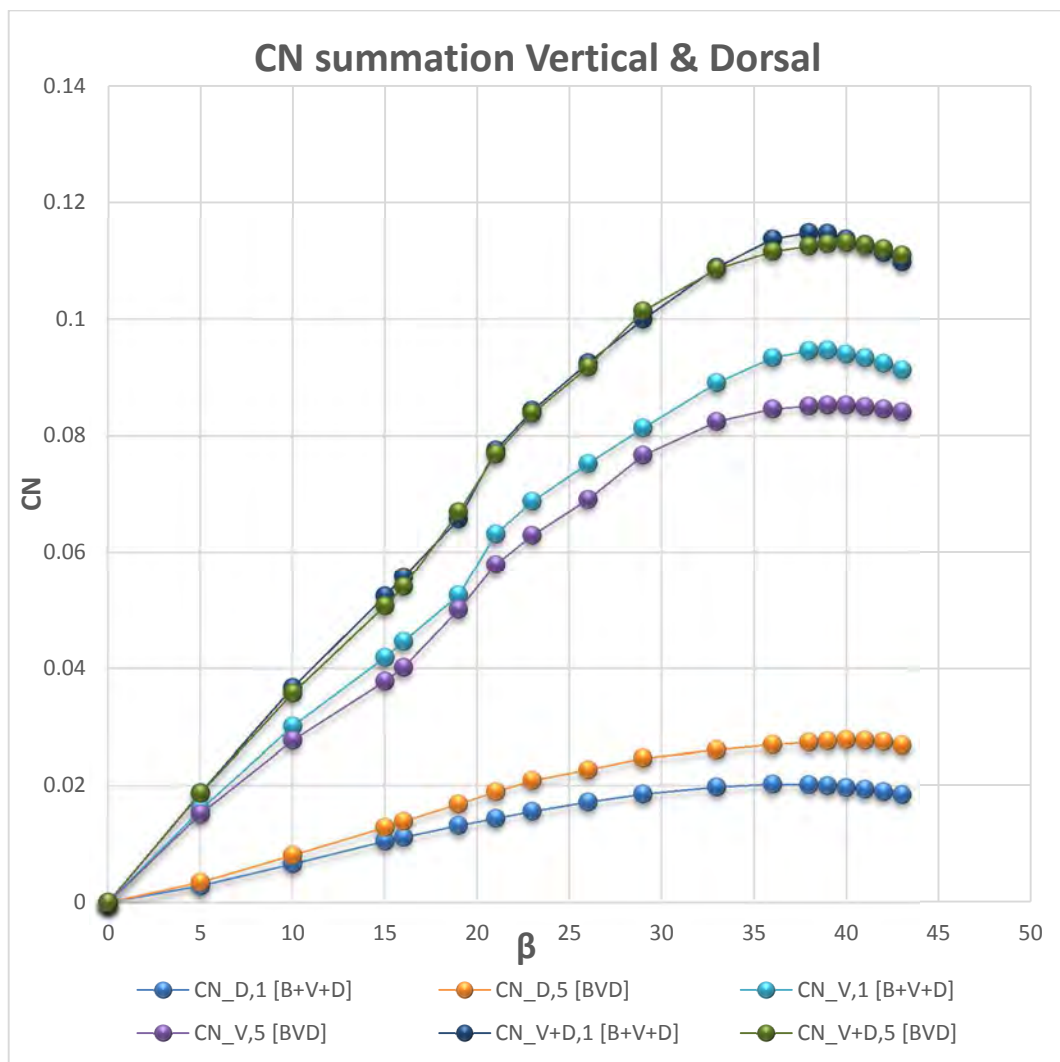


Figure 172 – Yawing moment coefficient of Vertical + Dorsal summation for Dorsal no.1 & Dorsal no.3 of BVD configuration.

The aspect that interests us is to understand what phenomenology is behind the ineffectiveness of the dorsal fin in the linear range, i.e. that there is an almost perfect correspondence between the curves of Vertical in BV configuration and of Vertical + Dorsal in BVD configuration, as show in Figure 173.

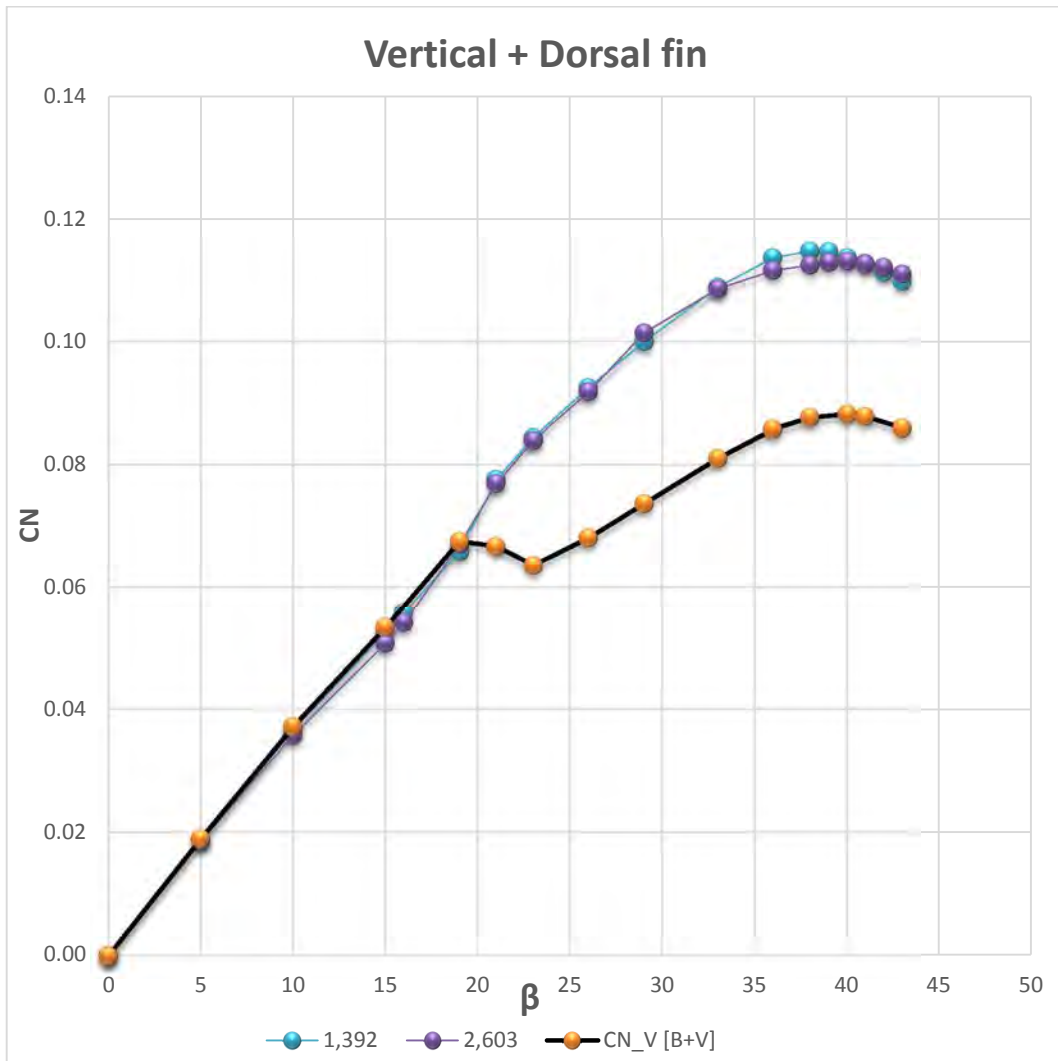


Figure 173 – Yawing moment coefficient coincidence between Vertical + Dorsal summation of BVD configuration and Vertical contribution of BV configuration for Dorsal no.1 & Dorsal no.3.

Again it may seem strange that, however is an area addition which intervenes in the aerodynamics. So with a larger area should be increased at least the slope in linear range.

Actually happens that with the addition of the dorsal, the vertical work less as explained in chapter 5. In Figure 174 there is the comparison between the curve of vertical in BV configuration and of the vertical in BVD configurations. We can evaluate for this parameterization the reduction of work of the vertical concern the 60 % of dorsal fin surface variation by changing h, df .

We see that the vertical tail, working less and less in proportion to the increase of the dorsal fin length. There is a difference of slope because we are neglecting the contribution of the dorsal fin that would bring the two gradients to coincide (see Figure 174 & 172).

These graphs make it possible to identify for example optimum geometry between those analyzed for a particular stability performance.

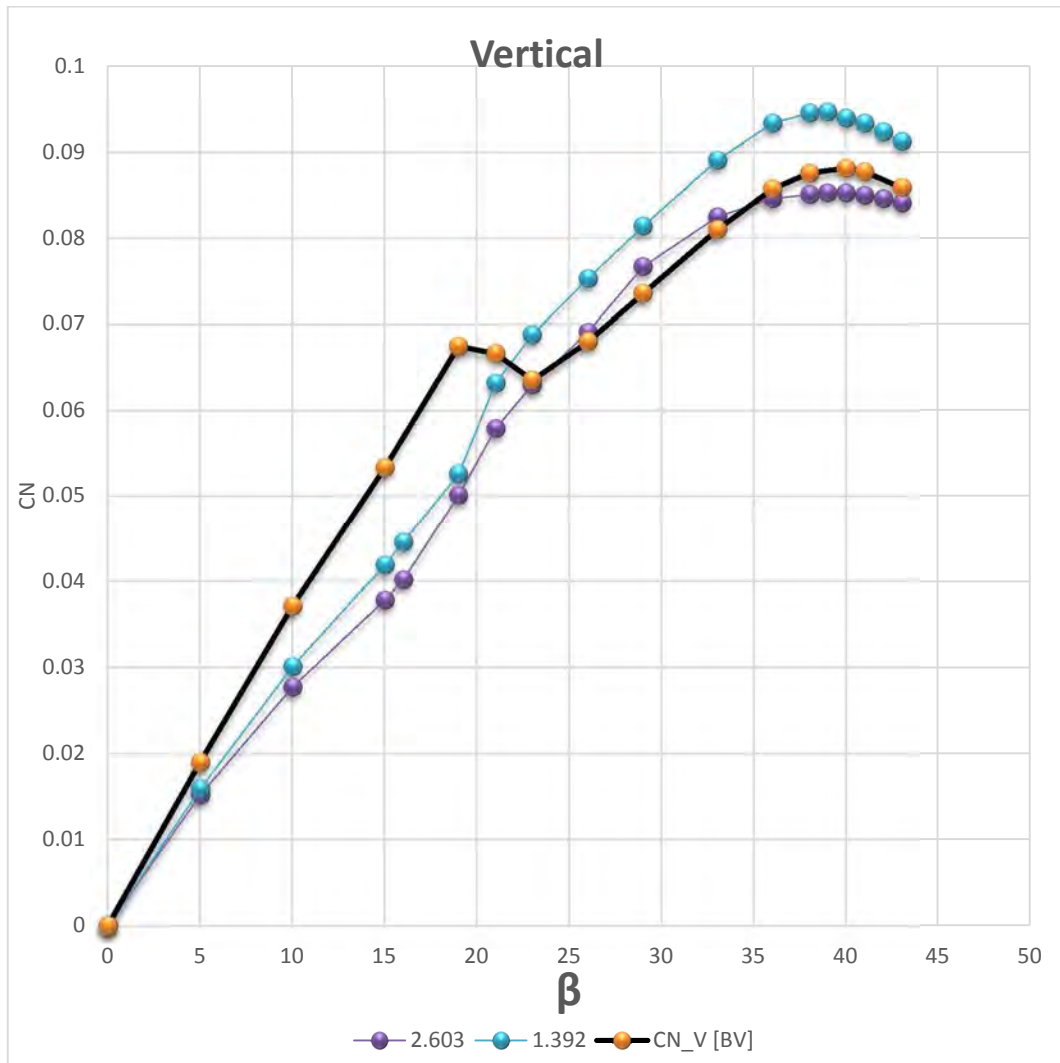
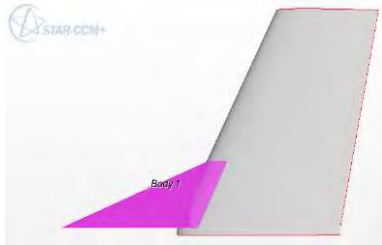


Figure 174 – How the vertical work less in BVD configuration with respect the Vertical contribution of BV configuration for Dorsal no.1 & Dorsal no.5.

6.5.3 COMPARISON OF EQUAL VARIATION OF SURFACE

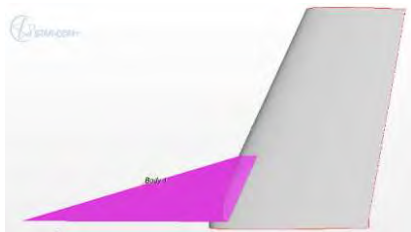
Exploiting these last two parameterizations is possible to make a comparison of the effects determined by an increase of 30 % or a decrease of 30 % of the dorsal surface obtained by varying the parameter $L_{,df}$ or $h_{,df}$.

No.1) $\Delta L_{,df}$ [$\Delta S_{,df} - 30\%$]



$h_{,v}$	$S_{,v}$	$S_{,df}$	$\varphi_{o,v}$
0.2434	0.040	0.009	26.600
$\varphi_{o,df}$	$h_{,fd}$	$L_{,df}$	$L_{,df}/Cr_{,v_mean}$
71.810	0.076	0.230	1.392
$Lv_{,df}$	$Lv_{,df}/L_{,df}$	$Cr_{,fd}$	$Cr_{,v}$
0.038	0.165	0.192	0.200
$Ldf/Cr_{,v}$	$L_{,df}/h_{,df}$	$S_{,df}/S_{,v}$	ΔAR
1.150	3.042	0.220	-22%

No.2) $\Delta L_{,df}$ [$\Delta S_{,df} + 30\%$]



$h_{,v}$	$S_{,v}$	$S_{,df}$	$\varphi_{o,v}$
0.2434	0.040	0.016	26.600
$\varphi_{o,df}$	$h_{,fd}$	$L_{,df}$	$L_{,df}/Cr_{,v_mean}$
80.034	0.076	0.430	2.603
$Lv_{,df}$	$Lv_{,df}/L_{,df}$	$Cr_{,fd}$	$Cr_{,v}$
0.038	0.088	0.392	0.200
$Ldf/Cr_{,v}$	$L_{,df}/h_{,df}$	$S_{,df}/S_{,v}$	ΔAR
2.150	5.688	0.411	-41%

No.3) $\Delta h_{,df}$ [$\Delta S_{,df} - 30\%$]



$h_{,v}$ [m]	$S_{,v}$ [m ²]	$S_{,df}$ [m ²]	$\varphi_{o,v}$ [°]
0.243	0.040	0.012	26.600
$\varphi_{o,df}$ [°]	$h_{,fd}$ [m]	$L_{,df}$ [m]	$L_{,df}/Cr_{,v_mean}$
81.706	0.048	0.329	1.992
$Lv_{,df}$	$Lv_{,df}/L_{,df}$	$Cr_{,fd}$	$Cr_{,v}$
0.024	0.073	0.305	0.200
$h_{,df}/h_{,v}$	$L_{,df}/h_{,df}$	$S_{,df}/S_{,v}$	ΔAR
0.197	6.855	0.200	-20%

No.4) $\Delta h_{,df}$ [$\Delta S_{,df} + 30\%$]



$h_{,v}$ [m]	$S_{,v}$ [m ²]	$S_{,df}$ [m ²]	$\varphi_{o,v}$ [°]
0.243	0.040	0.016	26.600
$\varphi_{o,df}$ [°]	$h_{,fd}$ [m]	$L_{,df}$ [m]	$L_{,df}/Cr_{,v_mean}$
73.740	0.096	0.329	1.992
$Lv_{,df}$	$Lv_{,df}/L_{,df}$	$Cr_{,fd}$	$Cr_{,v}$
0.048	0.146	0.281	0.200
$h_{,df}/h_{,v}$	$L_{,df}/h_{,df}$	$S_{,df}/S_{,v}$	ΔAR
0.394	3.427	0.400	-40%

Figure 175 – $L_{,df}$ & $h_{,df}$ parameterization to change $S_{,df}$, geometry viewing and characteristic values.

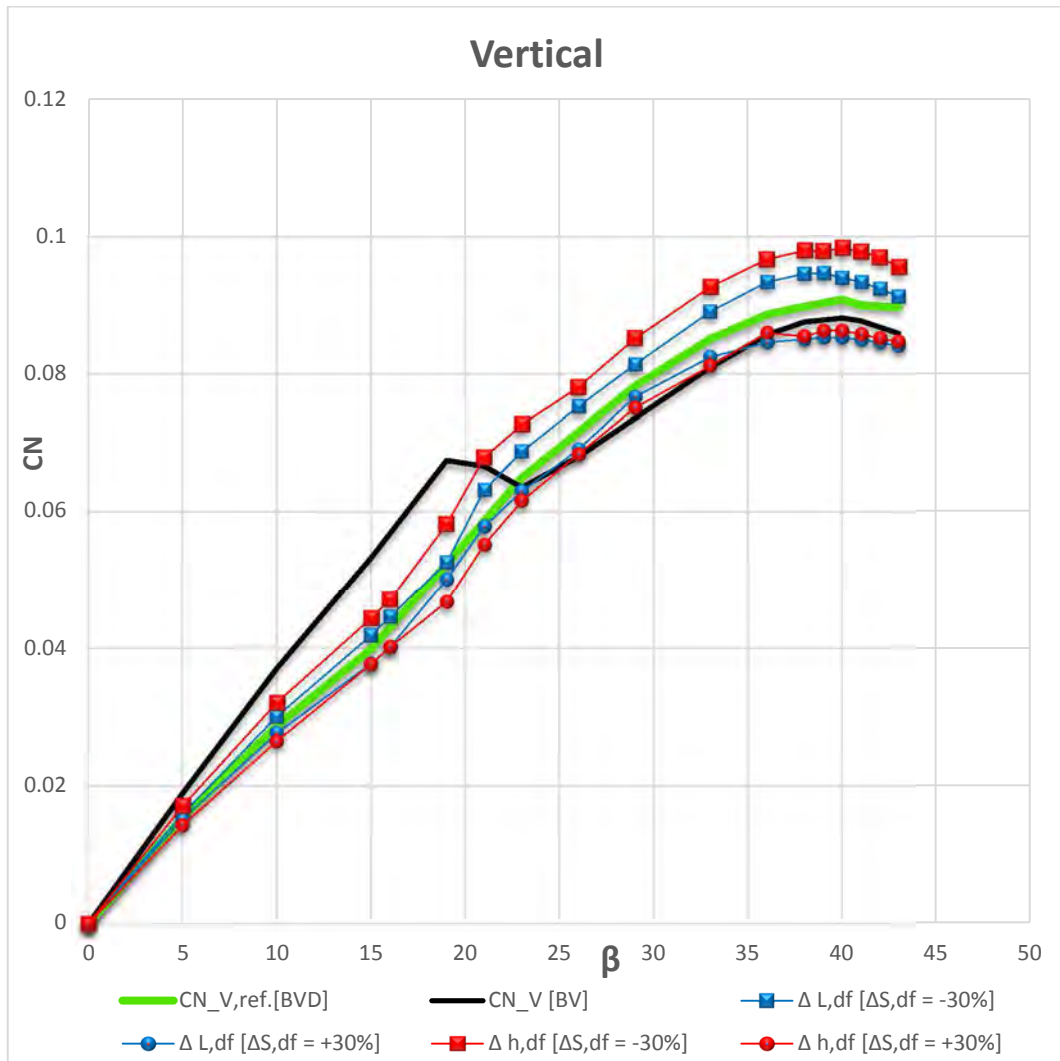


Figure 176 – How the vertical work less in BVD configuration respect an variation of $\pm 30\%$ obtained by changing h,df or L,df .

An increase of the dorsal surface 30% determines the same loss of work of the vertical, both if it is done by varying the parameter L,df that if is realized by varying the parameter h,df .

A reduction of the dorsal surface of 30% determines an increase of work for the vertical that is stronger if is achieved by varying the parameter h,df and that is weaker if is achieved by varying the parameter L,df .

So the variation of h,df is the one that has the most influence on the work of vertical. At the same time is the one that has the most influence on the work of the dorsal which compensates the variation of the vertical.

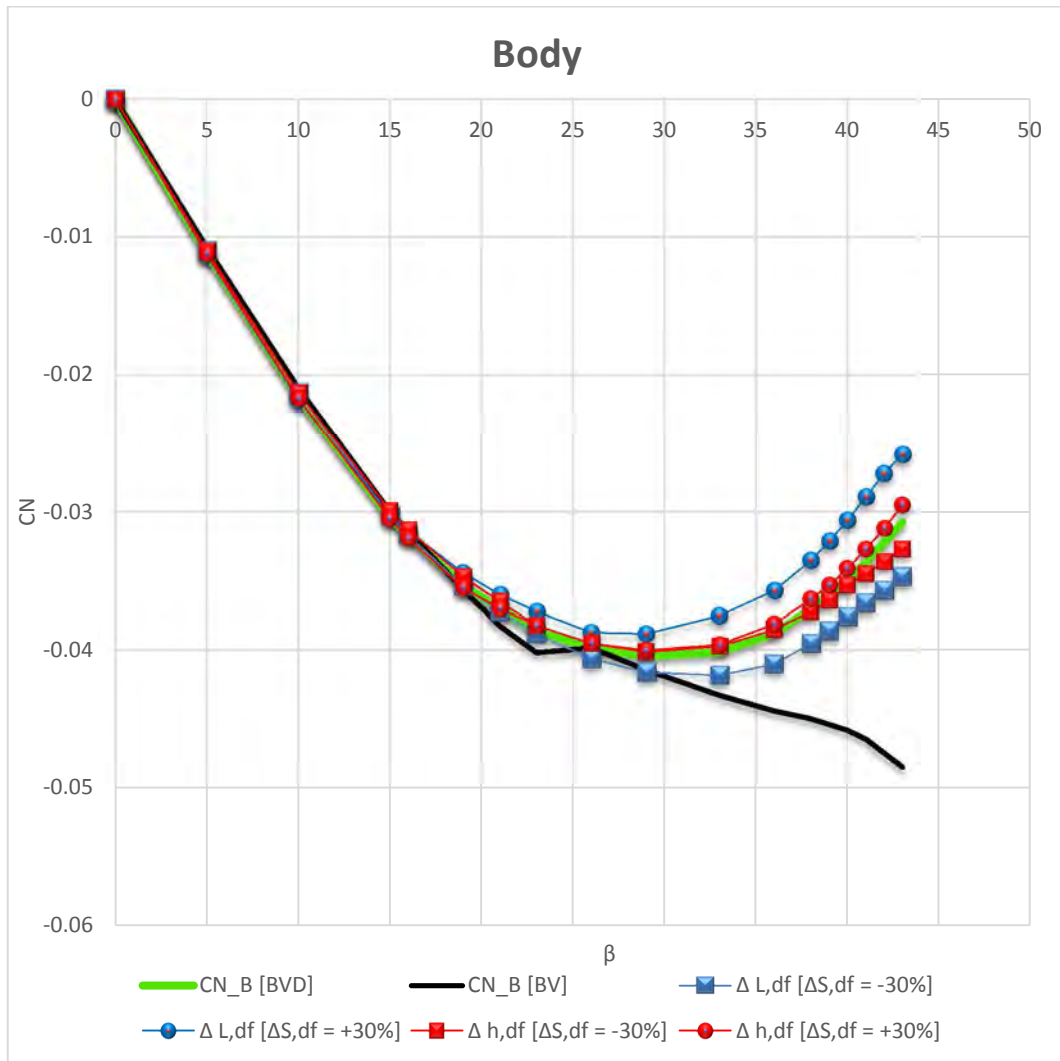


Figure 177 – How the fuselage modifies the stability in BVD configuration respect an variation of $\pm 30\%$ obtained by changing h,df or L,df .

A reduction of the dorsal surface of $\pm 30\%$ causes a different effect for the fuselage because, if it is done by varying the parameter L,df is obtained a greater reduction of stability than if it is done by varying the parameter h,df , for which the effect remains almost unchanged.

An increase of the dorsal surface of 30% determines a rise of stability for the fuselage that is stronger if is realized by varying the parameter L,df and is weaker if is realized by varying the parameter h,df for which the effect remains almost unaltered.

So the variation of L,df is the one that has the most influence on the stability of the fuselage.

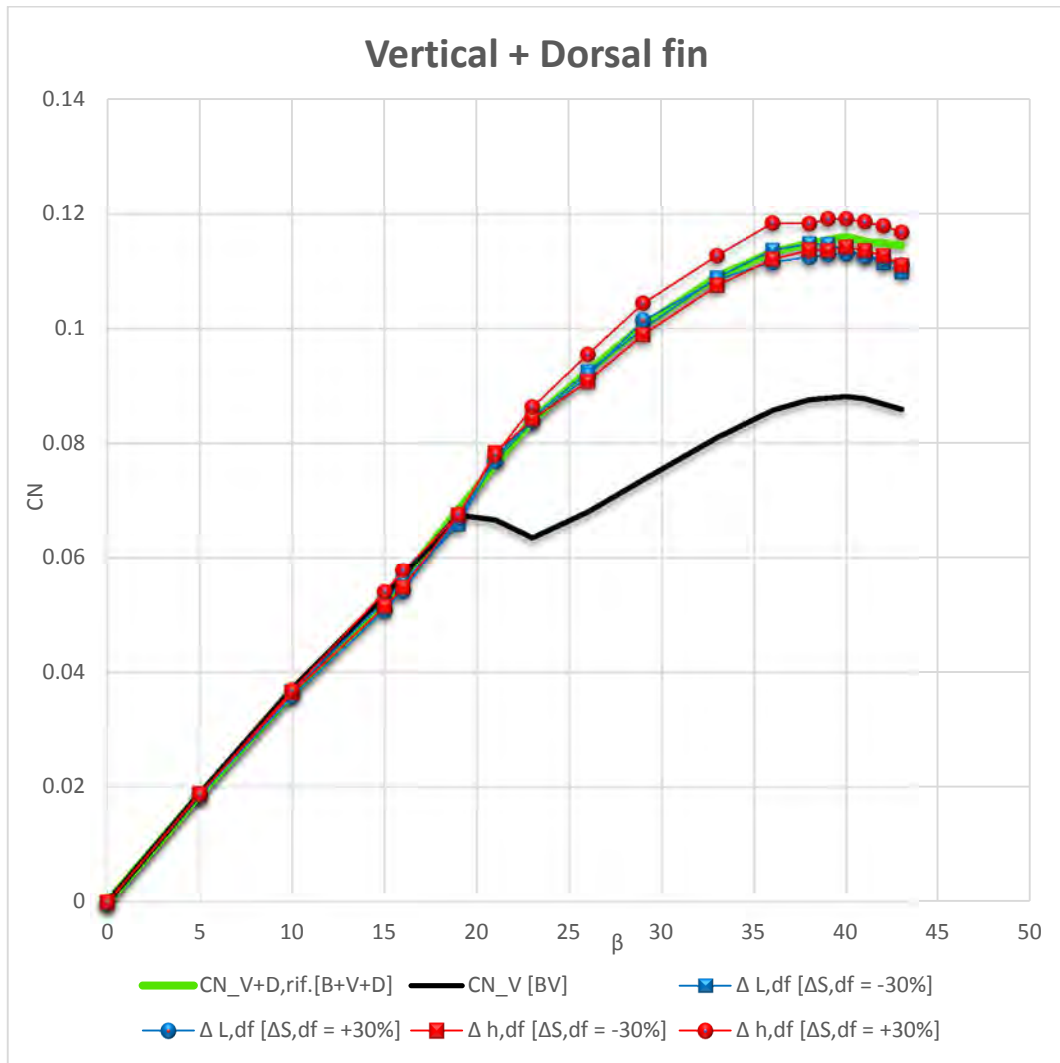


Figure 178 – How the Vertical +Dorsal modifies the stability in BVD configuration respect an variation of $\pm 30\%$ obtained by changing h,df or L,df .

The trends are almost similar. Only for the increase of S,df realized by varying h,df is obtained an increase of stability more evident, due to the shape of Vertical + Dorsal with this very high dorsal.

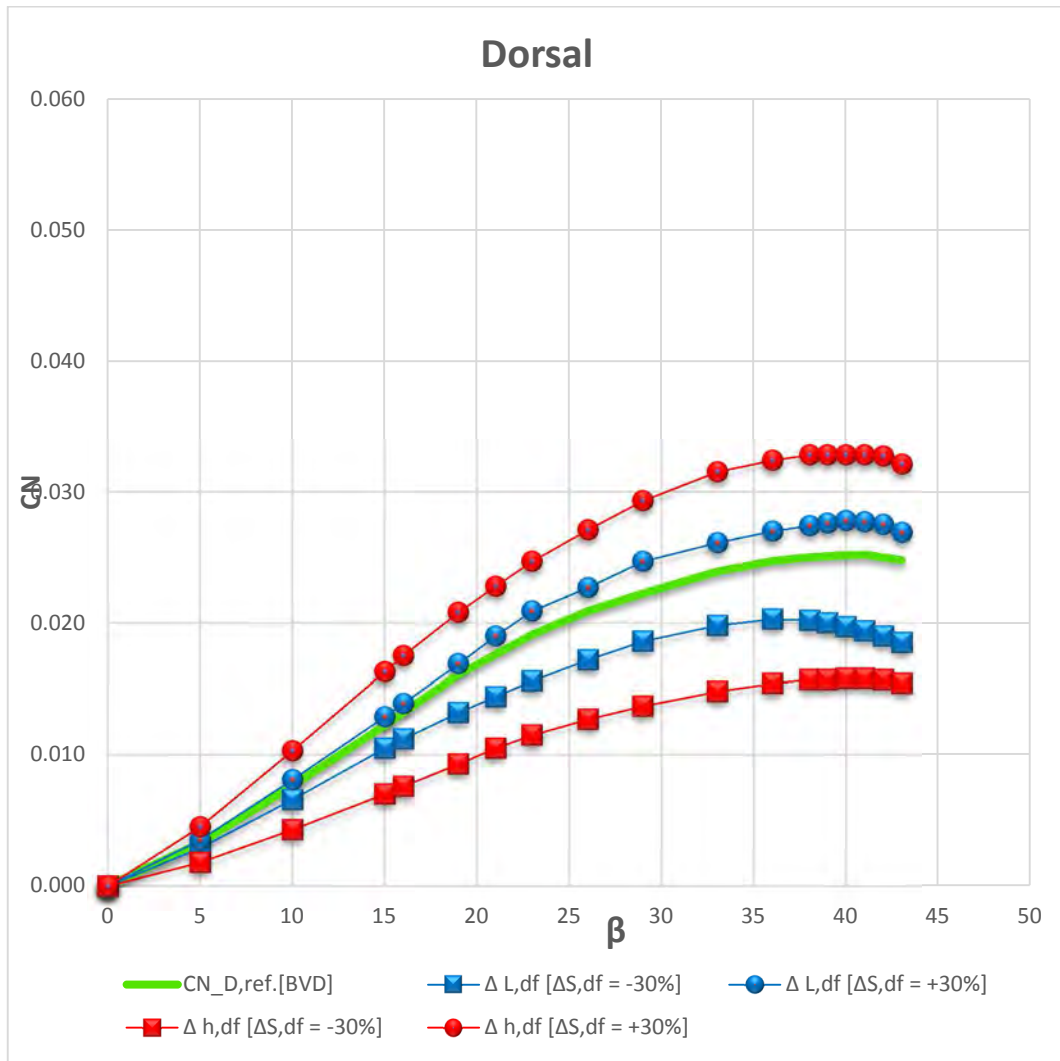


Figure 179 – How the Dorsal modifies the stability in BVD configuration respect an variation of $\pm 30\%$ obtained by changing h,df or L,df .

It is clearly seen that if the variation of dorsal surface (both in one way or another), is realized by varying the parameter h,df are obtained deviations of stability much stronger compared to the case where L,df is varied, which determines deviations of stability more limited.

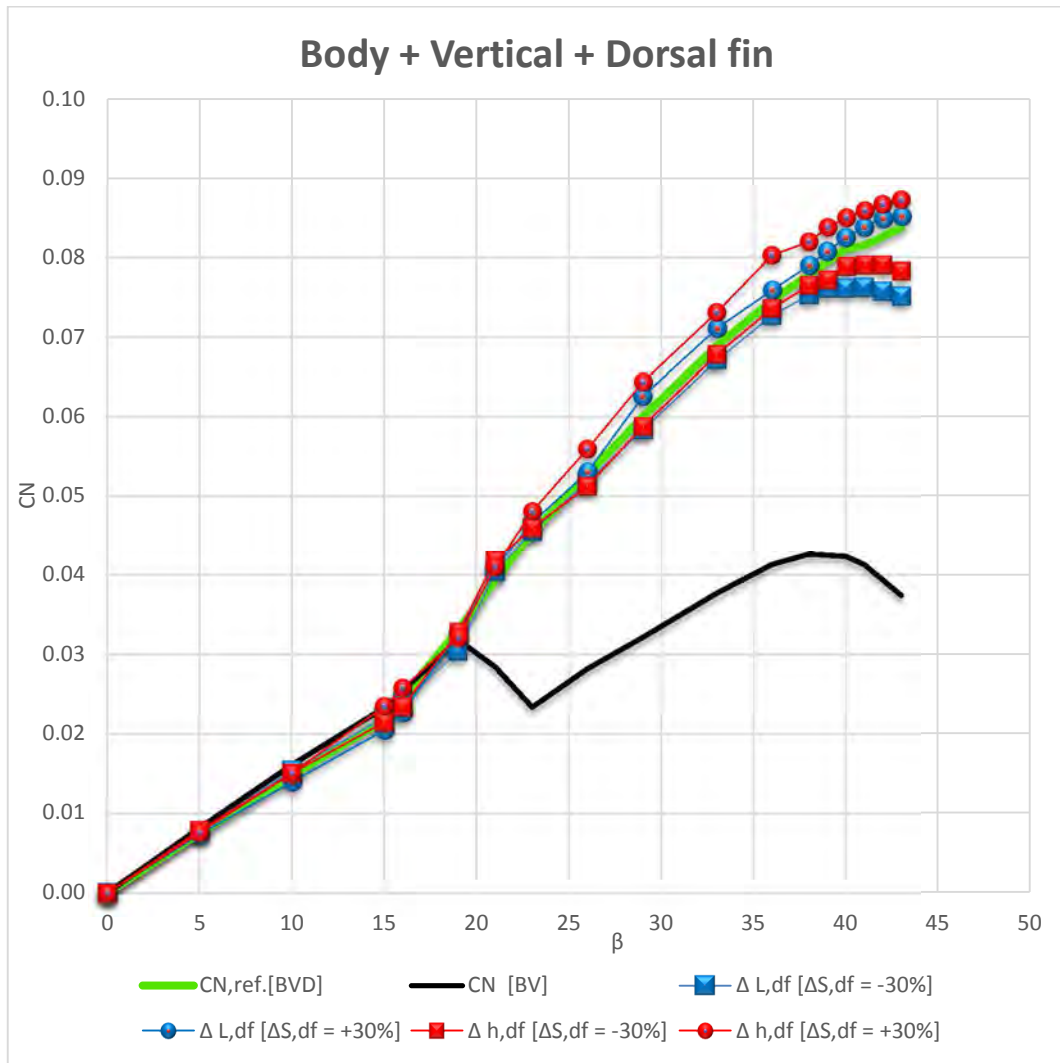


Figure 180 – How the total contribution modifies the stability in BVD configuration respect an variation of $\pm 30\%$ obtained by changing h,df or L,df .

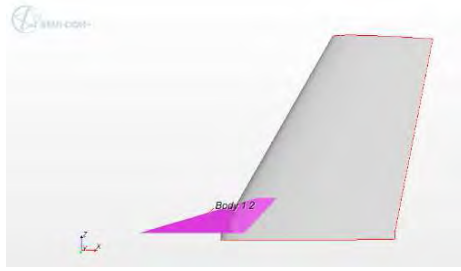
A reduction of 30% of dorsal surface cause an overall loss of stability in the non-linear range, that is stronger if is accomplished by varying L,df and is weaker if is realized varying h,df . An increase of 30% of dorsal surface cause an overall increase of stability in the non-linear range, stronger if is achieved by varying h,df and weaker if is realized varying L,df .

6.5.4 CHANGE OF L,df & h,df , TO KEEP CONSTANT ARROW AND VARY THE SURFACE.

I list below the analyzed dorsal for this parameterization flanking each image whit a summary table of the geometric parameters resulting.

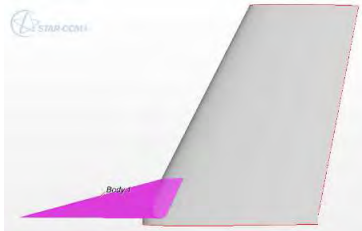
In red there is the parameter that we are changing for this specific parameterization, and in blue there is the considered parameter to distinguish one from the other, i.e. that one specified in the legend of the following graphs.

No.1)



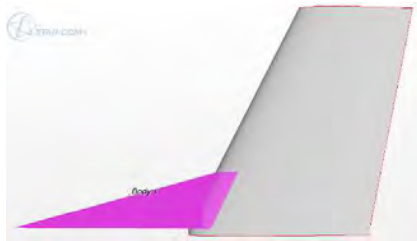
h,v [m]	S,v [m²]	S,df [m²]	φ_{o,v} [°]
0.243	0.040	0.004	26.600
φ_{o,df} [°]	h,fd [m]	L,df [m]	L,df/Cr,v
77.070	0.041	0.180	0.900
Lv-df	Lv-df/ L,df	Cr,fd	Cr,v
0.021	0.115	0.159	0.200
h,df/h,v	L,df/h,df	S,df/S,v	Δ AR
0.170	4.354	0.094	-10%

No.2)



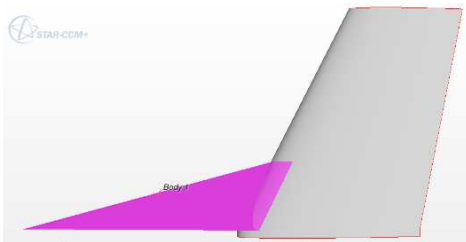
h,v [m]	S,v [m²]	S,df [m²]	φ_{o,v} [°]
0.2434	0.040	0.006	26.600
φ_{o,df} [°]	h,fd [m]	L,df [m]	L,df/Cr,v
77.070	0.053	0.230	1.150
Lv-df	Lv-df/ L,df	Cr,fd	Cr,v
0.026	0.115	0.204	0.200
h,df/h,v	L,df/h,df	S,df/S,v	Δ AR
0.217	4.354	0.154	-15%

No.3)



h,v [m]	S,v [m²]	S,df [m²]	φ_{o,v} [°]
0.2434	0.040	0.009	26.600
φ_{o,df} [°]	h,fd [m]	L,df [m]	L,df/Cr,v
77.070	0.064	0.280	1.400
Lv-df	Lv-df/ L,df	Cr,fd	Cr,v
0.032	0.115	0.248	0.200
h,df/h,v	L,df/h,df	S,df/S,v	Δ AR
0.264	4.354	0.228	-22%

No.4)



h,v [m]	S,v [m²]	S,df [m²]	φ_{o,v} [°]
0.2434	0.040	0.012	26.600
φ_{o,df} [°]	h,fd [m]	L,df [m]	L,df/Cr,v
77.065	0.0756	0.329	1.645
φ_{o,df} [°]	h,fd [m]	L,df [m]	L,df/Cr,v
0.0378	0.1150	0.291	0.2
φ_{o,df} [°]	h,fd [m]	L,df [m]	L,df/Cr,v
0.310	4.352	0.314	-31%

No.5)



h,v [m]	S,v [m²]	S,df [m²]	φ_{o,v} [°]
0.2434	0.040	0.017	26.600
φ_{o,df} [°]	h,fd [m]	L,df [m]	L,df/Cr,v
77.070	0.087	0.380	1.900
Lv-df	Lv-df/ L,df	Cr,fd	Cr,v
0.044	0.115	0.336	0.200
h,df/h,v	L,df/h,df	S,df/S,v	Δ AR
0.359	4.354	0.420	-42%

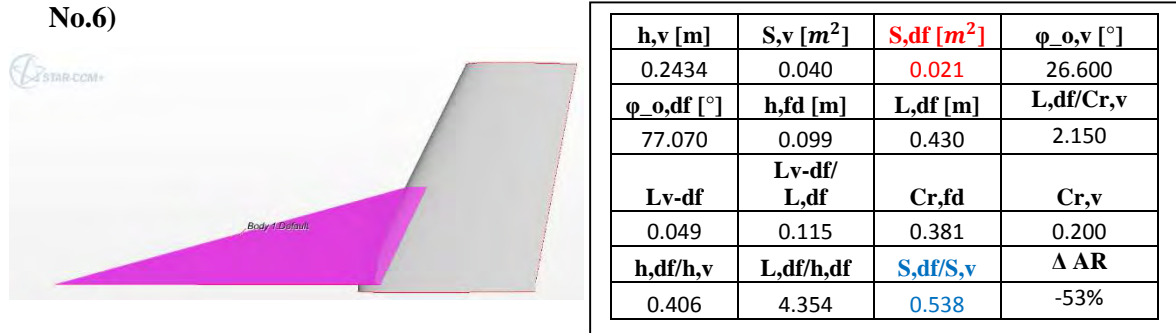


Figure 181 – S,df parameterization, geometry viewing characteristic values.

In the graphs the curves are distinguished according to the value of the ratio between S,df and vertical plane surface S,v .

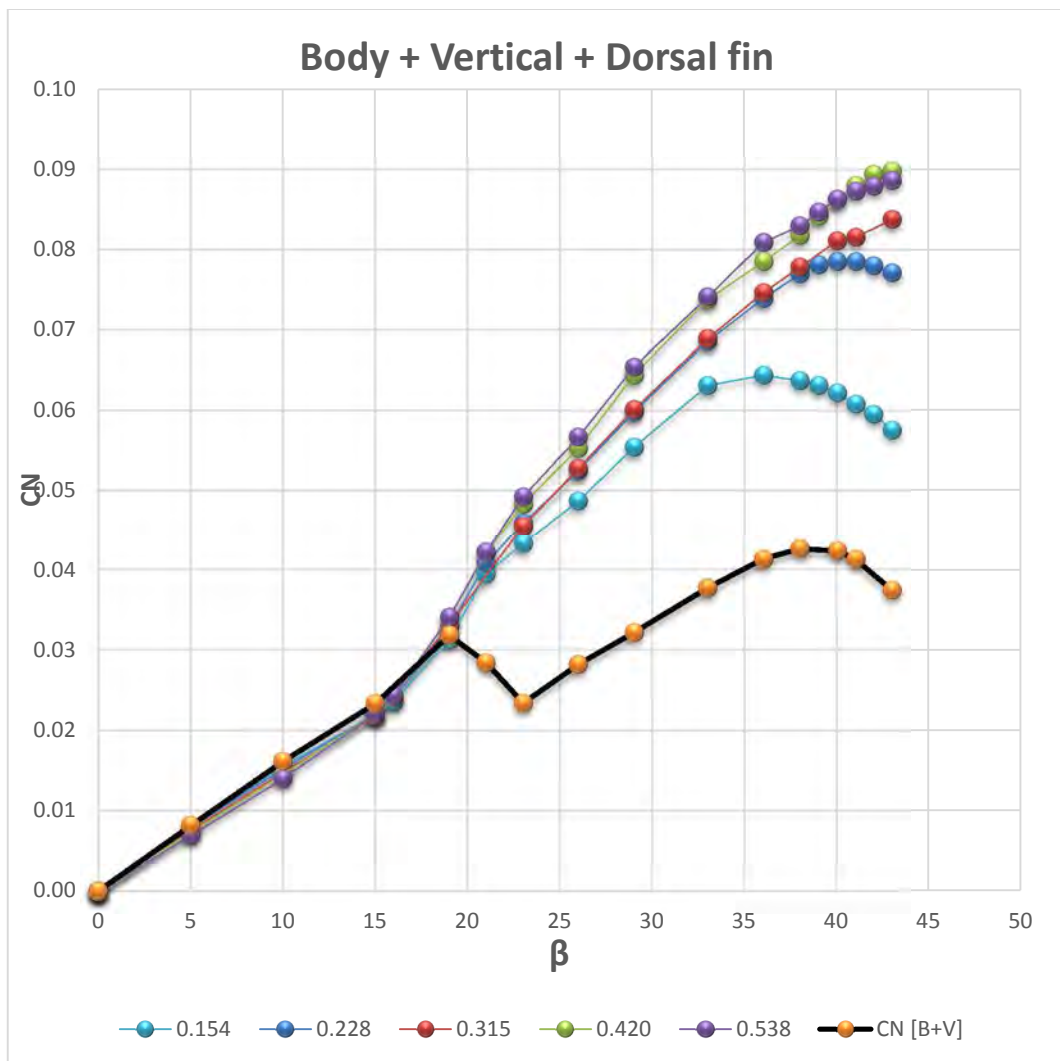


Figure 182 – Yawing moment coefficient of total contribution of BVD configuration.

As we can see in the **Figure 182** the trends in the linear range show a strong match for all curves. In general, a slight reduction of the slope increasing the dorsal surface. The trends in the non-linear range show a stability increase, growing the dorsal surface. We determine, a rise of angle-of-stall growing the dorsal surface. We note a different behavior only for the dorsal 0.15 which is

so small as not to allow the generation of an intense vortex at high sideslip angle, for this dorsal there is an anticipate stall.

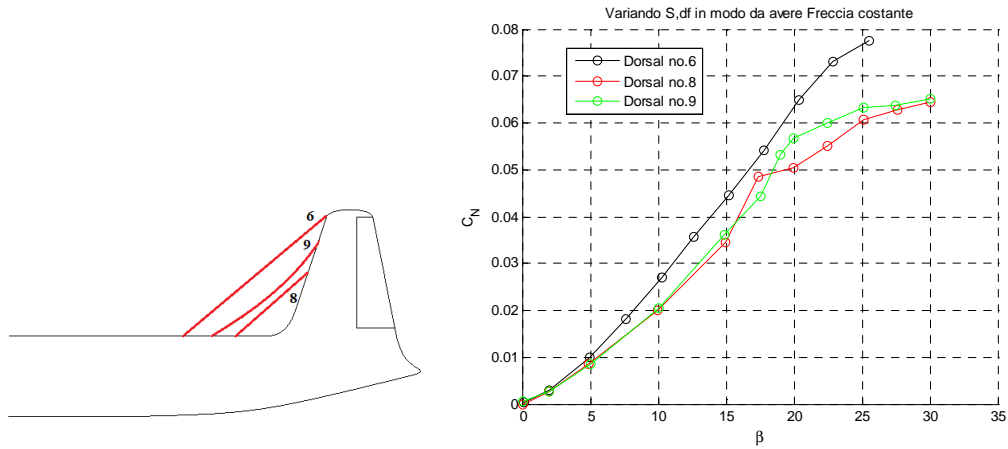


Figure 183 – Obert investigation results about Yawing moment coefficient.

There is a correspondence between the experimental and numerical data. Increasing S,df with constant sweep appears a slight decrease of slope in the linear range and a strong increase in the range nonlinear.

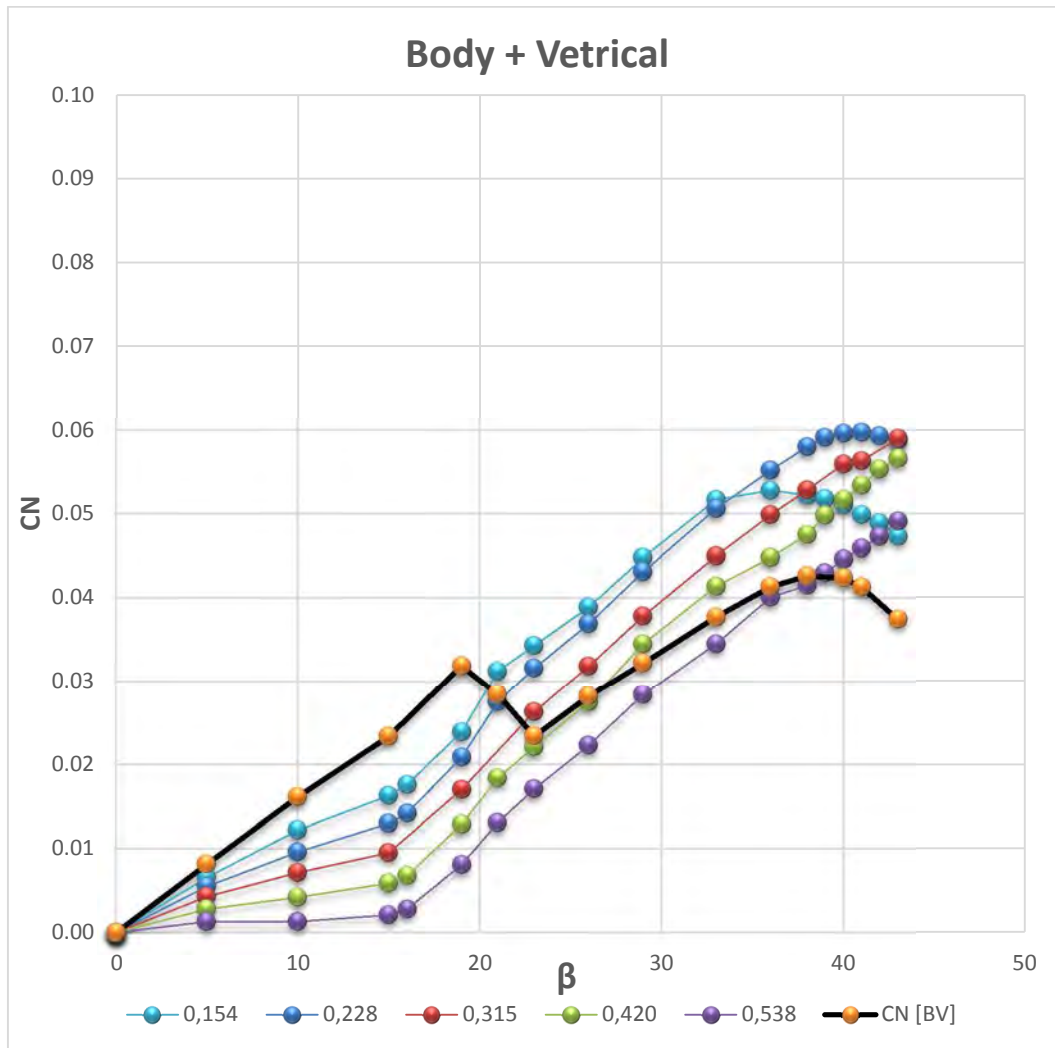


Figure 184 – Yawing moment coefficient of Body + Vertical contribution of BVD configuration.

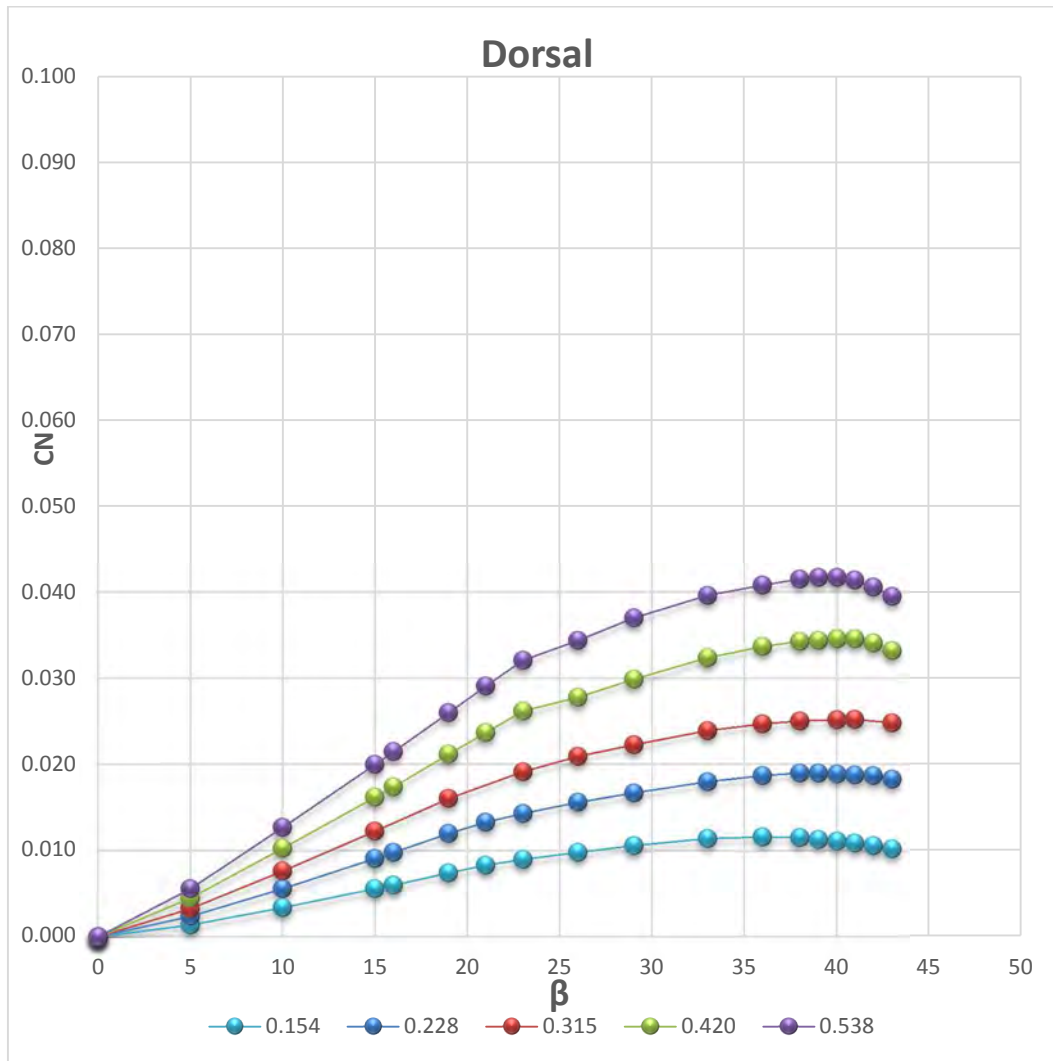


Figure 185 – Yawing moment coefficient of Dorsal fin contribution of BVD configuration.

Increasing the dorsal surface, as expected there is a larger growing of the work of the dorsal. For all the dorsal we note a constant angle of stall increasing dorsal surface.

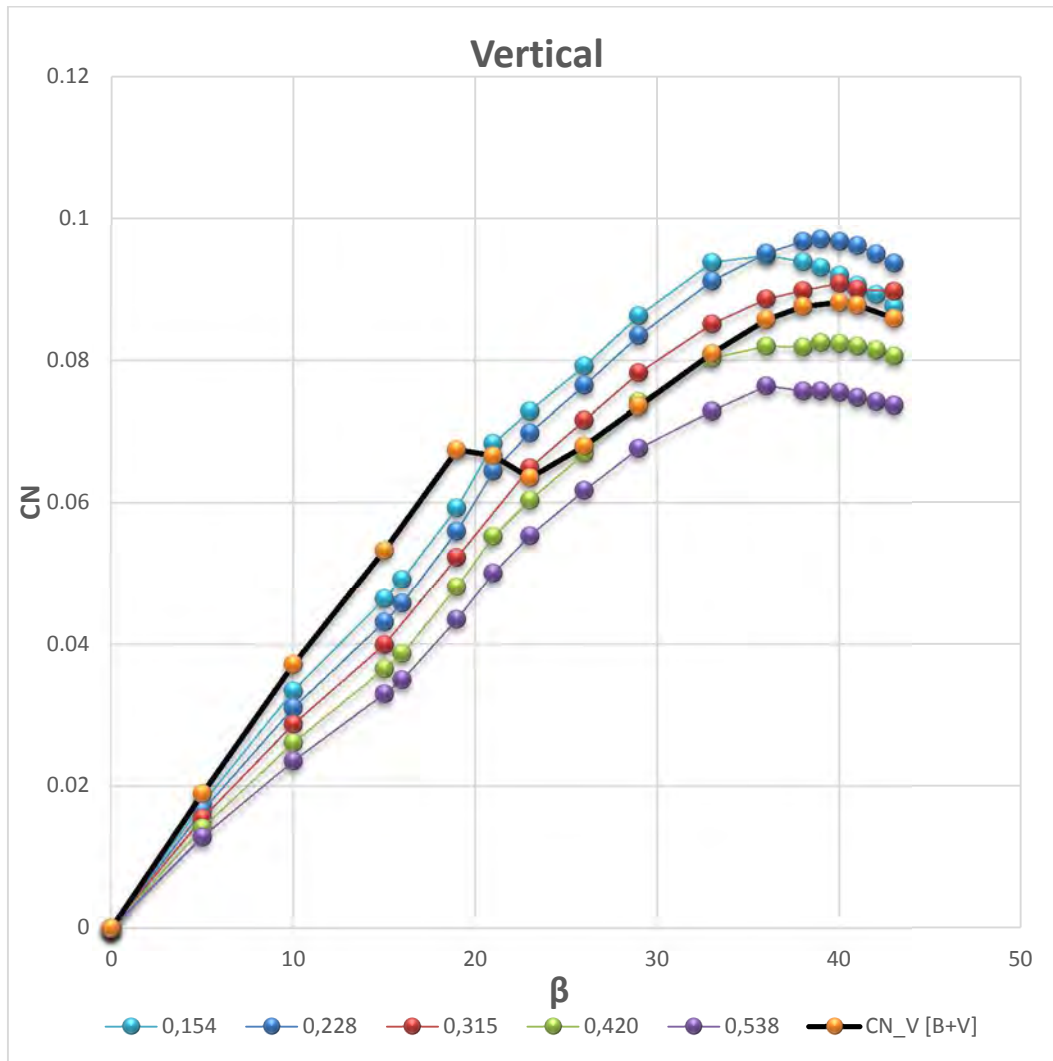


Figure 186 – Yawing moment coefficient of Body + Vertical total contribution of BVD configuration.

Increasing the dorsal surface there is a reduction increasingly strong of the Vertical plane work.

We start from the phenomena of BASELINE to evaluate the characteristic aspects of this parameterization.

Dorsal Fin primary effect on the vertical tail stability

We compare the graph that relates the contribution of vertical, in BV configuration, with the curve of the Vertical + Dorsal contribution in the BVD configuration;

This chart expresses the dorsal effect on the vertical empennage:

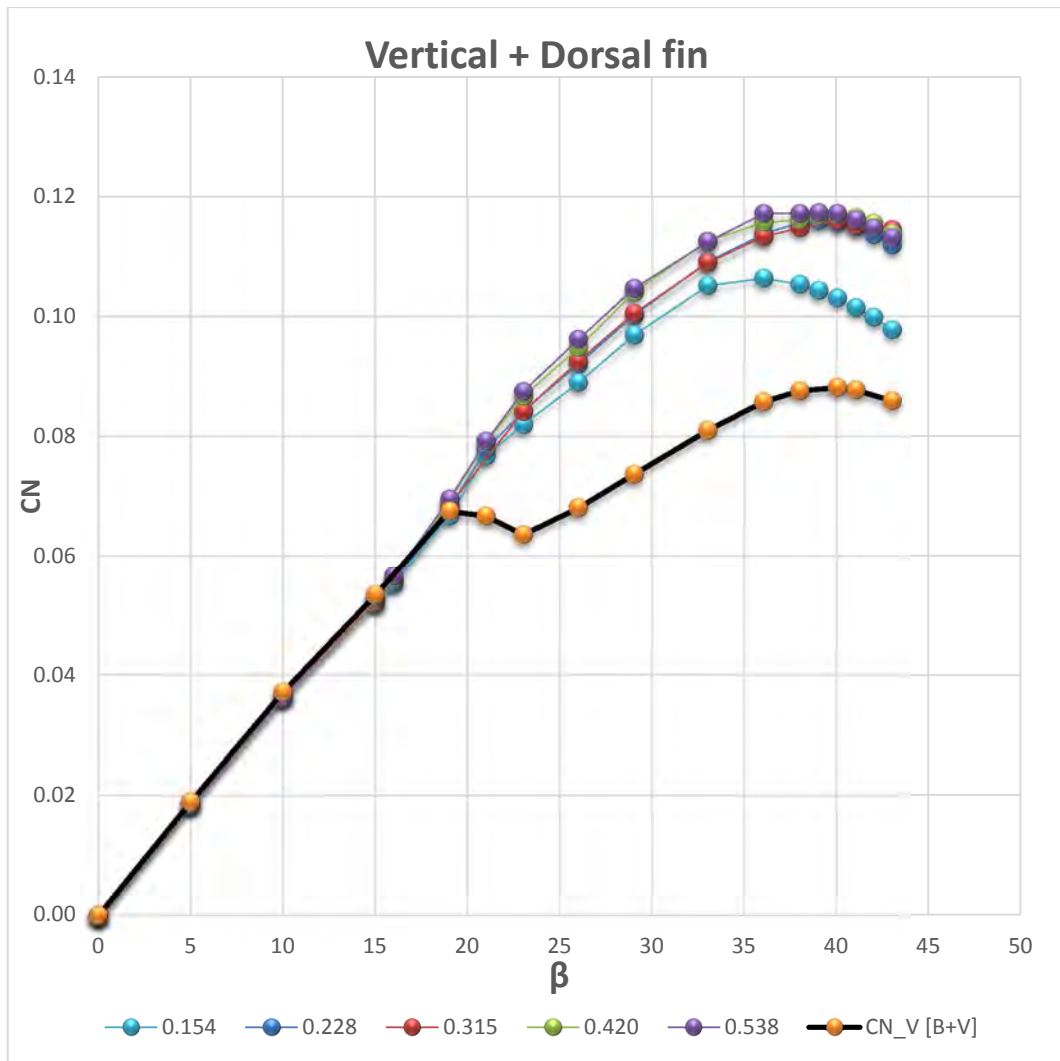


Figure 187 – Yawing moment coefficient of Vertical + Dorsal fin contribution of BVD configuration.

The trends in the linear range are exactly overlapped for different dorsal fin. The trends in non-linear range for the various dorsal fin are such that by increasing the dorsal surface is obtained a higher CN. In particular for the dorsal 0.15 we note a lower CN, this is due as mentioned above the dorsal is so small as not to be able to generate intense vortex at high sideslip angle.

Dorsal fin effect on the fuselage stability.

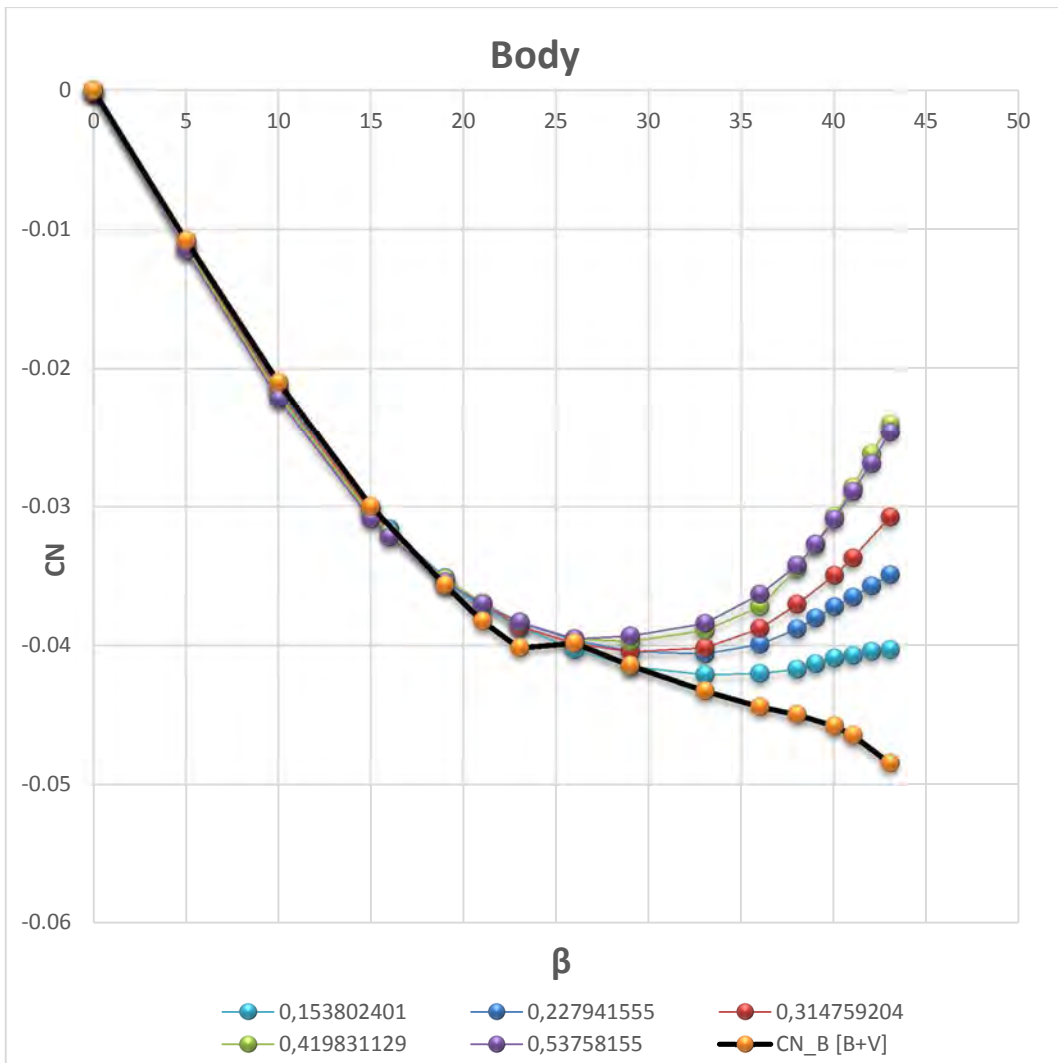


Figure 188 – Yawing moment coefficient of the Body contribution of BVD configuration.

It is clearly seen that the effect of dorsal fin is obtained for angles greater than 20/25°, providing a stabilizing contribution that makes the curve with positive derivative.

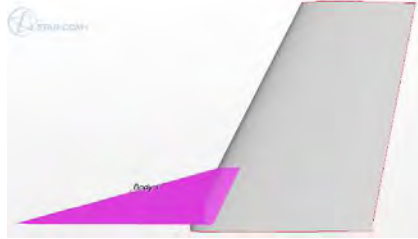
We should note that by varying this parameter, the geometry of the dorsal fin is modified by increasing both the surface of the lower part that of the upper part of the dorsal fin, In fact, we can see how the contribution of the fuselage between the various dorsal seems very different. We can then conclude that what determines the importance of the fuselage stability contribution is the surface of dorsal fin area near the fuselage. Compared to the L,df parameterization in which for the not linear range enough parallel curves were obtained, in this case we see that the variation of S,df also changes the slope of the curves. This indicates a very strong increase in stability (fuselage less unstable).

Dorsal Fin primary effect on the overall stability

We analyze the curve of the total CN for BV configuration with the curve of total CN of BVD configuration. Compared to the previous case, concerning just the vertical tail now there is a difference equal to the unstable fuselage contribution that reduce these curves.

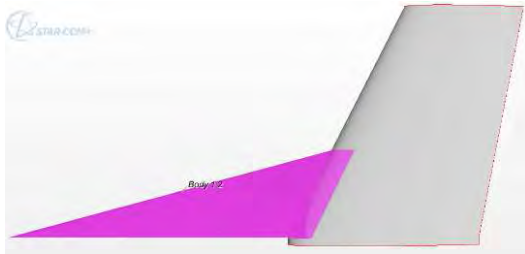
We can show how to subtract the fuselage contributions for two dorsal representing +30% and -30% of dorsal surface respect to the dorsal reference. (Dorsal no.3 & no53) It means that we are comparing the body effect for 60% of dorsal surface variation by changing S,df at constant sweep.

No.3) [$\Delta S_{df} - 30\%$] $\phi_{o,df}$: Constant



h,v [m]	S,v [m²]	S,df [m²]	$\phi_{o,v}$ [°]
0.2434	0.040	0.009	26.600
$\phi_{o,df}$ [°]	h,fd [m]	L,df [m]	L,df/Cr,v
77.070	0.064	0.280	1.400
Lv-df	Lv-df/L,df	Cr,fd	Cr,v
0.032	0.115	0.248	0.200
h,df/h,v	L,df/h,df	S,df/S,v	ΔAR
0.264	4.354	0.228	-22%

No.5) [$\Delta S_{df} + 30\%$] $\phi_{o,df}$: Constant



h,v [m]	S,v [m²]	S,df [m²]	$\phi_{o,v}$ [°]
0.2434	0.040	0.017	26.600
$\phi_{o,df}$ [°]	h,fd [m]	L,df [m]	L,df/Cr,v
77.070	0.087	0.380	1.900
Lv-df	Lv-df/L,df	Cr,fd	Cr,v
0.044	0.115	0.336	0.200
h,df/h,v	L,df/h,df	S,df/S,v	ΔAR
0.359	4.354	0.420	-42%

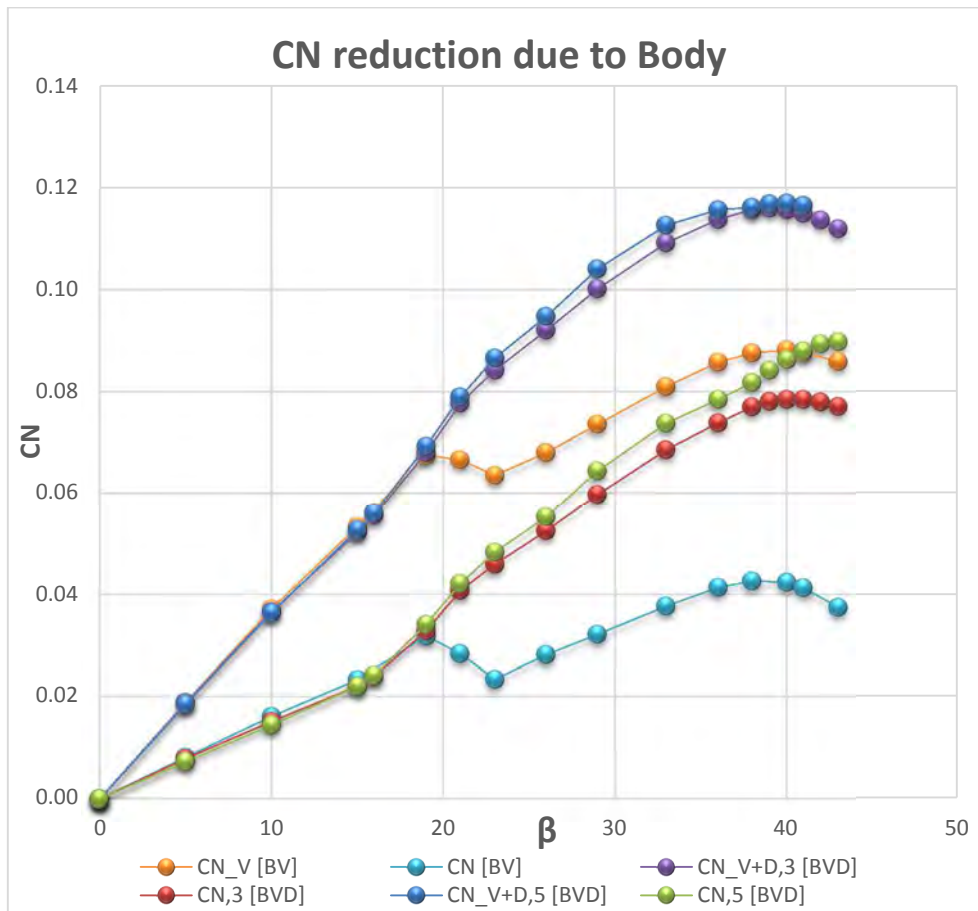


Figure 189 – Yawing moment coefficient reduction due to Body contribution for Dorsal no.3 & Dorsal no.5 of BVD configuration.

In particular greater reduction for the curve relative to BV configuration (for which the contribution of the fuselage is greater in absolute value), and a lower reduction for the curve relating to the BVD configuration (for which the fuselage contribution is lower in absolute value due the dorsal fin as mentioned above)

We propose as done in chapter 5 the concept of contribution redistribution

Again, we show how are the work redistribution of two configuration with dorsal representing +30% and - 30% of dorsal surface, compared to the dorsal reference. (Dorsal no.3 & no.5). It means that we are comparing the effects of 60% of dorsal surface variation keeping constant sweep.

Using the Figure 190 we can see how add up the contributions of Dorsal and Vertical to get Dorsal + Vertical and their relevance in terms of stability increase.

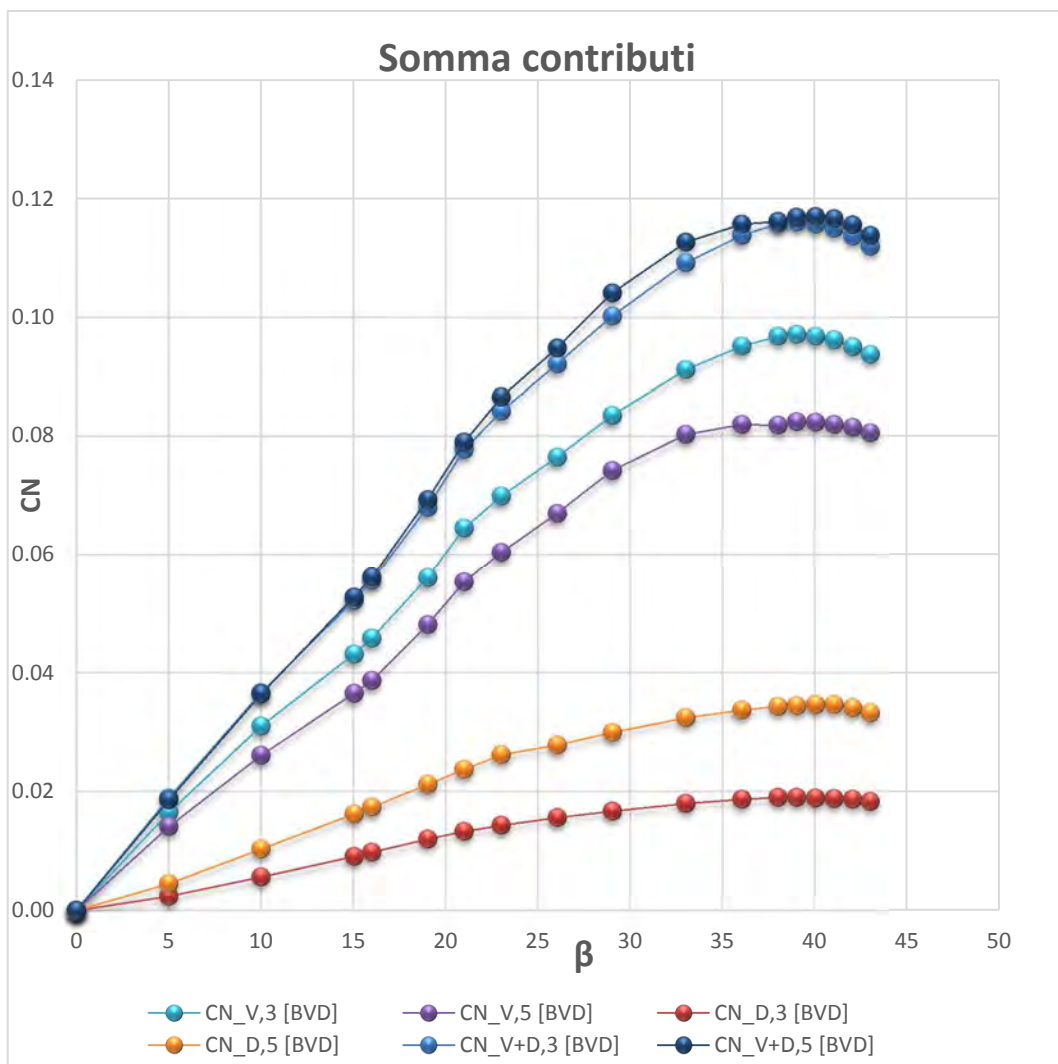


Figure 190 – Yawing moment coefficient of Vertical + Dorsal summation for Dorsal no.3 & Dorsal no.5 of BVD configuration.

The aspect that interests us is to understand what phenomenology is behind the fact that in the linear section dorsal fin is ineffective i.e. that there is an almost perfect correspondence between the curves of Vertical in BV configuration and of Vertical + Dorsal in BVD configuration as shown in Figure 191.

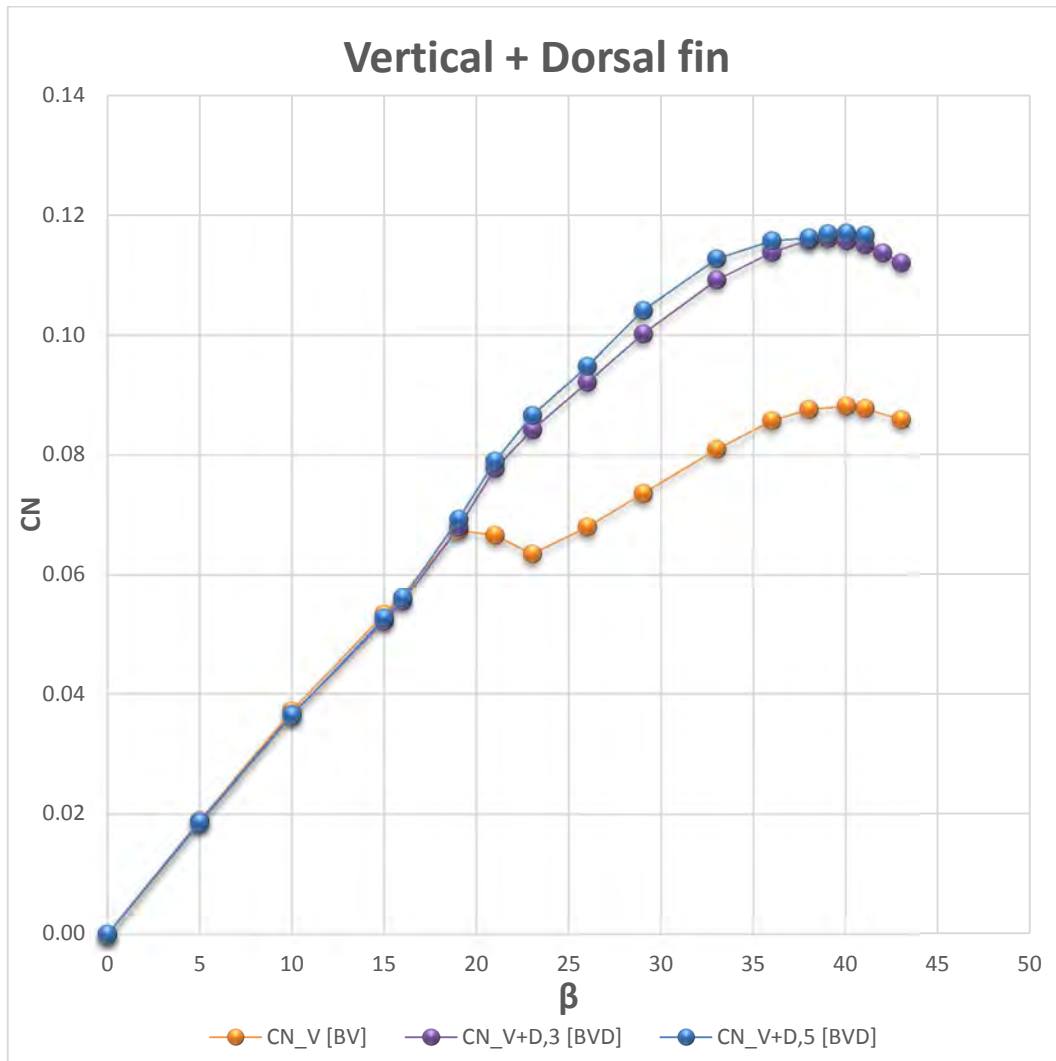


Figure 191 – Yawing moment coefficient coincidence between Vertical + Dorsal summation of BVD configuration and Vertical contribution of BV configuration for Dorsal no.3 & Dorsal no.5.

Again it may seem strange that, however is an area addition which intervenes in the aerodynamics. So with a larger area should be increased at least the slope in linear range.

Actually happens that with the addition of the dorsal, the vertical work less as explained in chapter 5. In Figure 192 there is the comparison between the curve of vertical in BV configuration and of the vertical in BVD configurations. We can evaluate for this parameterization the reduction of work of the vertical concern the 60 % of dorsal fin surface variation.

We see that the vertical tail, working less and less in proportion to the increase of the dorsal fin height. This proportionality is maintained both in the linear regime that in the nonlinear regime. There is a difference of slope because we are neglecting the contribution of the dorsal fin that would bring the two gradients to coincide (see Figure 192 & 190).

These graphs make it possible to identify for example optimum geometry between those analyzed for a particular stability performance.

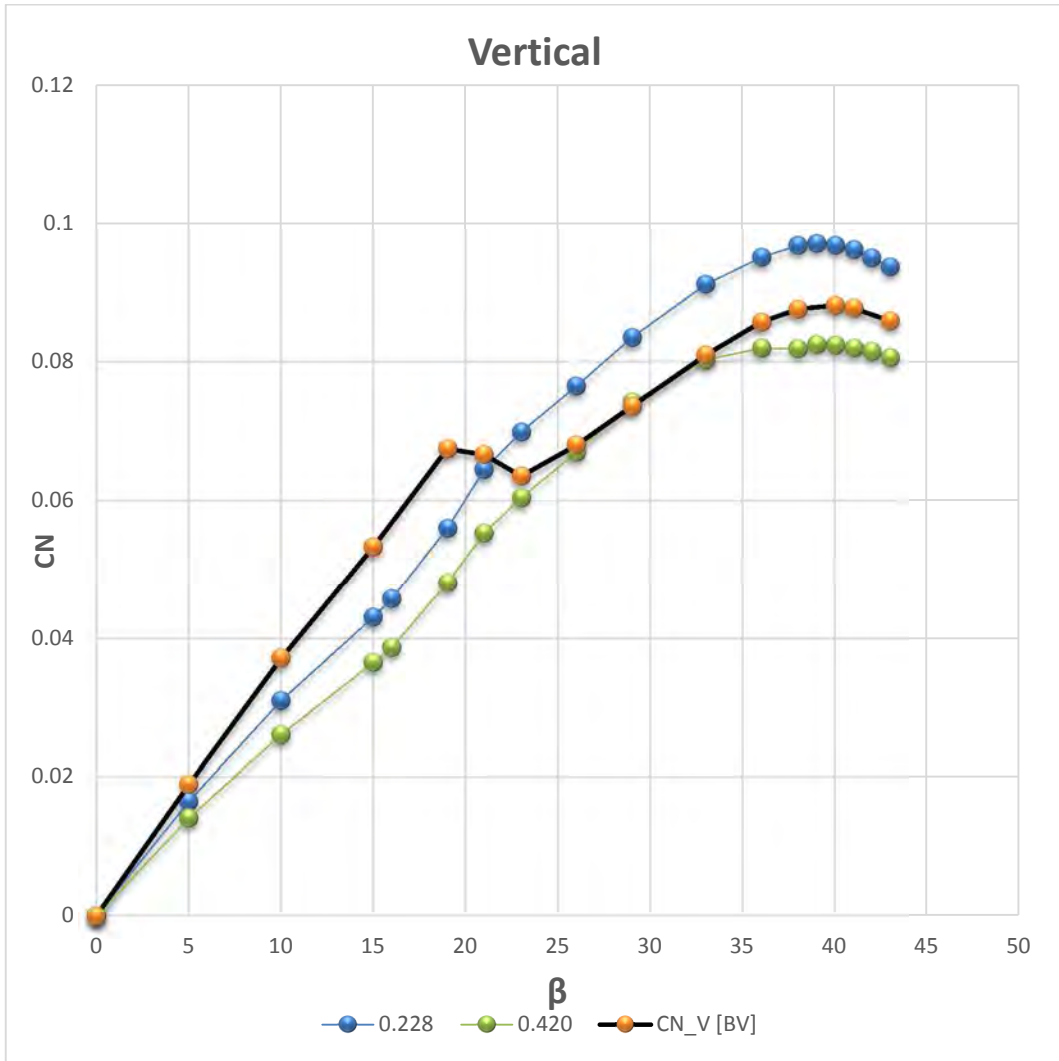
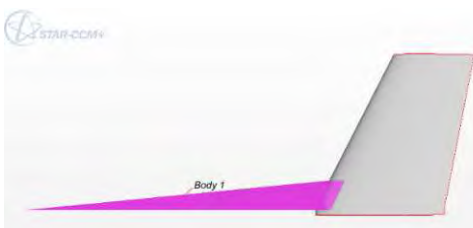


Figure 192 – How the vertical work less in BVD configuration with respect the Vertical contribution of BV configuration for Dorsal no.1 & Dorsal no.3.

6.5.5 CHANGE OF L,df & h,df, TO KEEP SURFACE CONSTANT AND VARY THE SWEEP

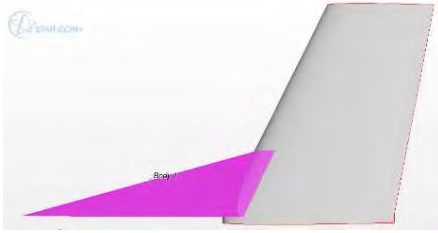
I list below the analyzed dorsal for this parameterization flanking each image whit a summary table of the geometric parameters resulting. In red there is the parameter that we are changing for this specific parameterization which is the considered parameter to distinguish one from the other, i.e., that one specified in the legend of the following graphs.

No.1)



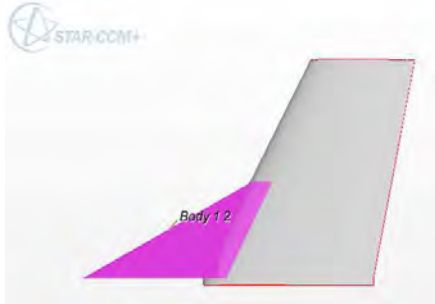
h_v [m]	S_v [m ²]	S_{df} [m ²]	$\phi_{o,v}$ [°]
0.2434	0.040	0.012	26.600
$\phi_{o,df}$ [°]	h_{fd} [m]	L_{df} [m]	L_{df}/Cr_v
85.010	0.047	0.533	2.665
L_{v-df}	L_{v-df}/L_{df}	Cr_{fd}	Cr_v
0.023	0.044	0.510	0.200
h_{df}/h_v	L_{df}/h_{df}	S_{df}/S_v	ΔAR
0.191	11.438	0.314	-31%

No.2)



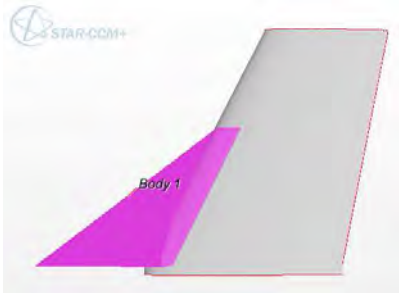
h,v [m]	S,v [m²]	S,df [m²]	φ_{o,v} [°]
0.2434	0.040	0.012	26.600
φ_{o,df} [°]	h,fd [m]	L,df [m]	L,df/Cr,v
77.065	0.0756	0.329	1.645
Lv-df	Lv-df/ L,df	Cr,fd	Cr,v
0.0378	0.1150	0.291	0.2
Ldf/Cr,v	L,df/h,df	S,df/S,v	Δ AR
1.645	4.352	0.314	-31%

No.3)



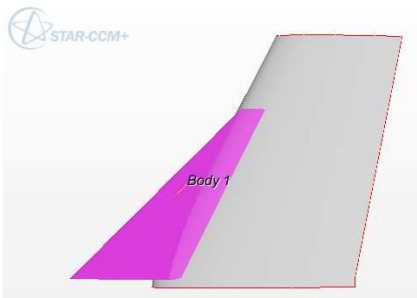
h,v [m]	S,v [m²]	S,df [m²]	φ_{o,v} [°]
0.2434	0.040	0.012	26.600
φ_{o,df} [°]	h,fd [m]	L,df [m]	L,df/Cr,v
64.959	0.108	0.231	1.154
Lv-df	Lv-df/ L,df	Cr,fd	Cr,v
0.054	0.234	0.177	0.200
h,df/h,v	L,df/h,df	S,df/S,v	Δ AR
0.443	2.140	0.315	-31%

No.4)



h,v [m]	S,v [m²]	S,df [m²]	φ_{o,v} [°]
0.2434	0.040	0.012	26.600
φ_{o,df} [°]	h,fd [m]	L,df [m]	L,df/Cr,v
49.950	0.145	0.172	0.860
Lv-df	Lv-df/ L,df	Cr,fd	Cr,v
0.072	0.421	0.100	0.200
h,df/h,v	L,df/h,df	S,df/S,v	Δ AR
0.594	1.189	0.315	-31%

No.5)



h,v [m]	S,v [m²]	S,df [m²]	φ_{o,v} [°]
0.2434	0.040	0.012	26.600
φ_{o,df} [°]	h,fd [m]	L,df [m]	L,df/Cr,v
40.037	0.172	0.145	
Lv-df	Lv-df/ L,df	Cr,fd	Cr,v
0.086	0.596	0.058	0.200
h,df/h,v	L,df/h,df	S,df/S,v	Δ AR
0.707	0.840	0.315	-31%

Figure 193 – φ_{o,df} parameterization, geometry viewing characteristic values.

In the graphs the curves are distinguished according to the value of φ_{o,df}.

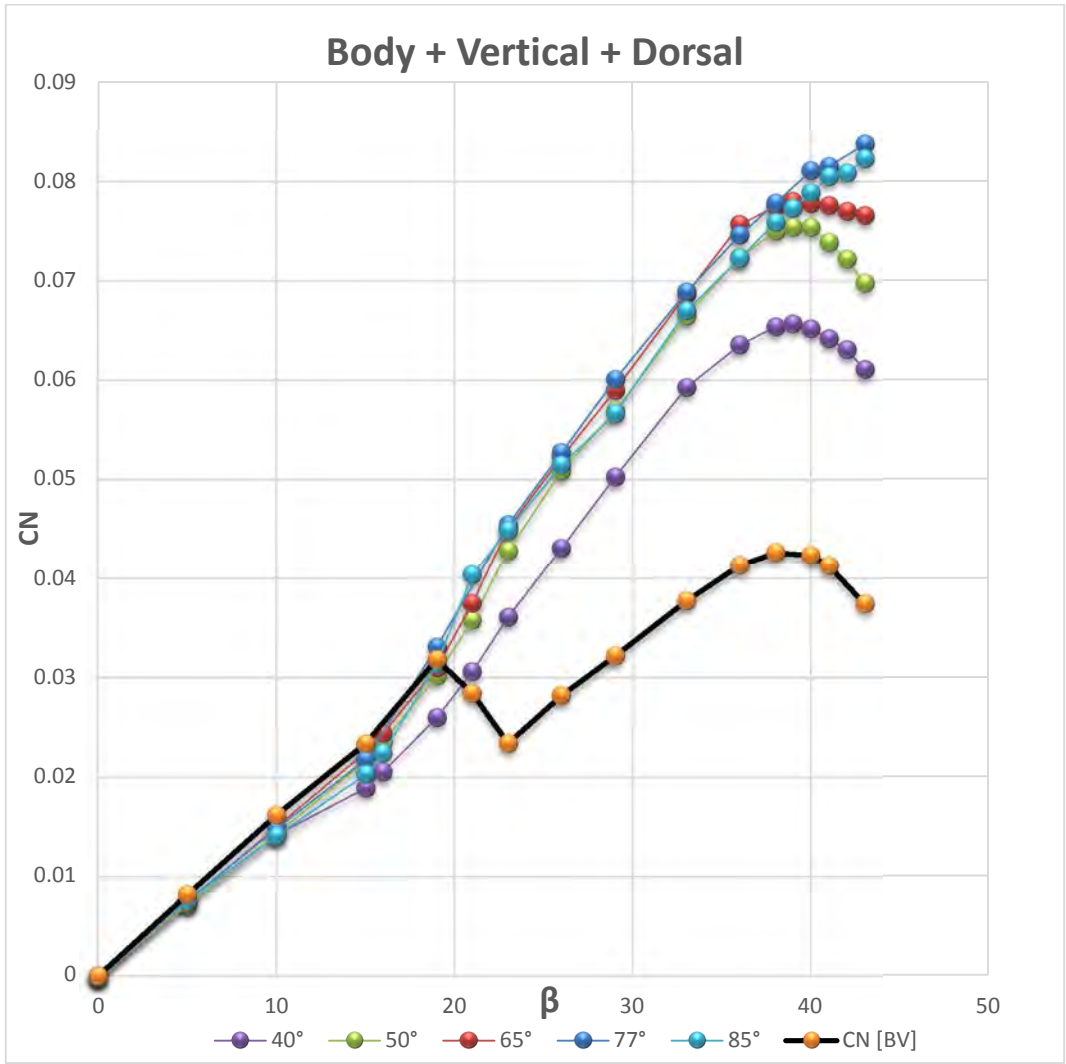


Figure 194 – Yawing moment coefficient of total contribution of BVD configuration.

As we can see in the Figure 194 the trends in the linear range show a correspondence to all the curves. In general, a slight decrease in slope by increasing sweep angle of the dorsal fin. In particular for the dorsal of 40° there is a slightly reduction of stability. The trends in the non-linear range show a rise in the CN increasing the sweep angle until the dorsal of 77°. A rise of the angle-of-stall is determined with increasing dorsal sweep angle. We note also a difference in the behavior only for the dorsal with lower sweep angle, which has a stability lower than 10% compared to the other.

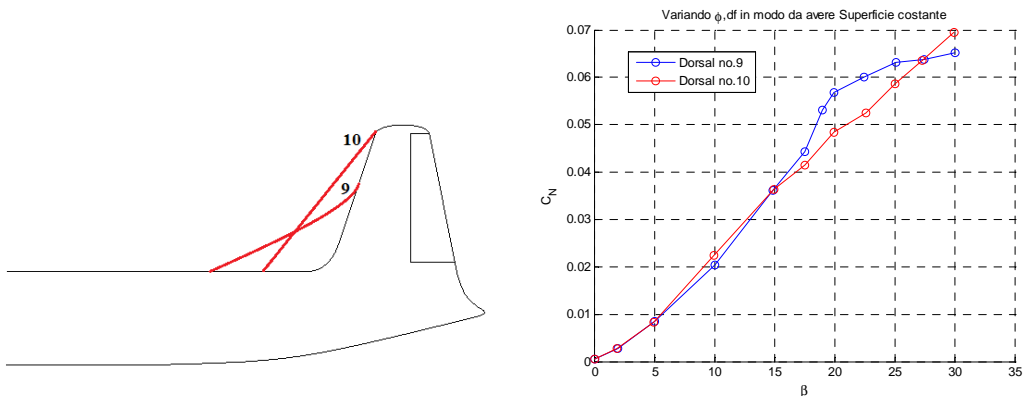


Figure 195 – Obert investigation results about Yawing moment coefficient.

There is a correspondence between the experimental and numerical data. Increasing $\varphi_{o,df}$ appears a slight increases of slope in the linear range, a strong increase of slope passing from the dorsal of 40° to the dorsal of 49° in the nonlinear range and a weak increase for the other until the dorsal of 77° .

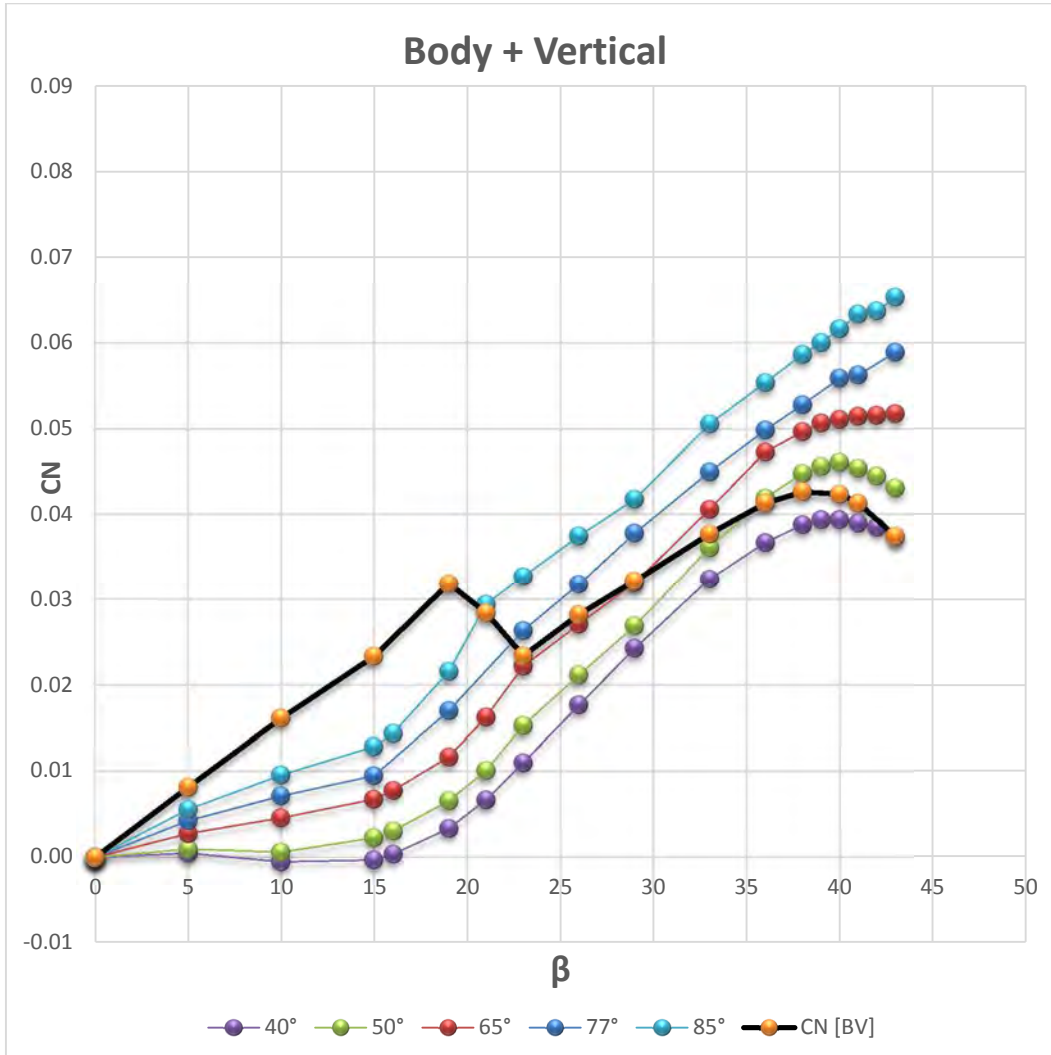


Figure 196 – Yawing moment coefficient of Body + Vertical contribution of BVD configuration.

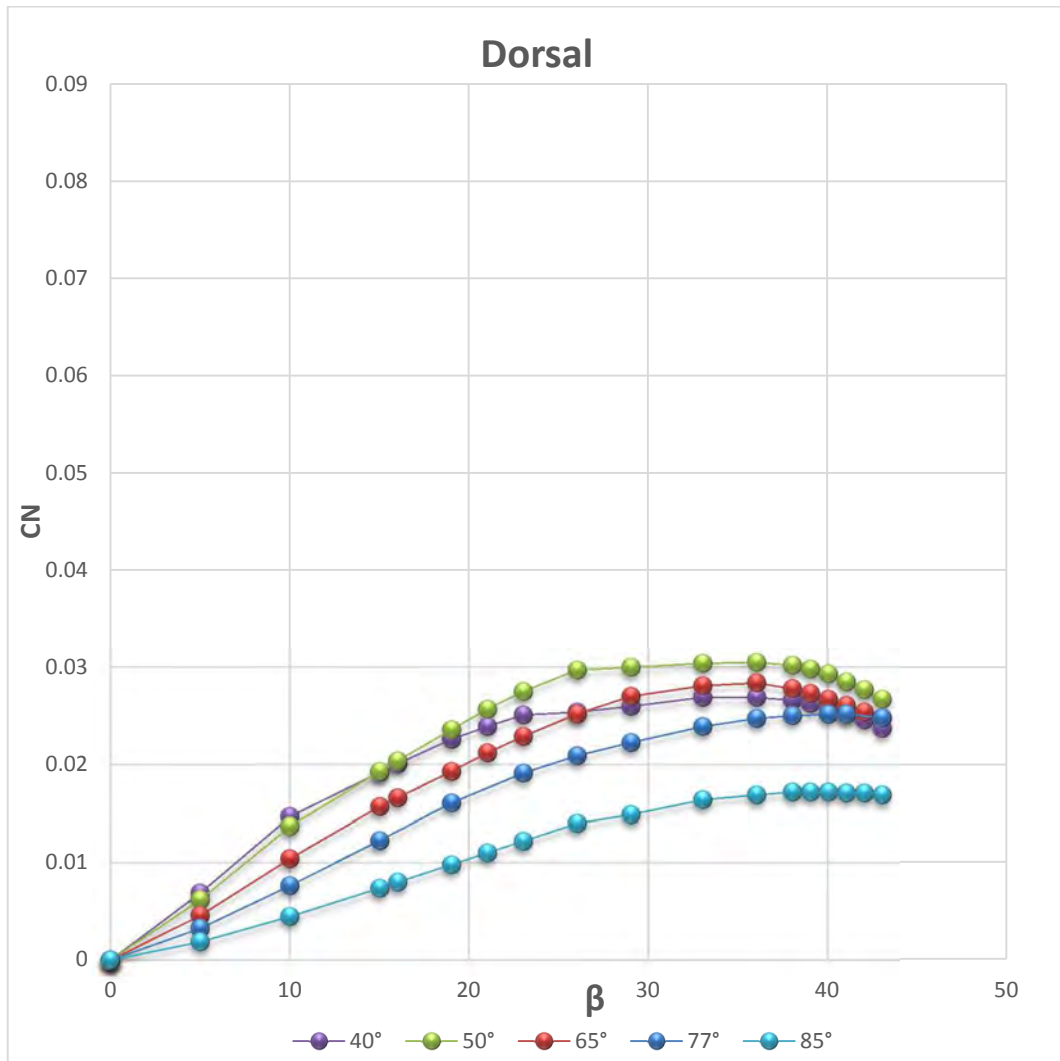


Figure 197 – Yawing moment coefficient of Dorsal fin contribution of BVD configuration.

Increasing the sweep there is initially growing of the work of the dorsal but after the dorsal of value 49° we can see a reduction of the contribution.

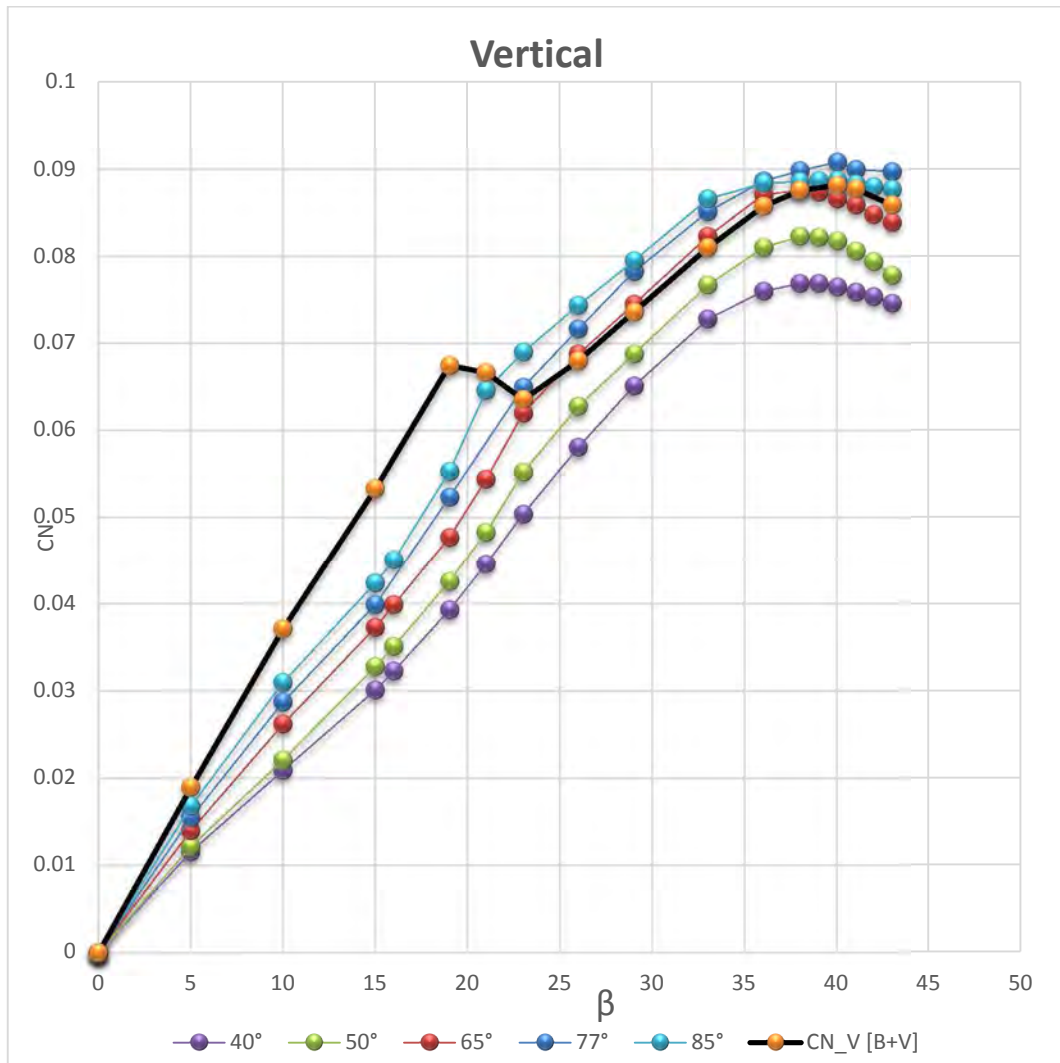


Figure 198 – Yawing moment coefficient of Body + Vertical total contribution of BVD configuration.

Increasing the sweep of the dorsal there is a strong rise of the Vertical plane work

We start from the phenomena of BASELINE to evaluate the characteristic aspects of this parameterization.

Dorsal Fin primary effect on the vertical tail stability

We compare the graph that relates the contribution of vertical, in BV configuration, with the curve of the vertical + Dorsal contribution in BVD configuration;

This chart expresses the effect of the Dorsal:

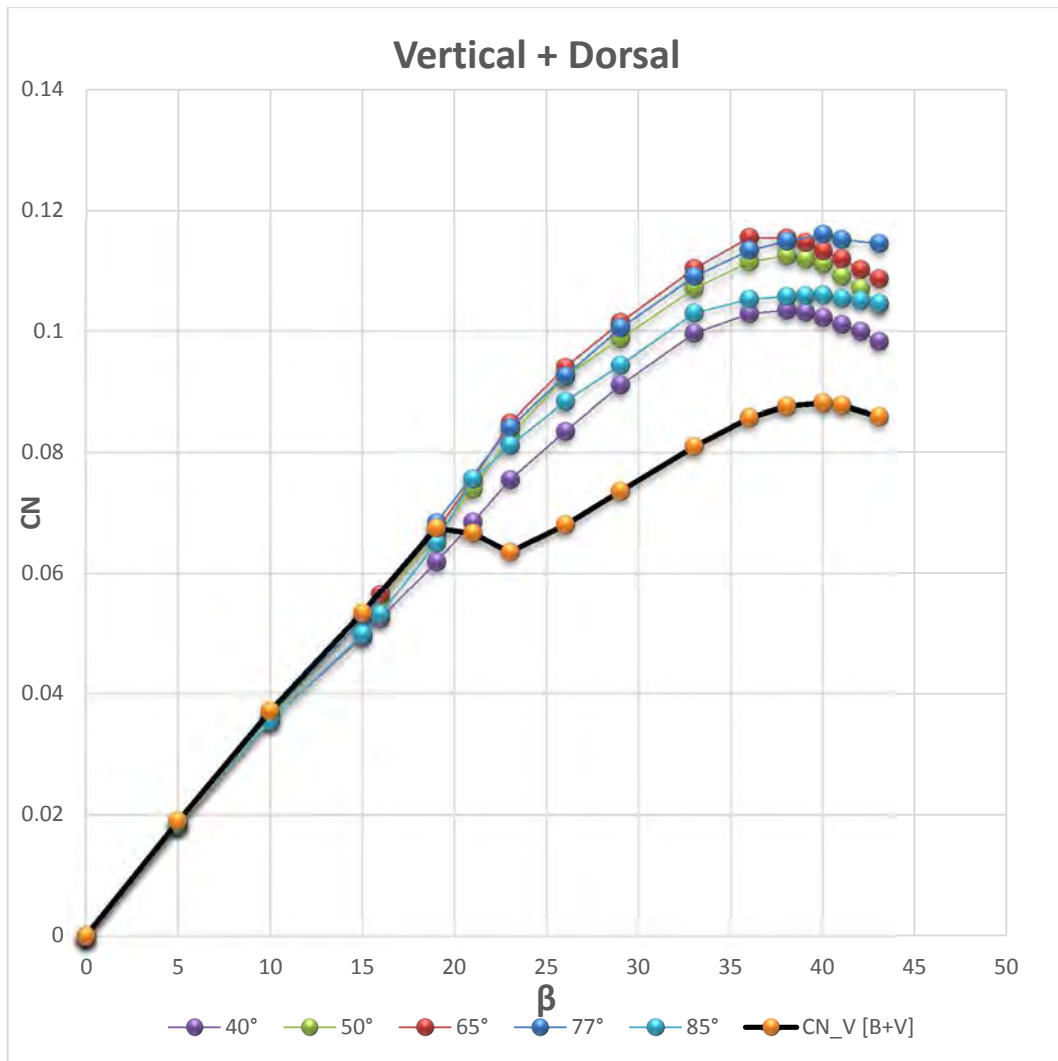


Figure 199 – Yawing moment coefficient of Vertical + Dorsal fin contribution of BVD configuration.

The trends in the linear range are exactly superimposed for different dorsal fin. The trends in non-linear range for the various dorsal fin are such that increasing the sweep angle of the dorsal a larger CN is obtained until the dorsal of 69°, after this dorsal there is a reduction of stability.

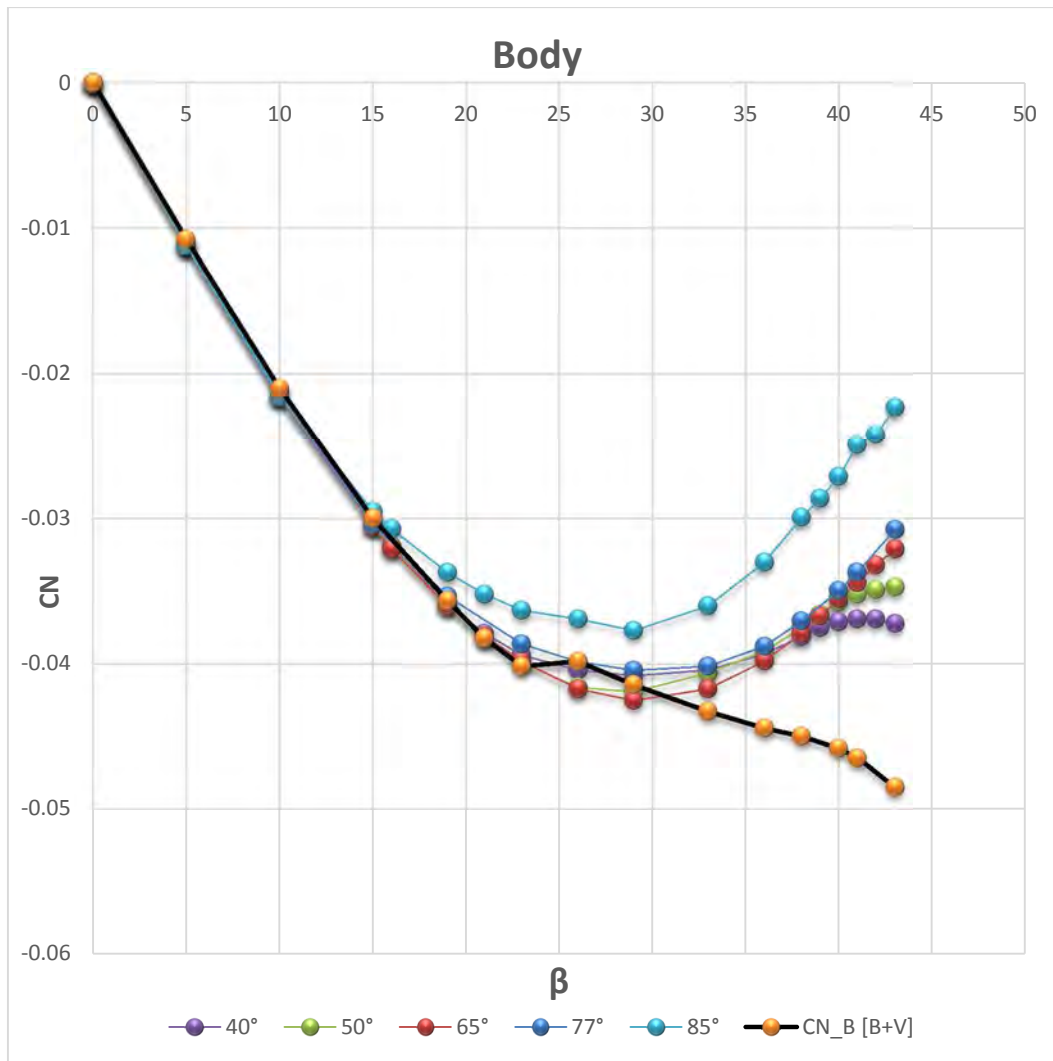
Dorsal fin effect on the fuselage stability.

Figure 200 – Yawing moment coefficient of Body contribution of BVD configuration.

It is clearly seen that the effect of dorsal fin is obtained for angles greater than 20/25°, providing a stabilizing contribution that makes the curve with positive derivative.

We should note that by varying this parameter, the geometry of the dorsal fin is modified increasing the surface area of the lower part and decreasing the surface of the upper part of the dorsal fin. With the previous parameterizations we demonstrated how the fuselage reduces its instability greater when the dorsal increases its surface extending in length, compared to height.

With this parameterization we can confirm this effect, because by increasing the arrow at constant surface it appears that the lower part of the dorsa increases and the upper part decreases. In fact, the greater effect is given by dorsal with greater sweep angle, so with a greater extension of the part close to the fuselage. In addition the dorsal with smaller sweep angle has the lower contribution at the last angle, in fact it has a particular shape where the lower part is quite negligible respect the upper part.

Dorsal Fin primary effect on the overall stability

We analyze the curve of the total CN for BV configuration with the curve of total CN of BVD configuration. Compared to the previous case concerning the effect on the vertical tail now there is a difference equal to the unstable fuselage contribution that reduce these curves.

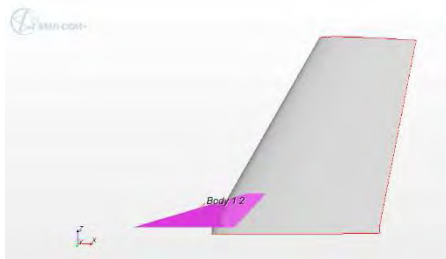
6.5.6 EQUAL SURFACE VARIATION AT TWO DIFFERENT ANGLES OF SWEEP

I list below the analyzed dorsal for this parameterization flanking each image whit a summary table of the geometric parameters resulting. In red there is the parameter that we are changing for this specific parameterization, and in blue is the considered parameter to distinguish one from the other, i.e. that one specified in the legend of the following graphs.

We propose now the comparison between two sets of curves:

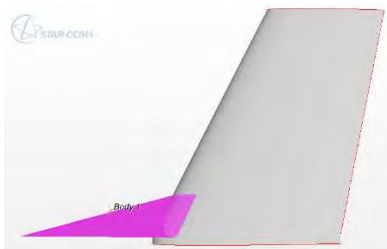
- a) Fixed angle of sweep at 77°

No.1) $S_{df}/S_v = 0.1$



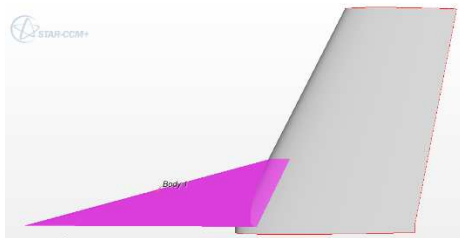
h,v [m]	S,v [m²]	S,df [m²]	φ_{o,v} [°]
0.243	0.040	0.004	26.600
φ_{o,df} [°]	h,fd [m]	L,df [m]	L,df/Cr,v
77	0.041	0.180	0.900
Lv-df	Lv-df/ L,df	Cr,fd	Cr,v
0.021	0.115	0.159	0.200
h,df/h,v	L,df/h,df	S,df/S,v	Δ AR
0.170	4.354	0.094	-10%

No.2) $S_{df}/S_v = 0.15$



h,v [m]	S,v [m²]	S,df [m²]	φ_{o,v} [°]
0.2434	0.040	0.006	26.600
φ_{o,df} [°]	h,fd [m]	L,df [m]	L,df/Cr,v
77	0.053	0.230	1.150
Lv-df	Lv-df/ L,df	Cr,fd	Cr,v
0.026	0.115	0.204	0.200
h,df/h,v	L,df/h,df	S,df/S,v	Δ AR
0.217	4.354	0.154	-15%

No.3) $S_{df}/S_v = 0.30$



h,v [m]	S,v [m²]	S,df [m²]	φ_{o,v} [°]
0.2434	0.040	0.012	26.600
φ_{o,df} [°]	h,fd [m]	L,df [m]	L,df/Cr,v
77	0.0756	0.329	1.645
Lv-df	Lv-df/ L,df	Cr,fd	Cr,v
0.0378	0.1150	0.291	0.2
Ldf/Cr,v	L,df/h,df	S,df/S,v	Δ AR
1.645	4.352	0.314	-31%

Figure 201 – S,df parameterization for φ_{o,df} = 77°, geometry viewing characteristic values.

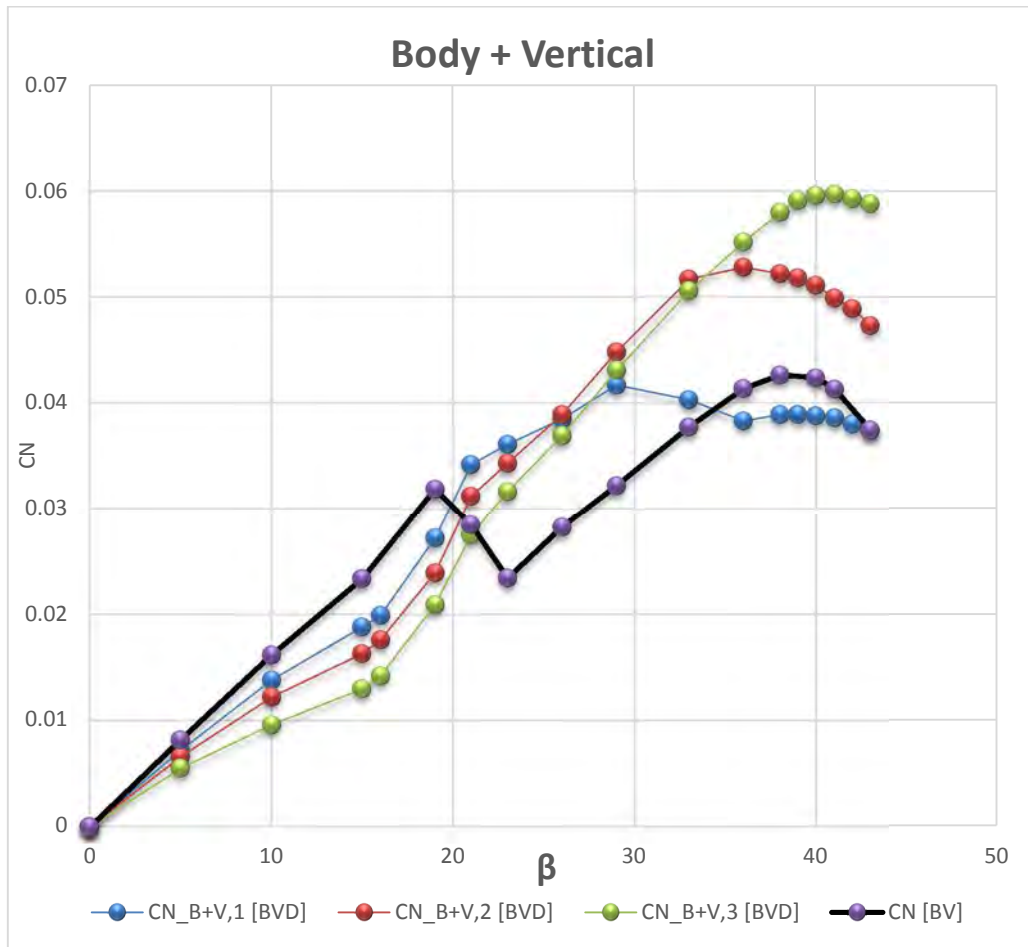


Figure 202 – Yawing moment coefficient of Body + Vertical contribution of BVD configuration for Surface variation, fixed sweep angle 77°.

Even with a very small surface we can avoid the stall that occurs without dorsal fin. For very high angles the characteristic increases of stability with dorsal fin is lost for areas too small as we can see about the smallest dorsal.

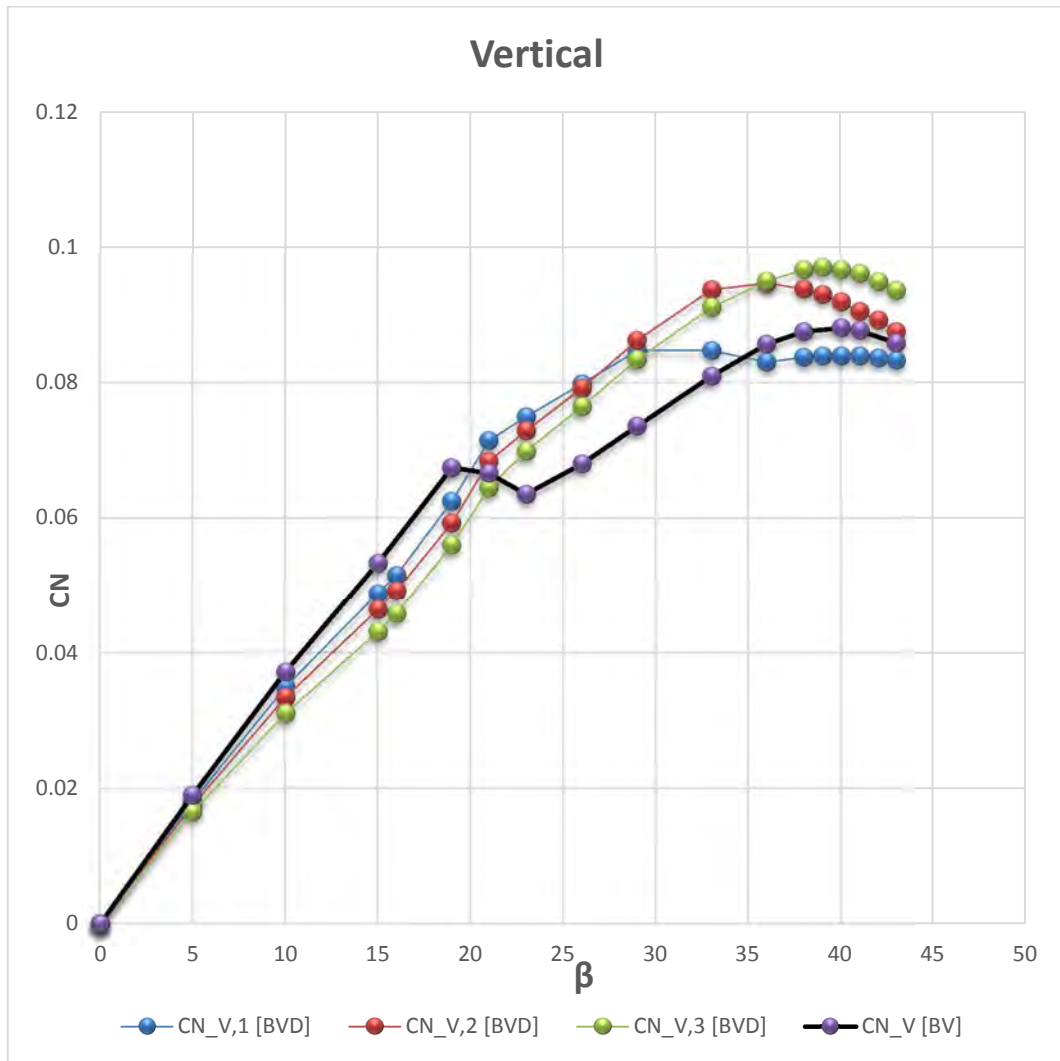


Figure 203 – Yawing moment coefficient of Vertical contribution of BVD configuration, for Surface variation fixed sweep angle 77°.

From figure 203 we can see that increasing the dorsal surface, the vertical work slightly less in the linear range. In nonlinear range there is a rise of the maximum value achievable increasing the dorsal surface. Even with a very small surface we can avoid the stall that occurs without dorsal fin. For very high angles the characteristic increases of stability with dorsal fin is lost for areas too small as we can see about the smallest dorsal.

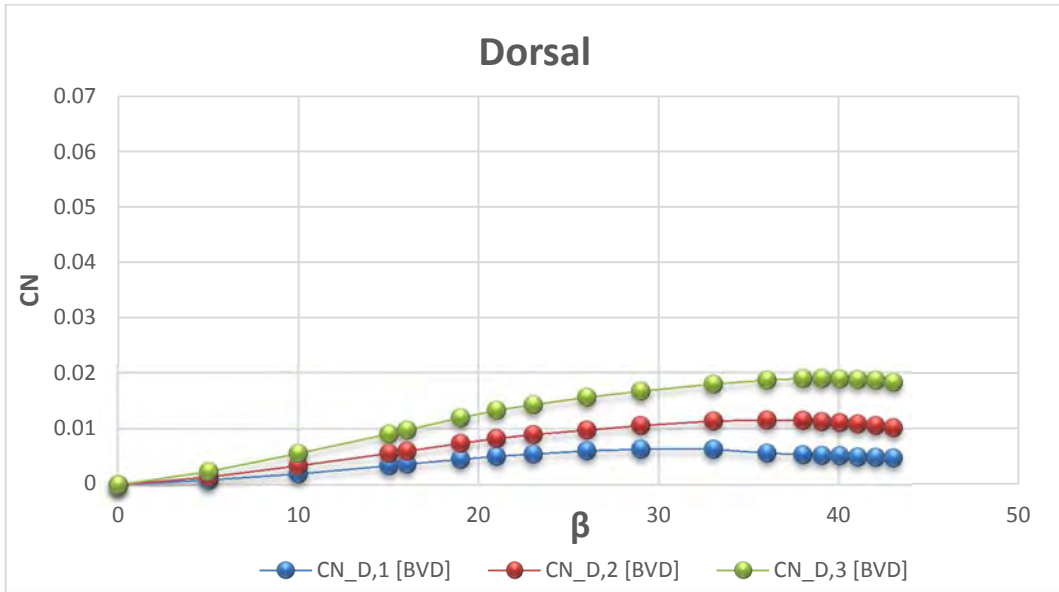


Figure 204 – Yawing moment coefficient of Dorsal fin contribution of BVD configuration, for Surface variation fixed sweep angle 77°.

Dorsal Fin primary effect on the vertical tail stability

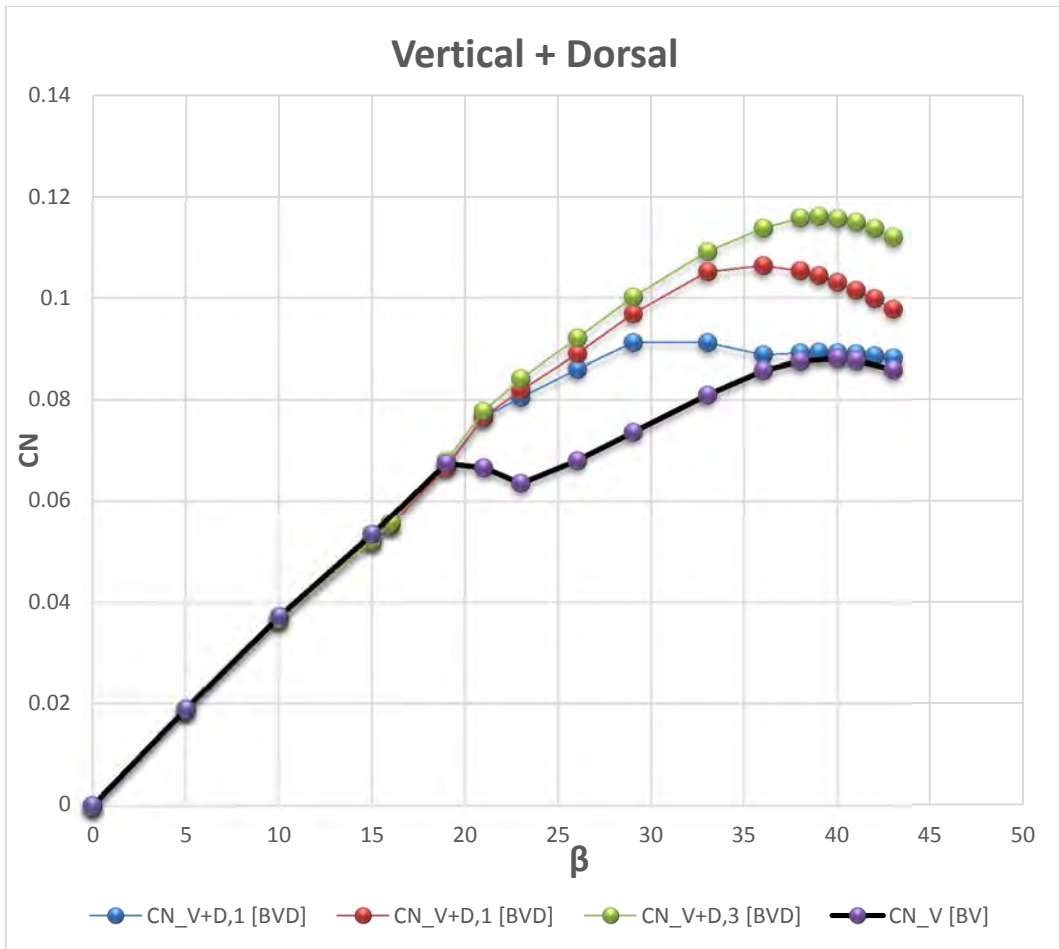


Figure 205 – Yawing moment coefficient of Vertical + Dorsal fin contribution of BVD configuration, for Surface variation fixed sweep angle 77°.

In nonlinear range there is a rise of the maximum value achievable increasing the dorsal surface. Even with a very small surface we can avoid the stall that occurs without dorsal fin. For very high angles the characteristic increases of stability with dorsal fin is lost for areas too small as we can see about the smallest dorsal.

Dorsal fin effect on the fuselage stability.

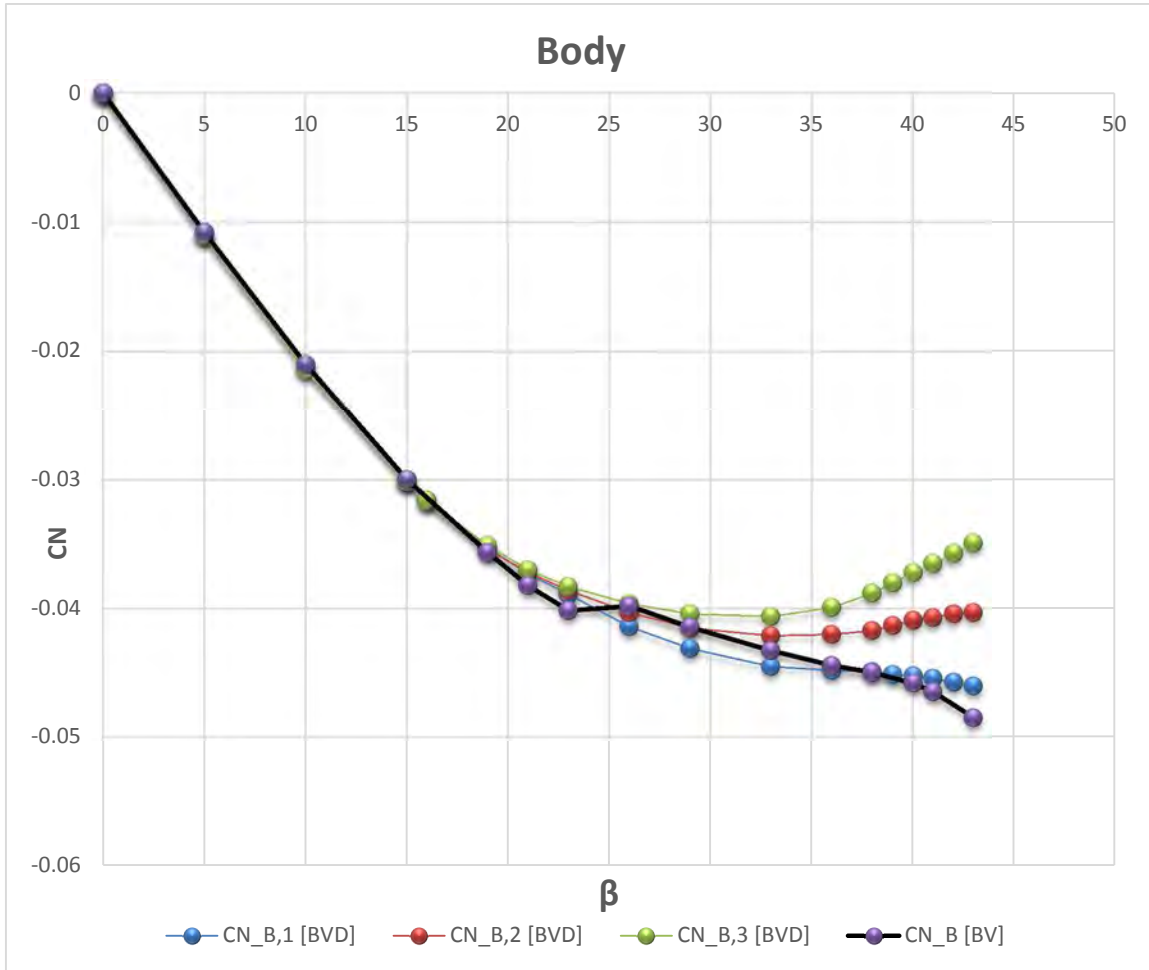


Figure 206 – Yawing moment coefficient of Body contribution of BVD configuration, for Surface variation fixed sweep angle 77°.

The smaller dorsal fin is not suitable to reduce the instability of the fuselage which still has a negative derivative. For more dorsal value 12:15, the derivative becomes positive and you get a real increase stability

Dorsal Fin primary effect on the overall stability

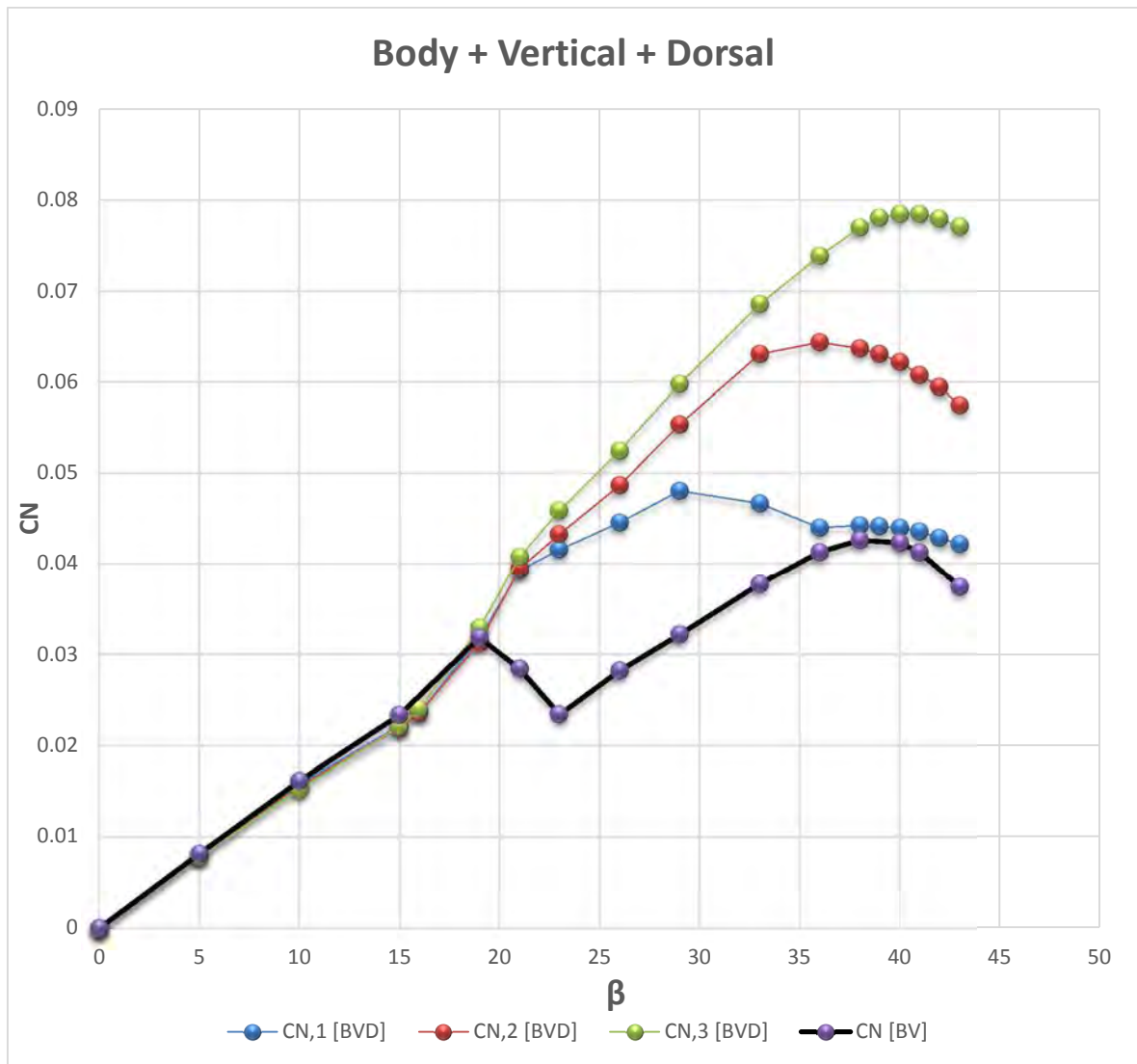
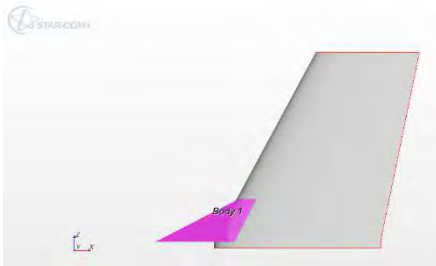


Figure 207 – Yawing moment coefficient of total contribution of BVD configuration, for Surface variation fixed sweep angle 77°.

Even with a very small surface we can avoid the stall that occurs without dorsal fin. For very high angles the characteristic increases of stability with dorsal fin is lost for areas too small as we can see about the smallest dorsal.

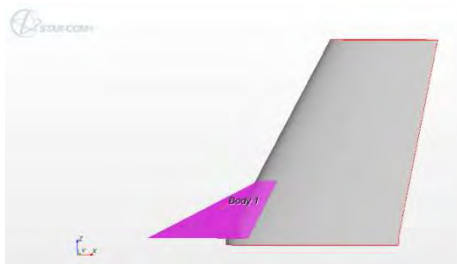
b) Fixed angle of sweep at 65°

No.1) $S_{df}/S_v = 0.1$



h,v [m]	S,v [m²]	S,df [m²]	φ_{o,v} [°]
0.243	0.040	0.004	26.600
φ_{o,df} [°]	h,fd [m]	L,df [m]	L,df/Cr,v
65	0.061	0.130	0.650
Lv-df	Lv-df/ L,df	Cr,fd	Cr,v
0.030	0.234	0.100	0.200
h,df/h,v	L,df/h,df	S,df/S,v	Δ AR
0.249	2.144	0.100	-10%

No.2) $S_{df}/S_v = 0.15$



h,v [m]	S,v [m²]	S,df [m²]	φ_{o,v} [°]
0.243	0.040	0.006	26.600
φ_{o,df} [°]	h,fd [m]	L,df [m]	L,df/Cr,v
65	0.075	0.160	0.800
Lv-df	Lv-df/ L,df	Cr,fd	Cr,v
0.037	0.234	0.123	0.200
h,df/h,v	L,df/h,df	S,df/S,v	Δ AR
0.307	2.144	0.151	-15%

No.3) $S_{df}/S_v = 0.3$



h,v [m]	S,v [m²]	S,df [m²]	φ_{o,v} [°]
0.243	0.040	0.016	26.600
φ_{o,df} [°]	h,fd [m]	L,df [m]	L,df/Cr,v
65	0.108	0.231	1.154
Lv-df	Lv-df/ L,df	Cr,fd	Cr,v
0.054	0.234	0.177	0.200
h,df/h,v	L,df/h,df	S,df/S,v	Δ AR
0.443	2.140	0.315	-31%

Figure 208 – S_{df} parameterization for $φ_{o,df} = 66°$, geometry viewing characteristic values.

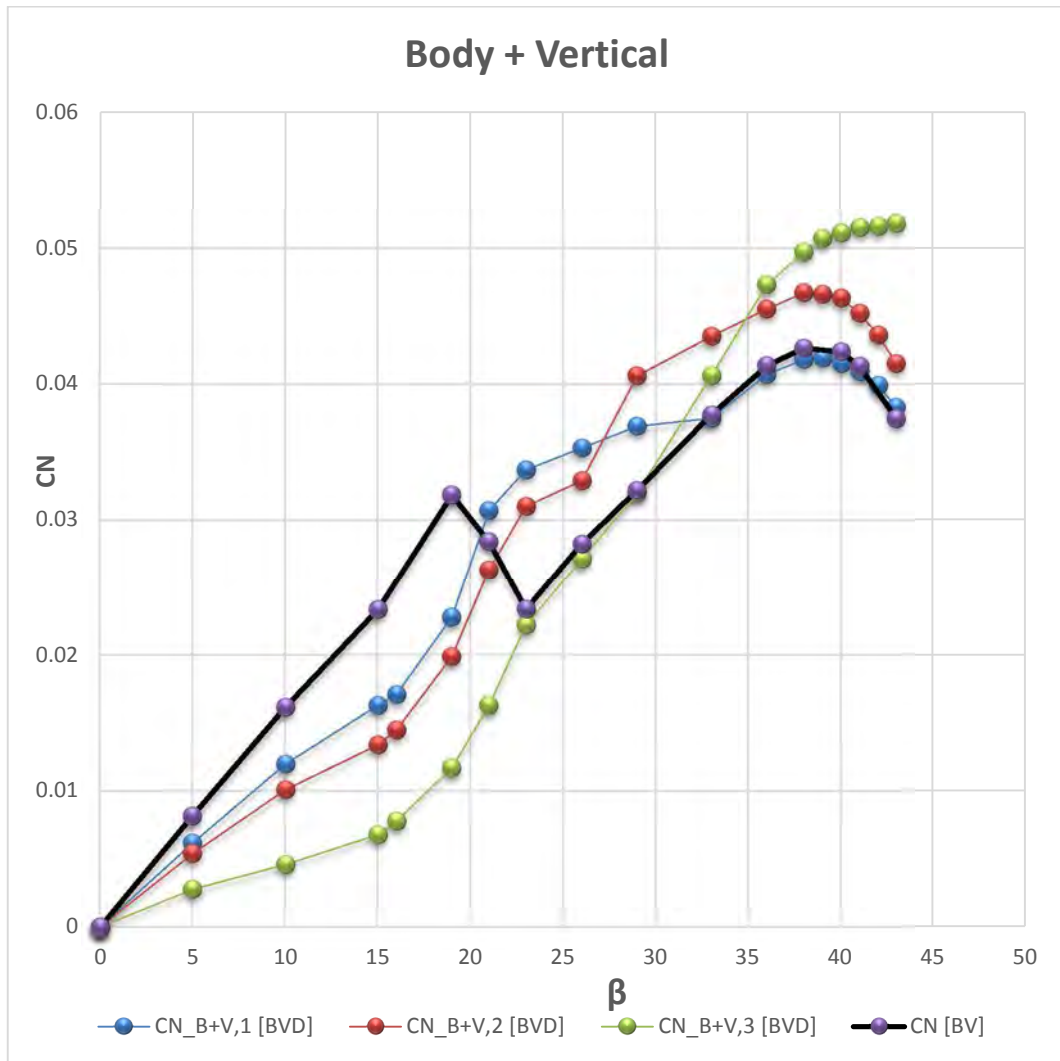


Figure 209 – Yawing moment coefficient of Body + Vertical contribution of BVD configuration fixed sweep angle 65°.

Even with a very small surface we can avoid the stall that occurs without dorsal fin. For very high angles the characteristic increases of stability with dorsal fin is lost for areas too small as we can see about the smallest dorsal.

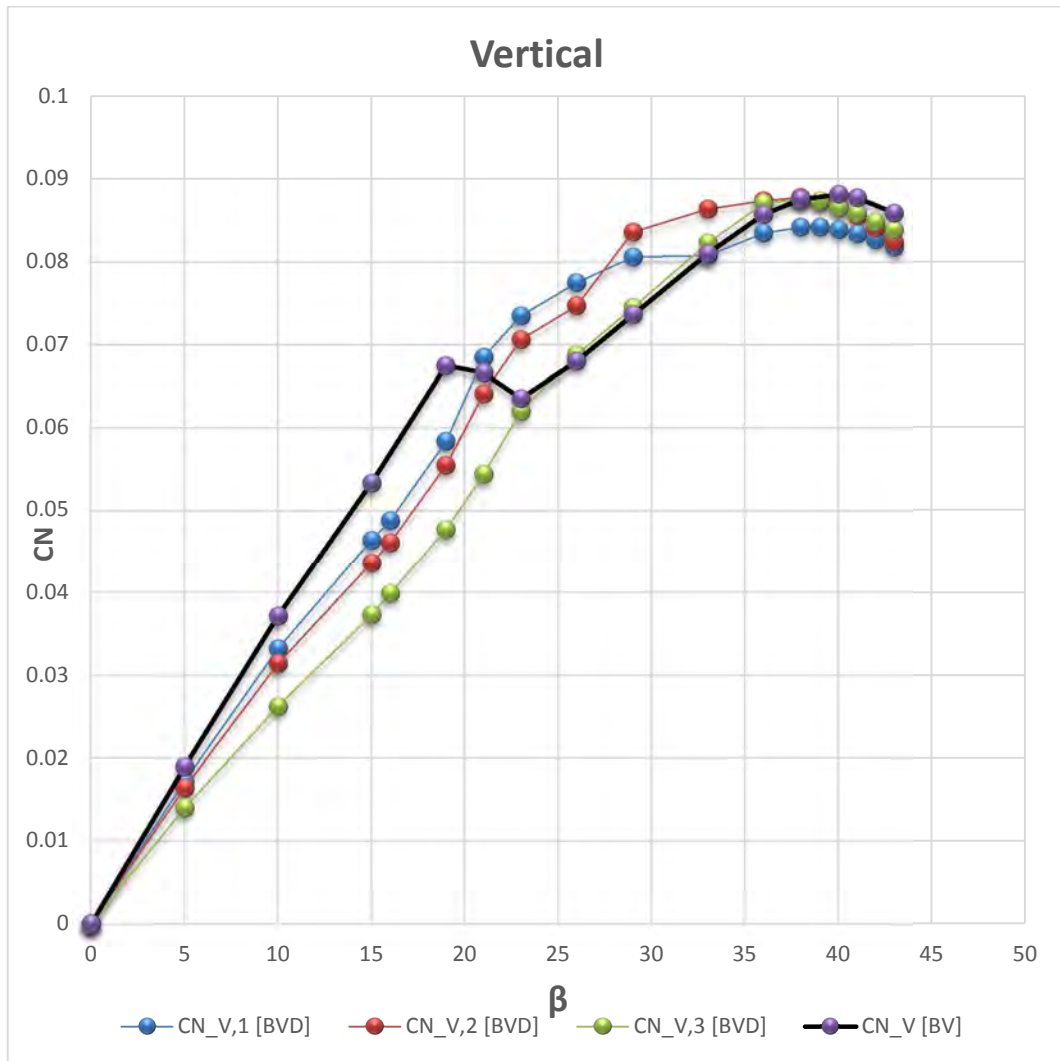


Figure 210 – Yawing moment coefficient of Body + Vertical total contribution of BVD configuration, fixed sweep angle 65°.

From figure 203 we can see that increasing the dorsal surface, the vertical work less in the linear range. This reduction is more intensive with respect the previous case about the dorsal fin with sweep angle of 77°. In nonlinear range there is a rise of the maximum value achievable increasing the dorsal surface

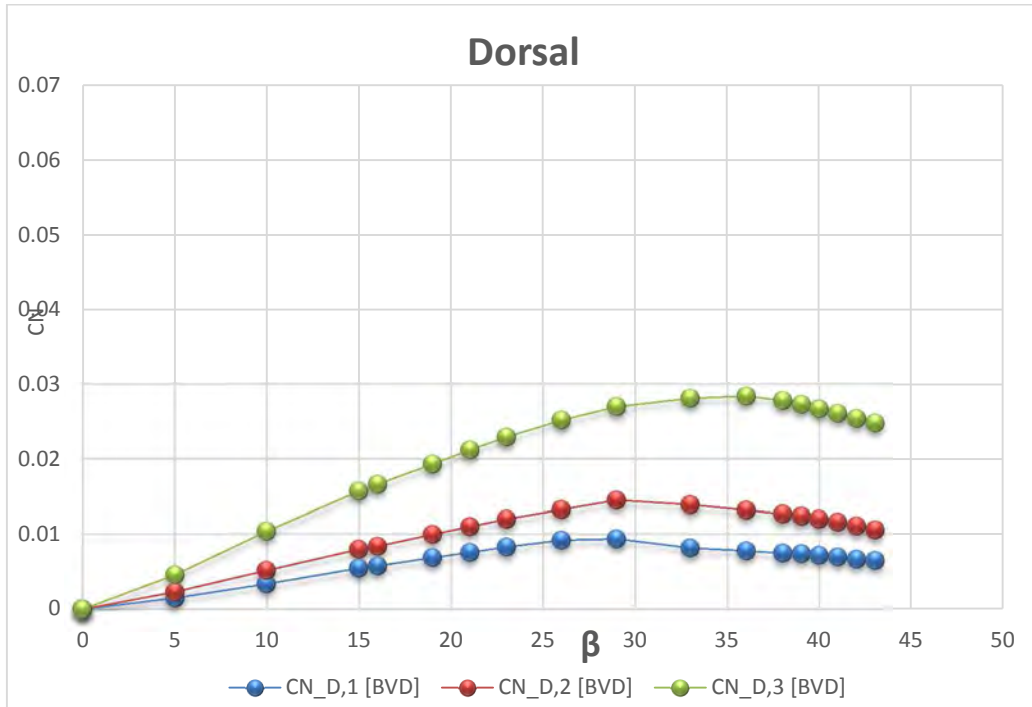


Figure 211 – Yawing moment coefficient of Dorsal fin contribution of BVD configuration fixed sweep angle 65°.

Dorsal Fin primary effect on the vertical tail stability

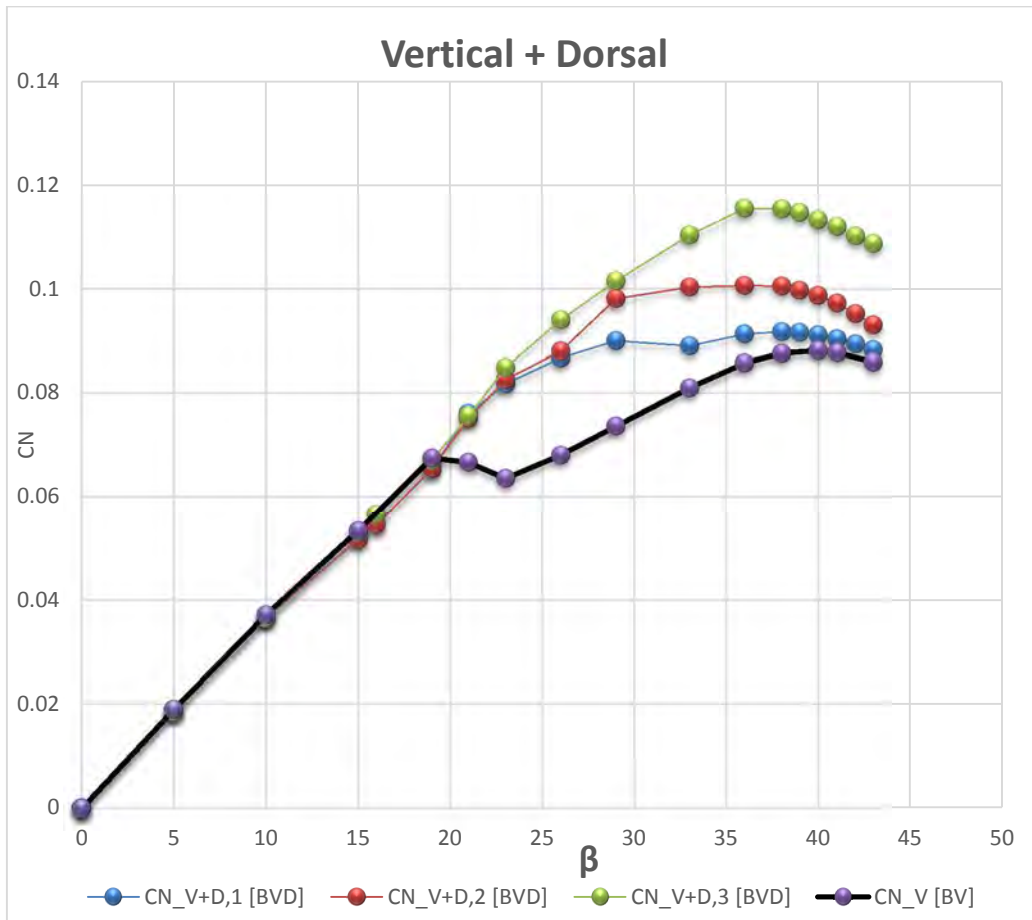


Figure 212 – Yawing moment coefficient of Vertical + Dorsal fin contribution of BVD configuration fixed sweep angle 65°.

In nonlinear range there is a rise of the maximum value achievable increasing the dorsal surface. Even with a very small surface we can avoid the stall that occurs without dorsal fin. For very high angles the characteristic increases of stability with dorsal fin is lost for areas too small as we can see about the smallest dorsal.

Dorsal fin effect on the fuselage stability.

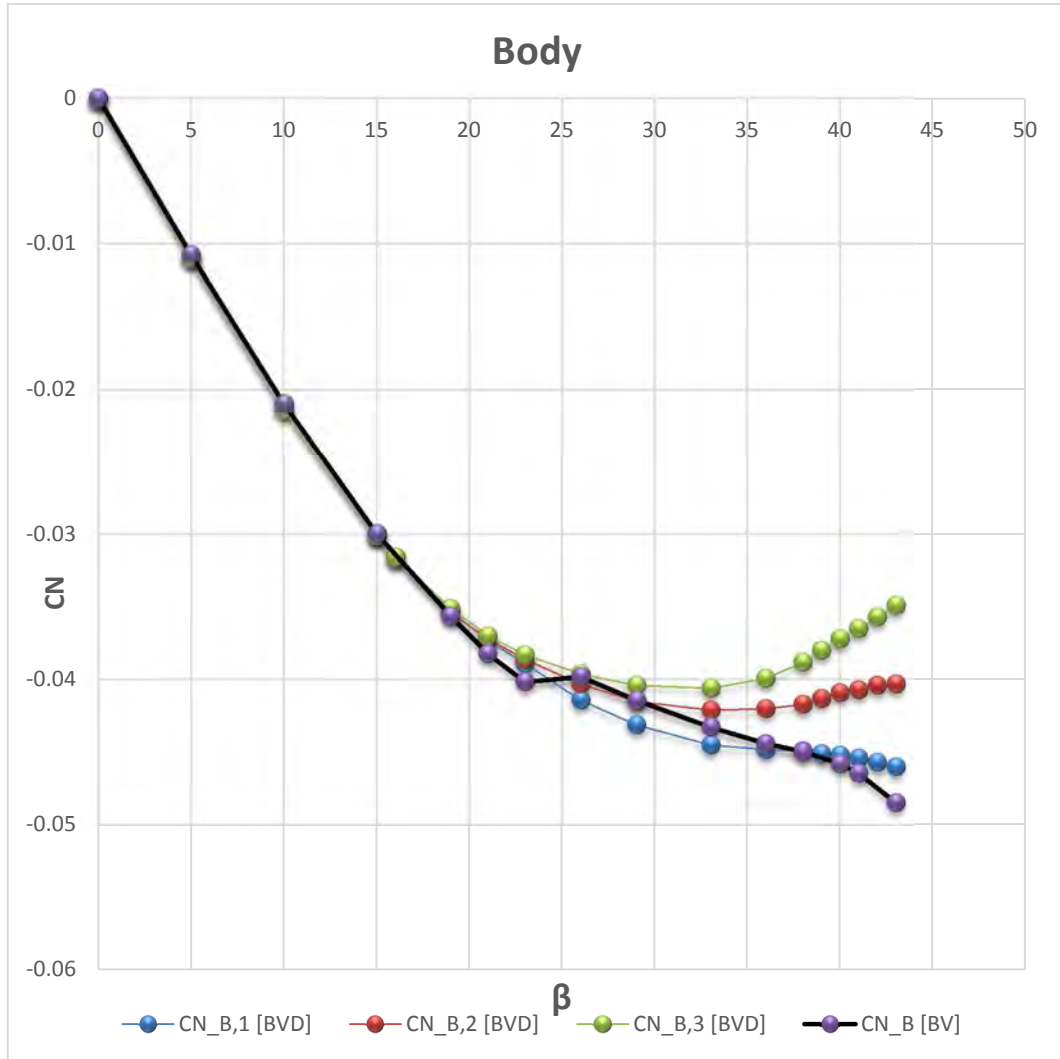


Figure 213 – Yawing moment coefficient of Body contribution of BVD configuration fixed sweep angle 65°.

The smaller dorsal fin is not suitable to reduce the instability of the fuselage which still has a negative derivative. For more dorsal value 12:15, the derivative becomes positive and you get a real increase stability

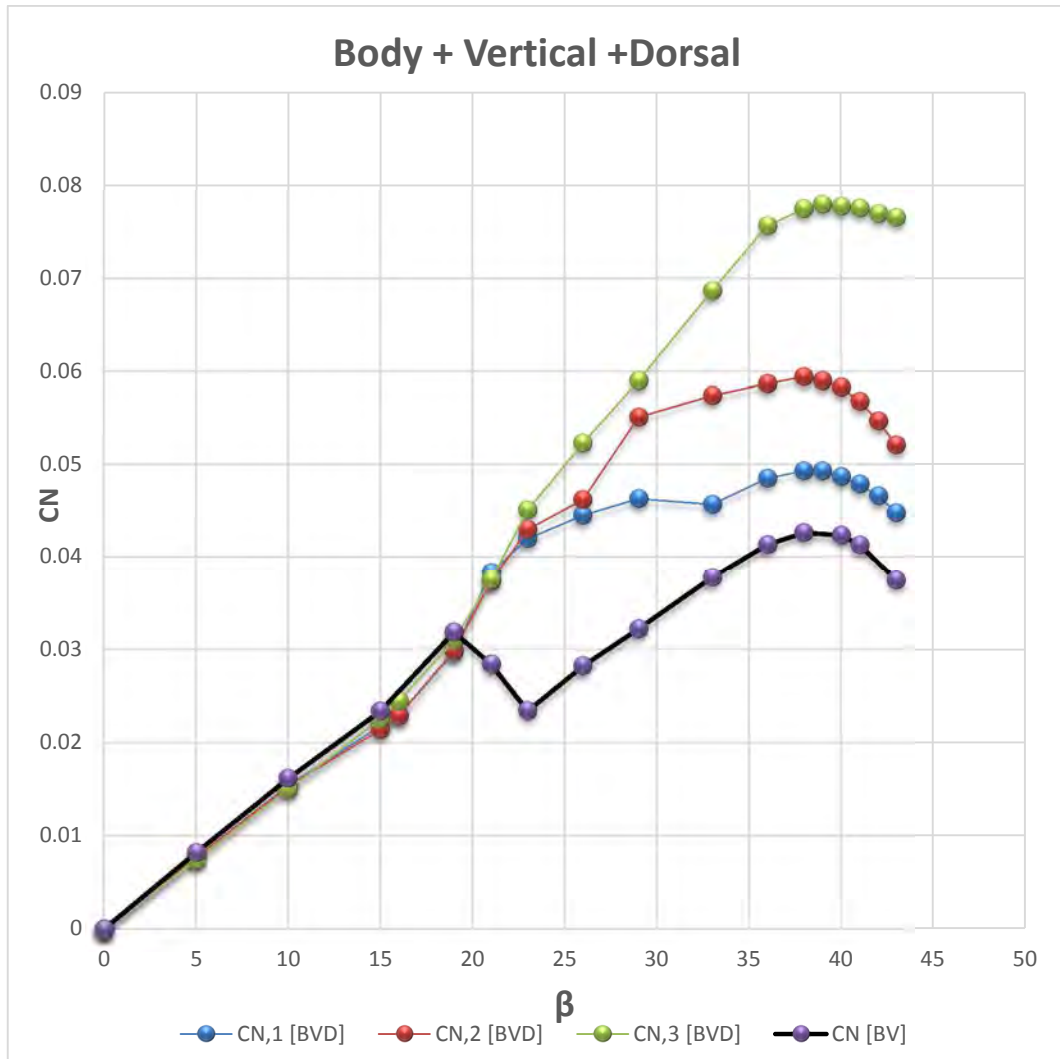
Dorsal Fin primary effect on the overall stability

Figure 214 – Yawing moment coefficient of total contribution of BVD configuration fixed sweep angle 65°.

In nonlinear range there is a rise of the maximum value achievable increasing the dorsal surface. Even with a very small surface we can avoid the stall that occurs without dorsal fin. For very high angles the characteristic increases of stability with dorsal fin is lost for areas too small as we can see about the smallest dorsal.

7 CORRELATED STUDIES

7.1 CHARACTERISTIC TIMES OF ANALYSIS

In this section we denote the characteristic times of analysis

Thanks to the calculation grid of SCOPE it was possible to perform the calculations in parallel and on multiple processors, so as to obtain a drastic reduction of the actual time of calculation.

We identify the CPU TIME that represents the necessary time machine to perform the numerical operations, which for each set of simulation involving 17 different attitude (17 angles of sideslip) is about 100 hours.

Since that on the SCOPE grid were analyzed 25 sets of simulations about different configuration are carried out in total 425 simulations for a computation time about 100(hours each set) * 25 (set) = 2500 hours.

We can sense thus temporal facilitating that gave us the using of computational grid, because thanks to it is possible to start at the same time parallel calculations to multiple sets of simulations.

Since the simulations were made starting in groups of four, the total number of hours for these analyzes was reduced by four times. $2500 \text{ (hours)}/4\text{(set each calculation)} = 625 \text{ hours}$.

But we have to consider the additional time when the calculations are failed for issues related to the management of the grid by the technical service of SCOPE.

Finally we can say that Scope allowed to perform the previous analysis in a time significantly smaller than it would have taken using a simple computer.

7.2 DRAG PENALTY

The drag penalty due to dorsal fin has been calculated by CFD and semi-empirical method.

The semi-empirical method calculates the dorsal fin contribution to aerodynamic drag as follows:

$$C_{D0} \text{ (dorsal fin)} = C_{fe} \cdot F_f \cdot \frac{S_{wet}}{S_w} = \frac{0.455}{\log(\text{Re})^{2.58}} \cdot \left[1.03 + 2 \cdot \frac{t}{c} + 60 \left(\frac{t}{c} \right)^4 \right] \cdot \frac{S_{wet}}{S_w} \quad (3)$$

Assuming an incompressible, fully turbulent flow. The form factor is that of a thin airfoil, the typical dorsal fin has 6% thickness ratio at root. In the following chart markers represent CFD results, whereas the solid line is the result of the semi-empirical formula. The circle symbol represents the friction (shear stress) contribution to drag, evaluated for the dorsal fin only. The diamond symbol represents the difference between the CD0 of the whole configuration with dorsal fin and the CD0 of the whole configuration without dorsal fin. The equivalent flat plate approximation (solid line) is closer to the CD0f calculated by CFD (circle markers).

The ΔCD_0 curve includes the aerodynamic interference effects. One expects that the difference between configurations with and without dorsal fin should be equal to the skin friction contribution, but the coupling of the dorsal fin with the vertical tailplane (and fuselage) is beneficial to the aerodynamic drag of the latter. The effect is that the skin friction of the dorsal fin is fairly predicted by the semi-empirical approach (circle markers), but the pressure drag of the vertical tailplane decreases, such that the whole drag coefficient is lower than predicted (diamond markers) by the equivalent flat plate approximation. The difference between circle and diamond markers is a coarse measure of the aerodynamic interference. It is interesting to note that for a dorsal fin planform area up to $\frac{1}{4}$ of the vertical tail planform area gives no increase in aerodynamic drag. Hence one can get the benefit of a dorsal fin without an aerodynamic drag penalty in cruise.

Data is reported in table.

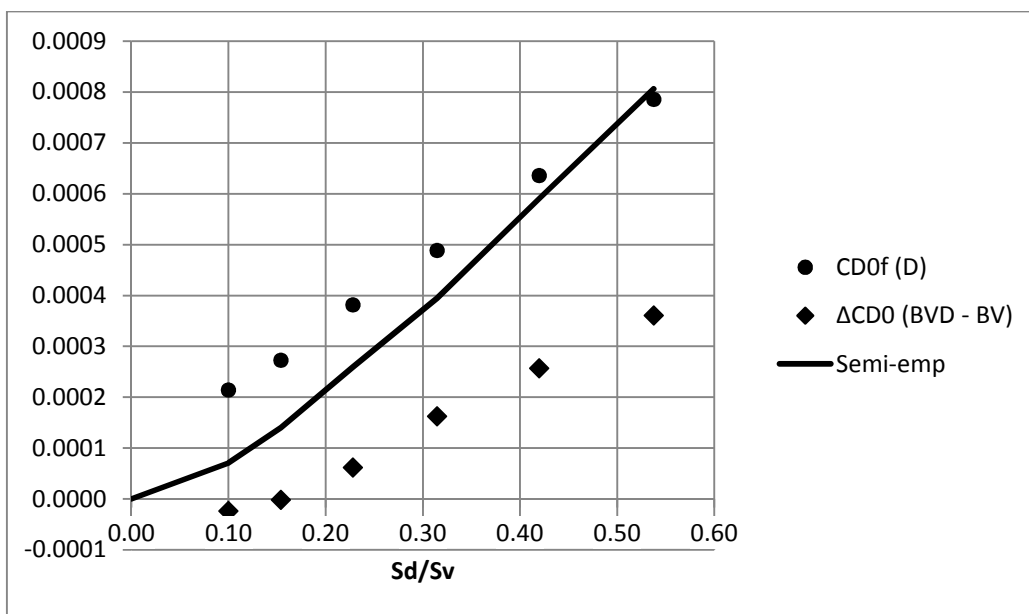


Figure 215 – Summary of drag penalty results compared with semi-empirical method.

		ΔCD_0 (BVD - BV)	CFD	
Swet (D) (m ²)	Sd/Sv	CFD	Semi-emp	CD0f (D)
0	0	-	0	0
0.003	0.10	0.0000	0.0001	0.0002
0.006	0.15	0.0000	0.0001	0.0003
0.012	0.23	0.0001	0.0003	0.0004
0.018	0.31	0.0002	0.0004	0.0005
0.027	0.42	0.0003	0.0006	0.0006
0.037	0.54	0.0004	0.0008	0.0008

Table 5 – Summary of drag penalty results and geometry indication.

We can therefore conclude that the choice of a dorsal fin can not be compromised by problems relating to the increase drag, in particular of CD_0 .

7.3 REYNOLDS EFFECT INVESTIGATION

To give general validity at this study it was decided to focus attention on the role of the Reynolds number which we can control easily with tools that offers the CFD. The Reynolds number was evaluated with respect to the size of the mean aerodynamic chord of the vertical.

Analyzes carried out up to this point were septate to the value of the Reynolds number of 9000000, which is representative for a model to be tested in the wind tunnel.

Analyzes were then conducted for a Reynolds number of 10 million, an order of magnitude larger than those carried out for the previous parametric study.

	Reynolds Number	Viscosity μ [Pa*s]
Caso 1	1.00E+07	1.67E-06
Caso 2	9.00E+05	1.86E-05
Parametri Fissati		
$\rho = 1.22$ [Kg/m ³]	Vel. = 83 [m/s]	Vertical m.a.c. = 0.165198 [m]

Table 6 – Parameter definition for Reynolds investigation.

In the Figures 218 there is a comparison between analyzes carried out with the two different Reynolds numbers cited in tab 7. It summarizes the effects of the contributions for Body and Vertical part of configuration BV.

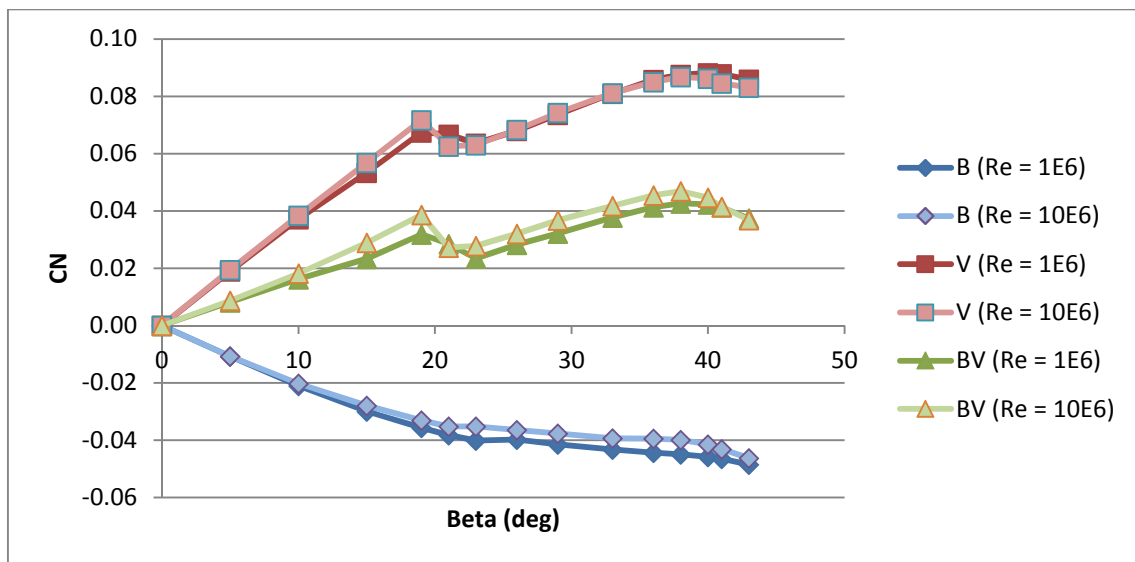


Figure 216 – Reynolds analysis for the contributions of BV configuration.

We can see a strong correlation between the two simulations results, so this lightens us of the Reynolds number problem. The level of this preliminary work aims to identifying qualitative trend, which as shown in Figures 217 do not change, and thus the feedback, certainly can't be compromised by errors on the Reynolds number evaluation.

We can also calculate the deviation between the two simulations for each individual contribution.

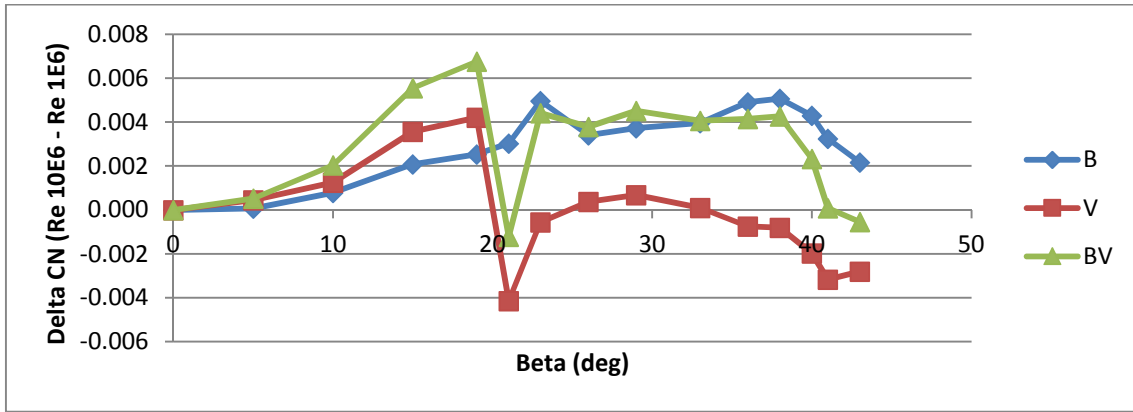


Figure 217 – Difference between the results with different Reynolds numbers for the contributions of BV configuration.

In the Figures 219 there is a comparison between analyzes carried out with the two different Reynolds numbers cited in tab 7. It summarizes the effects of the contributions for Body, Vertical and Dorsal part of configuration BVD.

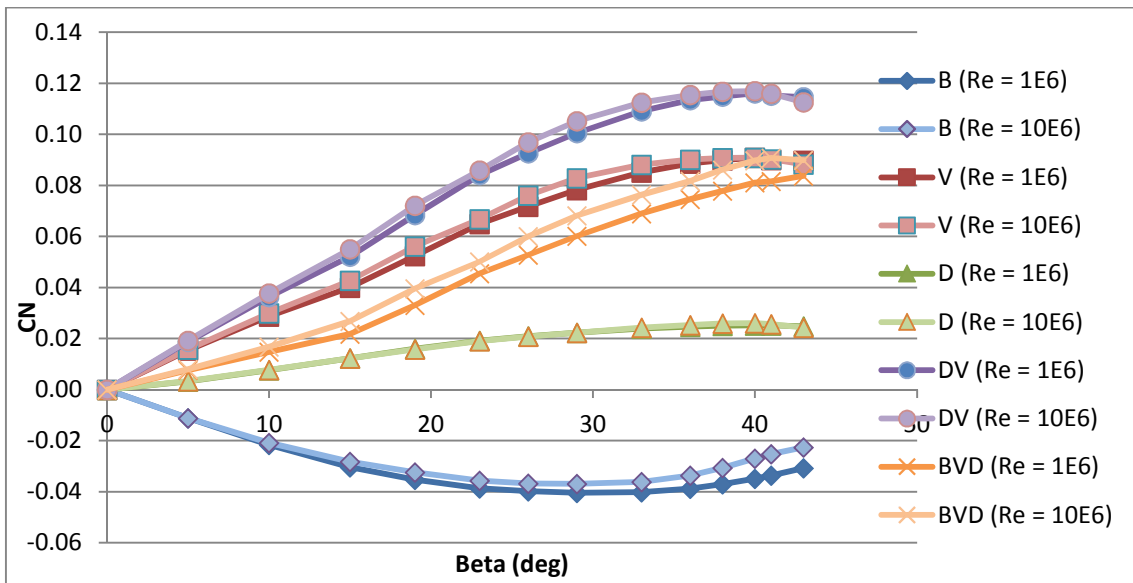


Figure 218 – Reynolds analysis for the contributions of BVD configuration.

We can also calculate the deviation between the two simulations for each individual contribution.

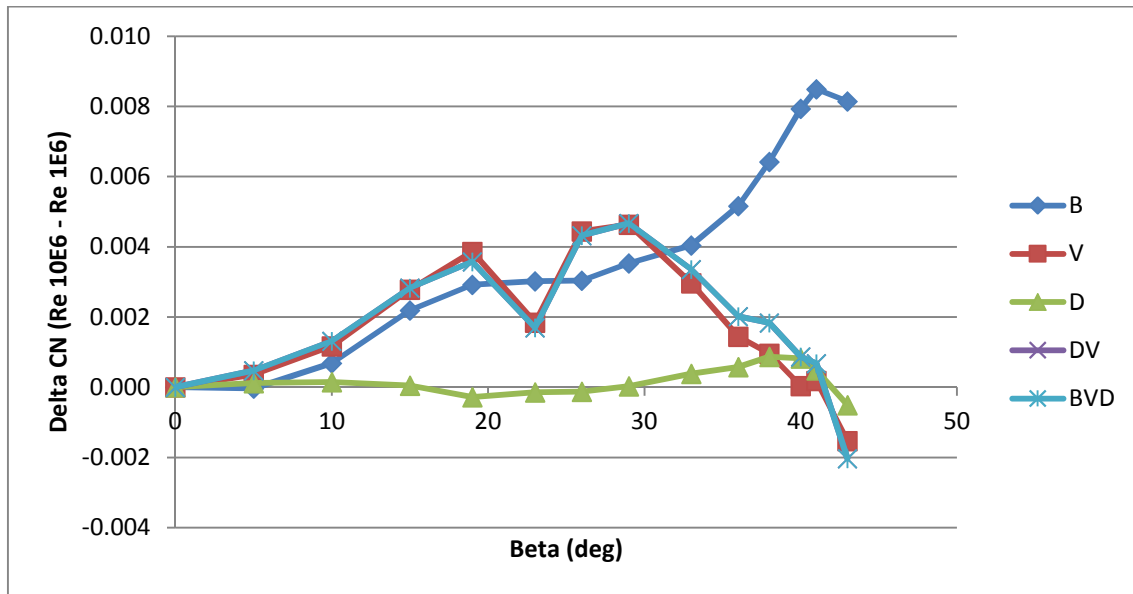


Figure 219 – Difference between the results with different Reynolds numbers for the contributions of BVD configuration.

For both cases we can say that the problem of the number of Reynolds number can't compromise the feedback on the results of the CFD. Trends between the curves strongly respondents is confirmation of little relevance that takes the problem of the Reynolds number than the preliminary level of the work that we are facing right now.

8. CONCLUSION

The CFD results confirm to what is stated by literature [3] relatively to the aerodynamics phenomenology that takes place in the presence of dorsal fin. Starting from the validity of the CFD method, thanks to the realized parametric study we can evaluate the qualitative trend varying the geometry. We can then identify how the variation of a particular geometric parameter affects the performance of directional stability, mainly on the yawing moment.

Are presents the qualitative trends for the dorsal fin height parameterization, then the behavior due to 60 % of dorsal fin surface variation by changing dorsal fin height. (Chapter 6.4.1).

Are presented qualitative trends for the dorsal fin length parameterization, then the behavior due to 60 % of dorsal fin surface variation by changing dorsal fin length. (Chapter 6.4.2)

Are presented qualitative trends for the dorsal fin surface parameterization keeping constant the dorsal fin sweep angle, then the behavior due to 60 % of dorsal fin surface variation (Chapter 6.4.5).

Are presented qualitative trends for the dorsal fin sweep angle parameterization keeping constant the dorsal fin surface (Chapter 6.4.5).

Are presented the comparison between the qualitative trends for the dorsal fin surface parameterization keeping constant the sweep angle at two different value (Chapter 6.4.6).

We can therefore conclude that the CFD analysis are a great method to evaluate such qualitative trend, and as cites the report [3] is an excellent tool to improve the knowledge and understanding of the stability increasing phenomena and work redistribution due to the dorsal fin presence.

Appendix A

1) MACRO JAVA

```
// STAR-CCM+ macro: betavar.java
package macro;
import java.util.*;
import star.common.*;
import star.base.neo.*;
import star.base.report.*;
import star.flow.*;
public class macro_betavar extends StarMacro {
    public void execute() {
        execute0();

    }
    private void execute0() {
Simulation simulation_0 = getActiveSimulation();
String simName = simulation_0.getPresentationName();
Region region_0 = simulation_0.getRegionManager().getRegion("Fluid Vert+Dors");
Boundary boundary_0 = region_0.getBoundaryManager().getBoundary("Inflow");
FlowDirectionProfileflowDirectionProfile_0=boundary_0.getValues().get(FlowDirectionProfile
.class);
stepStoppingCriterion_0=simulation_0.getSolverStoppingCriterionManager().getSolverStoppin
gCriterion("Maximum Steps");
        int beta[] = {5,10,15,19,23,26,29,33,36,38,40,41,43}
        for (int i = 0; i< beta.length; i++ )
{ flowDirectionProfile_0.getMethod(ConstantVectorProfileMethod.class).getQuantity().setCom
ponents(Math.cos(Math.toRadians(beta[i])), Math.sin(Math.toRadians(beta[i])), 0.0);
int MaximumNumberSteps = 2000 + 2000*(i);
stepStoppingCriterion_0.setMaximumNumberSteps(MaximumNumberSteps);
simulation_0.getSimulationIterator().run();
macrosimulation_0.saveState(resolvePath(simName + "_beta" + beta[i] + ".sim"));
        }
    }
}
}
```

2) ROUTINE TO CONTROL THE METHOD NO.1 OF [3]

% Statistics equation

$$S_{df} = 0.164 * S_v;$$

$$S_{df_plus} = 0.190 * S_v$$

$$\text{Phi}_{0_df} = 2.244 * \text{Phi}_{0_v}; \quad \text{o} \quad \text{Phi}_{0_df} = 70.49 + 0.141 * \text{Phi}_{0_v};$$

$$\text{Delta}_{\text{Phi}} = 70.49 - 0.859 * \text{Phi}_{0_v};$$

$$\text{Cr}_{df} = 2.699 * \text{Cr}_v;$$

$$\text{L}_{df} = 1.156 * \text{Cr}_{df};$$

$$\text{h}_{df} = 3.664 * \text{b}_v;$$

% Geometrical Input

$$S_v = 2.5 ; \quad \% \text{ m}^2$$

$$\text{Phi}_{0_v} = 26.6; \quad \% \text{Phi}_{0_v}(i);$$

% Geometrical-Statistici Dorsal Fin

$$\text{Phi}_{0_df} = 70.49 + 0.141 * \text{Phi}_{0_v};$$

$$S_{df} = 0.164 * S_v;$$

% h_df calculation by method [1]

$$\text{h}_{df} = \text{sqrt}((2 * 0.164 * S_v) / (\tan(70.49 / 57.3 + 0.141 * \text{Phi}_{0_v} / 57.3) - \tan(\text{Phi}_{0_v} / 57.3)));$$

% Geometrical Output

$$\text{L}_{df} = \text{h}_{df} * \tan(\text{Phi}_{0_df} / 57.3);$$

$$\text{L}_{v_df} = \text{h}_{df} * \tan(\text{Phi}_{0_v} / 57.3);$$

$$\text{Cr}_{df} = \text{L}_{df} - \text{L}_{v_df};$$

Bibliography

- [1] Danilo Ciliberti, Fabrizio Nicolosi, Pierluigi Della Vecchia, A NEW VERTICAL TAILPLANE DESIGNPROCEDURE THROUGH CFD, Università degli Studi di Napoli Federico II, 2012.
- [2] Snorri Gudmundsson, GENERAL AVIATION AIRCRAFT DESIGN: APPLIED METHODS AND PROCEDURES, Elsevier, 2014.
- [3] Priyanka Barua, Tahir Sousa, Dieter Scholz EMPENNAGE STATISTICS AND SIZING METHODS FOR DORSAL FINs, Aircraft Design and Systems Group (AERO) Department of Automotive and Aeronautical Engineering Hamburg University of Applied Sciences Berliner Tor 9 Aero_TN_TailSizing_15-04-2013.
- [4] Ed Obert. AERODYNAMIC DESIGN OF TRANSPORT AIRCRAFT. Delft, The Netherlands : Delft University of Technology, 2009
- [5] R. D. Finck. USAF STABILITY AND CONTROL DATCOM. AFWAL-TR- 83-3048. Wright Patterson Air Force Base, Ohio: McDonnell Douglas Corporation, 1978.
- [6] SCoPE. Università degli studi di Napoli 'Federico II'. 2015. url: <http://scope.unina.it/>
- [7] Pierluigi Della Vecchia, Danilo Ciliberti, NUMERICAL AERODYNAMIC ANALYSIS ON A TRAPEZOIDAL WING WITH HIGH LIFT DEVICES: A COMPARISON WITH EXPERIMENTAL DATA, XXII AIDAA Conference, Napoli (Italy), September 9-12, 2013.
- [8] National Advisory Committee for Aeronautics, Technical Note NO 785 WIND-TUNNEL INVESTIGATION OF FUSOLAGE STABILITY IN YAW WITH VARIOUS ARRANGEMENTS OF FINs H. Page Hoggard, Jr. Langley Memorial Aeronautical Laboratory , 11-1940
- [9] Edmund T. Allen and George S. Schairer, Seattle, Wash AIRCRAFT EMPENNAGE UNITED STATES; PATENT OFFICE , Boeing Aircraft Company, Seattle, Wash., a corporation of Washington ", Serial No. 350,512 1 g 12 Claims. 22-8-1944.
- [10] Courtland D. Perkins and Robert E. Hage. AIRPLANE PERFORMANCE STABILITY AND CONTROL. Wiley, 1949
- [11] Daniel P. Raymer. AIRCRAFT DESIGN: A CONCEPTUAL APPROACH. American Institute of Aeronautics and Astronautics, 2004.
- [12] Jan Roskam. AIRPLANE DESIGN. DAR Corporation, 1997.
- [13] Hermann Schlichting and Erich Truckenbrodt. Aerodynamics of the airplane. McGraw-Hill, 1979.
- [14] Egbert Torenbeek. SYNTHESIS OF SUBSONIC AIRPLANE DESIGN. Delft University Press, 1976.
- [15] Star-CCM+ Version 6.06.017 User Guide. CD-adapco. 2011.